Superconducting Nanowires for Soft X-Ray Single-Photon Detection

---

Dissertation
zur
Erlangung der naturwissenschaftlichen Doktorwürde
(Dr. sc. nat.)

vorgelegt der
Mathematisch-naturwissenschaftlichen Fakultät
der
Universität Zürich
von

Kevin Michel Inderbitzin

von

Baar ZG und Schwyz SZ

Promotionskomitee
Prof. Dr. Andreas Schilling (Vorsitz und Leitung)
Prof. Dr. Hugo Keller
Dr. Andreas Engel

Zürich, 2013

"So there is plenty of room at the bottom! Don't tell me about microfilm!"

Richard P. Feynman (1918-1988) in a seminal talk on the possibilities of manipulating matter at the nanoscale.

Caltech, Pasadena, December 1959

Contents

Abstract

Superconducting nanowire single-photon detectors (SNSPDs) are well studied detectors for the near-IR and visible energy range, allowing timing resolutions of less than 30 ps and photon count rates of up to 2 GHz. Detection of single massive particles, namely MeV-α-particles, keV-macromolecules, keV-electrons and keV-argon-ions, has also been demonstrated. Preliminary experiments on soft X-ray single-photon detection with thick-film SNSPDs (called "X-SNSPDs" throughout this thesis) by Gabutti *et al.* and a thin-film SNSPD by Perez de Lara *et al.* had also shown promising results. X-SNSPDs are therefore good candidates for the detection of single soft X-ray photons with a good timing resolution, very high count rates and negligible dark count rates. However, no studies on continuous X-ray photon counting by X-SNSPDs had been reported before.

The work presented in this thesis comprises the development and characterization of such X-SNSPDs for X-ray photons in the energy range between a few keV and 50 keV, including the detector fabrication and the construction of the experimental setup for detector characterization. X-SNSPDs were fabricated from three different types of superconducting films: 6 nm thin NbN, 100 nm thick Nb and 100 nm thick TaN.

Results from the experiments with the SNSPD from 6 nm thin NbN support the previously reported finding that soft X-ray photon detection in these thin-film detectors mostly occurs through photon absorption in the sapphire substrate and the successive energy diffusion to the superconducting meander structure. The soft X-ray device detection efficiency of such a thin-film detector is even larger than that of an X-SNSPD from the 100 nm thick superconducting films, as the thickness of the substrate allows for a better photon absorption in the substrate than in the superconducting films. It is very likely, however, that this indirect detection principle for X-ray photons results in an increased timing jitter compared to direct visible photon detection in the superconducting film, due to the random nature of the energy diffusion processes to the superconducting meander structure after photon absorption and the random photon absorption depth.

Therefore, X-SNSPDs from 100 nm thick films have been studied. We showed that a 100 nm thick Nb X-SNSPD is capable to detect photons ultrafast and even at reduced bias currents of 0.4%, which is in sharp contrast to thin-film SNSPDs detecting visible photons. No dark counts were recorded in extended measurement periods. Strikingly, the pulse amplitude distribution depends significantly on the photon energy spectrum, and we estimate that an energy resolution better than 1.5 keV is realized in the energy range $\approx 8 - 10$ keV.

X-SNSPDs from 100 nm thick TaN were then fabricated with various nanowire widths, and their properties were compared with corresponding data from the Nb X-SNSPD. The TaN X-SNSPDs offer an improved detector performance regarding device detection efficiency, latching and pulse amplitudes. Wide nanowires allow for a certain energy-resolving capability in contrast to narrow TaN nanowires. However, wide nanowires also limit the detection efficiency at low temperatures, which can be explained within a hot-spot model. Interestingly, this observed trend in the temperature dependence of the cut-off energy (the minimum photon energy being detectable) of the TaN X-SNSPD is the opposite to the trend we observed for optical photon detection in thin-film TaN SNSPDs, where the cut-off energy decreases for lower temperature probably due to a decreasing quasiparticle diffusion coefficient. This discrepancy can be explained by the orders of magnitude higher energy of the keV-photons compared to the optical photons in the eV-range, leading to the formation of a normal-conducting hot-spot immediately after photon absorption in the case of keV-photons, making the temperature dependence of the quasiparticle diffusion coefficient less important for the formation of a detectable normal domain.

Deutsche Zusammenfassung

Supraleitende Nanodraht-Einzelphotonen-Detektoren (SNEPDen) sind eine sehr gut studierte Art von Detektoren für Licht und Nahinfrarotstrahlung und erlauben eine Zeitauflösung von weniger als 30 ps und Photonen-Zählraten von bis zu 2 GHz. Auch die Detektion von einzelnen massiven Teilchen, namentlich MeV-α-Teilchen, keV-Makromolekülen, keV-Elektronen und keV-Argon-Ionen konnte bereits demonstriert werden. Erste Experimente zur Detektion weicher Röntgen-Photonen mit Dickfilm-SNEPDen (durch Gabutti *et al.*) und mit einem Dünnfilm-SNEPD (durch Perez de Lara *et al.*) erzielten ihrerseits vielversprechende Resultate. SNEPDen bieten sich entsprechend als gute Kandidaten für die Detektion von einzelnen weichen Röntgen-Photonen mit guter Zeitauflösung, hoher Zählrate und vernachlässigbaren Dunkelzähl-Ereignissen an. Jedoch wurden bis anhin noch keine erfolgreichen Versuche zu kontinuierlichem Röntgen-Photonen-Zählen mit Dickfilm-SNEPDen publiziert.

Die in dieser Dissertation präsentierten Untersuchungen umfassen die Entwicklung und Charakterisierung von solchen Dickfilm-SNEPDen für die Detektion von weichen Röntgen-Photonen im Energie-Bereich von einigen keV bis 50 keV, und beinhalten auch die Detektor-Herstellung sowie die Konstruktion des experimentellen Setups für die Detektor-Charakterisierung. Die SNEPDen wurden dabei aus drei verschiedenen supraleitenden Filmen hergestellt: 6 nm dünnem NbN, 100 nm dickem Nb und 100 nm dickem TaN.

Die Resultate der Experimente mit dem 6 nm dünnen NbN SNEPD untermauern die bereits bekannte Erkenntnis, dass Detektion weicher Röntgen-Photonen in Dünnfilm-SNEPDen hauptsächlich durch die Photonen-Absorption im Saphir-Substrat und die anschliessende Energie-Diffusion zur supraleitenden Mäander-Struktur möglich ist. Die Detektionseffizienz für weiche Röntgen-Photonen ist dabei sogar grösser als in SNEPDen aus 100 nm dicken Filmen, da durch die Dicke des Substrats eine grössere Absorptionswahrscheinlichkeit im Substrat als im supraleitenden Film ermöglicht wird. Es ist dabei sehr wahrscheinlich, dass auf Grund der zufälligen Natur der Energie-Diffusionsprozesse zur Mäander-Struktur wie auch der zufälligen Photonen-Absorptionstiefe dieses indirekte Detektionsprinzip für Röntgen-Photonen in einer schlechteren Zeitauflösung im Vergleich zur direkten Detektion von Photonen resultiert.

SNEPDen aus 100 nm dicken Filmen wurden deshalb vertieft studiert. Wir konnten dabei zeigen, dass 100 nm dicke Nb SNEPDen Photonen ultraschnell und sogar noch bei tiefen reduzierten Betriebsströmen von 0.4% detektieren können, im Gegensatz zur Detektion sichtbarer Photonen in Dünnfilm-Detektoren. Dabei wurden selbst in ausgedehnten Messperioden keine Dunkelzähl-Ereignisse aufgezeichnet. Interessanterweise hängt die Amplituden-Verteilung der Detektionspulse signifikant vom Energie-Spektrum der Röntgenstrahlung ab, und wir schätzen die erzielte Energieauflösung auf besser als 1.5 keV im Energiebereich $\approx 8 - 10$ keV.

Um die Leistungsfähigkeit dieses Detektor-Typs weiter zu verbessern, haben wir daraufhin Dickfilm-Detektoren aus 100 nm dickem TaN mit unterschiedlichen Nanodraht-Breiten hergestellt und diese verglichen mit dem 100 nm Nb Detektor. Die TaN Detektoren erzielen verbesserte Eigenschaften in Bezug auf Detektionseffizienz, Latching und Puls-Amplituden. Breitere Nanodrähte erlauben dabei eine gewisse Energieauflösung im Gegensatz zu den schmaleren Nanodrähten. Jedoch begrenzen breite Nanodrähte auch die Detektionseffizienz bei tieferen Temperaturen, was mit Hilfe eines thermodynamischen Modells erklärt werden konnte. Interessanterweise ist dieser Trend in der Temperatur-Abhängigkeit der minimal detektierbaren Photonen-Energie genau gegenteilig zum Trend, welchen wir bei der optischen Photonen-Detektion mit Dünnfilm-Detektoren beobachtet haben, wo diese Energie-Grenze abnimmt mit tieferer Temperatur. Diese scheinbare Diskrepanz kann erklärt werden durch die Tatsache, dass die Energien der weichen Röntgen-Photonen (im keV-Bereich) diejenige der sichtbaren Photonen (im eV-Bereich) um Grössenordnungen übersteigt, und dies bereits unmittelbar nach der Photonen-Absorption zur Bildung eines normalleitenden Bereichs im Nanodraht führt. Dies im Gegensatz zu den sichtbaren Photonen, wo sich erst durch Diffusion der entstandenen Quasiteilchen eine detektierbare normalleitende Domäne ausbilden kann und entsprechend die Temperatur-Abhängigkeit des Diffusionskoeffizienten im Detektionsprozess eine wichtige Rolle spielt, was den unterschiedlichen Trend in der Temperatur-Abhängigkeit der minimal detektierbaren Photonen-Energie erklären kann.

Chapter 1

Important Terms

In this introductory chapter, the relevant terms for the discussion of superconducting nanowire single-photon detectors, their performance and their superconducting properties in this thesis are introduced and discussed. Throughout this thesis the International System of Units (SI) applies.

1.1 Relevant terms for single-photon detection

1.1.1 Abbreviations SNSPD and X-SNSPD

The superconducting nanowire single-photon detector (SNSPD) is the type of single-photon detector which the research presented in this thesis has been conducted on. Its near-infrared (near-IR) and visible photon detection capability was first demonstrated by Golt'sman *et al.* [1] in 2001, using an $\approx$ 5 nm thin films of NbN, as reviewed in section 2.1. However, the original conceptual idea [2] and the first experiments [3–5] had the intention to detect keV-X-ray photons and MeV-α- and β-particles, using much thicker superconducting films (up to several 100 nm thick). In this work, we revive the idea of using thick superconducting films for soft X-ray single-photon detection, and call this type of detector "X-ray SNSPD" (X-SNSPD) to distinguish it from the thin-film detector type, as it performs differently.

1.1.2 Relevant electromagnetic spectrum

In the following table, the relevant types of electromagnetic radiation for this thesis are listed:

Radiation range	**Wavelength λ**	**Photon energy $E = hc/\lambda$**
Near-IR	2500-750 nm	0.5 eV – 1.7 eV
Visible	750-400 nm	1.7 eV – 3.1 eV
Ultraviolet	400-10 nm	3.1 eV – 0.1 keV
Soft X-ray	10-0.1 nm	0.1 keV – 10 keV
Hard X-ray	0.1-0.01 nm	10 keV – 100 keV

Plain SNSPDs without advanced optical structure integration (as, for example, into an optical cavity) are designed to detect efficiently in the near-IR and visible photon energy range at wavelengths 300 nm $\lesssim \lambda \lesssim$ 1850 nm [6]. Experiments on ultraviolet photon detection are rare [7]. However, SNSPDs have been shown to detect at wavelengths as small as 220 nm. X-SNSPDs are optimized for the photon detection in the soft and lower hard X-ray photon energy range up to a few 10 keV.

1.1.3 Performance metrics

An ideal single-photon detector produces an electrical signal well distinguishable from the noise signal whenever and only when a photon is incident on the detector. In practice, these ideal detector characteristics are usually not met, and performance metrics have to be defined (see also the review by Natarajan *et al.* [8]):

Coupling efficiency

In a photon-counting experiment, photons can be lost before reaching the detector due to absorption, scattering or reflection (for example in the air, at a cryostat window, a mirror, in a waveguide, optical fibers or others). The probability for a photon to reach the detector is defined as the coupling efficiency η_{coupl}.

Absorption efficiency

A photon incident on the active detector area can be absorbed, transmitted or reflected. The probability for the absorption of a photon is defined as the absorption efficiency η_{abs}, and depends on the photon energy, the detector material and geometry. The absorption efficiency η_{abs} of an (X-)SNSPD is therefore influenced by the geometric filling factor (the relative coverage of the active detector area by the superconducting structure), the superconducting film thickness and a possible photon polarization dependence induced by the detector geometry. Furthermore, detector integration into an advanced optical structure (as optical cavities, nano-antennas and others) can significantly increase η_{abs} for certain wavelengths.

Registering efficiency

A photon absorbed in the superconducting structure generates a detection event with a certain probability, defined as the registering efficiency η_{reg}, which in general depends on the photon energy.

System detection efficiency

The overall probability for a photon to be counted by a detection system, called "system detection efficiency" (SDE), is therefore a product of the coupling, absorption and registering efficiency:

$$SDE = \eta_{coupl} \cdot \eta_{abs} \cdot \eta_{reg}. \tag{1.1.1}$$

Device detection efficiency

The device detection efficiency (DDE) is defined as the number of counted photons normalized to the number of photons crossing the active detector area, and is often called "quantum efficiency" in literature. It is therefore the product of the absorption and registering efficiency:

$$DDE = \eta_{abs} \cdot \eta_{reg} \tag{1.1.2}$$

Therefore SDE and DDE are only equal for a perfect coupling efficiency ($\eta_{coupl} = 1$). If only the performance of a photon detector is of interest and not that of the whole detection system, DDE is the relevant quantity.

Normalized detection efficiency

In some situations it is useful to discuss DDE as a function of the photon energy E for different bias currents I_b normalized at a certain photon energy oder vice versa, as only the relative dependencies are of interest. These physical quantities are then referred to as normalized detection efficiencies.

Dark counts

Besides the different efficiency metrics discussed above, false counts not originating from a photon coupled into the detection system also limit the performance of a single-photon detector. They are called "dark counts" and are of different origin:

- **Background radiation:** Stray radiation emitted from outside the cryostat can often be completely shielded from the photon detector. However, the cryostat and sample is always at a finite temperature and therefore emits partially detectable thermal radiation according to the Stefan-Boltzmann law [9, 10], which cannot be completely shielded. In section 5.2 we present our measure to restrict the source of this radiation to cryostat surfaces which are as cold as liquid helium-4 temperature ($T \approx 4$ K at atmospheric pressure). Natural radioactivity and cosmic background radiation might also lead to false detection events. However, their contribution is assumed to be negligible due to the low DDE in this energy range for the detectors examined in this thesis.

- **Intrinsic fluctuations in the superconductor:** Superconductors are subject to intrinsic fluctuations which can induce false detection events in an SNSPD, as it will be discussed in more detail in section 2.1.5. Their frequency of occurrence strongly depends on the SNSPD dimensions and the operation conditions.

- **Electromagnetic noise:** Electromagnetic noise might induce a voltage signal larger than the signal threshold set, leading to a false count. In section 5.2.4 we will present our method to reduce the number of such false counts.

1.2 Relevant superconducting properties

1.2.1 Energy gap

Within the weak-coupling approximation, which is valid for TaN [11] ($T_{c,bulk} \approx 12 - 14$ K [12]), the BCS theory predicts an energy gap [13] at $T = 0$ K and zero magnetic field of

$$\Delta(0) = 1.764\ k_{\mathrm{B}} T_c, \tag{1.2.1}$$

where $k_{\mathrm{B}} = 1.381 \times 10^{-23}$ J/K $= 8.617 \times 10^{-5}$ eV/K is the Boltzmann constant and T_c is the critical temperature of the superconductor in zero magnetic field. It is also a good approximation for the intermediately-coupled superconductor Nb [14] ($T_{c,bulk} = 8.3$ K [12]). However, NbN ($T_{c,bulk} \approx 16$ K [12, 15]) is a strongly-coupled superconductor, and the energy gap at $T = 0$ K has been experimentally determined [16] to

$$\Delta(0) = 2.08\ k_{\mathrm{B}} T_c, \tag{1.2.2}$$

which slightly deviates from the expression above in Eq. 1.2.1.

The energy necessary to split up a Cooper pair is 2Δ, which corresponds to ≈ 3 meV for $T_c = 10$ K. The BCS theory also predicts the temperature dependence $\Delta = \Delta(T)$ in zero magnetic field by an analytical approximation (for weakly- [17] and strongly-coupled superconductors [18]):

$$\frac{\Delta(T)}{\Delta(0)} = \tanh\left(1.82\left[1.018\left(\frac{T_c}{T} - 1\right]\right)^{0.51}\right). \tag{1.2.3}$$

Therefore, the transition from the superconducting to the normal conducting state at T_c is accompanied with a vanishing energy gap $\Delta(T = T_c) = 0$.

1.2.2 Critical current

The transport current density j through a superconductor is always limited by a temperature- and material-dependent depairing critical current density $j_{c,dep}(T)$ [13] above which the energy gap Δ drops to zero. For nanowires with a width w fulfilling $w < \lambda_{eff}/2$, with λ_{eff} being the effective magnetic penetration depth resulting from the reduced dimensionality given by Eq. 1.2.15, it can be expressed at $T = 0$ K by

$$j_{c,dep} = \frac{n_s\,|e|\,\Delta(0)}{m_e v_F}, \tag{1.2.4}$$

where n_s is the Cooper pair density, v_F the Fermi velocity, $m_e = 9.109 \times 10^{-31}$ kg the electron rest mass and $|e| = 1.602 \times 10^{-19}$ C the positive elementary charge.

The experimentally determined critical current $I_{c,exp}$, however, is usually smaller than the expected depairing critical current $I_{c,dep}$ determined from $j_{c,dep}$, even in the case of a nanowire with a uniform width and thickness. The Bean-Livingston surface barrier [19], which prevents vortices (mainly created by the magnetic self-field of the bias current) from entering the superconductor at small bias currents, decreases with increasing bias current I_b and vanishes for $I_b > I_{c,barr}$ [20,21]. In the case of nanowires with a width $\xi \ll w \ll \lambda_{eff}$, length $L \gg w$ and thickness $d \approx \xi$ it was found that $I_{c,barr} \approx 83\%\, I_{c,dep}$ [20]. It is noteworthy that the application of the critical current $I_{c,barr}$ does not cause the phase transition into the normal state. Instead, the normal state resistivity is approached asymptotically with increasing $I_b > I_{c,barr}$ by increased dissipation originating in vortex crossing events.

The geometry of a real SNSPD differs from an ideal uniform nanowire in multiple ways, which results in a further reduction of the experimentally determined critical current $I_{c,exp}$: Firstly, SNSPDs are usually meander shaped (see Fig. 2.1 for an example), and it was shown [22–24] that the geometric 90°- and 180°-turns are accompanied by locally larger current densities in inner sharp corners due to current crowding, which leads to a local reduction of $I_{c,barr}$. In these sharp corners, normal domains can therefore nucleate and cause a reduction of $I_{c,exp}$. Secondly, imperfect nanofabrication can produce constrictions along a nanowire, leading to a local reduction of $I_{c,dep}$, hence $I_{c,barr}$ and possibly the overall $I_{c,exp}$ [25].

The applied bias current I_b is usually put in relation with the experimentally determined critical current $I_{c,exp}$, defining the "reduced bias current" $I_b/I_{c,exp}$.

1.2.3 Coherence lengths

The BCS coherence length [26] is given by

$$\xi_0 = \frac{\hbar v_F}{\pi \Delta(0)}, \tag{1.2.5}$$

with $\hbar = h/(2\pi)$ and $h = 6.626 \times 10^{-34}$ Js $= 4.136 \times 10^{-15}$ eVs being the Planck constant. ξ_0 is a measure for the average extension of a Cooper pair, or in other words, the distance over which the Cooper pair correlation is effective.

Within the Ginzburg-Landau (GL) theory the GL coherence length can be determined [27] for a type-II superconductor to

$$\xi(T) = \sqrt{\frac{\phi_0}{2\pi B_{c_2}(T)}} \tag{1.2.6}$$

with $\phi_0 = h/(2e) = 2.068 \times 10^{-15}$ Vs being the magnetic flux quantum and $B_{c_2}(T)$ the temperature-dependent upper critical magnetic induction. ξ is a measure for the smallest length scale over which the Cooper pair density can vary, and is naturally always larger than ξ_0 as such a variation can only exist on a length scale larger than the average extension of a Cooper pair.

1.2.4 Density of states at the Fermi energy

The total density of states N_0 at the Fermi energy E_F in the normal conducting state is an important quantity for discussing superconducting properties. It can be expressed by the normal-state resistivity ρ_n and the electron diffusivity $D = \frac{1}{3} v_F l$ (l is the mean free path) by the Einstein-Smoluchowski relation [28, 29]:

$$N_0 = \frac{1}{e^2 \rho_n D} \left(= \frac{3}{e^2 \rho_n v_F l} \right). \tag{1.2.7}$$

In the superconducting state within the BCS theory, the density of states is zero within the interval $E_F \pm \Delta$ and is diverging outside this interval at these interval boundaries [13].

1.2.5 Magnetic penetration depths

The London equations [30] imply that the magnetic flux density B in a superconductor obeys

$$\vec{\nabla}^2 \vec{B} = \frac{1}{\lambda_L^2} \vec{B}, \tag{1.2.8}$$

with λ_L being the London magnetic penetration depth, which in the case of a pure metal can be expressed by

$$\lambda_L = \sqrt{\frac{m_e}{\mu_0 n_s e^2}}, \tag{1.2.9}$$

with $\mu_0 = 4\pi \times 10^{-7}\, \frac{\mathrm{Vs}}{\mathrm{Am}}$ being the vacuum permeability. In a very large superconductor with its surface at $x = 0$, extending into the half space $x > 0$, an externally applied magnetic flux density in z-direction $\vec{B} = (0, 0, B_z)$ therefore vanishes exponentially on the length scale λ_L inside the superconductor,

$$B_z(x) = B_z(0) e^{-x/\lambda_L}. \tag{1.2.10}$$

Similarly, a bias current in a superconducting wire of circular cross-section with radius $r \gg \lambda_L$ only flows in a surface layer of thickness λ_L [13]. Wires with a radius $r \ll \lambda_L$, however, show a homogeneous current density in the whole cross-section. Within BCS theory, the London magnetic penetration depth can be expressed by the Fermi velocity v_F and the density of states at the Fermi energy N_0 [31],

$$\lambda_L(T = 0\ \mathrm{K}) = \sqrt{\frac{3}{\mu_0 e^2 v_F^2 N_0}}. \tag{1.2.11}$$

In the case of a dirty metal, which is equivalent to a small mean free path l, the magnetic penetration depth of a bulk superconductor λ_{bulk} increases beyond the London magnetic penetration depth λ_L. In the dirty limit defined as $l \ll \xi_0$ (which is valid for NbN and TaN), the bulk penetration depth can be approximated [13] by

$$\lambda_{bulk}(0) = \lambda_L(0) \cdot \sqrt{\frac{\xi_0}{l}}. \tag{1.2.12}$$

Using Eq. 1.2.11 for the London magnetic penetration depth, the Einstein-Smoluchowski relation (Eq. 1.2.7) and the expression for the BCS coherence length in Eq. 1.2.5, it can also be expressed by

$$\lambda_{bulk}(0) = \sqrt{\frac{\hbar \rho_n}{\pi \mu_0 \Delta(0)}}. \tag{1.2.13}$$

In this dirty limit, the temperature dependence of λ_{bulk} can be approximated [32] by

$$\frac{\lambda_{bulk}(T)}{\lambda_{bulk}(0)} = \left(1 - \left(\frac{T}{T_c}\right)^2\right)^{-0.5} \cdot \left(1 + \left(\frac{T}{T_c}\right)^{1.5}\right)^{-0.25}. \tag{1.2.14}$$

In thin superconducting films with a thickness $d \ll \lambda_{bulk}$, the reduced dimensionality leads to an effective magnetic penetration depth λ_{eff} larger than λ_{bulk} [33],

$$\lambda_{eff} = \frac{2\lambda_{bulk}^2}{d}. \tag{1.2.15}$$

The λ_{eff} can therefore deviate from λ_{bulk} by orders of magnitude, as in the case of a NbN SNSPD with $d \approx 5$ nm and $\lambda_{bulk} \approx 340$ nm (as in chapter 6), resulting in $\lambda_{eff} \approx 45$ μm, and a 100 nm thick TaN X-SNSPD with $\lambda_{bulk} \approx 1$ μm (as in chapter 7), resulting in $\lambda_{eff} \approx 19$ μm. Biasing these detectors with a current I_b therefore leads to a homogeneous current distribution in the entire nanowire cross-section.

1.2.6 Kinetic inductance

In superconducting films or nanowires, the inductance is mainly determined by the kinetic inductance L_{kin} and not by the magnetic inductance L_{magn} [34]. The energy of the magnetic field generated by an applied bias current I_b is given by L_{magn},

$$E_{magn} = \frac{1}{2} L_{magn} I_b^2. \tag{1.2.16}$$

Analogously, L_{kin} is associated with the bias current-induced kinetic energy of the current carriers

$$E_{kin} = \frac{1}{2} L_{kin} I_b^2. \tag{1.2.17}$$

For a $d = 40$ nm thick Nb SNSPD [34] with nanowire width and spacing $w = g = 1$ μm, for example, the values $L_{magn} = 7.0$ nH and $L_{kin} = 129$ nH were calculated [35], which correspond to the energies $E_{magn} = 4.5 \times 10^5$ eV and $E_{kin} = 8.4 \times 10^6$ eV for the bias current $I_b \approx 4.6$ mA, respectively.

The kinetic inductance of a nanowire with a thickness $d \ll \lambda_{bulk}$ can be calculated [36] by using Eq. 1.2.15 (valid for 5 nm thin NbN SNSPDs and 100 nm thick X-SNSPDs),

$$L_{kin} = \frac{\mu_0 \lambda_{eff} l}{w} = \frac{2\mu_0 \lambda_{bulk}^2 l}{wd}. \tag{1.2.18}$$

For superconducting films with $d \gtrsim \lambda$ (as in the case of a 100 nm thick Nb film with $\lambda \approx 100$ nm), this limit is no longer valid, and the kinetic inductance can then be estimated [37] from

$$L_{kin} \approx \frac{\mu_0 \lambda_{bulk} l}{w}. \tag{1.2.19}$$

Typical values for the kinetic inductance L_{kin} of SNSPDs and X-SNSPDs are of the order of $\approx 10 - 200$ nH.

Chapter 2

Review of SNSPD Properties and Their Advantages

This chapter discusses properties and detection principles of SNSPDs regarding the detection of near-IR and visible photons as well as keV-particles and -photons. In addition, the advantages of these detectors compared to other near-IR, optical and X-ray single-photon detectors are discussed.

This chapter is based to some extent on the extensive reviews by Engel *et al.* [38] and Natarajan *et al.* [8].

2.1 Near-IR and visible single-photon detection

The most basic form of an SNSPD consists of nanowires joined together to a meander as a means to cover the active detector area as efficiently as possible. Fig. 2.1 shows an example of such an SNSPD. Typically, the nanowires are fabricated from a thin superconducting film with a thickness of $d \lesssim 4.5 - 6$ nm and a width of $w \approx 30 - 200$ nm [1,39]. The most commonly used material today is NbN. However, SNSPDs based on other materials with a smaller energy gap $\Delta(0)$ such as a-$\mathrm{W}_x\mathrm{Si}_{1-x}$ [6], NbSi [40] and TaN [41] show a better sensitivity in the near-IR photon energy range.

SNSPDs are usually operated well below their critical temperature T_c. As the energy of an absorbed visible or near-IR photon with $E = h\nu \approx 1$ eV is orders of magnitude larger than the energy gap $\Delta(0)$, Cooper pairs are broken up into

$$M = \zeta \frac{h\nu}{\Delta} \tag{2.1.1}$$

quasiparticles in an avalanche multiplication process [43], where ζ is the quasiparticle multiplication efficiency, a material-dependent parameter less than unity accounting for

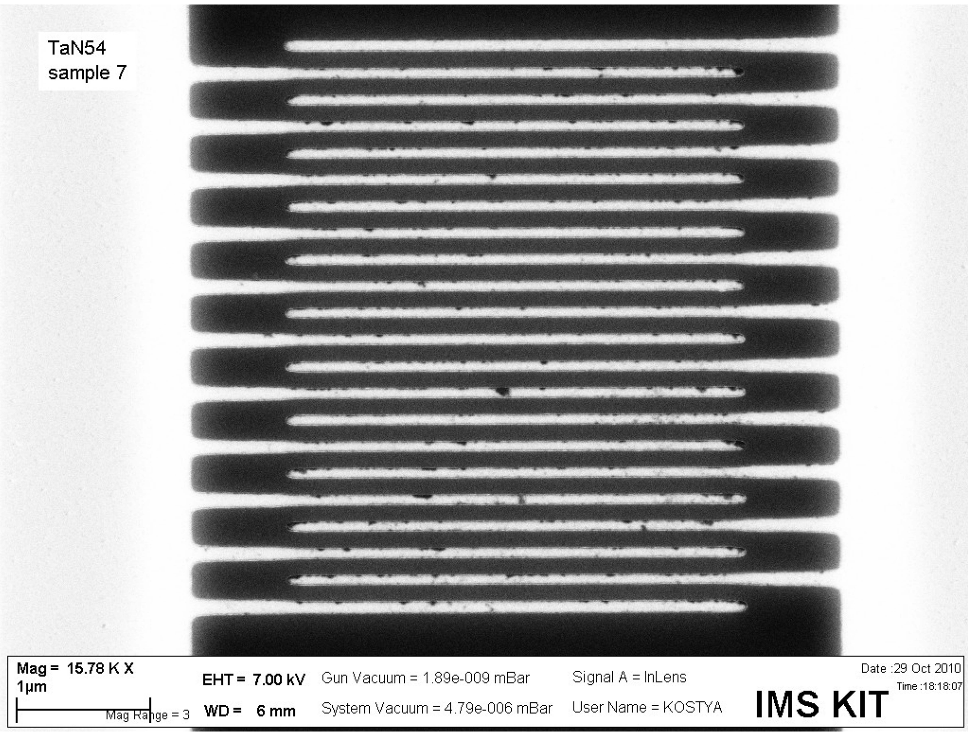

Figure 2.1: This SEM (scanning electron microscope) image shows a typical SNSPD, here fabricated from a 3.9 nm thick TaN film on sapphire. The detector covers an area of 4 μm $\times$ 3.5 μm with a 110 nm wide nanowire and a filling factor of 55%. Its photon detection capabilites are discussed in subsection 2.1.3 and in Ref. [41] (appended at the end of this chapter). This figure is taken from our work by Il'in *et al.* [42].

losses during the avalanche multiplication. For typical SNSPD from NbN [38] and TaN [41] thin-films, ζ is of the order of 0.1. Visible and near-IR photons therefore typically have enough energy to break up several hundreds of Cooper pairs.

2.1.1 Hot-spot model

In order for an SNSPD to detect near-IR and visible photons, a bias current I_b through the detector as close as possible to the experimentally determined critical current $I_{c,exp}$ is applied (Fig. 2.2(a)(i)). The current distribution is thereby homogeneous in the nanowire cross-section, as the effective magnetic penetration depth λ_{eff} is much larger than the nanowire width w (see section 1.2.5). Gol'tsman *et al.* [1] and Semenov *et al.* [44] introduced a first model to explain the near-IR and visible photon detection mechanism (illustrated in Fig. 2.2(a)), which was later refined by Semenov *et al.* [45] (see the next section 2.1.2 for the refined model). This first model claims that breaking up M Cooper pairs (see Eq. 2.1.1) leads to the energy gap being locally reduced to zero at the photon absorption point, and therefore to the suppression of superconductivity. At the same time, a cylindrically shaped normal-conducting area with diameter $2r_0$, a so called "hot-

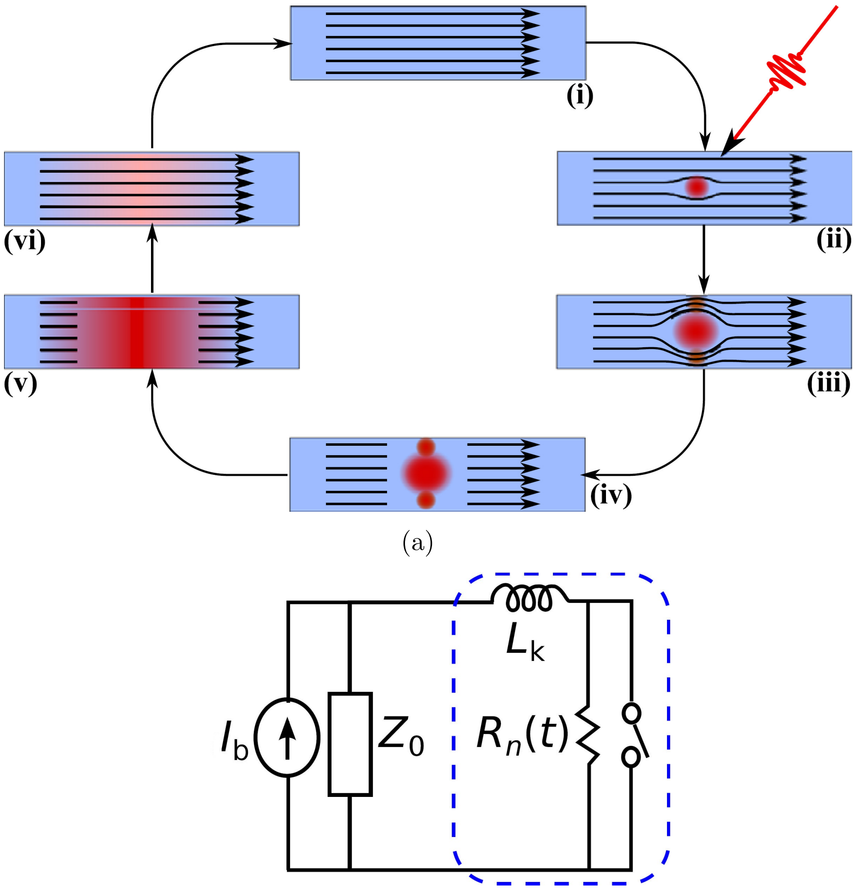

(a)

(b)

Figure 2.2: **(a)** Schematic illustration of the preliminary model explaining the SNSPD detection principle for near-IR and visible photons, the hot-spot model introduced by Gol'tsman *et al.* [1] and Semenov *et al.* [44]. Details are explained in the text. **(b)** Simple equivalent electrical circuit for an SNSPD biased with a current I_b, consisting of a domain resistance $R_n(t)$ and a kinetic inductance L_{kin}. Both images are adapted from Ref. [8].

spot", is created (Fig. 2.2(a)(ii)). The hot-spot diameter is smaller than the nanowire width, and therefore the externally applied bias current I_b with current density j_b is expelled from the (normal) hot-spot and diverted around it into the superconducting region (Fig. 2.2(a)(iii)), with the bias current density locally increasing to

$$j_b' = \frac{wd}{wd - 2r_0 d} j_b = \frac{w}{w - 2r_0} j_b > j_b. \tag{2.1.2}$$

If the bias current fulfills the condition

$$I_b \geq \frac{w - 2r_0}{w} I_{c,dep} = \left(1 - \frac{2r_0}{w}\right) I_{c,dep} \tag{2.1.3}$$

after photon absorption, the local current density j_b' around the hot-spot exceeds the local critical current density $j_{c,dep}$. This in turn leads to the formation of a resistive domain across the entire width of the nanowire (Fig. 2.2(a)(iv)) with the time-dependent resistance $R_n(t)$. Joule heating then leads to a growth of the resistive region along the nanowire [46].

Fig. 2.2(b) shows a simple equivalent electrical circuit for an SNSPD biased with I_b. The SNSPD itself is modeled by a normal domain resistance $R_n(t)$ in parallel to a switch which opens if a photon is detected, and the kinetic inductance L_{kin} of the detector. Since R_n grows to at least hundreds of Ohms or even kilo-Ohms [47,48] by Joule heating when a photon is detected (and as therefore the switch is open), the bias current will be diverted into the $Z_0 = 50\ \Omega$-impedance read-out line. The hot-spot then cools down to operation temperature due to vanishing Joule heating if no detector latching occurs (see section 2.1.9 for a detailed discussion), and the superconducting state is recovered.

2.1.2 Refined detection model

The maximum diameter $2r_0$ of the hot-spot for the absorption of a 1 eV-photon can be estimated, which is smaller than the GL coherence length ξ of a typical SNSPDs [45]. According to the hot-spot detection model [1], such small hot-spots cannot trigger the formation of a resistive domain. However, experimentally the detection of 1 eV-photons is clearly observed. Therefore a refined detection model was developed by Semenov *et al.* [45], which takes into account the full number of photon-induced quasiparticles and their spatial distribution, which is discussed in the following.

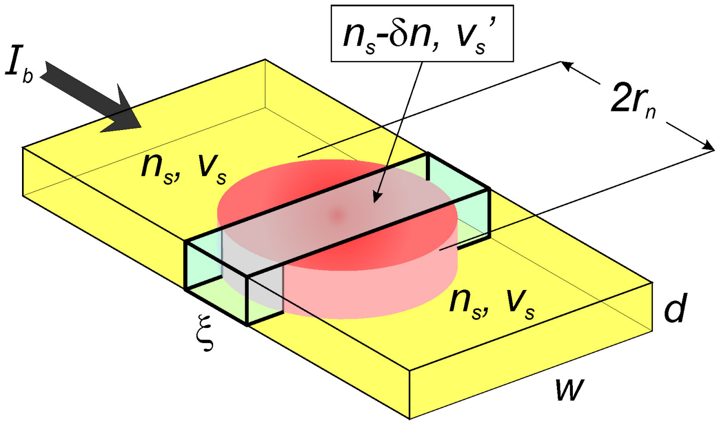

Figure 2.3: Scheme of a thin-film nanowire biased with a current I_b after photon absorption. The red cylinder with diameter $2r_0$ outlines the cloud of nonequilibrium quasiparticles. The bold lines indicate the smallest volume (called "ξ-slab" in this work) where the reduction of the Cooper pair density n_s by δn_s can cause a change of their mean velocity (from v_s to v_s'). This figure is adapted from Ref. [38].

As the current density is homogeneous in the nanowire cross-section, it can be expressed as

$$j_s = 2en_s v_s, \tag{2.1.4}$$

with the mean pair velocity v_s and the mean density n_s of Cooper pairs with charge $2e$. Without magnetic perturbations, the local current density can only vary along the nanowire axis and only if n_s varies along the axis over a distance of ξ or larger. Shorter perturbations are tunneled by Cooper pairs without energy dissipation. Therefore, the smallest volume relevant to a current density variation has the dimensions $d \times w \times \xi$, as indicated in Fig. 2.3 by bold lines, which we call "ξ-slab" in this work. An absorbed photon locally reduces the Cooper pair density n_s by δn_s and hence locally weakens superconductivity. However, the region around the absorption point does not necessarily turn normal conducting, as the hot-spot model assumed. Nevertheless, due to charge-flow conservation, the mean pair velocity inside the ξ-slab has to increase to

$$v_s' = \frac{n_s}{n_s - \delta n_s} v_s. \tag{2.1.5}$$

The ξ-slab only switches into the normal conducting state if v_s' exceeds the local critical velocity v_c^*, determined from the pre-photon-absorption local critical current density $j_c^* = 2en_s v_c^*$. The incident photon therefore needs to have an energy E larger than a certain cut-off energy E_{co} in order to excite enough nonequilibrium quasiparticles δn_s to trigger the formation of a resistive domain. In the original publication [45], j_c^* and I_c^* have the values of the depairing values $j_{c,dep}$ and $I_{c,dep}$, respectively. However, future studies will have to examine, whether the detection process leads to vortex entry after photon absorption or not, and thus j_c^* and I_c^* should be better approximated by $j_{c,barr}$ and $I_{c,barr}$.

2.1.3 Cut-off energy and bias-current threshold

The cut-off energy E_{co} can be determined within the hot-spot model [49]. However, in the literature it is common to discuss the cut-off wavelength λ_{co} instead:

$$\lambda_{co} = \frac{hc}{E_{co}} \propto \frac{1}{N_0 \Delta^2 w^2 d (1 - \frac{I_b}{I_c^*})^2}. \tag{2.1.6}$$

Within the refined detection model discussed above one arrives at a slightly different expression [38] which also includes quasiparticle diffusion,

$$\lambda_{co} = \frac{hc}{E_{co}} = \frac{\zeta h c e^2}{\sqrt{\pi \tau_{therm}}} \rho_n \sqrt{D} \frac{1}{\Delta^2 A (1 - \frac{I_b}{I_c^*})}, \tag{2.1.7}$$

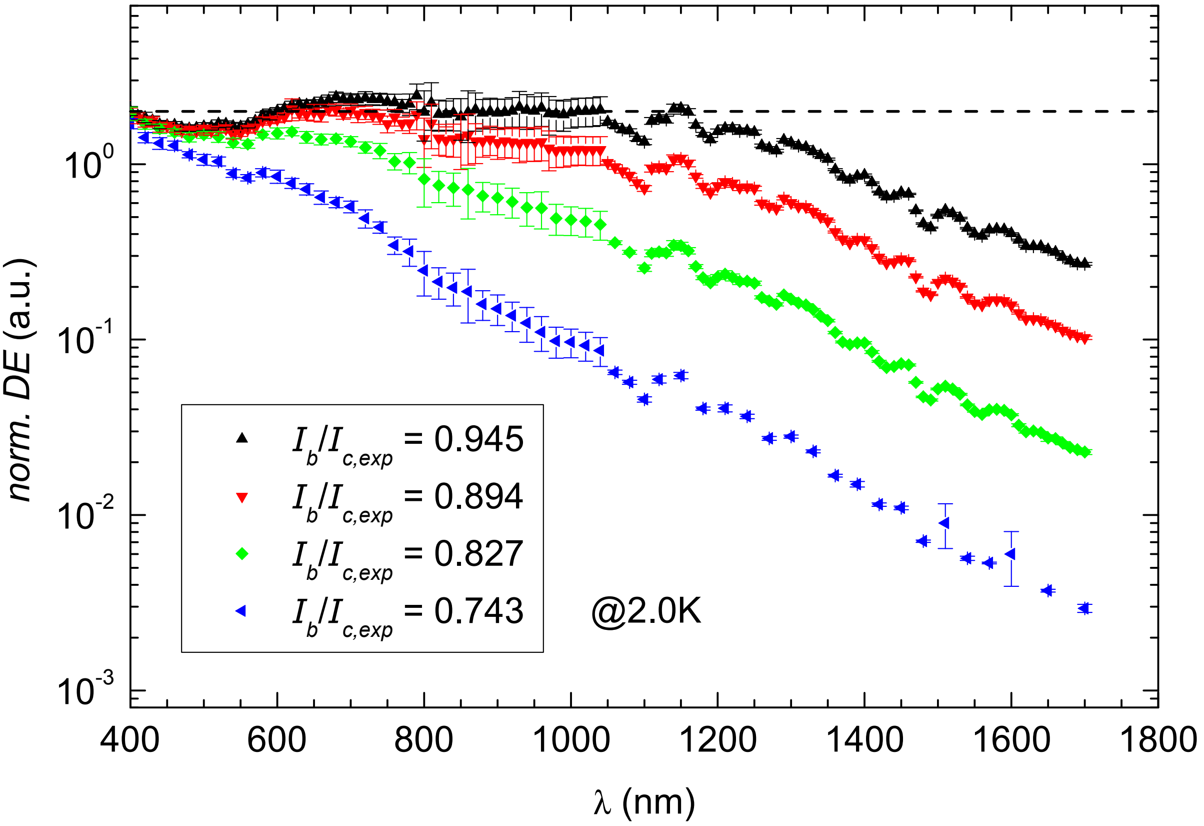

Figure 2.4: Normalized DE plotted versus the wavelength λ for different bias currents at $T = 2.0$ K. The horizontal dashed line marks the averaged maximum DE, at which the plots were normalized. The cut-off wavelength λ_{co} is here defined as the wavelength for which DE reaches half of its maximum value, which corresponds to the crossing point with $DE = 10^0 = 1$ in this plot. This figure is adapted from our work by Engel *et al.* [41].

with the normal state resistivity $\rho_n = 1/(N_0 e^2 D)$ (see Eq. 1.2.7), the nanowire cross-sectional area $A = wd$, the electron thermalization time τ_{therm} (the characteristic time after which most nonequilibrium electrons have thermalized to an energy level of only Δ above E_F and start to recombine again) and the speed of light in vacuum c. It follows that the cut-off wavelength strongly depends on the bias current I_b in relation to the local critical current I_c^*, but also on material parameters such as the normal state resistivity ρ_n and the critical temperature T_c via the energy gap Δ. For a fixed photon wavelength λ, it is possible to rewrite Eq. 2.1.7 in order to give the bias current threshold I_{th}, which is the minimum bias current applicable for the SNSPD to detect photons with wavelength λ:

$$\frac{I_{th}}{I_c^*} = 1 - \frac{\zeta h c e^2}{\sqrt{\pi \tau_{therm}}} \rho_n \sqrt{D} \frac{1}{\Delta^2 A \lambda_{co}}. \tag{2.1.8}$$

In order to illustrate these dependencies, measurements of a normalized detection efficiency (DE) on a 3.9 nm thin TaN SNSPD (SEM image shown in Fig. 2.1) from our work

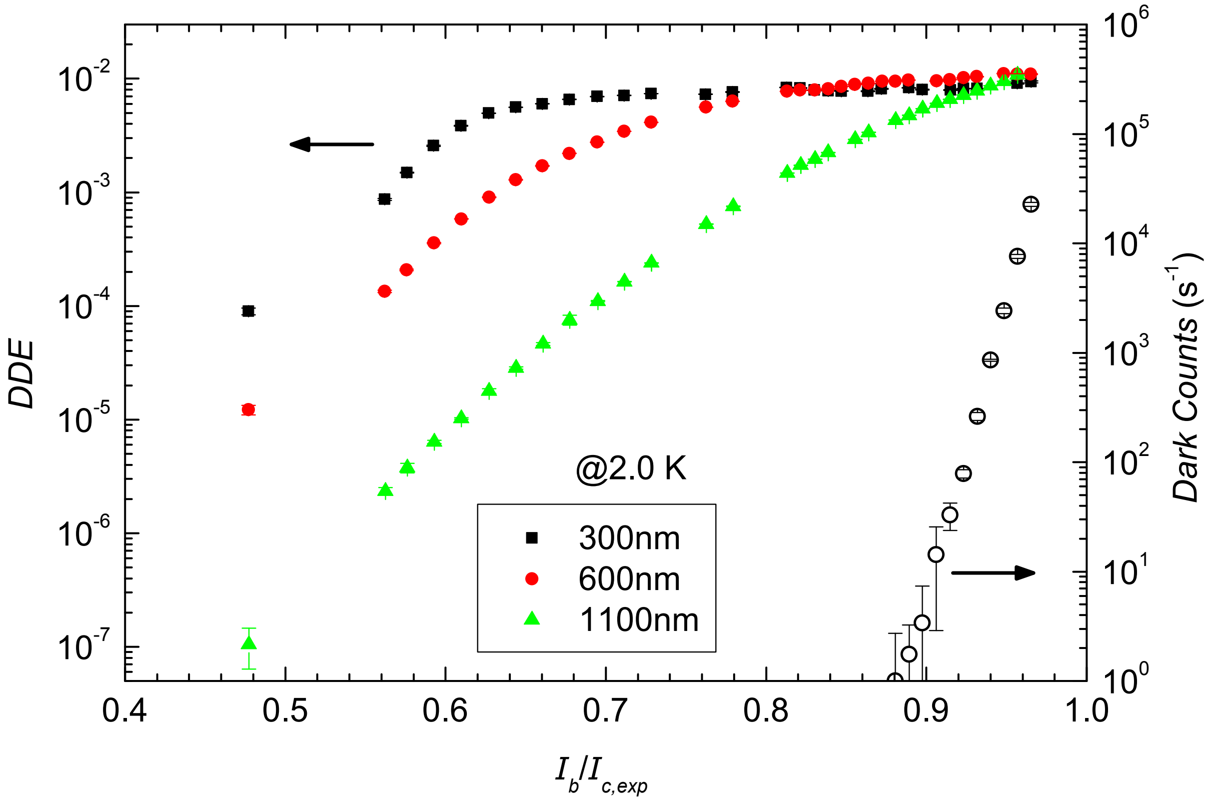

Figure 2.5: Measured *DDE* as functions of the reduced bias current $I_b/I_{c,exp}$ at $T = 2.0$ K (left axis). The bias current threshold I_{th} is defined as the bias current I_b at half of the maximum value of *DDE*. The open symbols show the dark count rates (right axis) at the same temperature, which are negligible for the qualitative discussion here. This figure is adapted from our work by Engel *et al.* [41].

in Ref. [41] (appended at the end of this chapter) as a function of the photon wavelength λ are shown in Fig. 2.4 for different reduced bias currents. *DE* shows a certain repeating noise pattern, which is at least partially caused by an elliptical polarization of the incident light and the polarization dependence of the SNSPD [7]. Therefore, the maximum *DE* was found by averaging *DE* in the range $\lambda = 300 - 1000$ nm for the highest presented I_b, as shown by the horizontal dashed line, and all plots were normalized to this maximum *DE* at $\lambda = 400$ nm. The cut-off photon wavelength λ_{co} can be defined as the wavelength, where *DE* reaches half of the maximum *DE*, and λ_{co} obviously decreases significantly with lower reduced bias currents $I_b/I_{c,exp}$ as expected by Eq. 2.1.7. In other words, the photon energy needs to be larger for the photon to be detected if the SNSPD is biased with a smaller current I_b.

In Fig. 2.5 measurements of *DDE* as a function of the reduced bias current $I_b/I_{c,exp}$ for different wavelengths are shown. For $\lambda = 300$ nm, a clearly identifiable plateau exists for bias currents above a certain bias current threshold I_{th}, which is here again defined as

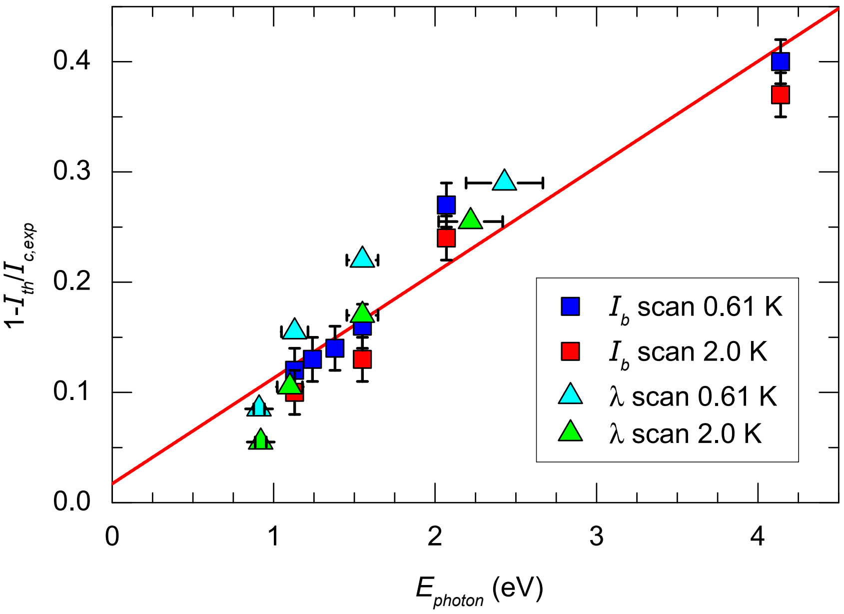

Figure 2.6: Summarized pairs of determined threshold currents I_{th} and minimum detectable photon energy E_{co} at both 0.61 K and 2.0 K, together with a least-square fit according to Eq. 2.1.7 and 2.1.8. The error bars are estimates of the accuracy in determining the cut-off criterion. This figure is adapted from our work by Engel *et al.* [41].

the bias current I_b for which DDE shows half of its maximum value. Obviously, $I_{th}/I_{c,exp}$ increases for larger wavelengths, in accordance to Eq. 2.1.8.

The resulting pairs of threshold currents and minimum photon energies E_{co} for $T =$ 0.61 K and 2.0 K are summarized in Fig. 2.6. According to Eq. 2.1.7 and 2.1.8, the corresponding $(1 - I_{th}/I_{c,exp})$ vs. E_{co} data points should lie on a single straight line through the origin, which is, within the accuracy of our data, indeed the case.

This TaN SNSPD was compared to an SNSPD made from NbN with a roughly equal nanowire cross-sectional area A, and a plot of their normalized DE in dependence of the reduced bias current for $\lambda = 300$ nm photons is shown in Fig. 2.7. The TaN SNSPD shows a lower reduced threshold bias current $I_{th}/I_{c,exp}$, as expected from Eq. 2.1.7, as the superconducting energy gap Δ of TaN is lower than for NbN, and its values for ρ_n and D are larger. In conclusion, the use of TaN as SNSPD material improves the DE at longer wavelengths as compared to the most commonly used NbN as detector material.

2.1.4 Temperature dependence of cut-off wavelength

The temperature dependence of the cut-off wavelength λ_{co} was examined in our work by Engel *et al.* [50], which is also appended to this chapter.

$\lambda_{co}(T)$ for a $\approx$ 5 nm thin TaN SNSPD at the fixed reduced bias current $I_b(T)/I_{c,dep}(T) =$ 0.36 is shown to increase with decreasing temperature T, as shown by the red circles in

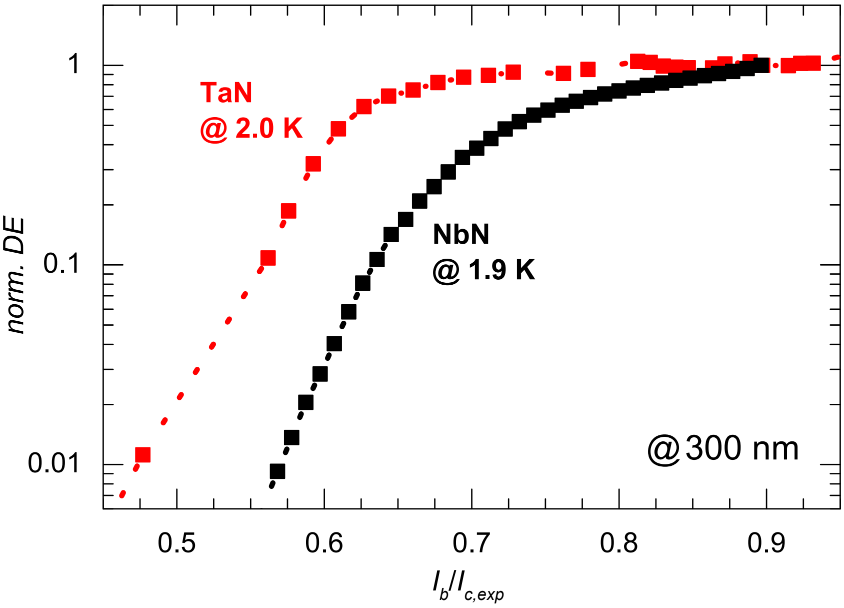

Figure 2.7: A comparison of the performance of the TaN and a NbN SNSPD with a similar nanowire cross-sectional area A at comparable temperatures. The figure shows the normalized DE for 300 nm photons as a function of the reduced bias current $I_b/I_{c,exp}$ for both detectors. This figure is adapted from our work by Engel *et al.* [41].

Fig. 2.8. In a first approach the temperature dependence of $\lambda_{co}(T)$ at fixed values for $I_b(T)/I_{c,dep}(T)$ is calculated in the hot-spot model according to Eq. 2.1.6 assuming the density of states at the Fermi energy N_0 is temperature-independent. The only temperature-dependent quantity in this equation is therefore the energy gap $\Delta(T)$, and thus the model predicts an increase of $\lambda_{co}(T)$ with an increasing temperature T, as indicated by the dashed line in Fig. 2.8, which is clearly incompatible with the trend in the data.

Taking into account the diffusion of the quasiparticles and the fact that non-equilibrium quasiparticles lead to a reduction of $I_{c,dep}$, the refined detection model (see Eq. 2.1.7) has to be applied and thus the temperature dependence of the diffusion coefficient $D(T)$ has also to be taken into consideration (while the electron thermalization time τ_{therm} is assumed to be temperature-independent). $D(T)$ can be numerically calculated [50], and the resulting temperature-dependent $\lambda_{co}(T)$ is plotted as a solid blue line in Fig. 2.8. For $T < 2$ K the trend in the data is reproduced well. However, for temperatures closer to T_c, the strong temperature dependence of $\Delta(T)$ should dominate and lead again to an increase in $\lambda_{co}(T)$. Unfortunately, it was not possible to extend our measurements to higher temperatures, due to rapidly decreasing critical-currents, resulting in small bias currents I_b and therefore small signal amplitudes. Also, the detector became increasingly unstable at elevated temperatures.

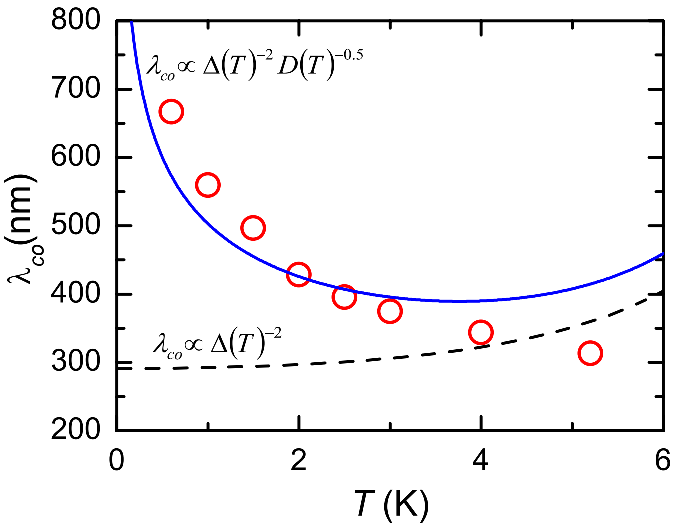

Figure 2.8: Data for the temperature-dependent cut-off wavelength $\lambda_{co}(T)$ (red circles) and two theoretical models: the hot-spot model incorporating the T-dependence of $\Delta(T)$ (dashed black line) cannot reproduce the data trend, while the refined detection model (blue solid line), which also takes into account the T-dependence of the diffusion coefficient $D(T)$, follows the trend for low temperatures. This figure is adapted from our work by Engel *et al.* [50].

2.1.5 Dark counts and fluctuation-assisted detection

Bulaevskii *et al.* [21] found that detector counts in typical thin-film SNSPDs can be caused by two more mechanisms besides the direct photon detection described by the refined detection model (see section 2.1.2): dark counts and vortex-assisted single-photon detection counts.

Several possible dark count mechanisms in SNSPDs have been discussed in the literature [20]: phase-slips, single-vortex crossings and vortex-antivortex pair nucleation. Bulaevskii *et al.* [21] argue that only single-vortices crossing a nanowire need to be considered, as the other mechanisms are exponentially suppressed due to their larger energy barrier. The count rate for this process increases with increasing bias current I_b due to a vanishing energy barrier. At a sufficiently large I_b this process dissipates enough energy to trigger the transition to the normal state of a strip across the whole width of the nanowire. This is a consequence of the Lorentz force acting on the vortex, leading to a dark count event.

A single absorbed photon of insufficient energy to trigger a normal conducting domain can nevertheless be detected if it initiates a subsequent single-vortex crossing of the nanowire by reducing the vortex-entry barrier into the nanowire via the local reduction of the critical current $I_{c,barr}$ [21] by the absorbed photon. This vortex crossing in turn provides the rest of the energy needed to create the normal conducting domain, similar to the dark count mechanism described in the paragraph above. This process is called "fluctuation-assisted photon detection", and it is relevant for wavelengths λ larger the cut-off wavelength λ_{co} at fixed bias currents I_b or for bias currents smaller than the threshold bias current I_{th} at a fixed photon wavelength λ. Obviously, photon detection in this regime is still possible, as shown for the TaN SNSPD in Fig. 2.4 and 2.5, even though DE is significantly reduced.

2.1.6 Device detection efficiency

The absorption efficiency of an SNSPD is given by its geometry and the superconducting material. As SNSPDs have typical thicknesses of only a few nanometers, some photons are not absorbed in the superconducting structure, but are transmitted or reflected. For a ≈ 5 nm thick NbN film, Semenov *et al.* [51] calculated the absorptance to $P_{abs} \approx 0.3$ for photons with wavelengths between 250 nm and 2500 nm. From an optical standpoint, a meander-shaped SNSPD is essentially a sub-wavelength grating, and it has indeed been shown to possess a noticeable polarization sensitivity that varies with wavelength, with a significantly worse absorptance for a electric field polarization perpendicular to the nanowire orientation [52]. As such a polarization-dependent absorption efficiency is often unwanted in experiments, SNSPDs with advanced designs were developed and shown to detect practically polarization-independently [53], namely spiral-shaped detectors and detectors including both perpendicular nanowire orientations. In addition, the filling factor of the active detector area reduces the absorption probability, usually on the order of 50% [54].

The registering efficiency for an SNSPD can, in principle, be close to unity for photon wavelengths smaller than the bias current-dependent cut-off wavelength λ_{co}, and has been shown to be polarization-independent [51]. However, as explained in section 1.2.2, constrictions in an otherwise uniform nanowire can prevent the SNSPD to be biased at a current I_b close to the critical current $I_{c,barr}$ of the corresponding ideally uniform nanowire. The local registering efficiency is therefore close to unity at the constriction sites for large enough bias currents. However, it might be significantly reduced at every other location along the nanowire, thereby hampering the overall SNSPD registering efficiency significantly [55].

As defined in section 1.1.3, SDE consists of the coupling, absorption and registering efficiency. Baek *et al.* [6] achieved a SDE of 19%-40% over a wavelength range of 1280-1650 nm with a a-W_xSi_{1-x} SNSPD with a standard design.

Sophisticated SNSPD integration has been used in recent years to increase SDE for SNSPDs beyond the limits given by the geometry and material restrictions discussed above, for example with optical cavity integration [56], addition of gold nano-antennas [57], underlying distributed Bragg mirrors [58] and optical waveguide integration [59].

2.1.7 Energy resolution

Semenov *et al.* [47, 60, 61] demonstrated an energy resolution of 0.55 eV for single photons in the near-IR energy range between 0.8 eV and 1.2 eV with a NbN SNSPD from 4.5 nm thin and 100 nm wide nanowires by discriminating the different pulse amplitudes of detected photons. Photons with a lower energy resulted in larger pulse amplitudes on average, which is at first glance in contradiction to the detection model, as larger photon energies also lead to a larger number of nonequlibrium quasiparticles. However, the absorbed energy of a detected photon in this energy-range is negligible compared to the energy stored in the bias current by the kinetic inductance [62] (see Eq. 1.2.17), which eventually is, to a large part, converted to Joule heat in the normal conducting domain [44, 46, 62]. Therefore, the energy or photon number resolution within the direct photon detection regime (as described by the refined detection model introduced in section 2.1.2) is lost due to the Joule heating in the normal conducting domain.

However, the energy range given above for which the photon energy resolution was observed corresponds to the regime (for the examined SNSPD) where the photon detection mechanism changes from direct photon detection (i.e. $\lambda \lesssim \lambda_{co}$) to fluctuation-assisted photon detection (i.e. $\lambda > \lambda_{co}$) at $I_b/I_{c,exp} = 0.98$ [60]. It is argued that in the fluctuation-assisted regime vortices moving across a nanowire lead to significantly larger normal domains than without crossing events in the direct photon detection regime, resulting in measurably larger pulse amplitudes. Outside this energy range of a crossover between two detection mechanisms, the energy resolution deteriorates significantly.

2.1.8 Single-photon detection mode

We now assume that an SNSPD is irradiated by a pulsed laser source. The absorption probability for n photons from a single laser pulse with a mean number of m photons per pulse incident on the SNSPD is $P(n) \propto (e^{-m}m^n)/(n!)$ [1]. For $m \ll 1$ this simplifies to

$$P(n) \propto \frac{m^n}{n!}. \tag{2.1.9}$$

Therefore, the probability for the absorption of one photon from a single pulse is $\propto m$, while for two photons it is $\propto m^2/2$.

Gol'tsman *et al.* [1] proved in experiments with 100-fs-laser pulses at $\lambda = 810$ nm that SNSPD are true single-photon detectors for bias currents I_b close enough to the critical current $I_{c,exp}$. The open rectangles in Fig. 2.9 show the count rate of a 1 μm long

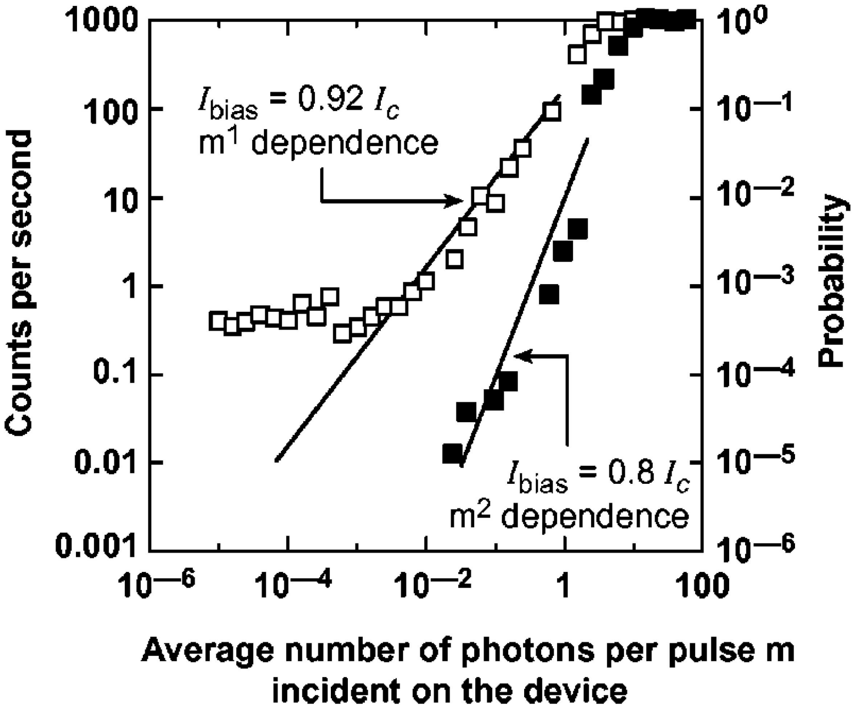

Figure 2.9: Photon count rate at $\lambda = 810$ nm as a function of the number of photons m per laser pulse incident on the nanowire, for two different bias currents. Fits proportional to m and m^2 are shown, in order to demonstrate single-photon and two-photon detection. This figure is taken from Ref. [1].

and 200 nm wide NbN bridge at $I_b = 0.92\ I_{c,exp}$, in dependence of m. Apart from the saturation for very high photon fluxes and the domination of the dark count rate for low photon fluxes, the count rate shows a linear behavior, proving single-photon detection. For a lower bias current of $I_b = 0.8\ I_{c,exp}$, the expected dependence on m^2 was observed (shown by the filled rectangles), as single-photon detection at this wavelength is obviously suppressed.

2.1.9 Dead time and latching

The characteristic time scale for alterations of the Cooper pair velocity is practically equal to the Ginzburg-Landau relaxation time [45] $\tau_{\mathrm{GL}} \approx h/\Delta \approx 2-3$ ps. Therefore, the mean velocity v_s in the ξ-slab instantaneously follows the alterations of the pair density n_s after photon absorption, according to the refined photon detection model, and consequently a normal domain forms. As already briefly discussed in section 2.1.1, the bias current is then almost completely diverted into the $Z_0 = 50\ \Omega$-impedance read-out line [46]. Following the simple model in Ref. [8], this current re-distribution occurs on a time scale of $\tau_1 = L_{kin}/(Z_0+R_n) \approx 10$ ps [63], which limits the rise time of the photon detection voltage pulse. R_n denotes here a temporally averaged value of the normal domain resistance.

The reduction of the current through the SNSPD results in the normal domain to cool down to operation temperature and to eventually restore its superconducting state. The relevant time scales are longer than τ_{GL}, giving rise to the formation of a normal domain in the first place: In NbN nanowires, electron-phonon scattering occurs on a time-scale $\tau_{e-p} \approx 10$ ps [8, 64], and the phonon escape time is reported to be $\tau_{es} \approx 160$ ps [63]. The bias current, however, is redistributed through the SNSPD on a much longer time scale of $\tau_2 = L_{kin}/Z_0 \approx 1 - 10$ ns [63]. Only after restoring the original bias current through the SNSPD, the SNSPD reaches its original DDE again.

The dead time of an SNSPD is therefore given by

$$\tau = \tau_1 + \tau_2 = L_{kin}\left(\frac{1}{Z_0 + R_n} + \frac{1}{Z_0}\right). \tag{2.1.10}$$

For thin-film SNSPDs, R_n is much larger than Z_0, and consequently the dead time is $\tau = \tau_1 + \tau_2 \approx \tau_2 = L_{kin}/Z_0$. For fast SNSPDs, τ is therefore on the order of 1 ns.

Following Eq. 2.1.10, the dead time of an SNSPD can be reduced by reducing its kinetic inductance L_{kin} (given by Eq. 1.2.18), for example by reducing the total nanowire length and thereby the active detector area. However, the kinetic inductance cannot be chosen arbitrarily small: If L_{kin} is too small, the bias current returns through the SNSPD too rapidly after being diverted to the $Z_0 = 50\ \Omega$ read-out line, and the normal conducting domain cannot cool down in the meantime and restore its superconducting state due to Joule heating. The SNSPD is then trapped in a so called “latched state”, where parts of the nanowire remain normal conducting. In order to recover its photon detection capability, the bias current I_b needs to be significantly reduced manually or electronically [65] after such an event. In this thesis, such an SNSPD operation mode is called “gated detection mode”, in contrast to the self-recovering mode discussed above, which is called “continuous detection mode”.

With SNSPDs, counting rates for near-IR and optical photons up to 2 GHz were achieved [66, 67].

2.1.10 Timing resolution (timing jitter)

When the arrival time of a photon is known extremely precisely (for example in experiments with short-pulsed lasers), the major part of the timing uncertainty (timing jitter) arises from the single-photon detector. SNSPDs offer a very low timing jitter, which makes them very attractive for time-correlated quantum optics experiments [8, 68]. The lowest timing jitter ever reported is 18 ps [66], but this result has not been widely reproduced, and the dimensions of the device and photon flux used are unclear [8] from the reports. A jitter of 29 ps has been demonstrated with small area (4.0 μm × 4.2 μm) single- and multi-pixel SNSPDs [69]. Larger area SNSPDs typically show a larger timing jitter: a 68 ps timing jitter has been communicated for 10 μm × 10 μm meander devices [70]. The reported results and nano-optical studies on SNSPDs [48] indicate that more uniform nanowires result in smaller timing jitters [8] (which is more easily achieved with a shorter nanowire length), due to less variable hot-spot resistances and thus less variable voltage pulse rise times. Larger critical currents have been observed to improve the timing jitter in uniform devices [71] as well, allowing 40 ps FWHM to be demonstrated in 15 μm × 15 μm meander devices [72]. This improvement is explainable with the larger amplitudes of the resulting photon detection voltage pulses at larger bias currents I_b, as a larger current is re-distributed into the $Z_0 = 50\ \Omega$ read-out line. The influence of the electronic noise on the voltage pulses and therefore the pulse rise time distribution is reduced for larger pulse amplitudes, and therefore the timing jitter improves for larger bias currents I_b.

2.2 High-energy massive particle detection

Nowadays the research in the field of single-photon/particle detection with superconducting nanowires mainly focuses on the detection of near-IR and visible photons on the one hand, because quantum optics experiments mainly concentrate on this energy range ($0.8 - 4.0$ eV), and on the detection of molecules in the energy range $\approx 1 - 20$ keV for time-of-flight mass spectrometry (TOF-MS) on the other hand. The first proposal for a single-particle detector from a narrow thin-film superconducting structure was published in 1962 by N. K. Sherman [2], and was theoretically studied regarding its MeV-α-particle detection capability. In 1965 Spiel *et al.* [3] then demonstrated the successful detection of 5.3 MeV α-particles with a 34 μm wide strip from a 100 nm thick indium film. In 1989/90 Gabutti *et al.* could show the detection of 6 keV photons [4] with a 0.2 μm wide and 0.4 μm thick Nb strip and of MeV-electrons [5] with a 2 μm wide and 0.4 μm thick strip from granular aluminum. It was only in 2001 when the first working SNSPD in the near-IR and visible energy range was examined by Gol'tsman *et al.* [1], thereby opening the doors for this vivid research field. In the following years, the successful detection of ionized macromolecules [73] (in 2008) with a kinetic energy of 17.5 keV by a 7 nm thin NbN SNSPD from 200 nm wide nanowires and detection of keV-argon ions [74] (in 2011) by superconducting NbN nanowires of 10 nm thickness could be demonstrated by Suzuki *et al.*, enabling TOF-MS with superconducting nanowires.

In this section, established concepts and properties that are characteristic for high-energy single-massive particle detectors from superconducting nanowires are discussed, in perspective of the discussion of X-ray single-photon detectors described in this thesis.

2.2.1 Hot-spot formation from secondary excitations

When a massive high-energy particle hits a superconducting nanowire, all of its kinetic energy E_{kin} is transfered to secondary excitations [75] within the sample, namely quasiparticles, phonons and photons, which couple to each other. The excitation of quasiparticles can lead to the formation of a hot-spot immediately after particle impact due to the high particle energy [75], even when only a part of E_{kin} remains within the nanowire. This is in contrast to the case of near-IR and visible photon detection with SNSPDs, where the refined detection model (discussed in section 2.1.2) assumes that a normal conducting hot-spot has not necessarily to form out despite the local Cooper pair density reduction.

2.2.2 Application of the hot-spot model

The hot-spot model explaining visible photon detection in thin-film SNSPDs (see subsection 2.1.1) in which a cylindrical hot-spot shape was assumed, was originally introduced by Spiel *et al.* [3] to determine the hot-spot radius from the incident MeV-α-particles in indium strips. Due to the high kinetic energy of these particles, also an average hot-spot shape in form of a cylinder is assumed, and therefore the reduced threshold bias current can be expressed by

$$\frac{I_{th}}{I_{c,exp}} = \frac{wd - 2r_0 d}{wd} = 1 - \frac{2r_0}{w}, \tag{2.2.1}$$

Therefore, by measuring $I_{th}/I_{c,exp}$, the radius r_0 can thus be determined. For 5.3 MeV α-particles in 100 nm thin and 34 μm wide indium strips a hot-spot radius of $r_0 \gtrsim 3$ μm [3] was found, which is significantly larger than the thickness d, justifying the cylindrical approximation.

With increasing particle energy, the hot-spot radius r_0 also increases. Identical atoms or molecules with mass m and charge z and accelerated by the same voltage V_A have a kinetic energy $E_{kin} = zV_A$ after acceleration, and therefore deposit an energy in the superconducting nanowires depending on their charge state z. Suzuki *et al.* [76] could demonstrate that a 10 nm thick NbN detector shows a decreasing threshold bias current I_{th} with increasing E_{kin} for macromolecules at $V_A = 17.5$ kV and of different charge states z. Hence, the corresponding hot-spot radius r_0 increases with E_{kin}. Consequently, it is possible to distinguish between different charge states z (with multiple measurements, not from single-shot), which is not possible with conventional mass spectrometry, which only allows for the determination of the ratio m/z.

Studies on the detection of ionized argon ions Ar^{+z} with an identical detector showed a very sharp bias current threshold I_{th} that was decreasing with increasing kinetic energy $E_{kin}(z, V_A)$ [74], varied by z and V_A. The measured dependence of I_{th} on $E_{kin}(z, V_A)$ could be well described by assuming a cylindrically shaped hot-spot with a volume proportional to E_{kin}.

It follows that the reduced threshold bias current $I_{th}/I_{c,exp}$ can be reduced sufficiently by a large enough acceleration voltage V_A and hence particle kinetic energy E_{kin}, so that dark counts become completely negligible.

2.2.3 Limitations of the hot-spot model

A massive high-energy particle incident on the detector eventually scatters inelastically until it has lost all its original kinetic energy E_{kin}, having traveled an average distance R. In general, R decreases with the particle size and charge, and increases with the kinetic energy E_{kin}. Ionized macromolecules with a kinetic energy of several keV are trapped at the surface of the nanowire [77] due to their dimensions, while 6 keV electrons [78] travel a average distance of $R \approx 170$ nm in Nb (see subsection 2.3.3 for details). The range of 5 MeV α-particles in Nb can be roughly estimated [79] to $R \approx 1$ mm.

The secondary excitations produced in the inelastic scatter processes of the particle diffuse away from the scatter location. In addition, the travel distance R of keV-electrons and MeV-α-particles described above is longer than the 100 nm thickness of the thickest superconducting nanowire single-particle detector reportedly used [80]. For high-energy particles with a kinetic energy E_{kin}, it can therefore be assumed that a only a fraction of the excitations induced after impact of the high-energy particle, and therefore only an average fraction $Q_E E_{kin}$ of the original particle energy ($0 < Q_E < 1$), remains inside the nanowire until a resistive domain has formed and the particle is detected.

Secondary electrons also show a randomly kinked trajectory inside the sample [81]. The shape of the resulting hot-spot inside the nanowire is therefore different for every particle impact event and not necessarily cylindrical as originally assumed, even though this is a good approximation for the average shape of the hot-spot [74].

2.2.4 Consequences for the detector geometry

As a means to increase the probability for inelastic scattering of high-energy massive particles inside the superconducting nanowires and to increase the fraction $Q_E E_{kin}$, their thickness d was often increased from the typical ≈ 5 nm thickness of SNSPDs up to 100 nm. Increasing d also increases the X-ray photon absorptance of X-SNSPDs, as it will be discussed in more detail in subsection 2.3.2. Assuming Q_E is close enough to unity, increasing d is in agreement with Eq. 2.1.7 describing the dependence of the threshold particle energy on the nanowire dimensions: As energies in the keV or MeV range are 3-6 orders of magnitude larger than in the case of near-IR and visible photon detection, the width w and the thickness d of the nanowires in an SNSPD can be chosen much larger. In addition, an increased film thickness allows for a larger active detector area (i.e. nanowire length) without changing its kinetic inductance L_{kin} (see Eq. 1.2.18) and therefore the response and dead time of the detector [77]. Furthermore, wider nanowires can reduce the difficulties in nanofabrication of the detectors.

Following this strategy, the nanowire thickness was increased to 50 nm [34] for continuous-mode detection and 100 nm [80] for gated-mode detection of keV-macromolecules. Casaburi *et al.* [77] have shown in experiments with 17.5 keV macromolecules that an increase of the NbN nanowire thickness from 9 nm to 40 nm increases DDE. Suzuki *et al.* [74] calculated the penetration depth of 9 keV Ar^{3+} ions used in their experiments to about 6 nm in NbN, resulting in the transmission of ≈ 12% of the ions through the 10 nm thick NbN, and indicating that a thicker NbN film would be favorable for even higher kinetic energies. Rosticher *et al.* [78] showed that DDE for keV-electrons detected with a 6 nm thick $Nb_{0.7}Ti_{0.3}N$ SNSPD decreases with higher energies from 100% at 15 keV to ≈ 50% at 30 keV.

2.2.5 Performance of SNSPDs for single-particle detection

Rosticher *et al.* [78] showed, that indeed single electrons (with $E_{kin} = 10$ keV) were detected with their SNSPD, analogous to the near-IR and visible single-photon detection [1] described in section 2.1.8.

Already in the first experiment with a MeV-α-particle detector by Spiel *et al.* [3] in 1965, fast pulse rise times of ≈ 15 ns and pulse lengths of ≈ 70 ns were observed in continuous-detection mode. In 2011, Casaburi *et al.* [77] reported keV-macromolecule detection with ultrafast pulse rise times down to 380 ps ± 50 ps and pulse lengths of about 1 ns.

2.3 X-ray photon detection in the keV-energy range

In this section, concepts and properties essential for the detection of X-ray photons with energies up to 50 keV with (X-)SNSPDs are discussed. Similar to the detection of high-energy massive particles (as discussed in subsection 2.2.1) and in opposite to the case of near-IR and visible photon detection, the formation of a hot-spot immediately after the X-ray photon absorption can be assumed due to the high photon energy.

2.3.1 Application of the hot-spot model

A simple model was used by Gabutti *et al.* [4] to estimate the radius r_0 of the hot-spot around the absorption point of a keV-photon. For X-ray photons, the hot-spot shape can be assumed to be spherical instead of cylindrical (as it was assumed for high-energy massive particles in subsection 2.2.2), since the momentum of a photon (of energy E) $p_{ph} = E/c$ is always significantly smaller than the momentum $p_{part} = \sqrt{2mE}$ of a non-relativistic massive particle with the same energy, and the excitations in the sample therefore propagate in a much more isotropic way. In this model, the energy ΔE deposited by a photon in a nanowire equals the difference in enthalpy in the hot-spot:

$$\Delta E = (h(T_c) - h(T))\, \frac{4}{3}\pi r_n^3, \tag{2.3.1}$$

with $h(T)$ being the specific enthalpy at temperature T. The difference in enthalpy can be calculated from the temperature-dependent specific heat $c_p(T)$ [82],

$$\Delta h = \int_T^{T_c} c_p(T')\, \mathrm{d}T'. \tag{2.3.2}$$

From the discussion in subsection 2.1.9 it follows, that the electronic system of the superconductor thermalizes on a much faster time scale than the phononic part. Thus, most of the energy ΔE remains in the electronic system of the superconductor on the relevant time scale, and hence only the electronic contribution c_{es} of the specific heat is included for this calculation, i.e., $c_p(T) \approx c_{es}(T)$. $c_{es}(T)$ can be approximated within the BCS theory [83] as a function of the Sommerfeld constant γ,

$$c_{es} = 9.17\,\gamma\, T_c \exp\left(-\frac{1.50\, T_c}{T}\right). \tag{2.3.3}$$

For Nb the Sommerfeld constant $\gamma_{\mathrm{Nb}} = 7.80$ mJmol^{-1}K^{-2} $= 1.63 \times 10^3$ Jm^{-3}K^{-2} can be found in literature [12], using the density $\rho_{\mathrm{Nb}} = 8.57$ gcm^{-3}. For low-temperature superconductors (as for example TaN), it can be estimated from the density of states at the Fermi-energy [13],

$$\gamma = \frac{\pi^2}{3} k_{\mathrm{B}}^2 N_0. \tag{2.3.4}$$

Using $N_0 = 3 \times 10^{47}$ m^{-3}J^{-1} as reported for a TaN SNSPD [41], the Sommerfeld constant can be calculated to $\gamma_{\mathrm{TaN}} = 380$ Jm^{-3}K^{-2}.

Gabutti *et al.* [4] demonstrated the detection of 6 keV photons with a 0.2 μm wide and 0.4 μm thick Nb strip. We calculated the hot-spot radius to $r_0 \approx 170$ nm, using above Eqs. 2.3.1, 2.3.2 and 2.3.3. It is therefore justified to assume a spherically shaped hot-spot for the discussion of such experiments.

Analogous to Eq. 2.2.1 for high-energy particle detection, the reduced threshold bias current in the case of a spherical hot-spot becomes

$$\frac{I_{th}}{I_{c,exp}} = \frac{wd - \pi r_0^2}{wd} = 1 - \frac{\pi r_0^2}{wd}. \tag{2.3.5}$$

From Eq. 2.3.2 we can conclude that at an operation temperature T closer to T_c the difference in enthalpy decreases, and thus the hot-spot radius r_0 becomes larger for a given photon energy. Hence, the reduced threshold bias current $I_{th}/I_{c,exp}$ decreases for higher operation temperatures. Gabutti *et al.* [5] observed this behavior for a 0.4 μm thick and 2 μm wide granular aluminum nanowire with a critical temperature of $T_c = 1.5$ K, where $I_{th}/I_{c,exp}$ decreased from 0.45 to 0.3 when the operation temperature was increased from $T = 1.31$ K to 1.39 K. This improved detection efficiency at higher operation temperature was also observed for the detection of MeV-electrons with the same device in the same study.

2.3.2 X-ray photon absorptance

Since photons are uncharged massless particles, they penetrate deeper into the sample on average to interact with matter for the first time as compared to massive particles with identical energy (like ionized atoms, α- and β-particles).

The absorption probability $P_{abs}(d, E)$, or absorptance, of a photon with energy E in a film with thickness d is a function of the energy- and material-dependent penetration depth $\lambda(E)$,

$$P_{abs}(d, E) = 1 - e^{-\frac{d}{\lambda(E)}}. \tag{2.3.6}$$

Fig. 2.10 shows plots of P_{abs} [84] in the energy range of 1 to 50 keV for TaN, Nb and NbN films of 5 nm and 100 nm thickness, configurations used in the experiments with (X-)SNSPDs discussed in this thesis. Generally, the absorption probability P_{abs} decreases with E. However, characteristic absorption lines of the material result in several points of discrete "step-like" absorption enhancement. TaN shows an at least 1.8 times larger absorption probability than NbN between 2 and 50 keV, and even 6 times larger between 10 and 19 keV. This makes TaN the favorable X-SNSPD material in terms of X-ray absorptance. For a 100 nm thick film, $P_{abs} > 5\%$ is achieved below 6 keV and 4 keV for TaN and NbN, respectively, and $P_{abs} > 1\%$ is achieved below 19 keV and 8 keV for TaN and NbN, respectively. The aborption propability at 5.9 keV is important for calibration purposes, as a radioactive Fe-55 isotope source mainly emits at this energy (see subsection 5.2.5), and we find $P_{abs}(5.9\text{ keV}) = 5.2\%$ and 2.8% for 100 nm thick TaN and Nb [85], respectively, which are the materials used for the X-SNSPD presented in this thesis.

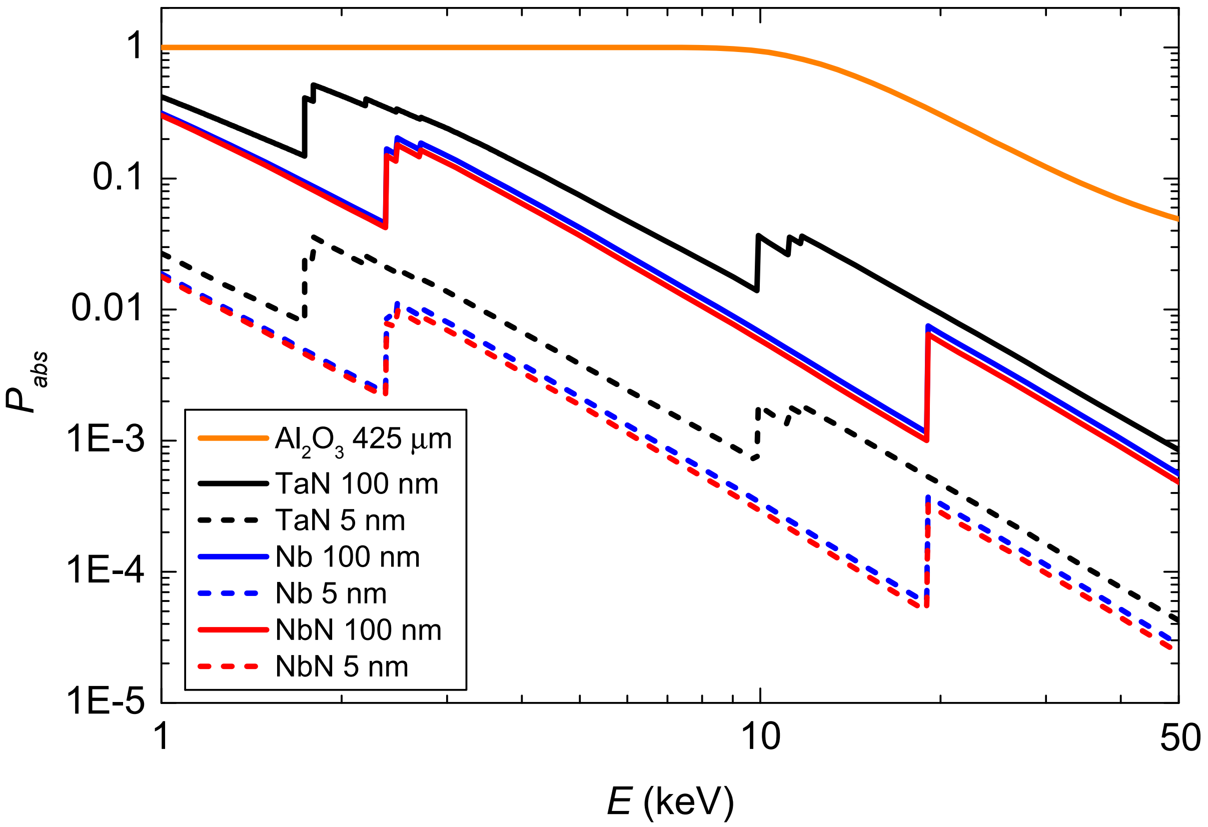

Figure 2.10: Plots of the photon absorption probability P_{abs} for 5 nm and 100 nm thick TaN, Nb and NbN films and for a 425 μm thick sapphire (i.e. Al_2O_3) substrate in dependence of the X-ray photon energy. The data is taken from Ref. [84].

2.3.3 Excitations from X-ray photons absorbed in a superconductor

Van Vechten *et al.* [81] examined in detail the processes which occur after absorption of a keV-photon in elemental superconductors: Initially, the X-ray photon energy is transferred to a primary photoelectron, which then scatters inelastically to produce secondary electrons causing the path of the primary to be irregularly kinked. The distance R_e that the primary electron will have traveled before becoming indistinguishable from all the other electrons in the system (called "primary range") depends on its initial energy, and can be estimated in the keV-energy range by

$$R_e(E) = \frac{3.52 \times 10^{-3}\,\frac{\mathrm{kg}}{\mathrm{m}^2}}{\rho} \left(\frac{E}{10\ \mathrm{keV}}\right)^{1.754}, \tag{2.3.7}$$

where ρ is the material density. For Nb, R_e is therefore about 170 nm for a 6 keV photon, about 2.8 μm for a 30 keV photon and about 6.9 μm for a 50 keV photon. For TaN, it is found to be slightly smaller due to the larger density, namely about 100 nm, 1.7 μm and 4.1 μm for a 6 keV, 30 keV and 50 keV photon, respectively.

This process takes place within 1 ps or less, and another upper bound of $\approx 10^{-13}$ s for Nb and TaN can be calculated by assuming a uniform deceleration from $v = \sqrt{2/(m_e E_{kin})}$ given by $E_{kin} = 1 - 50$ keV to zero velocity within the distance $R_e(E_{kin})$. Excited quasiparticles are created during this process, which eventually relax to energies of a few meV on a time scale of a few Picoseconds and finally recombine into Cooper pairs within < 1 ns if no bias current is applied, similarly to the quasiparticle diffusion in SNSPDs. This timescale is orders of magnitude longer than the time necessary for the primary electron to lose its energy. Hence, the emerging hot-spot will not have a spherical or cylindrical shape in most cases, as already indicated in the discussion of high-energy particle detection in subsection 2.2.3, but rather the shape of a growing quasiparticle cloud along the random paths of the primary and secondary electrons. However, spherically or cylindrically shaped hot-spots are good models to include an average hot-spot shape into the analysis, allowing to estimate the average volume inside the nanowire which turns normal conducting after photon absorption.

2.3.4 Indirect (substrate-mediated) soft X-ray photon detection

When a conventional 5 nm thin NbN SNSPD is irradiated by keV-photons, the number of photons absorbed by the substrate is orders of magnitudes larger than the number of photons absorbed in the superconducting nanowires. Fig. 2.10 shows the absorption probability [84] for a sapphire (i.e. Al_2O_3) substrate of 425 μm thickness, which is the typical substrate for our (X-)SNSPDs. Photons are absorbed almost completely up to 8 keV, 50% at 16 keV and 5% at 50 keV. It was shown by Perez de Lara *et al.* [75] that the 6 keV photon detection in thin-film SNSPDs mostly occurs through photon absorption in the substrate and the successive energy diffusion to the superconducting meander structure, as the 6 keV photon absorption probability for the nanowires is orders of magnitude smaller. In the reported case, this leads to a DDE which is higher than the photon absorption probability of the superconducting detector, even though photons absorbed directly inside the nanowires also contribute to the photon counts.

Furthermore, Q_E has to be smaller than unity for $E = 6$ keV photons absorbed by the substrate, as not the entire photon energy E will diffuse into the SNSPD. The reduced bias threshold current is larger than 70% in the study by Perez de Lara *et al.* [75], which is in agreement with this hypothesis, as excitations of a total energy of 6 keV within a nanowire would lead to a hot-spot covering the whole nanowire cross-section [75], therefore leading to a vanishing threshold bias current I_{th}.

This work by Perez de Lara *et al.* [75] is the only report on continuous X-ray photon counting with SNSPDs besides our reports [86, 87] on soft X-ray photon counting with

X-SNSPDs. The high *DDE* achieved with thin-film SNSPDs is useful in terms of efficient X-ray photon counting. However, the substrate-mediated detection process discussed above might lead to increased timing jitters (as it will be described in chapter 3). In addition, the thin thickness d of SNSPDs do not allow for an energy resolution in the X-ray energy range as found and discussed for X-SNSPDs in chapter 7.

2.3.5 Latching and ultrafast detection

The issue of latching has been discussed for thin-film SNSPDs in section 2.1.9, where domain resistances $R_n \gg 50\ \Omega$ form during detection events. This is not necessarily the case for (thick-film) X-SNSPDs, as the nanowire cross-sections are significantly larger, and the domain resistance R_n can therefore be $\leq 50\ \Omega$. When such a domain forms, the bias current is only partially diverted into the $Z_0 = 50\ \Omega$-impedance read-out line, which leads to self-heating of the domain and latching at large bias currents I_b. Such devices are therefore often run in gated-mode [4, 5, 80, 82]. However, reducing the bias current externally after every detection event (as discussed in section 2.1.9) results in long dead times and therefore limits the count rate.

The first X-SNSPDs demonstrated by Gabutti *et al.* [4, 5], made from niobium, suffered from this latching effect. These detectors had a strip cross-section more than two orders of magnitude larger than typical thin-film SNSPDs, which, combined with the orders of magnitude lower resistivity of Nb ($\rho_n = 1.9\ \mu\Omega$cm in their study) compared to (the typical SNSPD material) NbN, leads to small domain resistances. In addition, the used strip geometry used resulted in a smaller kinetic inductance than is typical for SNSPDs. Gabutti *et al.* [88] solved this problem by choosing a material with larger resistivity (granular tungsten with $\rho_n = 620\ \mu\Omega$cm), which allowed pulse lengths of 30 ns in continuous-mode for 6 keV-photon detection.

However, the critical temperature of granular tungsten ($T_c = 2.16$ K in Ref. [88]) is significantly lower than for TaN ($T_c \approx 7$ K, see chapter 7), which offers a similarly large normal-state resistivity ($\rho_n = 500\ \mu\Omega$cm) and was already successfully used for near-IR and optical photon detection with thin-film SNSPDs, allowing very short pulse lengths on the order of 1 ns, as shown in our work in Ref. [41]. Moreover, the granular structure of g-W could make the nanofabrication of nanowires with a uniform width difficult.

2.4 Comparison to other near-IR, visible and X-ray keV-energy single-photon detectors

In this section, several important single-photon detector types are briefly introduced and compared to SNSPDs in their performance in the near-IR and visible as well as in the

X-ray keV-energy range. This section is based on reviews in Refs. [8, 68].

2.4.1 Single-photon avalanche photodiodes

Single-photon avalanche photodiodes (SPADs) are based on an avalanche photodiode structure, as p-n or p-i-n junctions. Carriers generated by photon absorption undergo avalanche gain, as the diode is reverse-biased above the breakdown voltage, thereby triggering a macroscopic breakdown of the diode junction [89] which can be registered. Finally, the avalanche has to be stopped and the device reset by a quenching circuit [90, 91].

SNSPDs have excellent potential for time-correlated single-photon counting in the near-IR wavelength regime. SPADs are the main competitors of SNSPDs in this field, and have superseded bulky photomultiplier tubes [68] (which, however, offer much larger active areas). However, the long wavelength sensitivity of the SNSPD extends far beyond that of the Si SPAD, even though Si SPADs can show a high DDE of 65% at 650 nm. Si SPADs can be operated at 250 K, in contrast to the liquid-helium-temperatures necessary for SNSPDs. Si SPADs show comparably low timing jitters compared to SNSPDs ($\approx$ 35 ps), at lower maximum count rates ($\approx$ 10 MHz), however.

In order to extend the long-wavelength value of DDE for SPADs, lower-bandgap semiconductors as Ge and InGaAs are used, and a DDE of 10% at 1550 nm, a maximum count rate of 100 MHz and a dark count rate of 16 kHz were realized with InGaAs SPADs [92]. The SNSPD is superior to the InGaAs SPAD in terms of dark counts ($<$ 1 Hz at $I_b/I_{c,exp} = 98\%$ [6]). However, dark counts can be significantly reduced (to $\approx$ 90 Hz) in these SPADs by cooling them down to 200 K [93], at the cost of reducing the maximum count rate significantly to 10 kHz.

In the X-ray energy range, an energy resolution as high as $\Delta E/E \approx 3 \times 10^{-2}$ at 6 keV can be achieved with SPADs, with maximum count rates of only 2×10^5 s^{-1} [94], however. This maximum count rate can be increased to $\approx 10^8$ s^{-1} at the expense of a decrease in energy resolution to $\Delta E/E \approx 0.2$ [94].

2.4.2 Transition edge sensors

In a transition edge sensor (TES), the detector element is a superconducting film with its temperature maintained within the superconducting-to-normal transition region of a width less than 1 mK, where any change in temperature will cause an abrupt change in resistance [95]. The absorption of an incident photon heats the device, causing a measurable change in the resistance. The signal therefore allows to measure the energy of the photon or, at fixed energy, the photon number [96].

These detectors operate at transition temperatures of roughly 100 mK in order to achieve a comparably low dark count rate [97] as SNSPDs. However, the resulting very long quasiparticle relaxation time leads to minimum dead times of 100 ns [68] and similarly long timing jitters, which are therefore orders of magnitude longer than for SNSPDs and SPADs.

TES exhibit an energy resolution of 0.15 eV at 1 eV, and improvements of a factor of 2 or 3 are expected [98], which is significantly better than the energy resolution demonstrated for SNSPDs (see section 2.1.7), where an energy resolution is only possible in a very limited photon energy regime. The photon-number-resolving capabilities of TES are excellent: up to eight photons were shown to be clearly resolvable [99].

Tungsten-based TESs have a detection efficiency of 20% at near-IR and visible wavelengths, which can be improved to a near-unity-efficiency at any wavelength in this regime by embedding them into an optical cavity structure [100].

In the X-ray energy range, TES show an excellent photon energy resolution of 2 eV at 6 keV, which corresponds to a $\Delta E/E \approx 3 \times 10^{-4}$ [101]. This is significantly better than for SPADs. DDE for thin-film devices is low. However, by attaching a bulk tin absorber on top of a TES, DDE at 100 keV could be increased to 24% [102].

2.4.3 Superconducting tunnel junctions

A superconducting tunnel junction (STJ) consists of two superconductors separated by a very thin layer of an insulating material [103] across which a constant voltage bias smaller than twice the gap-equivalent ($V_b < 2\Delta/|e|$) is applied. An absorbed photon breaks Cooper pairs and creates quasiparticles, which can then tunnel across the junction. The number of these quasiparticles is a measure for the photon energy and detectable as a current pulse.

The development of STJs has now approached the same energy resolution as TES in the near-IR and visible energy regime, namely about 0.15 eV at 1 eV [98], and there is a fundamental limit to the energy resolution of STJs set by statistical fluctuations of quasiparticle generation and tunneling [104] of 0.09 eV at 2.4 eV.

Commonly, STJs are operated at sub-Kelvin temperatures, very similarly to TES, in order to increase the quasiparticle lifetime and reduce the thermal background of tunneling quasiparticles. However, this also leads to longer dead times [97] than for SNSPD and resulting maximum photon count rates of the order of 10^4 counts/s, and up to 10^5 counts/s at a reduced energy resolution [104]. STJs therefore tend to be used in applications which require a higher energy resolution than SPADs and a higher speed than TES offer.

A DDE of 70% has been detemined for the wavelength range 310-720 nm [105], which is significantly larger than for a non-cavity-embedded TES.

In the soft X-ray energy range, STJs show a very good photon energy resolution of 10 eV at 6 keV (corresponding to $\Delta E/E \approx 2\times10^{-3}$ [98]), which is close to the fundamental limit of STJs of 2.5-6.3 eV in this energy range [104]. At 6 keV, a high DDE of 50% has been achieved [106].

2.4.4 Streak cameras

In an optoelectronic streak camera a photon hits a photocathode, which can emit a photoelectron into a cathode ray tube where it is accelerated along the tube axis by an electric field. An additional time-varying electric field orthogonal to the tube axis deflects it to a time-dependent location onto a streak on the phosphor screen. A charge-coupled device (CCD) array is then used to image the pattern on the screen, and thus the temporal profile of the light pulse. Furthermore, it is possible to detect photons with a certain energy resolution by adding a slit perpendicular to the streak direction.

Streak cameras can be operated at different speeds with excellent temporal resolutions. The commercial manufacturer Hamamatsu offers, for example, streak cameras with a temporal resolution of less than 0.2 ps [107], which is significantly better than for SNSPDs. However, the devices have to be reset after performing a complete streak measurement, which, at the best temporal resolution, can only be performed during consecutive 60 ps.

Streak cameras can be optimized to match any photon energy range from near-IR to X-ray radiation. X-ray streak cameras have been developed that have temporal resolutions of around 0.35 ps [94]. If the angle of photon incidence onto the streak camera is optimized, a high DDE can be achieved in the keV-range, with unity DDE shown for 1 keV photons at 0.6 ps temporal resolution [108].

2.5 Publications related to this chapter

These two publications are appended in the following:

- **Tantalum nitride superconducting single-photon detectors with low cut-off energy**
  A. Engel, A. Aeschbacher, K. Inderbitzin, A. Schilling, K. Il'in, M. Hofherr, M. Siegel, A. Semenov, H.-W. Hübers
  Applied Physics Letters **100**, 062601 (2012)

  DOI: 10.1063/1.3684243
  Open access repositories: `http://arxiv.org/abs/1110.4576`

- **Temperature-dependence of detection efficiency in NbN and TaN SNSPD**

  A. Engel, K. Inderbitzin, A. Schilling, R. Lusche, A. Semenov, H.-W. Hübers, D. Henrich, M. Hofherr, K. Il'in, M. Siegel

  IEEE TRANSACTIONS ON APPLIED SUPERCONDUCTIVITY **23**, 2300505 (2013)

  DOI: 10.1109/TASC.2013.2239345

  Open access repositories: http://arxiv.org/abs/1210.5395

APPLIED PHYSICS LETTERS **100**, 062601 (2012)

Tantalum nitride superconducting single-photon detectors with low cut-off energy

A. Engel,[1,a)] A. Aeschbacher,[1] K. Inderbitzin,[1] A. Schilling,[1] K. Il'in,[2] M. Hofherr,[2] M. Siegel,[2]
A. Semenov,[3] and H.-W. Hübers[3]
[1] *Physics Institute, University of Zurich, Winterthurerstr. 190, Zurich, Switzerland*
[2] *Institute for Micro- and Nano-Electronic Systems, Karlsruhe Institute of Technology, Hertzstr. 16, 76187 Karlsruhe, Germany*
[3] *DLR Institute of Planetary Research, Rutherfordstr. 2, 12489 Berlin, Germany*

(Received 19 October 2011; accepted 23 January 2012; published online 10 February 2012)

Materials with a small superconducting energy gap are expected to favor a high detection efficiency of low-energy photons in superconducting nanowire single-photon detectors. We developed a TaN detector with smaller gap and lower density of states at the Fermi energy than in comparable NbN devices, while other relevant parameters remain essentially unchanged. The observed reduction of the minimum photon energy required for direct detection is in line with model predictions of ≈1/3 as compared to NbN. © *2012 American Institute of Physics.* [doi:10.1063/1.3684243]

Superconducting nanowire single-photon detectors (SNSPD) (Ref. 1) are viable detectors for applications where speed is critical, both in terms of small jitter and short reset times. To date the majority of SNSPD have been made from NbN thin films due to their favorable characteristics. Superconducting NbN films with a $T_c \approx 15\,\mathrm{K}$ can be made a few nanometer thin,[2] and the resulting films can be structured down to strip widths of a few tens of nanometers[3,4] without destruction of superconductivity. According to simple detection models,[5] the threshold energy for direct detection decreases for materials with shorter thermalization time τ_{th}, small electron-diffusion coefficient D, low density of states at the Fermi energy N_0, and small superconducting energy gap Δ. Newer results also indicate that a large magnetic penetration depth λ_L leading to a larger kinetic inductance $L_k \propto \lambda_L^2$ is beneficial to avoid latching into the normal conducting state.[6]

All of these requirements limit the number of superconducting materials that are suitable for SNSPD, and there have been only a few publications about detectors made from alternative materials. Results on Nb-based SNSPD (Refs. 7 and 8) highlighted the importance of D and N_0 and confirmed the importance of L_k. Thin films from NbTiN offer advantages in fabrication, and the resulting SNSPD may have lower dark-count rates.[9] Detectors made from $\mathrm{MgB_2}$ still suffer from the low quality ultra-thin $\mathrm{MgB_2}$ films.[10] Very recently, two reports with similar objectives have been published. In one work, the use of a-$\mathrm{W}_x\mathrm{Si}_{1-x}$ with $T_c \approx 3\,\mathrm{K}$ resulted in increased detection efficiencies (*DE*) at lower energies.[11] The other study compared *DE* of SNSPD from NbSi ($T_c \approx 2\,\mathrm{K}$) with NbTiN, but although relative *DE* increased at long wavelengths for NbSi, absolute values of *DE* were very low.[12] In this letter, we report results on a SNSPD made from ultra-thin TaN films. TaN is chemically and physically very similar to NbN and so are most of the relevant parameters, except for T_c (≈6–10.5 K) and the associated energy gap Δ, which both are significantly smaller, and a moderate reduction of N_0. Any difference in detector performance can thus be linked to a change in these parameters.

Ultrathin TaN films were grown by DC reactive magnetron sputtering in an Ar/$\mathrm{N_2}$ atmosphere on R-plane cut sapphire substrates. The sputter target was pure (99.95%) Ta and the sapphire substrates were heated to 750 °C. The critical temperature of the as grown films varied between ≈10.5 K for film thicknesses $d \geq 10\,\mathrm{nm}$ and 6 K for a thickness of only 2.3 nm. From these films, SNSPD with the typical meander geometry were fabricated using electron-beam lithography and ion milling. More details about the fabrication process have been published elsewhere.[13]

The optical detector-measurements have been performed in a He-3 bath cryostat. The temperature could be stabilized to ≈±10 mK at 5 K and ±1 mK below 2 K. The detector signal was transmitted to a cryogenic amplifier at the 4 K-stage and then further to a second amplifier at room temperature before fed into a 3.5 GHz digital oscilloscope or a pulse counter. The amplifier chain had an effective bandwidth of about 40 MHz to 1.9 GHz. The bias current was applied in constant-voltage mode and passed through a series of low-pass filters. The light from a xenon discharge lamp was passed through a grating monochromator and then fed into the cryostat using a free-space setup. Although an absolute calibration of the light intensity was difficult, the lamp spectrum at the detector has been measured and the intensity was monitored during experiments to account for variations in the lamp output. The beam was slightly defocused to obtain a uniform photon-flux density over the meander area (max. $\sim 10^6$ photons $\mu\mathrm{m}^{-2}\,\mathrm{s}^{-1}$). However, the measurements are prone to systematic errors. The given DE should therefore be taken as relative numbers. In another setup with a different TaN SNSPD an absolute DE ≈ 20% has been determined.[13] Complimentary resistance R *vs.* temperature T measurements were performed in a *Quantum Design* PPMS-9.

The detection mechanism of SNSPD relies on the conversion of the energy of the absorbed photon into elementary

---

[a)] Author to whom correspondence should be addressed. Electronic mail: andreas.engel@physik.uzh.ch.

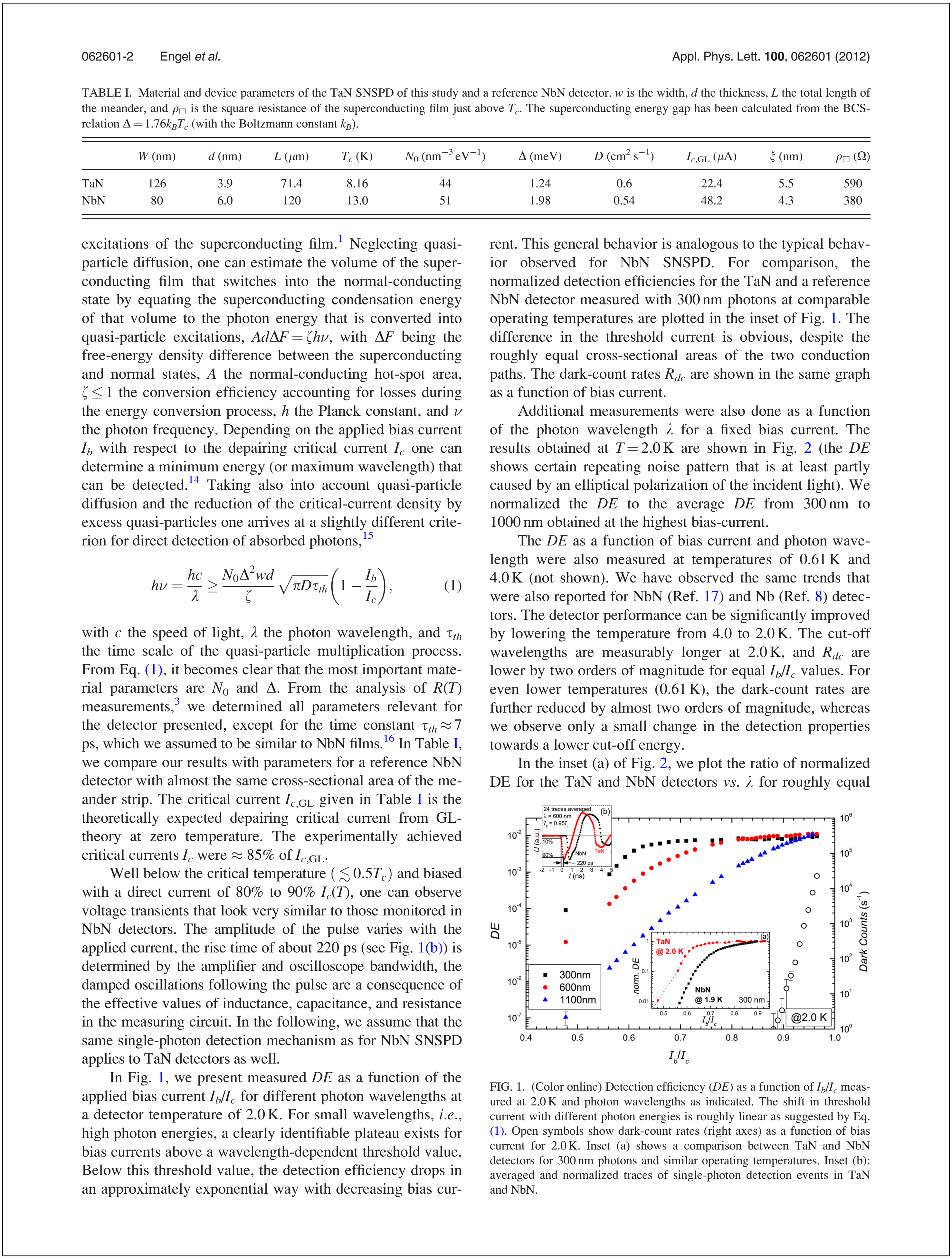

TABLE I. Material and device parameters of the TaN SNSPD of this study and a reference NbN detector. w is the width, d the thickness, L the total length of the meander, and $\rho_\square$ is the square resistance of the superconducting film just above T_c. The superconducting energy gap has been calculated from the BCS-relation $\Delta = 1.76 k_B T_c$ (with the Boltzmann constant k_B).

	W (nm)	d (nm)	L (μm)	T_c (K)	N_0 (nm^{-3} eV^{-1})	Δ (meV)	D (cm^2 s^{-1})	$I_{c,\mathrm{GL}}$ (μA)	ξ (nm)	$\rho_\square$ (Ω)
TaN	126	3.9	71.4	8.16	44	1.24	0.6	22.4	5.5	590
NbN	80	6.0	120	13.0	51	1.98	0.54	48.2	4.3	380

excitations of the superconducting film.[1] Neglecting quasi-particle diffusion, one can estimate the volume of the superconducting film that switches into the normal-conducting state by equating the superconducting condensation energy of that volume to the photon energy that is converted into quasi-particle excitations, $Ad\Delta F = \zeta h\nu$, with ΔF being the free-energy density difference between the superconducting and normal states, A the normal-conducting hot-spot area, $\zeta \leq 1$ the conversion efficiency accounting for losses during the energy conversion process, h the Planck constant, and ν the photon frequency. Depending on the applied bias current I_b with respect to the depairing critical current I_c one can determine a minimum energy (or maximum wavelength) that can be detected.[14] Taking also into account quasi-particle diffusion and the reduction of the critical-current density by excess quasi-particles one arrives at a slightly different criterion for direct detection of absorbed photons,[15]

$$h\nu = \frac{hc}{\lambda} \geq \frac{N_0 \Delta^2 wd}{\zeta} \sqrt{\pi D \tau_{th}} \left(1 - \frac{I_b}{I_c}\right), \qquad (1)$$

with c the speed of light, λ the photon wavelength, and τ_{th} the time scale of the quasi-particle multiplication process. From Eq. (1), it becomes clear that the most important material parameters are N_0 and Δ. From the analysis of $R(T)$ measurements,[3] we determined all parameters relevant for the detector presented, except for the time constant $\tau_{th} \approx 7$ ps, which we assumed to be similar to NbN films.[16] In Table I, we compare our results with parameters for a reference NbN detector with almost the same cross-sectional area of the meander strip. The critical current $I_{c,\mathrm{GL}}$ given in Table I is the theoretically expected depairing critical current from GL-theory at zero temperature. The experimentally achieved critical currents I_c were $\approx 85\%$ of $I_{c,\mathrm{GL}}$.

Well below the critical temperature ($\lesssim 0.5 T_c$) and biased with a direct current of 80% to 90% $I_c(T)$, one can observe voltage transients that look very similar to those monitored in NbN detectors. The amplitude of the pulse varies with the applied current, the rise time of about 220 ps (see Fig. 1(b)) is determined by the amplifier and oscilloscope bandwidth, the damped oscillations following the pulse are a consequence of the effective values of inductance, capacitance, and resistance in the measuring circuit. In the following, we assume that the same single-photon detection mechanism as for NbN SNSPD applies to TaN detectors as well.

In Fig. 1, we present measured DE as a function of the applied bias current I_b/I_c for different photon wavelengths at a detector temperature of 2.0 K. For small wavelengths, *i.e.*, high photon energies, a clearly identifiable plateau exists for bias currents above a wavelength-dependent threshold value. Below this threshold value, the detection efficiency drops in an approximately exponential way with decreasing bias current. This general behavior is analogous to the typical behavior observed for NbN SNSPD. For comparison, the normalized detection efficiencies for the TaN and a reference NbN detector measured with 300 nm photons at comparable operating temperatures are plotted in the inset of Fig. 1. The difference in the threshold current is obvious, despite the roughly equal cross-sectional areas of the two conduction paths. The dark-count rates R_{dc} are shown in the same graph as a function of bias current.

Additional measurements were also done as a function of the photon wavelength λ for a fixed bias current. The results obtained at $T = 2.0$ K are shown in Fig. 2 (the DE shows certain repeating noise pattern that is at least partly caused by an elliptical polarization of the incident light). We normalized the DE to the average DE from 300 nm to 1000 nm obtained at the highest bias-current.

The DE as a function of bias current and photon wavelength were also measured at temperatures of 0.61 K and 4.0 K (not shown). We have observed the same trends that were also reported for NbN (Ref. 17) and Nb (Ref. 8) detectors. The detector performance can be significantly improved by lowering the temperature from 4.0 to 2.0 K. The cut-off wavelengths are measurably longer at 2.0 K, and R_{dc} are lower by two orders of magnitude for equal I_b/I_c values. For even lower temperatures (0.61 K), the dark-count rates are further reduced by almost two orders of magnitude, whereas we observe only a small change in the detection properties towards a lower cut-off energy.

In the inset (a) of Fig. 2, we plot the ratio of normalized DE for the TaN and NbN detectors *vs.* λ for roughly equal

FIG. 1. (Color online) Detection efficiency (DE) as a function of I_b/I_c measured at 2.0 K and photon wavelengths as indicated. The shift in threshold current with different photon energies is roughly linear as suggested by Eq. (1). Open symbols show dark-count rates (right axes) as a function of bias current for 2.0 K. Inset (a) shows a comparison between TaN and NbN detectors for 300 nm photons and similar operating temperatures. Inset (b): averaged and normalized traces of single-photon detection events in TaN and NbN.

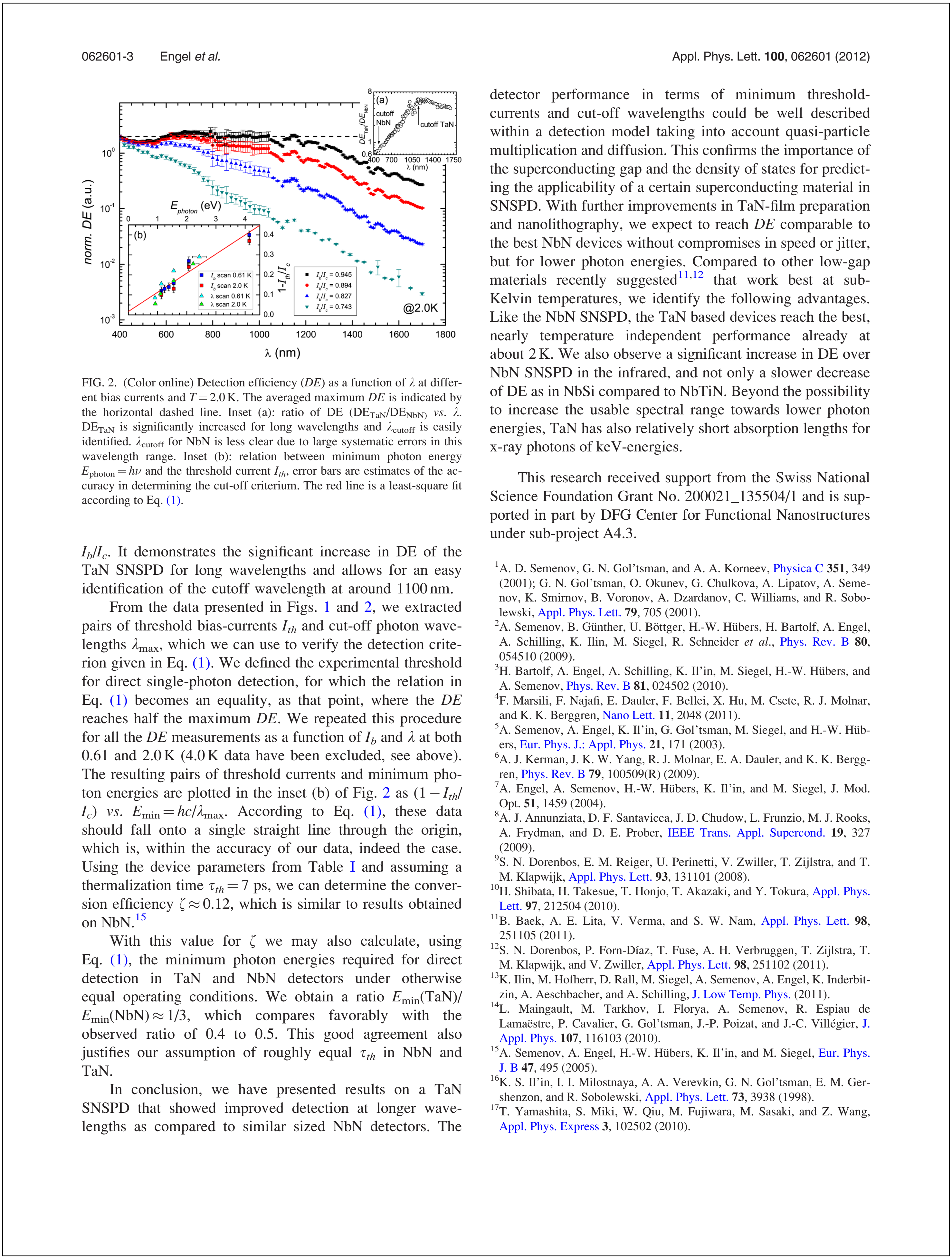

FIG. 2. (Color online) Detection efficiency (*DE*) as a function of λ at different bias currents and $T = 2.0$ K. The averaged maximum *DE* is indicated by the horizontal dashed line. Inset (a): ratio of DE (DE_{TaN}/DE_{NbN}) *vs.* λ. DE_{TaN} is significantly increased for long wavelengths and λ_{cutoff} is easily identified. λ_{cutoff} for NbN is less clear due to large systematic errors in this wavelength range. Inset (b): relation between minimum photon energy $E_{photon} = h\nu$ and the threshold current I_{th}, error bars are estimates of the accuracy in determining the cut-off criterium. The red line is a least-square fit according to Eq. (1).

I_b/I_c. It demonstrates the significant increase in DE of the TaN SNSPD for long wavelengths and allows for an easy identification of the cutoff wavelength at around 1100 nm.

From the data presented in Figs. 1 and 2, we extracted pairs of threshold bias-currents I_{th} and cut-off photon wavelengths λ_{max}, which we can use to verify the detection criterion given in Eq. (1). We defined the experimental threshold for direct single-photon detection, for which the relation in Eq. (1) becomes an equality, as that point, where the *DE* reaches half the maximum *DE*. We repeated this procedure for all the *DE* measurements as a function of I_b and λ at both 0.61 and 2.0 K (4.0 K data have been excluded, see above). The resulting pairs of threshold currents and minimum photon energies are plotted in the inset (b) of Fig. 2 as $(1 - I_{th}/I_c)$ *vs.* $E_{min} = hc/\lambda_{max}$. According to Eq. (1), these data should fall onto a single straight line through the origin, which is, within the accuracy of our data, indeed the case. Using the device parameters from Table I and assuming a thermalization time $\tau_{th} = 7$ ps, we can determine the conversion efficiency $\zeta \approx 0.12$, which is similar to results obtained on NbN.[15]

With this value for ζ we may also calculate, using Eq. (1), the minimum photon energies required for direct detection in TaN and NbN detectors under otherwise equal operating conditions. We obtain a ratio $E_{min}(\text{TaN})/E_{min}(\text{NbN}) \approx 1/3$, which compares favorably with the observed ratio of 0.4 to 0.5. This good agreement also justifies our assumption of roughly equal τ_{th} in NbN and TaN.

In conclusion, we have presented results on a TaN SNSPD that showed improved detection at longer wavelengths as compared to similar sized NbN detectors. The detector performance in terms of minimum threshold-currents and cut-off wavelengths could be well described within a detection model taking into account quasi-particle multiplication and diffusion. This confirms the importance of the superconducting gap and the density of states for predicting the applicability of a certain superconducting material in SNSPD. With further improvements in TaN-film preparation and nanolithography, we expect to reach *DE* comparable to the best NbN devices without compromises in speed or jitter, but for lower photon energies. Compared to other low-gap materials recently suggested[11,12] that work best at sub-Kelvin temperatures, we identify the following advantages. Like the NbN SNSPD, the TaN based devices reach the best, nearly temperature independent performance already at about 2 K. We also observe a significant increase in DE over NbN SNSPD in the infrared, and not only a slower decrease of DE as in NbSi compared to NbTiN. Beyond the possibility to increase the usable spectral range towards lower photon energies, TaN has also relatively short absorption lengths for x-ray photons of keV-energies.

This research received support from the Swiss National Science Foundation Grant No. 200021_135504/1 and is supported in part by DFG Center for Functional Nanostructures under sub-project A4.3.

[1] A. D. Semenov, G. N. Gol'tsman, and A. A. Korneev, Physica C **351**, 349 (2001); G. N. Gol'tsman, O. Okunev, G. Chulkova, A. Lipatov, A. Semenov, K. Smirnov, B. Voronov, A. Dzardanov, C. Williams, and R. Sobolewski, Appl. Phys. Lett. **79**, 705 (2001).
[2] A. Semenov, B. Günther, U. Böttger, H.-W. Hübers, H. Bartolf, A. Engel, A. Schilling, K. Ilin, M. Siegel, R. Schneider *et al.*, Phys. Rev. B **80**, 054510 (2009).
[3] H. Bartolf, A. Engel, A. Schilling, K. Il'in, M. Siegel, H.-W. Hübers, and A. Semenov, Phys. Rev. B **81**, 024502 (2010).
[4] F. Marsili, F. Najafi, E. Dauler, F. Bellei, X. Hu, M. Csete, R. J. Molnar, and K. K. Berggren, Nano Lett. **11**, 2048 (2011).
[5] A. Semenov, A. Engel, K. Il'in, G. Gol'tsman, M. Siegel, and H.-W. Hübers, Eur. Phys. J.: Appl. Phys. **21**, 171 (2003).
[6] A. J. Kerman, J. K. W. Yang, R. J. Molnar, E. A. Dauler, and K. K. Berggren, Phys. Rev. B **79**, 100509(R) (2009).
[7] A. Engel, A. Semenov, H.-W. Hübers, K. Il'in, and M. Siegel, J. Mod. Opt. **51**, 1459 (2004).
[8] A. J. Annunziata, D. F. Santavicca, J. D. Chudow, L. Frunzio, M. J. Rooks, A. Frydman, and D. E. Prober, IEEE Trans. Appl. Supercond. **19**, 327 (2009).
[9] S. N. Dorenbos, E. M. Reiger, U. Perinetti, V. Zwiller, T. Zijlstra, and T. M. Klapwijk, Appl. Phys. Lett. **93**, 131101 (2008).
[10] H. Shibata, H. Takesue, T. Honjo, T. Akazaki, and Y. Tokura, Appl. Phys. Lett. **97**, 212504 (2010).
[11] B. Baek, A. E. Lita, V. Verma, and S. W. Nam, Appl. Phys. Lett. **98**, 251105 (2011).
[12] S. N. Dorenbos, P. Forn-Díaz, T. Fuse, A. H. Verbruggen, T. Zijlstra, T. M. Klapwijk, and V. Zwiller, Appl. Phys. Lett. **98**, 251102 (2011).
[13] K. Ilin, M. Hofherr, D. Rall, M. Siegel, A. Semenov, A. Engel, K. Inderbitzin, A. Aeschbacher, and A. Schilling, J. Low Temp. Phys. (2011).
[14] L. Maingault, M. Tarkhov, I. Florya, A. Semenov, R. Espiau de Lamaëstre, P. Cavalier, G. Gol'tsman, J.-P. Poizat, and J.-C. Villégier, J. Appl. Phys. **107**, 116103 (2010).
[15] A. Semenov, A. Engel, H.-W. Hübers, K. Il'in, and M. Siegel, Eur. Phys. J. B **47**, 495 (2005).
[16] K. S. Il'in, I. I. Milostnaya, A. A. Verevkin, G. N. Gol'tsman, E. M. Gershenzon, and R. Sobolewski, Appl. Phys. Lett. **73**, 3938 (1998).
[17] T. Yamashita, S. Miki, W. Qiu, M. Fujiwara, M. Sasaki, and Z. Wang, Appl. Phys. Express **3**, 102502 (2010).

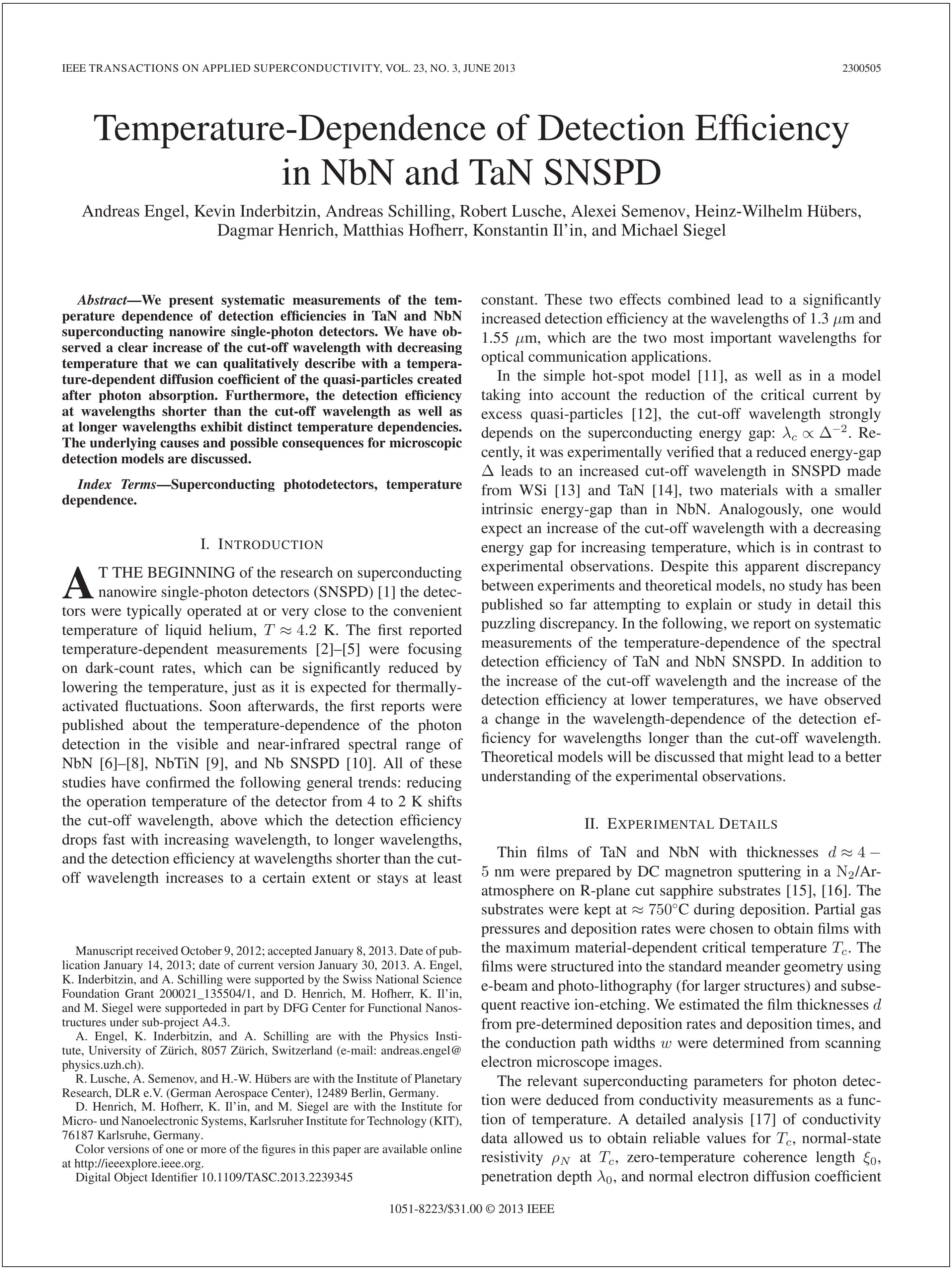

IEEE TRANSACTIONS ON APPLIED SUPERCONDUCTIVITY, VOL. 23, NO. 3, JUNE 2013 2300505

Temperature-Dependence of Detection Efficiency in NbN and TaN SNSPD

Andreas Engel, Kevin Inderbitzin, Andreas Schilling, Robert Lusche, Alexei Semenov, Heinz-Wilhelm Hübers,
Dagmar Henrich, Matthias Hofherr, Konstantin Il'in, and Michael Siegel

***Abstract*—We present systematic measurements of the temperature dependence of detection efficiencies in TaN and NbN superconducting nanowire single-photon detectors. We have observed a clear increase of the cut-off wavelength with decreasing temperature that we can qualitatively describe with a temperature-dependent diffusion coefficient of the quasi-particles created after photon absorption. Furthermore, the detection efficiency at wavelengths shorter than the cut-off wavelength as well as at longer wavelengths exhibit distinct temperature dependencies. The underlying causes and possible consequences for microscopic detection models are discussed.**

***Index Terms*—Superconducting photodetectors, temperature dependence.**

I. INTRODUCTION

AT THE BEGINNING of the research on superconducting nanowire single-photon detectors (SNSPD) [1] the detectors were typically operated at or very close to the convenient temperature of liquid helium, $T \approx 4.2$ K. The first reported temperature-dependent measurements [2]–[5] were focusing on dark-count rates, which can be significantly reduced by lowering the temperature, just as it is expected for thermally-activated fluctuations. Soon afterwards, the first reports were published about the temperature-dependence of the photon detection in the visible and near-infrared spectral range of NbN [6]–[8], NbTiN [9], and Nb SNSPD [10]. All of these studies have confirmed the following general trends: reducing the operation temperature of the detector from 4 to 2 K shifts the cut-off wavelength, above which the detection efficiency drops fast with increasing wavelength, to longer wavelengths, and the detection efficiency at wavelengths shorter than the cut-off wavelength increases to a certain extent or stays at least constant. These two effects combined lead to a significantly increased detection efficiency at the wavelengths of 1.3 μm and 1.55 μm, which are the two most important wavelengths for optical communication applications.

In the simple hot-spot model [11], as well as in a model taking into account the reduction of the critical current by excess quasi-particles [12], the cut-off wavelength strongly depends on the superconducting energy gap: $\lambda_c \propto \Delta^{-2}$. Recently, it was experimentally verified that a reduced energy-gap Δ leads to an increased cut-off wavelength in SNSPD made from WSi [13] and TaN [14], two materials with a smaller intrinsic energy-gap than in NbN. Analogously, one would expect an increase of the cut-off wavelength with a decreasing energy gap for increasing temperature, which is in contrast to experimental observations. Despite this apparent discrepancy between experiments and theoretical models, no study has been published so far attempting to explain or study in detail this puzzling discrepancy. In the following, we report on systematic measurements of the temperature-dependence of the spectral detection efficiency of TaN and NbN SNSPD. In addition to the increase of the cut-off wavelength and the increase of the detection efficiency at lower temperatures, we have observed a change in the wavelength-dependence of the detection efficiency for wavelengths longer than the cut-off wavelength. Theoretical models will be discussed that might lead to a better understanding of the experimental observations.

II. EXPERIMENTAL DETAILS

Thin films of TaN and NbN with thicknesses $d \approx 4-5$ nm were prepared by DC magnetron sputtering in a N_2/Ar-atmosphere on R-plane cut sapphire substrates [15], [16]. The substrates were kept at $\approx 750^\circ$C during deposition. Partial gas pressures and deposition rates were chosen to obtain films with the maximum material-dependent critical temperature T_c. The films were structured into the standard meander geometry using e-beam and photo-lithography (for larger structures) and subsequent reactive ion-etching. We estimated the film thicknesses d from pre-determined deposition rates and deposition times, and the conduction path widths w were determined from scanning electron microscope images.

The relevant superconducting parameters for photon detection were deduced from conductivity measurements as a function of temperature. A detailed analysis [17] of conductivity data allowed us to obtain reliable values for T_c, normal-state resistivity ρ_N at T_c, zero-temperature coherence length ξ_0, penetration depth λ_0, and normal electron diffusion coefficient

---

Manuscript received October 9, 2012; accepted January 8, 2013. Date of publication January 14, 2013; date of current version January 30, 2013. A. Engel, K. Inderbitzin, and A. Schilling were supported by the Swiss National Science Foundation Grant 200021_135504/1, and D. Henrich, M. Hofherr, K. Il'in, and M. Siegel were supporteded in part by DFG Center for Functional Nanostructures under sub-project A4.3.

A. Engel, K. Inderbitzin, and A. Schilling are with the Physics Institute, University of Zürich, 8057 Zürich, Switzerland (e-mail: andreas.engel@physics.uzh.ch).

R. Lusche, A. Semenov, and H.-W. Hübers are with the Institute of Planetary Research, DLR e.V. (German Aerospace Center), 12489 Berlin, Germany.

D. Henrich, M. Hofherr, K. Il'in, and M. Siegel are with the Institute for Micro- und Nanoelectronic Systems, Karlsruher Institute for Technology (KIT), 76187 Karlsruhe, Germany.

Color versions of one or more of the figures in this paper are available online at http://ieeexplore.ieee.org.

Digital Object Identifier 10.1109/TASC.2013.2239345

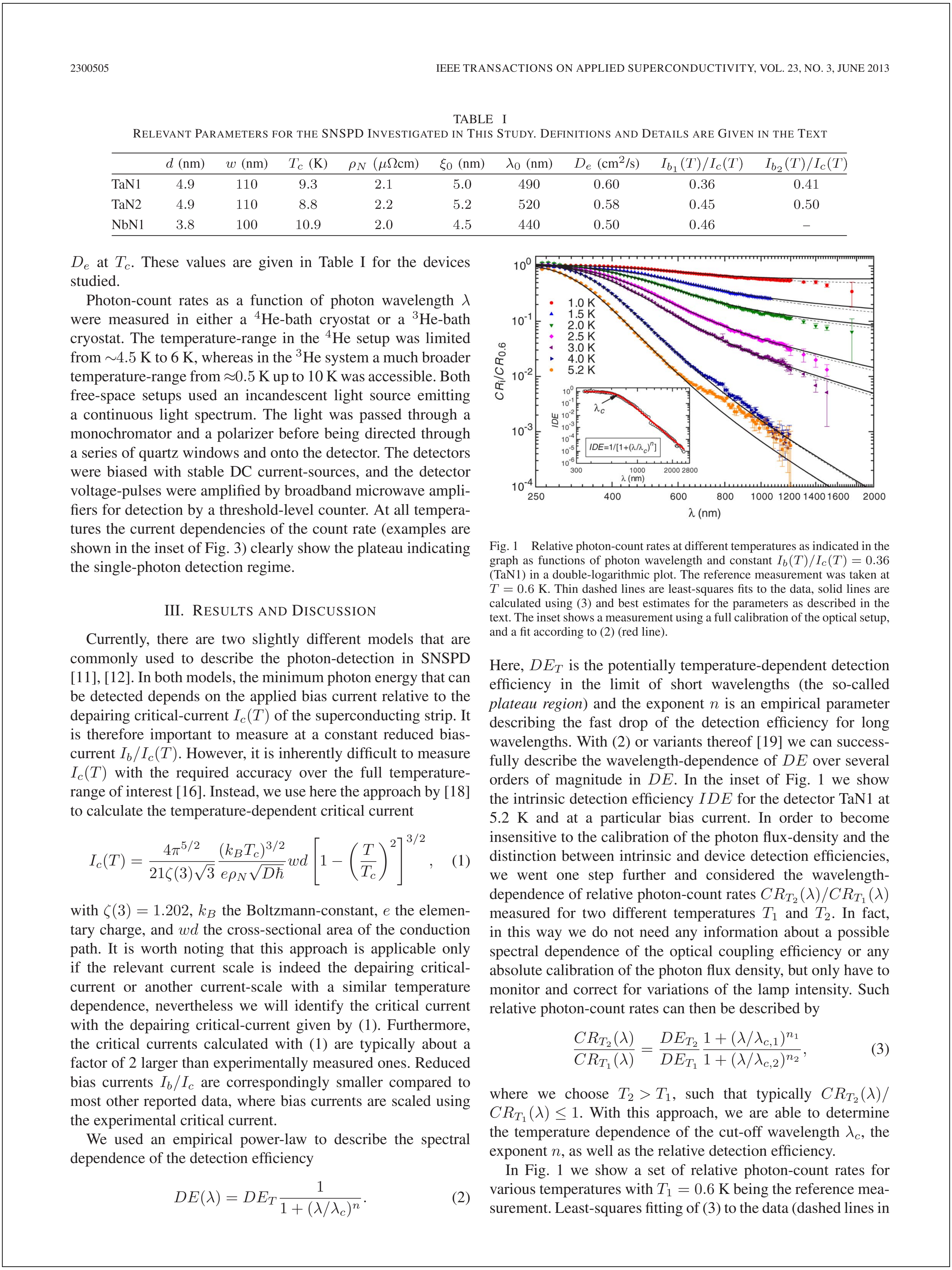

TABLE I
RELEVANT PARAMETERS FOR THE SNSPD INVESTIGATED IN THIS STUDY. DEFINITIONS AND DETAILS ARE GIVEN IN THE TEXT

	d (nm)	w (nm)	T_c (K)	ρ_N ($\mu\Omega$cm)	ξ_0 (nm)	λ_0 (nm)	D_e (cm^2/s)	$I_{b_1}(T)/I_c(T)$	$I_{b_2}(T)/I_c(T)$
TaN1	4.9	110	9.3	2.1	5.0	490	0.60	0.36	0.41
TaN2	4.9	110	8.8	2.2	5.2	520	0.58	0.45	0.50
NbN1	3.8	100	10.9	2.0	4.5	440	0.50	0.46	–

D_e at T_c. These values are given in Table I for the devices studied.

Photon-count rates as a function of photon wavelength λ were measured in either a ^{4}He-bath cryostat or a ^{3}He-bath cryostat. The temperature-range in the ^{4}He setup was limited from ∼4.5 K to 6 K, whereas in the ^{3}He system a much broader temperature-range from ≈0.5 K up to 10 K was accessible. Both free-space setups used an incandescent light source emitting a continuous light spectrum. The light was passed through a monochromator and a polarizer before being directed through a series of quartz windows and onto the detector. The detectors were biased with stable DC current-sources, and the detector voltage-pulses were amplified by broadband microwave amplifiers for detection by a threshold-level counter. At all temperatures the current dependencies of the count rate (examples are shown in the inset of Fig. 3) clearly show the plateau indicating the single-photon detection regime.

III. RESULTS AND DISCUSSION

Currently, there are two slightly different models that are commonly used to describe the photon-detection in SNSPD [11], [12]. In both models, the minimum photon energy that can be detected depends on the applied bias current relative to the depairing critical-current $I_c(T)$ of the superconducting strip. It is therefore important to measure at a constant reduced bias-current $I_b/I_c(T)$. However, it is inherently difficult to measure $I_c(T)$ with the required accuracy over the full temperature-range of interest [16]. Instead, we use here the approach by [18] to calculate the temperature-dependent critical current

$$I_c(T) = \frac{4\pi^{5/2}}{21\zeta(3)\sqrt{3}} \frac{(k_B T_c)^{3/2}}{e\rho_N \sqrt{D\hbar}} wd \left[1 - \left(\frac{T}{T_c}\right)^2\right]^{3/2}, \quad (1)$$

with $\zeta(3) = 1.202$, k_B the Boltzmann-constant, e the elementary charge, and wd the cross-sectional area of the conduction path. It is worth noting that this approach is applicable only if the relevant current scale is indeed the depairing critical-current or another current-scale with a similar temperature dependence, nevertheless we will identify the critical current with the depairing critical-current given by (1). Furthermore, the critical currents calculated with (1) are typically about a factor of 2 larger than experimentally measured ones. Reduced bias currents I_b/I_c are correspondingly smaller compared to most other reported data, where bias currents are scaled using the experimental critical current.

We used an empirical power-law to describe the spectral dependence of the detection efficiency

$$DE(\lambda) = DE_T \frac{1}{1 + (\lambda/\lambda_c)^n}. \quad (2)$$

Fig. 1 Relative photon-count rates at different temperatures as indicated in the graph as functions of photon wavelength and constant $I_b(T)/I_c(T) = 0.36$ (TaN1) in a double-logarithmic plot. The reference measurement was taken at $T = 0.6$ K. Thin dashed lines are least-squares fits to the data, solid lines are calculated using (3) and best estimates for the parameters as described in the text. The inset shows a measurement using a full calibration of the optical setup, and a fit according to (2) (red line).

Here, DE_T is the potentially temperature-dependent detection efficiency in the limit of short wavelengths (the so-called *plateau region*) and the exponent n is an empirical parameter describing the fast drop of the detection efficiency for long wavelengths. With (2) or variants thereof [19] we can successfully describe the wavelength-dependence of DE over several orders of magnitude in DE. In the inset of Fig. 1 we show the intrinsic detection efficiency IDE for the detector TaN1 at 5.2 K and at a particular bias current. In order to become insensitive to the calibration of the photon flux-density and the distinction between intrinsic and device detection efficiencies, we went one step further and considered the wavelength-dependence of relative photon-count rates $CR_{T_2}(\lambda)/CR_{T_1}(\lambda)$ measured for two different temperatures T_1 and T_2. In fact, in this way we do not need any information about a possible spectral dependence of the optical coupling efficiency or any absolute calibration of the photon flux density, but only have to monitor and correct for variations of the lamp intensity. Such relative photon-count rates can then be described by

$$\frac{CR_{T_2}(\lambda)}{CR_{T_1}(\lambda)} = \frac{DE_{T_2}}{DE_{T_1}} \frac{1 + (\lambda/\lambda_{c,1})^{n_1}}{1 + (\lambda/\lambda_{c,2})^{n_2}}, \quad (3)$$

where we choose $T_2 > T_1$, such that typically $CR_{T_2}(\lambda)/CR_{T_1}(\lambda) \leq 1$. With this approach, we are able to determine the temperature dependence of the cut-off wavelength λ_c, the exponent n, as well as the relative detection efficiency.

In Fig. 1 we show a set of relative photon-count rates for various temperatures with $T_1 = 0.6$ K being the reference measurement. Least-squares fitting of (3) to the data (dashed lines in

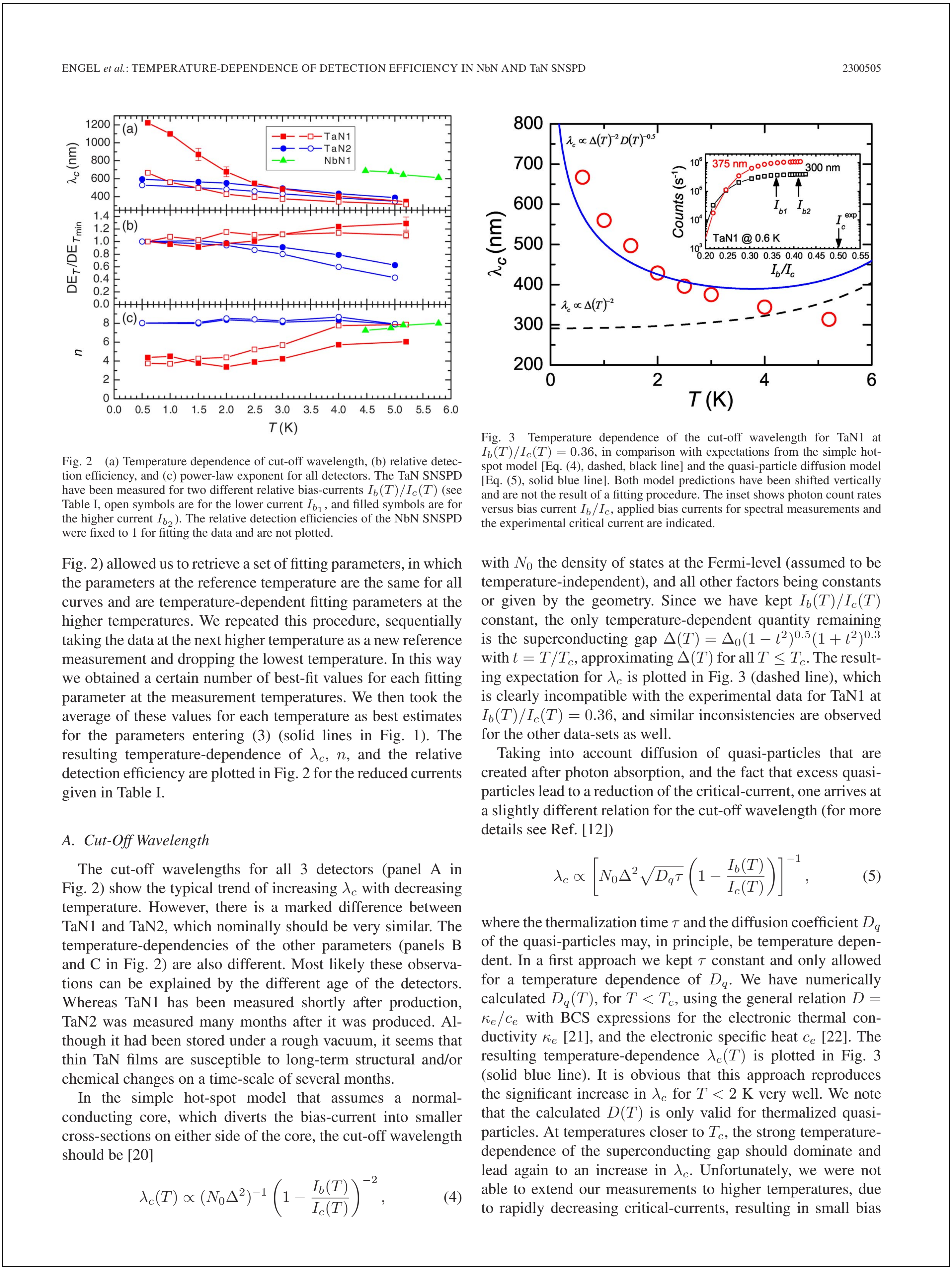

Fig. 2 (a) Temperature dependence of cut-off wavelength, (b) relative detection efficiency, and (c) power-law exponent for all detectors. The TaN SNSPD have been measured for two different relative bias-currents $I_b(T)/I_c(T)$ (see Table I, open symbols are for the lower current I_{b_1}, and filled symbols are for the higher current I_{b_2}). The relative detection efficiencies of the NbN SNSPD were fixed to 1 for fitting the data and are not plotted.

Fig. 3 Temperature dependence of the cut-off wavelength for TaN1 at $I_b(T)/I_c(T) = 0.36$, in comparison with expectations from the simple hot-spot model [Eq. (4), dashed, black line] and the quasi-particle diffusion model [Eq. (5), solid blue line]. Both model predictions have been shifted vertically and are not the result of a fitting procedure. The inset shows photon count rates versus bias current I_b/I_c, applied bias currents for spectral measurements and the experimental critical current are indicated.

Fig. 2) allowed us to retrieve a set of fitting parameters, in which the parameters at the reference temperature are the same for all curves and are temperature-dependent fitting parameters at the higher temperatures. We repeated this procedure, sequentially taking the data at the next higher temperature as a new reference measurement and dropping the lowest temperature. In this way we obtained a certain number of best-fit values for each fitting parameter at the measurement temperatures. We then took the average of these values for each temperature as best estimates for the parameters entering (3) (solid lines in Fig. 1). The resulting temperature-dependence of λ_c, n, and the relative detection efficiency are plotted in Fig. 2 for the reduced currents given in Table I.

A. *Cut-Off Wavelength*

The cut-off wavelengths for all 3 detectors (panel A in Fig. 2) show the typical trend of increasing λ_c with decreasing temperature. However, there is a marked difference between TaN1 and TaN2, which nominally should be very similar. The temperature-dependencies of the other parameters (panels B and C in Fig. 2) are also different. Most likely these observations can be explained by the different age of the detectors. Whereas TaN1 has been measured shortly after production, TaN2 was measured many months after it was produced. Although it had been stored under a rough vacuum, it seems that thin TaN films are susceptible to long-term structural and/or chemical changes on a time-scale of several months.

In the simple hot-spot model that assumes a normal-conducting core, which diverts the bias-current into smaller cross-sections on either side of the core, the cut-off wavelength should be [20]

$$\lambda_c(T) \propto (N_0\Delta^2)^{-1}\left(1 - \frac{I_b(T)}{I_c(T)}\right)^{-2}, \tag{4}$$

with N_0 the density of states at the Fermi-level (assumed to be temperature-independent), and all other factors being constants or given by the geometry. Since we have kept $I_b(T)/I_c(T)$ constant, the only temperature-dependent quantity remaining is the superconducting gap $\Delta(T) = \Delta_0(1-t^2)^{0.5}(1+t^2)^{0.3}$ with $t = T/T_c$, approximating $\Delta(T)$ for all $T \leq T_c$. The resulting expectation for λ_c is plotted in Fig. 3 (dashed line), which is clearly incompatible with the experimental data for TaN1 at $I_b(T)/I_c(T) = 0.36$, and similar inconsistencies are observed for the other data-sets as well.

Taking into account diffusion of quasi-particles that are created after photon absorption, and the fact that excess quasi-particles lead to a reduction of the critical-current, one arrives at a slightly different relation for the cut-off wavelength (for more details see Ref. [12])

$$\lambda_c \propto \left[N_0\Delta^2\sqrt{D_q\tau}\left(1 - \frac{I_b(T)}{I_c(T)}\right)\right]^{-1}, \tag{5}$$

where the thermalization time τ and the diffusion coefficient D_q of the quasi-particles may, in principle, be temperature dependent. In a first approach we kept τ constant and only allowed for a temperature dependence of D_q. We have numerically calculated $D_q(T)$, for $T < T_c$, using the general relation $D = \kappa_e/c_e$ with BCS expressions for the electronic thermal conductivity κ_e [21], and the electronic specific heat c_e [22]. The resulting temperature-dependence $\lambda_c(T)$ is plotted in Fig. 3 (solid blue line). It is obvious that this approach reproduces the significant increase in λ_c for $T < 2$ K very well. We note that the calculated $D(T)$ is only valid for thermalized quasi-particles. At temperatures closer to T_c, the strong temperature-dependence of the superconducting gap should dominate and lead again to an increase in λ_c. Unfortunately, we were not able to extend our measurements to higher temperatures, due to rapidly decreasing critical-currents, resulting in small bias

currents and therefore small signal amplitudes. Also, the detectors became increasingly unstable at elevated temperatures.

It is interesting to note that the recently developed X-ray superconducting nanowire single-photon detectors (X-SNSPD) [23] seem to show a different temperature dependence of the minimum detectable photon energy. Results obtained for a 100 nm-thick TaN X-SNSPD indicate a decreasing threshold energy (*i.e.* increasing λ_c) with increasing operation temperature [24].

B. Relative Detection Efficiency

In panel B of Fig. 2 we show the relative detection efficiency versus temperature. It is remarkable that the detection efficiency in the plateau region remains essentially constant for the high-quality detector TaN1, whereas the somewhat degraded detector TaN2 shows a pronounced reduction of the detection efficiency with increasing temperature. The exact reason for this behavior is unclear at this stage, but we expect that an increased level of inhomogeneities plays an important role here. Measuring the detection efficiency as a function of temperature may therefore be a tool to determine a the quality of a detector.

C. Power-Law Exponent

In panel C of Fig. 2 we plot the power-law exponents n in (3) as a function of temperature. This quantity describes the decrease of the detection efficiency beyond the cut-off wavelength λ_c for photons with energies that are insufficient to trigger a normal-conducting domain in the superconducting strip without any additional contribution from fluctuations. A thermally-activated crossing of vortices has been suggested as a possible mechanism to describe the detection of such photons [25]. However, recent measurements of the magnetic-field dependence of photon-count rates raised serious doubts about the role of vortices in this regime [26].

Interestingly, the power-law exponents of the degraded TaN2 detector are consistent with a temperature independent behavior, while the data of the high-quality TaN1 and NbN1 SNSPD suggest an increasing exponent with increasing temperature. At this point of our investigations we have no explanation for such a behavior, but we believe that it may give helpful clues to uncover the true mechanism of low-energy photon detection in these devices.

IV. CONCLUSION

We have presented systematic measurements of the temperature dependence of the spectral detection-efficiency of SNSPD. We have tried to eliminate the temperature-dependence of the critical current by measuring at a constant reduced bias-current $I_b(T)/I_c(T)$, where we have used Bardeen's result for the depairing critical current. We have found that the wavelength-dependence of the detection efficiency can be accurately described by a simple power-law, which in turn allowed us to extract not only the temperature dependence of the cut-off wavelength, but also the temperature dependencies of the detection efficiency for wavelengths shorter than λ_c, as well as of the power-law exponent in (3) for wavelengths $\lambda > \lambda_c$.

We have confirmed that the cut-off wavelength increases with decreasing temperature and suggested a temperature-dependent diffusion coefficient as the main underlying cause. This observation is strong evidence for the important role of quasi-particle or energy diffusion for a correct understanding of the detection mechanism. These results may further stimulate theoretical developments of a microscopic detection model [27].

High-quality SNSPD, defined as detectors with a low level of inhomogeneities, are most likely characterized by a temperature-independent detection efficiency for $\lambda < \lambda_c$. In that case the device detection efficiency appears to be given by the absorption probability and an intrinsic detection efficiency close to unity. Detectors with non-negligible inhomogeneities can still reach high detection efficiencies by operating them at low temperatures.

The fluctuation-enhanced detection of photons with $\lambda < \lambda_c$ remains an interesting topic. We have found that in this regime the decrease in detection efficiency can be well described by a power-law, $DE \propto \lambda^{-n}$, over many orders of magnitude in DE. Furthermore, it seems that the reduction of the detection efficiency with increasing photon wavelength is slower at low temperatures, particularly in high-quality devices. Any correct description of the detection mechanism in this regime will have to be able to explain these observations.

REFERENCES

[1] G. N. Gol'tsman, O. Okunev, G. Chulkova, A. Lipatov, A. Semenov, K. Smirnov, B. Voronov, A. Dzardanov, C. Williams, and R. Sobolewski, "Picosecond superconducting single-photon optical detector," *Appl. Phys. Lett.*, vol. 79, no. 6, pp. 705–707, Aug. 2001.

[2] A. Engel, A. Semenov, H.-W. Hübers, K. Il'in, and M. Siegel, "Superconducting single-photon detector for the visible and infrared spectral range," *J. Mod. Opt.*, vol. 51, no. 9/10, pp. 1459–1466, Jun. 15–Jul. 10, 2004.

[3] A. Semenov, A. Engel, K. Il'in, M. Siegel, and H.-W. Hübers, "Noise of a superconducting photon detector," *IEEE Trans. Appl. Supercond.*, vol. 15, no. 2, pp. 518–521, Jun. 2005.

[4] J. Kitaygorsky, J. Zhang, A. Verevkin, A. Sergeev, A. Korneev, V. Matvienko, P. Kouminov, K. Smirnov, B. Voronov, and G. Gol'tsman, "Origin of dark counts in nanostructured NbN single-photon detectors," *IEEE Trans. Appl. Supercond.*, vol. 15, no. 2, pp. 545–548, Jun. 2005.

[5] J. Kitaygorsky, I. Komissarov, A. Jukna, D. Pan, O. Minaeva, N. Kaurova, A. Divochiy, A. Korneev, M. Tarkhov, B. Voronov, I. Milostnaya, G. Gol'tsman, and R. R. Sobolewski, "Dark counts in nanostructured NbN superconducting single-photon detectors and bridges," *IEEE Trans. Appl. Supercond.*, vol. 17, no. 2, pp. 275–278, Jun. 2007.

[6] K. M. Rosfjord, J. K. W. Yang, E. A. Dauler, A. J. Kerman, V. Anant, B. M. Voronov, G. N. Gol'tsman, and K. K. Berggren, "Nanowire single-photon detector with an integrated optical cavity and anti-reflection coating," *Opt. Exp.*, vol. 14, no. 2, pp. 527–534, Jan. 2006.

[7] G. Gol'tsman, O. Minaeva, A. Korneev, M. Tarkhov, I. Rubtsova, A. Divochiy, I. Milostnaya, G. Chulkova, N. Kaurova, B. Voronov, D. Pan, J. Kitaygorsky, A. Cross, A. Pearlman, I. Komissarov, W. Slysz, M. Wegrzecki, P. Grabiec, and R. Sobolewski, "Middle-infrared to visible-light ultrafast superconducting single-photon detectors," *IEEE Trans. Appl. Supercond.*, vol. 17, no. 2, pp. 246–251, Jun. 2007.

[8] A. J. Kerman, E. A. Dauler, J. K. W. Yang, K. M. Rosfjord, V. Anant, K. K. Berggren, G. Gol'tsman, and B. Voronov, "Constriction-limited detection efficiency of superconducting nanowire single-photon detectors," *Appl. Phys. Lett.*, vol. 90, no. 10, pp. 101110-1–101110-3, Mar. 2007.

[9] S. N. Dorenbos, E. M. Reiger, U. Perinetti, V. Zwiller, T. Zijlstra, and T. M. Klapwijk, "Low noise superconducting single photon detectors on silicon," *Appl. Phys. Lett.*, vol. 93, no. 13, pp. 131101-1–131101-3, Sep. 2008.

[10] A. J. Annunziata, D. F. Santavicca, J. D. Chudow, L. Frunzio, M. J. Rooks, A. Frydman, and D. E. Prober, "Niobium superconducting nanowire

single-photon detectors," *IEEE Trans. Appl. Supercond.*, vol. 19, no. 3, pp. 327–331, Jun. 2009.

[11] A. D. Semenov, G. N. Gol'tsman, and A. A. Korneev, "Quantum detection by current carrying superconducting film," *Phys. C*, vol. 351, no. 4, pp. 349–356, Apr. 2001.

[12] A. Semenov, A. Engel, H.-W. Hübers, K. Il'in, and M. Siegel, "Spectral cut-off in the efficiency of the resistive state formation caused by absorption of a single-photon in current-carrying superconducting nano-strips," *Eur. Phys. J. B*, vol. 47, no. 4, pp. 495–501, Oct. 2005.

[13] B. Baek, A. E. Lita, V. Verma, and S. W. Nam, "Superconducting a-W_xSi_{1-x} nanowire single-photon detector with saturated internal quantum efficiency from visible to 1850 nm," *Appl. Phys. Lett.*, vol. 98, no. 25, pp. 251105-1–251105-3, Jun. 2011.

[14] A. Engel, A. Aeschbacher, K. Inderbitzin, A. Schilling, K. Il'in, M. Hofherr, M. Siegel, A. Semenov, and H.-W. Hübers, "Tantalum nitride superconducting single-photon detectors with low cut-off energy," *Appl. Phys. Lett.*, vol. 100, no. 6, pp. 062601-1–062601-3, Feb. 2012.

[15] K. Il'in, M. Siegel, A. Engel, H. Bartolf, A. Schilling, A. Semenov, and H.-W. Hübers, "Current-induced critical state in NbN thin-film structures," *J. Low Temp. Phys.*, vol. 151, no. 1/2, pp. 585–590, 2008.

[16] K. S. Il'in, D. Rall, M. Siegel, and A. Semenov, "Critical current density in thin superconducting TaN film structures," *Phys. C*, vol. 479, pp. 176–178, Sep. 2012.

[17] H. Bartolf, A. Engel, A. Schilling, K. Il'in, M. Siegel, H.-W. Hübers, and A. Semenov, "Current-assisted thermally activated flux liberation in ultrathin nanopatterned NbN superconducting meander structures," *Phys. Rev. B*, vol. 81, no. 2, pp. 024502-1–024502-12, Jan. 2010.

[18] J. Bardeen, "Critical fields and currents in superconductors," *Rev. Mod. Phys.*, vol. 34, no. 4, pp. 667–681, Oct.–Dec. 1962.

[19] R. Lusche, A. Semenov, K. Il'in, Y. Korneeva, A. Trifonov, A. Korneev, H.-W. Hübers, M. Siegel, and G. Golâtsman, "Effect of the wire width and magnetic field on the intrinsic detection efficiency of superconducting nanowire single-photon detectors," *IEEE Trans. Appl. Supercond.*, vol. 23, no. 3, p. 2200205, Jun. 2013.

[20] L. Maingault, M. Tarkhov, I. Florya, A. Semenov, R. Espiau de Lamaëstre, P. Cavalier, G. Gol'tsman, J.-P. Poizat, and J.-C. Villégier, "Spectral dependency of superconducting single photon detectors," *J. Appl. Phys.*, vol. 107, no. 11, pp. 116103-1–116103-3, Jun. 2010.

[21] A. A. Abrikosov, *Fundamentals of the Theory of Metals*. New York: Elsevier, 1988.

[22] M. Tinkham, *Introduction to Superconductivity*, 2nd ed. New York: McGraw-Hill, 1996.

[23] K. Inderbitzin, A. Engel, A. Schilling, K. Il'in, and M. Siegel, "An ultrafast superconducting Nb nanowire single-photon detector for soft X-rays," *Appl. Phys. Lett.*, vol. 101, no. 16, pp. 162601-1–162601-5, Oct. 2012.

[24] K. Inderbitzin, A. Engel, and A. Schilling, "Soft X-ray single-photon detection with superconducting tantalum nitride and niobium nanowires," *IEEE Trans. Appl. Supercond.*, DOI: 10.1109/TASC.2012.2234496, to be published.

[25] L. N. Bulaevskii, M. J. Graf, and V. G. Kogan, "Vortex-assisted photon counts and their magnetic field dependence in single-photon detectors," *Phys. Rev. B*, vol. 85, no. 1, pp. 014505-1–014505-10, Jan. 2012.

[26] A. Engel, A. Schilling, K. Il'in, and M. Siegel, "Magnetic-field dependence of count rates in superconducting thin-film TaN single-photon detectors," *Phys. Rev. B*, vol. 86, pp. 140506-1–140506-4, Oct. 2012.

[27] A. N. Zotova and D. Y. Vodolazov, "Photon detection by current-carrying superconducting film: A time-dependent Ginzburg-Landau approach," *Phys. Rev. B*, vol. 85, no. 2, pp. 024509-1–024509-9, Jan. 2012.

Chapter 3

Motivation for the Adaption of SNSPDs as X-Ray Photon Detectors

SNSPDs have been shown to allow timing resolutions of less than 30 ps [69] and count rates of up to 2 GHz [66] in the near-IR and visible photon energy range. Preliminary experiments on soft X-ray photon detection with thick-film X-SNSPDs by Gabutti *et al.* [88] and a thin-film SNSPD by Perez de Lara *et al.* [75] have shown promising results. X-SNSPDs are therefore good candidates for the detection of single soft X-ray photons with a good timing resolution, very high count rates and a negligible dark count rate.

Potential applications for such detectors comprise experiments with synchrotron X-ray sources, free-electron lasers and hot plasmas (as in nuclear fusion experiments), all emitting bright and pulsed X-ray radiation. In many medical imaging systems ultrafast X-ray single-photon detectors with energy resolution are desirable in order to reduce patient radiation dose. In the recently developing photon-counting X-ray computer tomography for example, long photon detection pulse durations can compromise the image quality by a possible overlap of succeeding photon pulses, as high photon fluxes have to be used in order to prevent motion blur [109]. Ultrafast energy-resolving single-photon detectors could therefore be useful to circumvent this problem.

As explained in section 2.3.4 and shown by Perez de Lara *et al.* [75], soft X-ray photon detection in typical thin-film SNSPDs mostly occurs by photon absorption in the substrate and the successive energy diffusion to the superconducting meander structure. It is very likely, however, that this indirect detection principle for X-ray photons results in an increased timing jitter as compared to the direct photon detection in the superconducting film, due to the random nature of the energy diffusion processes to the superconducting meander structure after photon absorption and the depth distribution of the photon absorption point.

In order to confirm the successful demonstration of X-ray photon detection with SNSPDs by Perez de Lara *et al.* [75], we performed similar measurements with a 6 nm thin NbN SNSPD, which will be discussed in chapter 6, however, with the possibilities offered by a much more intense X-ray source. As our results were qualitatively in agreement, X-SNSPDs from much thicker films were fabricated and characterized in order to enhance the absorptance of the X-SNSPD and therefore promote a more direct detection principle. Gabutti *et al.* [88] managed to fabricate an X-SNSPD from granular tungsten showing 6 keV photon detection in continuous-mode. However, no photon counting experiments could be performed with this detector in continuous-mode at that time, due to small pulse amplitudes and limitations of the electronic threshold counter. In addition, the lacking understanding of the detection processes in X-SNSPDs (especially regarding the requirements on the kinetic inductance of the detectors and the material resistivity) did not allow to read-out functional X-SNSPDs. The progress in understanding visible photon detection with SNSPDs in the last decade, in combination with the tremendous progress in micro- and nanofabrication, should allow for the development and operation of functional X-SNSPDs nowadays.

We fabricated and characterized X-SNSPDs from 100 nm thick Nb and TaN, as presented in chapter 7. Nb films are easier to sputter than the commonly used nitride-compounds (as for example NbN, NbTiN or TaN). Furthermore, it has an about two orders of magnitude lower resistivity than the latter materials, which opens up room for new phenomena in X-SNSPDs. For example, resulting domain resistances smaller than the 50 Ω impedance of the read-out line open the possibility of photon energy-dependent pulse amplitudes (see chapter 7). Such an energy dependence could also be of interest for TOF-MS of keV-molecules [73]. However, small domain resistances can also promote latching and lead to problems in differentiating small-amplitude detection pulses from electronic noise, and therefore X-SNSPDs from TaN have also been fabricated and characterized. In addition, TaN also offers a larger X-ray absorptance [85] than Nb and NbN.

Chapter 4

Detector Fabrication

In this chapter, the established fabrication of thin-film SNSPDs and its adaption for 100 nm thick X-SNSPDs is summarized on the basis of our work by Bartolf *et al.* [110]. The (X-)SNSPDs used for the X-ray photon detection experiments described in chapter 6 and 7 have been fabricated by the methods presented here.

Two different lithographic methods are used throughout this fabrication process. For both methods, a thin layer of resist is deposited onto the sample by spinning the sample with several thousands of rotations per minute. The resist is then exposed at specific areas to either UV photons or keV-electrons, leading to a resist soluble by a certain developer only at the exposed (in the case of so called "positive resist") or only at the non-exposed areas ("negative resist"), if the exposure dose per area AED (called "area exposure dose") is larger than a certain critical dose per area AED_c, called "clearing dose". AED_c is usually given as the critical amount of energy incident per area (i.e. $\mathrm{mJ/cm^2}$) for UV exposure and as the critical amount of charge incident per area (i.e. $\mu\mathrm{C/cm^2}$) in the case of electron exposure. The used resists are optimized for either exposure by UV photons or keV-electrons, defining the lithographic method:

1. **Photolithography:** UV light (in our case mainly with wavelengths $320\ \mathrm{nm} < \lambda < 405\ \mathrm{nm}$) is applied to expose specific areas of the resist through the non-chromium-covered parts of a quartz-mask. In photolithography, a sample can therefore be exposed simultaneously at every position, and with the equipment employed, wafers with a diameter of up to 3 inch (≈ 7.6 cm) can be exposed. For our photolithography steps the resists AZ5214E and AZ6632 are used.

2. **Electron-beam lithography (EBL):** This well established nanolithographic method basically consists of an SEM (scanning electron microscope) with the electron-beam deflected raster-like only over the desired design pattern, thereby exposing the resist. The design pattern is transformed into single points of electron irradia-

tion, with a gap in between given by the so called "area step size" (set to 10 nm in our case), and the single point-exposure time (the "area dwell time") given by the user-defined exposure dose per area AED. EBL therefore writes the design pattern point-by-point, and only small areas (the "write fields") can be exposed during a single run. In our fabrication recipe 100 μm and 200 μm square write fields, an electron-beam acceleration voltage of 30 kV and the EBL-resist ZEP520A are used.

In principle, there are two basic fabrication methods using these two lithographic methods, both involving the lithographic patterning of a resist layer:

1. **Lift-off deposition:** A resist layer is structured by photo- or EBL-lithography, and subsequently metallic layers are evaporated onto the sample. The metallic layers on top of the resist detach from the sample in an acetone bath as the resist is dissolved. However, the metallic layers evaporated directly onto the substrate or superconducting film remain attached. Therefore, a specific metallic pattern can be transferred onto a sample by such a lift-off deposition process.
2. **Dry etching:** The dry etching method of reactive ion etching (RIE) removes, by a combination of chemical reactions and physical sputtering, the part of the superconducting film which is not protected by a lithographically structured resist. Therefore, a specific pattern can be transferred by RIE into the superconducting film.

In the following sections, the applied fabrication steps are presented separately, and a schematic summary is shown in Fig. 4.1:

4.1 Sputtering of the superconducting film

For conventional thin-film SNSPDs a 4-6 nm thin NbN film (colored in red in Fig. 4.1) is deposited onto an R-plane cut sapphire substrate at 750 °C by DC reactive magnetron sputtering of a pure Nb target in a Ar/N_2 gas mixture at a total pressure of $\approx 10^{-3}$ mbar. The sputtering process is optimized with respect to the partial pressure of N_2 and the deposition rate to achieve the highest T_c [51, 111], and is performed at the Karlsruhe Institute of Technology by K. Il'in *et al.*

For the X-SNSPDs, $\approx$ 100 nm thick Nb and TaN films are deposited onto an R-plane cut sapphire substrate. The Nb films is deposited at room temperature by DC magnetron sputtering in an Ar atmosphere at the Karlsruhe Institute of Technology by K. Il'in *et al.* The TaN film is deposited at $T = 700$ °C by DC reactive magnetron sputtering in an Ar/N_2 atmosphere by A. Engel.

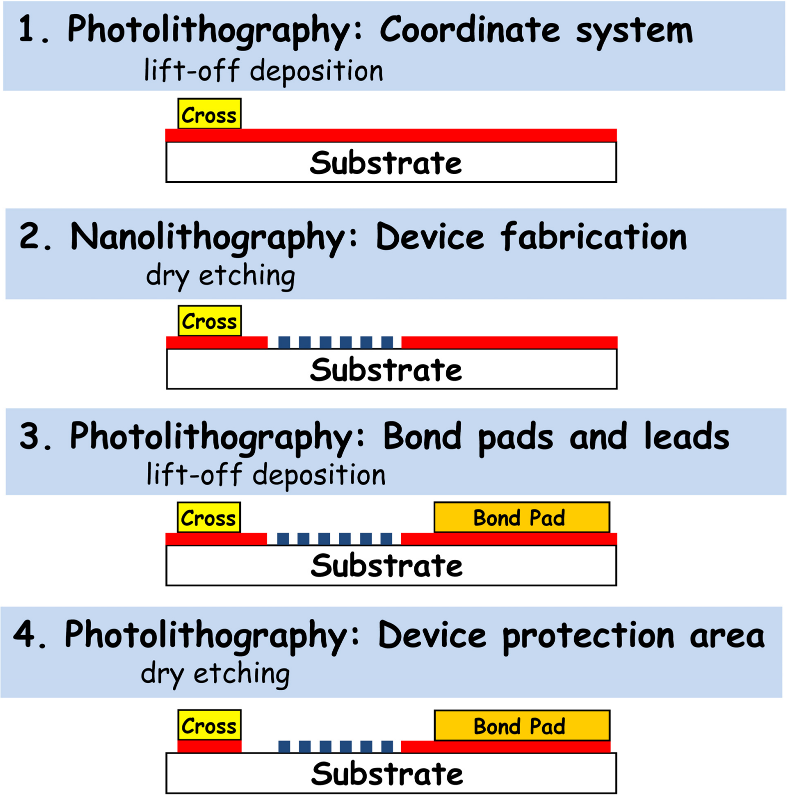

Figure 4.1: Schematics of the (X-)SNSPD fabrication steps. The Ti/Au coordinate system is colored yellow, the Ti/Au bond pads orange, the superconducting film red and the (X-)SNSPD nanowires fabricated from it blue. This figure is taken from our work by Bartolf *et al.* [110].

4.2 Coordinate system deposition

A coordinate system is defined on top of the superconducting film (colored in yellow in Fig. 4.1) by photolithography of a 1.3 μm thick AZ5214E resist layer and lift-off deposition of two types of markers:

1. **EBL markers:** Allow for the alignment of the EBL write field to the defined coordinate system, as necessary in the subsequent nanofabrication step.

2. **Photolithography markers:** Allow for the alignment of a photolithography mask to the defined coordinate system, which is necessary for the deposition of the bond pads and the removal of the residual superconducting film after device fabrication.

For the thin-film SNSPDs a 10 nm Ti layer (for proper adhesion to the superconducting film) and a 90 nm Au layer on top are evaporated.

It is necessary to use significantly thicker EBL resist layers for the nanolithography of the 100 nm thick superconducting films than for the thin-films, as it will be described in the next section. Therefore, thicker Au layers are evaporated for the definition of the coordinate system in order to achieve a sufficiently high SEM contrast of the metal markers against the substrate when covered with EBL resist. 10/600 nm thick Ti/Au layers are deposited onto the Nb film, and 10/190 nm thick layers onto the TaN film.

4.3 Nanofabrication of the (X-)SNSPD nanowires

For thin-film SNSPDs, a 70 nm thin ZEP520 resist is deposited onto the sample by spinning of a ZEP/Anisole mixture with ratio 1:2. The nanowire structure of the SNSPD is then written onto the resist by EBL with an area dose $AED = 56\ \mu\text{C/cm}^2$ using a 100 μm square write field, which is then developed by n-Amylacetate. The nanowire pattern (colored in blue in Fig. 4.1) is transferred into the superconducting thin film by RIE using an Ar/SF$_6$ gas mixture of 3:1 at a pressure of $13 - 14\ \mu$bar, 19 W power and 70 V tension. The etching rate for the NbN films at these RIE settings is determined to be ≈ 2.2 nm/min, and therefore the etching time is set to 3 min 15 s to ensure the complete removal of the NbN in the desired areas. The corresponding ZEP520A etch rate is determined to ≈ 17 nm/min, resulting in the 70 nm resist thickness.

The parameters for the RIE of the thicker superconducting films remained unchanged as compared to the thin-film SNSPD parameters. Due to the finite etch rate of the ZEP520A resists, it had therefore to be chosen thicker to protect the film areas which should not be etched during the whole RIE process. As a means to achieve this, pure ZEP520A was spun onto the sample instead of a mixture with anisole, as it results in thicker resist layers. The etch rate for Nb was determined to ≈ 2 nm/min in preliminary studies, and the total etch time was therefore set to 58 min. For the 100 nm thick Nb film, three layers of resist had to be spun onto the sample, resulting in a $\approx 1\ \mu$m thick ZEP520A layer in total. For TaN, the etch rate was determined to ≈ 4.5 nm/min and the etch time was set to 24 min 50 s. For the 100 nm thick TaN film, it was therefore sufficient to spin only one layer of undiluted ZEP520A resist, with a thickness of about 460-510 nm.

4.4 EBL exposure dose optimization

The EBL proximity effect leads to an exposure of the resist around the actual position of the incident electron beam by electron backscattering in the substrate [110] within a characteristic distance of $\beta \approx 2.4\ \mu$m [112] for a sapphire substrate and a 30 kV electron beam acceleration voltage. ZEP520A is a positive EBL resist, and therefore the resist parts to become soluble are exposed. The proximity effect leads to an increased effective area exposure dose around the written structures, possibly leading to the undesired development of resist parts close to written areas. Fig. 4.2 shows an SEM image of a developed 470-480 nm thick ZEP520A resist structure on top of a 100 nm thick TaN film on a sapphire substrate, covered with a ≈ 5 nm thin film of Pd and Au, as the resist itself is non-conductive. The nanowire at the top was additionally exposed by backscattered electrons from the large exposed area at the top of the image, and the resulting enhanced undercut led to a tilting of the nanowire.

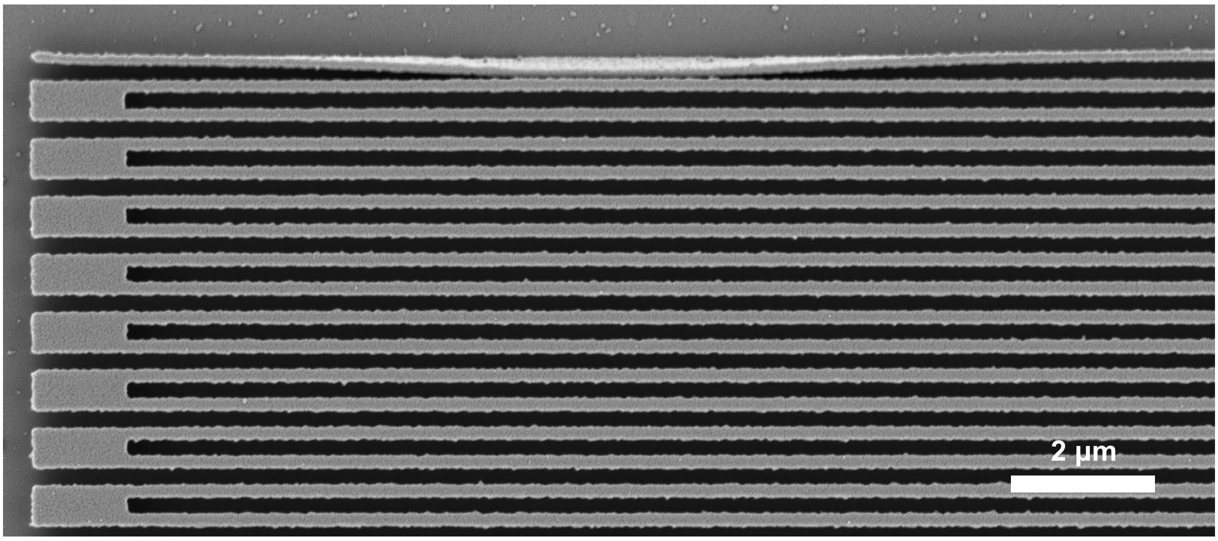

Figure 4.2: SEM image of a developed ZEP520A resist structure, covered with a ≈ 5 nm thin film of Pd and Au. The substrate is a 100 nm thick TaN film on top of sapphire. The nanowires have a width and spacing of about 200 nm, with the nanowire at the top of the image being tilted due to additional exposure by the proximity effect, which led to an increased undercut and hence a reduced mechanical stability of the nanowire (see text).

The nanowire width of an (X-)SNSPD can therefore vary within the meander structure. As a means to reduce this problem, additional inactive nanowires are written next to the active detector area, continuing the periodicity (as was done, for example, in Ref. [52]). Fig. 4.3 shows an example of a ZEP520A resist structure fabricated in the same run as the structure above (Fig. 4.2) and with the same material parameters. The nanowires to the right (left) of the right (left) lead are inactive and not connected the lead.

If meander resist structures of nanowires with width w and a fixed gap g are written, the effective area exposure dose in the gaps decreases with increasing w due to a reduced proximity effect, as the distance between the exposed gaps increases. The area dose set for the exposure has therefore to be increased from the value used for the thin-film SNSPDs (which was 56 μC/cm^2 for nanowires of 80 nm width and 120 nm gap), depending on the nanowire width. The corresponding clearing doses AED_c were determined from pretests on 200 nm thick Nb or 100 nm thick TaN films on sapphire, leading to a proper

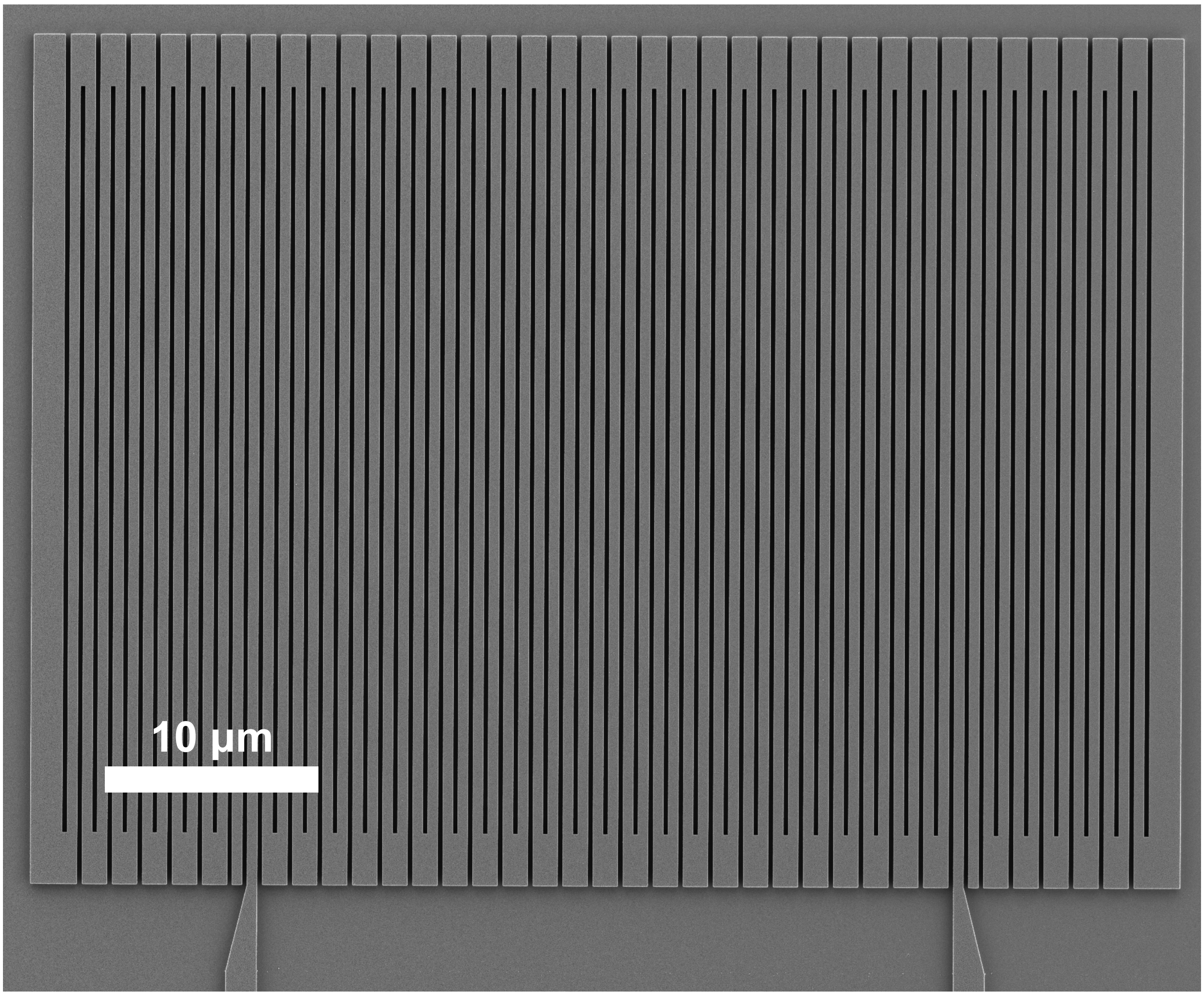

Figure 4.3: SEM image of a developed ZEP520A resist structure, fabricated in the same way as the structure described in the caption of Fig. 4.2, but with a nanowire width $w \approx 500$ nm and gap $g \approx 200$ nm. Inactive, non-connected nanowires are added to both sides of the meander structure to achieve a better nanowire width homogeneity within the active detector area.

development of the exposed resist areas. The resulting applied area doses AED for the different X-SNSPDs are as follows:

Material:	**Designed nanowire width/gap:**	**Area exposure dose AED (μC/cm^2):**
Nb	500 nm/150 nm	84
TaN	500 nm/200 nm	78
TaN	2 μm/200 nm	80

4.5 Bond pads and leads deposition

The bond pads and leads to the thin-film SNSPDs (colored in orange in Fig. 4.1) are deposited onto the sample by lift-off deposition with the identical resist and evaporation parameters as for the coordinate system definition described in section 4.2.

For the X-SNSPDs the bond pads and leads are defined of 10/250 nm Ti/Au layers for the Nb and of 10/190 nm Ti/Au layers for the TaN detector.

4.6 Short-circuit removal

The superconducting film around the EBL write fields has to be removed to prevent a short-circuit between the leads. The write field areas (including the (X-)SNSPDs) are therefore protected by a 2.6 μm thick photolithographically structured AZ6632 resist, while the surrounding areas are etched by RIE during 6 min for the thin-film SNSPD (or 75 min and 30 min for the Nb and TaN X-SNSPDs, respectively) with the same etching parameters as used for (X-)SNSPD nanofabrication described above in section 4.3. During this process step, the superconducting film underneath the bond pads and leads is not etched as it is protected by the metallic layers. Finally, the remaining AZ6632 resist residuals are stripped.

Chapter 5

Experimental Methods

5.1 Electronic resistance measurements in a PPMS

Electronic resistance measurements were performed in a Physical Property Measurement System (PPMS) by Quantum Design. The characterized (X-)SNSPDs were fabricated with a four-point contact-geometry (as for example shown in Fig. 6.1). Hence four-point-measurements were performed to determine the actual resistance of the detectors and eliminate the contribution of the contact resistance. In the PPMS setup used, the sample could be cooled down to $T = 2.0$ K, and magnetic flux densities of up to $B = 9$ T could be applied.

The resistance measurement data for the (X-)SNSPDs examined can be found in chapter 7.

5.1.1 Resistance measurements in zero magnetic field

The sample resistance $R(T)$ was measured as a function of the sample temperature T at a vanishing magnetic field. The critical temperature T_c was then determined using a 50% resistance criterion. The temperature-dependent normal-state resistivity $\rho_n(T)$ of a detector can be determined from $R(T)$ if the detector geometry is known:

$$\rho_n(T) = R(T)\frac{wd}{L}. \tag{5.1.1}$$

The value for the normal-state resistivity ρ_n used for the calculation of further superconducting properties of the detector is extracted at a temperature T_n close above T_c at which $\rho_n(T)$ only varies slowly with T (see Fig. 7.10 and Table 7.1: $T_n \approx 10$ K for the X-SNSPDs and $T_n \approx 15$ K for the SNSPD).

Following subsection 1.2.1, the energy gap $\Delta(0)$ can then be calculated from the critical temperature T_c. Together with the normal-state resistivity ρ_n, the magnetic bulk penetration depth $\lambda_{bulk}(0)$ can thus be calculated according to Eq. 1.2.13 in the dirty limit.

5.1.2 Resistance measurements in finite magnetic fields

A finite magnetic flux density B perpendicular to the superconducting film surface was applied and by measurement of the temperature-dependent sample resistance $R_B(T)$ the critical temperature $T_c(B)$ was determined, again using a 50% resistance criterion. B is therefore the upper critical magnetic induction at the temperature T_c, and it can be written as a function $B_{c_2}(T)$. From a linear extrapolation of $B_{c_2}(T)$ to $T = 0$ K, a value for $B_{c_2}(0)$ can be estimated. In the dirty limit, a more realistic value is found with the help of a correction factor [51, 113]

$$B_{c_2}(0) = 0.69\, T_c \left[\frac{dB_{c_2}(T)}{dT}\right]_{T=T_c}, \tag{5.1.2}$$

which in turn allows for the determination of the GL coherence length $\xi(0)$ by Eq. 1.2.6.

5.2 Dark count and X-ray photon counting measurements

5.2.1 Cryostat-system

The X-ray detection measurements have been performed in a He-3 bath cryostat by Janis Research, allowing sample temperatures down to ≈ 0.35 K. When the cryostat is cooled down, the sample chamber is at a pressure of $< 10^{-5}$ mbar due to the increased adsorbance of the inner cryostat wall at low temperatures.

The sample to be examined is clamped onto a sample holder (see Fig. 5.1), and a small amount of Apiezon N (a cryogenic vacuum grease) in between improves the thermal contact. The sample temperature is measured with a thin film Cernox sensor, mounted directly next to the sample. As a means to control the sample temperature, a heater is attached to the He-3 pot, controlled by a LakeShore Temperature Controller 340 and using the sample temperature as a reference in a PID-control loop.

5.2.2 Electronic bias and read-out setup

The detector is bonded to a printed circuit board on the sample holder, consisting of an SMA connector for the coaxial detector signal cable, bond pads for the bias current supply cable and a bias current-low-pass filter, which consists of an inductance of 80 nH and a capacitance of 10 pF (see Fig. 5.2). An additional low pass filter at room temperature improves low-pass filtering of the quasi-constant-current bias generated by a Keithley

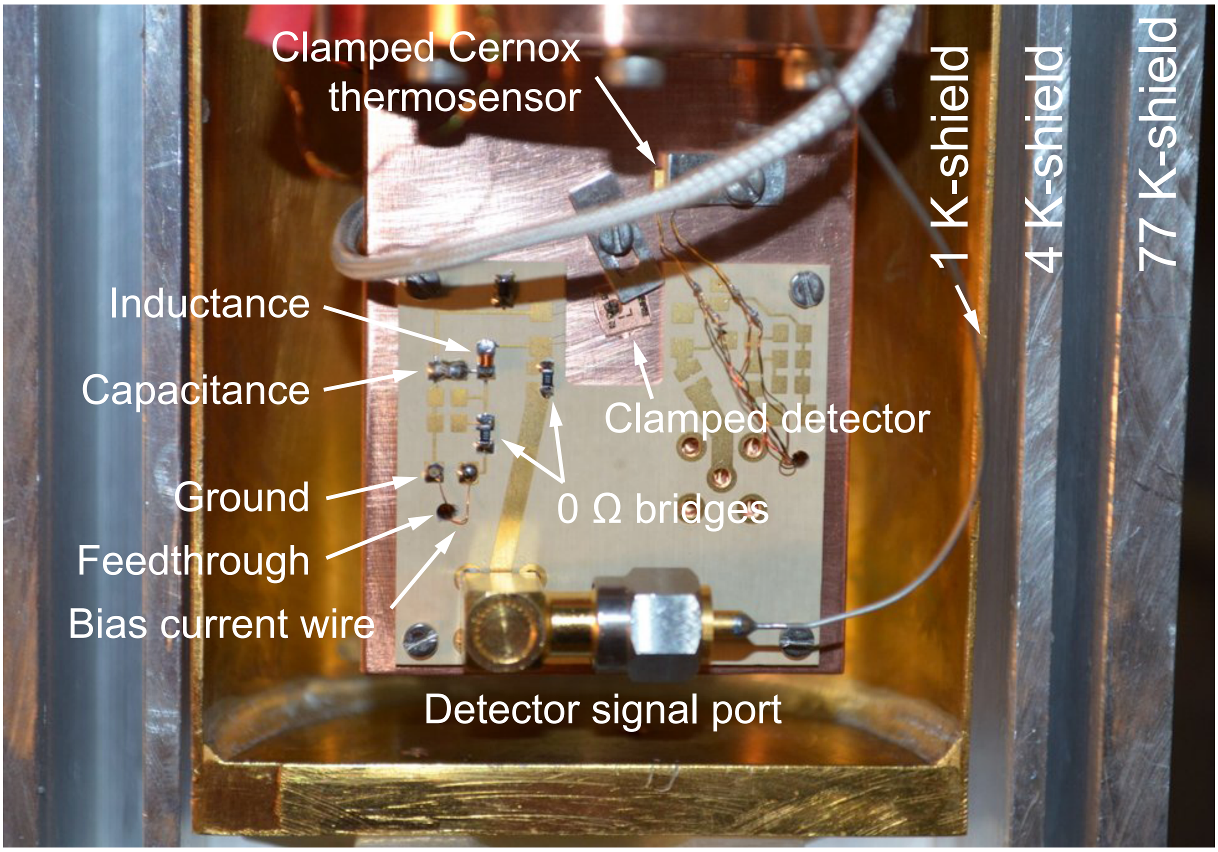

Figure 5.1: Sample holder for the photon counting experiments connected to the He-3 pot at the top. The golden sub-1-K- and the silver 4-K- and 77-K-thermal shields are shown in cross-section.

Source Meter 2410. The detector signal is transmitted by a coaxial cable to a cryogenic amplifier at the 4-K-stage, and then further over a capacitance to a second amplifier at room temperature before fed into a 3.5 GHz digital oscilloscope and/or a 250-MHz-bandwidth threshold pulsecounter. The amplifier chain had an effective bandwidth of $\approx$ 40 MHz to 1.9 GHz. A -3-dB-attenuator is added between the two amplifiers and a -6-dB-attenuator between room temperature amplifier and oscilloscope to damp possible reflections. In addition, the -6-dB-attenuator reduces the signal amplitude to the input specifications of the oscilloscope. An unterminated $\lambda/4$-cable (310 mm long) is added to the oscilloscope-input port to reduce noise of unknown origin around 240 MHz.

As a means to determine the experimental critical current $I_{c,exp}$ of the detector, a bias current I_b is applied and increased stepwise from zero, which increases the measured voltage V over the bias line (read out also by the biasing Keithley Source Meter), which is mainly given by the contact resistance on the order of $R_{cont} \approx 300\ \Omega$ for $I_b < I_{c,exp}$ and is therefore $V = R_{cont} I_b$. At $I_b = I_{c,exp}$ superconductivity is destroyed at least partially in the detector, and the resistance and hence the voltage drop V over the detector increases

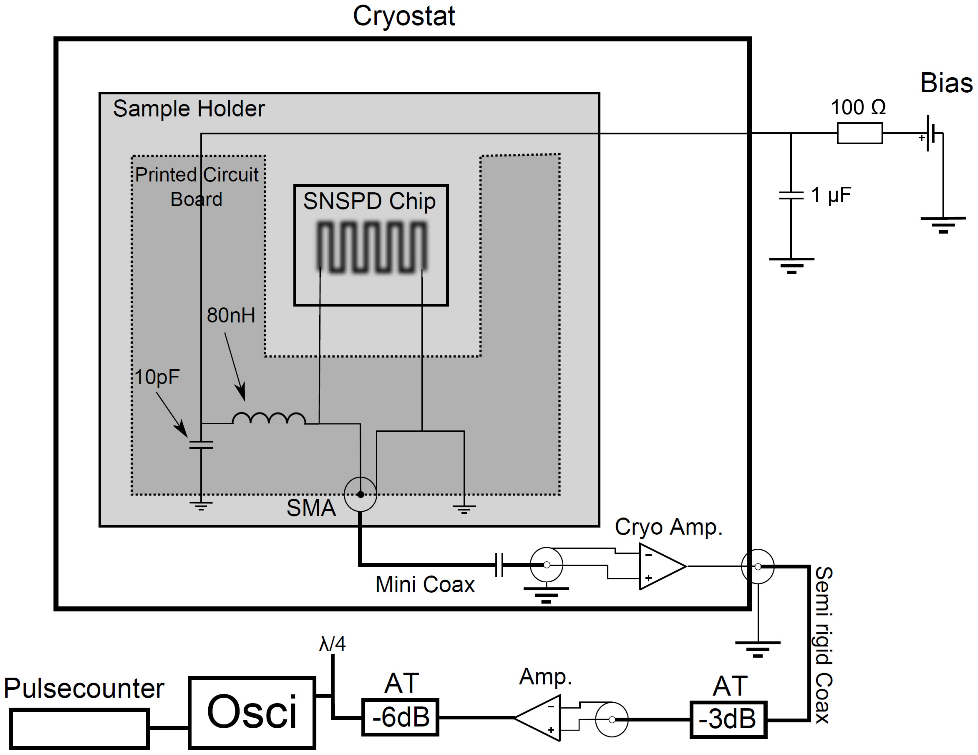

Figure 5.2: Electronics setup for biasing and read-out of an (X-)SNSPD. Two low-pass filters reduce the noise on the bias current. The detector signal is amplified by two amplifiers (at 4 K and room temperature), and attenuators ("AT") are used as a means to prevent signal reflections. The use of the pulsecounter is optional and can be combined with the oscilloscope. The oscilloscope can also be used for the determination of count rates $\Gamma < \Gamma_{max} = 3.1 \times 10^5$. This figure is adapted from Ref. [7].

substantially, which we use as the criteria to determine the experimental critical current $I_{c,exp}$ of a detector.

5.2.3 Signal pulse shape

As discussed within a simple model in subsection 2.1.9, a detected photon corresponds to a voltage pulse with a rise time on the order of $\tau_1 \approx 10$ ps and a decay time of $\tau_2 \approx 1 - 10$ ns. The (X-)SNSPDs examined in this thesis typically show a voltage signal shape qualitatively very similar to the pulse shapes recorded for the TaN and NbN thin-film SNSPD in our work by Engel *et al.* [41]. Fig. 5.3 shows typical voltage pulses recorded for the TaN X-SNSPDs presented in chapter 7. The damped oscillations following the pulse are a consequence of the fact that the detector is effectively part of an LC circuit [41]. It is therefore not possible to precisely determine the pulse decay time τ_2, which would require an exponentially decaying voltage pulse [114]. However, its order of magnitude can be determined by defining a pulse length time T_P as indicated in Fig. 5.3, i.e., as the

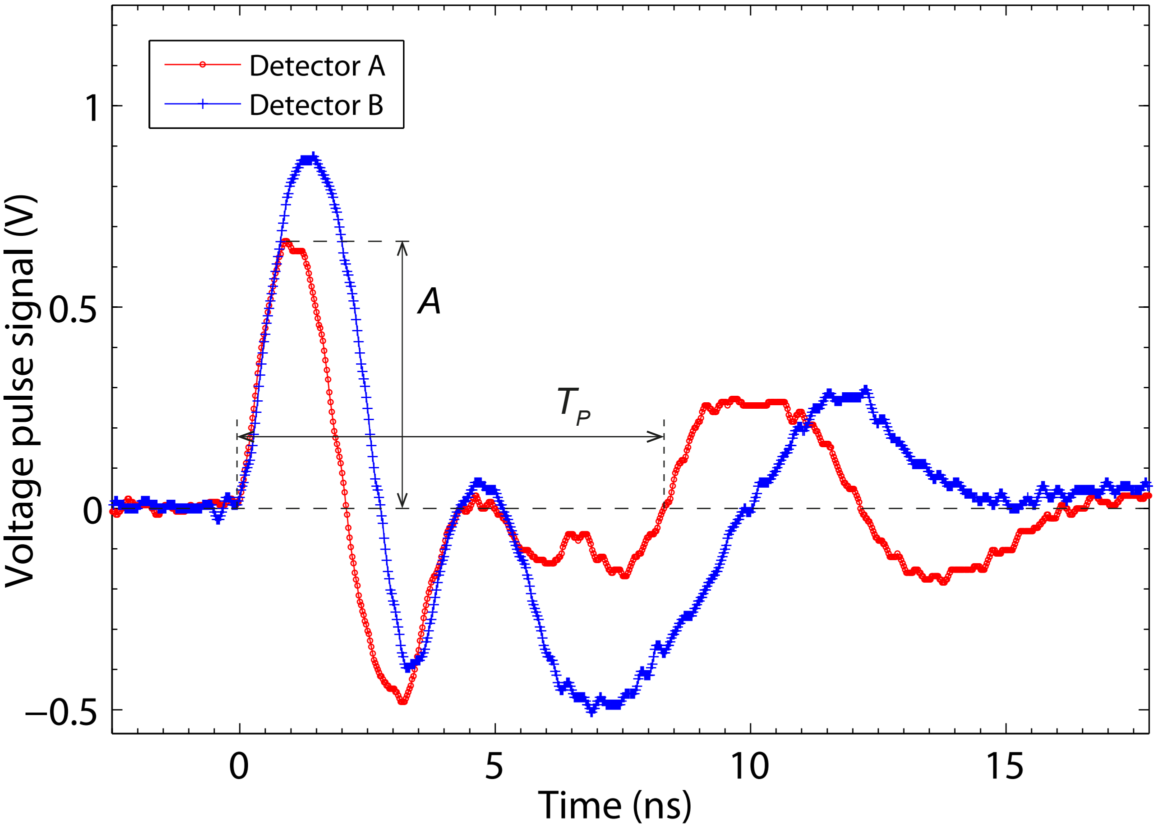

Figure 5.3: Typical voltage pulses recorded for the TaN X-SNSPDs (detector TaN-A and TaN-B) presented in chapter 7, with the definition of the pulse amplitude A and the pulse length T_P indicated.

period of the first major pulse oscillation.

The pulse amplitude A is defined as the absolute value of the first pulse maximum, and the rise time as the time span between the absolute values $10\% \, A$ and $90\% \, A$. The minimum rise time to be resolved in principle from the recorded signals is $\approx 0.35/BW \approx$ 190 ps [115], since the effective bandwidth $BW = 1.9$ GHz of our electronics setup results in a limiting minimum rise time.

5.2.4 Signal recording by the oscilloscope

A Tektronix DPO 7354 oscilloscope with a bandwidth of 3.5 GHz and a sampling rate of 40 GS/s is used to record and save triggered voltage signals and their time stamps. Therefore, the detector count rate can, in principle, be determined by the sole use of the oscilloscope. However, the manufacturer specifies a dead time of about 3 μs between consecutive signals, or a corresponding maximum count rate of up to $\Gamma_{max} = 3.1 \times 10^5$ signals per second. The X-ray photon count rates determined with the oscilloscope in our experiments with X-SNSPDs were significantly smaller than Γ_{max} (namely $\lesssim 2 \times 10^4$ s^{-1}) and they could therefore be determined correctly with the oscilloscope. This use of such an oscilloscope makes a subsequent detailed signal analysis possible, for example to distinguish between detector pulses (including possible dark counts) and unexpected noise signals with a much larger voltage amplitude, which is not possible with the threshold pulsecounter. Another advantage of the oscilloscope used is its larger bandwidth of 3.5 GHz, in contrast to the 250 MHz bandwidth of the pulsecounter, which significantly alters the shape of the input voltage signal and can even lead to a incorrect determination of the count rate if the signal threshold is chosen incorrectly. However, for the determination of photon count rates $\Gamma \gtrsim \Gamma_{max}$ as, for example, in our experiments on X-ray photon detection with thin-film SNSPDs the pulsecounter is the preferable tool.

5.2.5 X-ray photon sources

Two qualitatively different X-ray sources were used to irradiate the SNSPD and X-SNSPDs: A 50 kV tungsten target X-ray tube and a radioactive Fe-55 isotope source. The emission characteristics of these sources and the geometry of the experimental setup allowed a homogeneous irradiation of the (X-)SNSPDs with both sources. In the following, these two sources are described in more detail.

W-target 50 kV X-ray tube:

The X-ray tube spectrum consists of two parts: the continuous background radiation ("Bremsstrahlung") with its upper limit at $E_{\text{max}} = |e| \cdot V_A$ given by the acceleration voltage V_A, which can be chosen between 5 kV and 49.9 kV, and the characteristic emission lines given by the tungsten target. Fig. 5.4 shows a typical emission spectrum for the used X-ray tube [116] at $V_A \approx 30$ kV. The tungsten target leads to two main characteristic emission peaks at 8.3-8.4 keV (the Lα_1 and Lα_2 emission lines) and 9.7-10.0 keV (Lβ_1 and Lβ_2), and two an order of magnitude weaker emission peaks at 7.4 keV (Ll) and 11.3 keV (Lγ_1) [94] (see Fig. 5.4). The emission line at 1.8 keV (Mα_1) is negligible. Characteristic emission lines can only be observed if a minimum acceleration voltage of $V_A = E_b / |e|$ is applied, with E_b being the larger of the two absolute binding energies of the electronic states involved in the X-ray emitting electronic transition. For the two main emission peaks, this corresponds to minimum acceleration voltages of 10.2 kV and 11.5 kV [94], respectively, depending on the specific emission line.

The X-ray tube emitted flux can be varied linearly by the tube anode current I_A, adjustable in the range 0-2.00 mA, keeping the relative photon energy distribution constant [117] for a fixed acceleration voltage V_A. The emitted X-ray radiation follows Poissonian photon statistics [118].

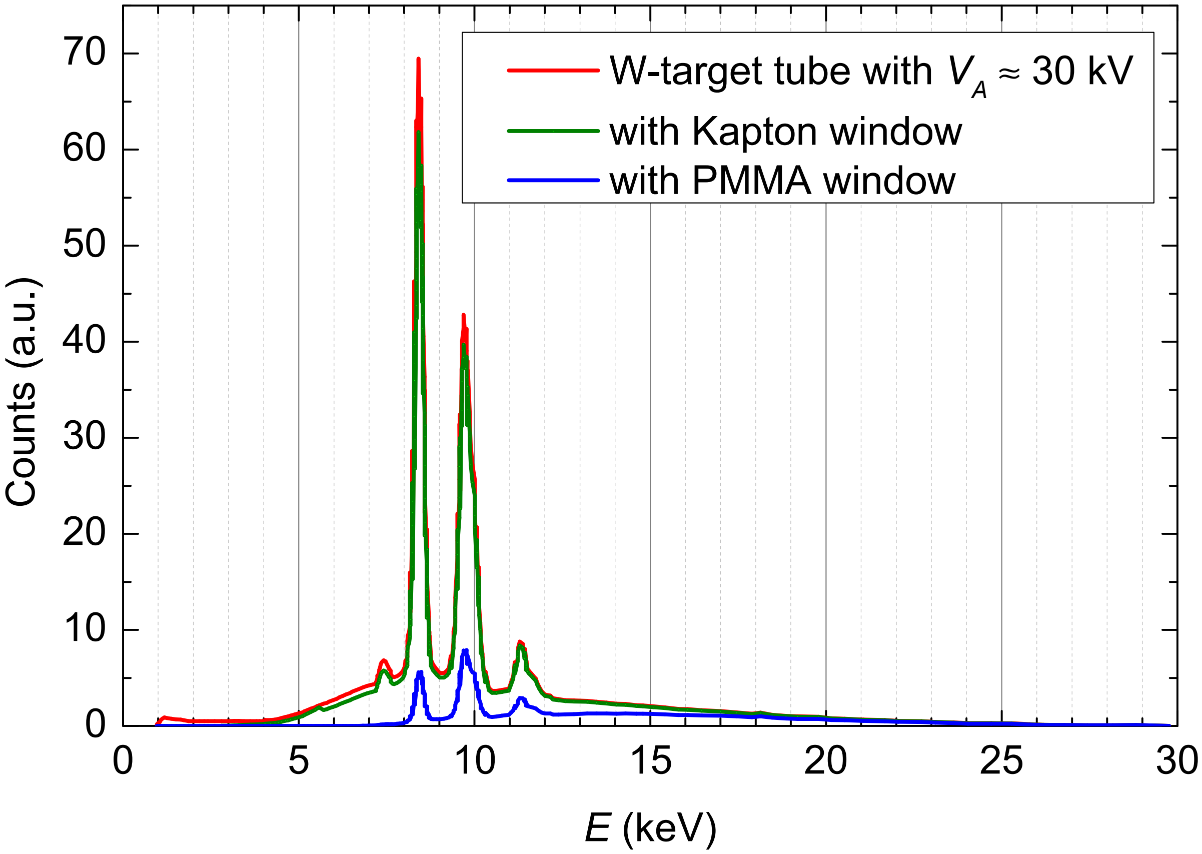

Figure 5.4: Typical emission spectrum (red curve) of the used X-ray tube for $V_A \approx 30$ kV. These measurements were performed by the X-ray tube manufacturer [116]. The other curves show the same spectrum, calculated after transmission through the materials [84] and air [85] between X-ray tube and (X-)SNSPD, in the cases of a 4 mm thick PMMA (blue curve) and 100 μm Kapton window (green curve).

The spectrum emitted by the X-ray tube is partially absorbed by the air and the cryostat windows, as discussed in more detail below. Fig. 5.4 shows the corresponding X-ray tube spectra including the absorption in the cases of a 4 mm thick PMMA (blue curve) and 100 μm Kapton window (green curve).

Fe-55 isotope source:

A radioactive Fe-55 isotope source with a nominal activity of 3.7 GBq was used in addition to the X-ray tube, as it emits photons with well defined energies around 6 keV. The manufacturer specified [119] an emission rate of 12.7×10^6 s^{-1} steradian^{-1} (reference date: 30.1.2012) and $< 0.001\%$ radioactive impurities.

Fe-55 decays via electron capture to Mn-55 with a half-life of 2.74 years [120]. In the process of electron capture, an inner atomic electron is captured by a proton in the nucleus, forming a neutron and an electron neutrino: ($\text{p} + e^- \rightarrow \text{n} + \nu_e$). As the electron shell of the resulting Mn-55 atom is excited, energy is released by Auger electron or photon emission at various energies [121]:

Emitted particle	**Particle energy**	**Relative emission probability**
Auger electron	5.19 keV	60.7%
Photon	5.888 keV	8.2%
Photon	5.889 keV	16.2%
Photon	6.49 keV	2.85%
Rest: Auger electrons & photons	various other energies	12%

The emission lines at 5.888 keV and 5.889 keV are often used in detector characterization measurements (as for example with TES [101], see subsection 2.4.2) in order to verify a very good energy resolution on the order of 1 eV. The total emission probability for a photon with an energy between $5.8 - 6.5$ keV sums up to $\approx 27\%$. Therefore the Fe-55 X-ray radiation is often specified as mono-energetic at 5.9 keV. For the experiments presented in this work, this simplification is sufficient.

5.2.6 X-ray transmission to the detector

As already mentioned above, the X-ray radiation emitted by the X-ray tube or the radioactive Fe-55 source has to be transmitted through various materials and air before it is incident on the (X-)SNSPD. The corresponding photon energy-dependent transmission probabilities between 1 keV and 50 keV were calculated and are summarized in Fig. 5.5, and are discussed in detail in the following paragraphs in the correct order. In general, the transmission probability for this energy range increases with increasing photon energy. However, characteristic absorption lines can locally decrease the transmission probability in the energy range above the absorption energy.

X-ray tube window and coating:

The X-ray tube emits the X-ray radiation through a 0.005 inch (= 0.127 mm) thin beryllium window, which transmits 95% of the photons at ≈ 6 keV, and 10% at ≈ 2 keV [85]. Beryllium is sensitive to corrosion by exposure to moisture (such as atmospheric humidity or water droplets) and other compounds [122], which can result in vacuum leaks. Thus the window is covered on the outside with a protective, highly X-ray transmitting epoxy coating, which transmits 95% of the photons at 4 keV [122].

The thermal radiation emitted from the focal spot (of the incident electrons) on the tungsten target in the X-ray tube is absorbed completely by the thin Be window [123] due to its metallic nature, and is not transmitted to the (X-)SNSPD.

Air:

The emitted photons have to be transmitted through approximatively 35 mm of air. Assuming standard ambient temperature and pressure (i.e. $T = 25$ °C and $p = 100$ kPa), about 95% of the photons are transmitted at ≈ 7 keV, and 10% at ≈ 2 keV [85]. These values only change slightly for an elevated air temperature of 60 °C (the maximum temperature to which the outer side of the X-ray tube package heats up). The transmission through air is therefore slightly worse than through the Be X-ray tube window and cannot be neglected.

Optional aluminum filter for radiation hardening:

If a block of aluminum is added as a radiation filter, the low-energy part of the X-ray photon energy spectrum is significantly suppressed by absorption in the aluminum. In medical X-ray diagnostics this effect is called "radiation hardening", as mostly soft X-ray photons are absorbed. A 1 mm thick block of aluminum absorbs $\geq 99.9\%$ of the photons with an energy $E \leq 10$ keV. However, photons with higher energies are also affected, and at ≈ 22 keV still 50% of the photons are absorbed [85].

Cryostat window:

The cryostat window which allows to transmit X-ray radiation to the (X-)SNSPD has to be vacuum-proof. The first experiments with the 6 nm thin NbN SNSPD described in chapter 6 have been performed with a rigid 3.7 mm thick cryostat window made from polymethyl methacrylate (PMMA), offering a better X-ray transmission than the standard quartz window used in optical experiments. 10% of the photons are transmitted at ≈ 9 keV and only 50% of the photons are transmitted at ≈ 13 keV through such a window [84].

For the experiments with X-SNSPDs presented in chapter 7, a 100 μm thin window of Kapton (polyimide) was used in order to optimize X-ray transmission and therefore to increase the maximum achievable X-ray photon flux in our setup. This window is, like the PMMA window, pressed against an O-ring to achieve a vacuum-proof cryostat sealing. However, it has to be screwed to the cryostat at four points to prevent it from being sucked into the cryostat due to the pressure difference of about 1 bar. 95% of the photons are transmitted through this window at ≈ 9 keV, and 10% at ≈ 3 keV [84].

Thermal shield at 4 K:

A 1 μm thin aluminum film is installed at the 4 K-heat shield as a means to minimize thermal radiation into the sample chamber. Otherwise, the sample would be partially

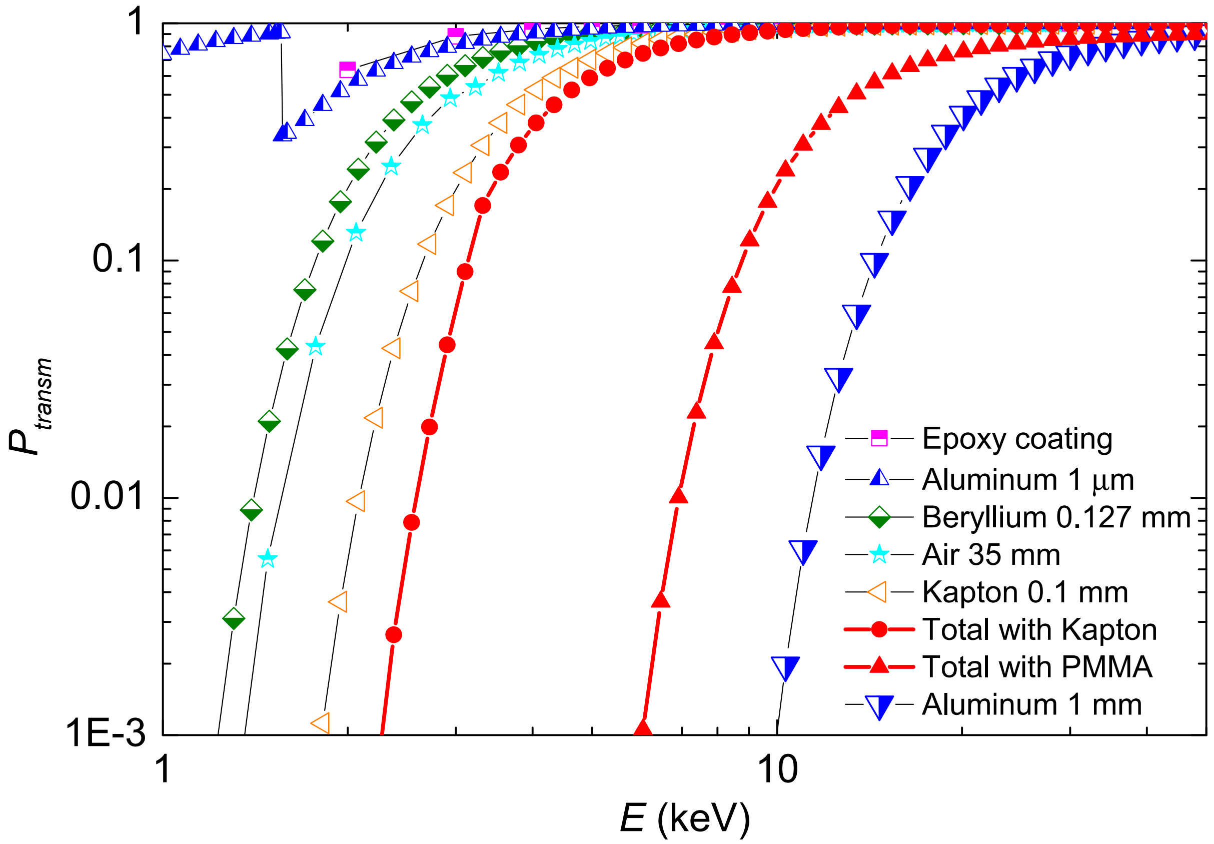

Figure 5.5: Transmission probability for a photon with energy E through different materials and air [84,85,122] situated between X-ray tube and the (X-)SNSPD. The curves in red show the total transmission probability for the Kapton (red circles) or the PMMA window (red triangles) installed including all components except the optional 1 mm thick aluminum filter block. These total transmission probabilities are mainly given by the transmission characteristics of the used cryostat window. The transmission probability through the PMMA window alone is therefore not shown, as it is practically identical to the corresponding total transmission probability.

irradiated and heated by room temperature thermal radiation from the outermost (vacuum) cryostat cover, preventing to achieve sample temperatures as low as ≈ 0.35 K. The shield transmits about 95% at ≈ 5 keV with a transmission minimum of 34% right above 1.57 keV due to resonant absorption [85].

Total transmission:

The total transmission characteristics through the windows, filter and shields described above is mainly given by the transmission properties of the PMMA or Kapton cryostat window (as shown in Fig. 5.5), or, if included, the optional thick aluminum filter. With the Kapton window, the 10% X-ray transmission threshold is reduced from 9 keV to 3 keV as compared to the PMMA window. The 6 keV photons emitted by the Fe-55 isotope source are transmitted with a probability of 70% through the Kapton window, and only with 0.1% probability through the PMMA window.

5.2.7 Radiation shielding

In order to prevent radiation leakage during the experiments and to comply with the laws for radiation protection, a radiation shielding box was constructed. The box consists of 3 mm of lead glued to 8 mm thick aluminum walls, and is designed to contain the X-ray tube or radioactive isotope source and the entire lower part of the cryostat including the sample chamber. The entire experiment can therefore be treated legally as a “closed X-ray experiment”, and the operator does not need to undertake any other radiation protection measures (as for example carrying a dosimeter) if the equipment is properly used. A safety interlock with electric switches (miniature snap-action switches) turns off the X-ray tube power instantly if the box cover is opened.

Chapter 6

A Conventional NbN Thin-Film SNSPD for X-Ray Photon Detection

6.1 Device fabrication and geometry

A conventional SNSPD from 6 nm thin NbN on a sapphire substrate was fabricated as described in detail in chapter 4. Table 7.1, Fig. 7.10 and 7.11, placed at the end of the next chapter for easier comparability, show a compilation of the most important detector properties used for the discussion of the experiments with the SNSPD in this chapter and the three X-SNSPDs in the next chapter. Fig. 6.1 displays an optical image and details of the original digital design layout of this SNSPD. The width of the meander nanowires is estimated by considering the SEM measurements in Ref. [110] on SNSPDs fabricated after the same fabrication recipe. It was reported [124] that in such an ultra-thin NbN film superconductivity is destroyed in a surface and an interface layer due to oxidation and atomic diffusion (during sputtering), respectively, thereby reducing the effective thickness of the superconducting film by $\approx$ 1 nm. The superconducting NbN part of the SNSPD examined is therefore only $d_{sup} \approx 5\ nm$ thick, despite its $d \approx 6$ nm geometrical thickness.

Fig. 7.10 (placed in the next chapter) shows temperature-dependent resistance measurements on the four (X-)SNSPDs, allowing the determination of the critical temperature T_c and the normal-state resistivity ρ_n according to subsection 5.1.1.

In Fig. 7.11 (placed also in the next chapter) measurements of the upper critical magnetic flux density B_{c_2} as a function of the temperature T are plotted for the four (X-)SNSPDs together with the corresponding linear fits. This fit for the NbN SNSPD data allows for an estimate of $B_{c_2}(0)$ and therefore the GL coherence length $\xi(0)$ of this detector according to Eq. 5.1.2.

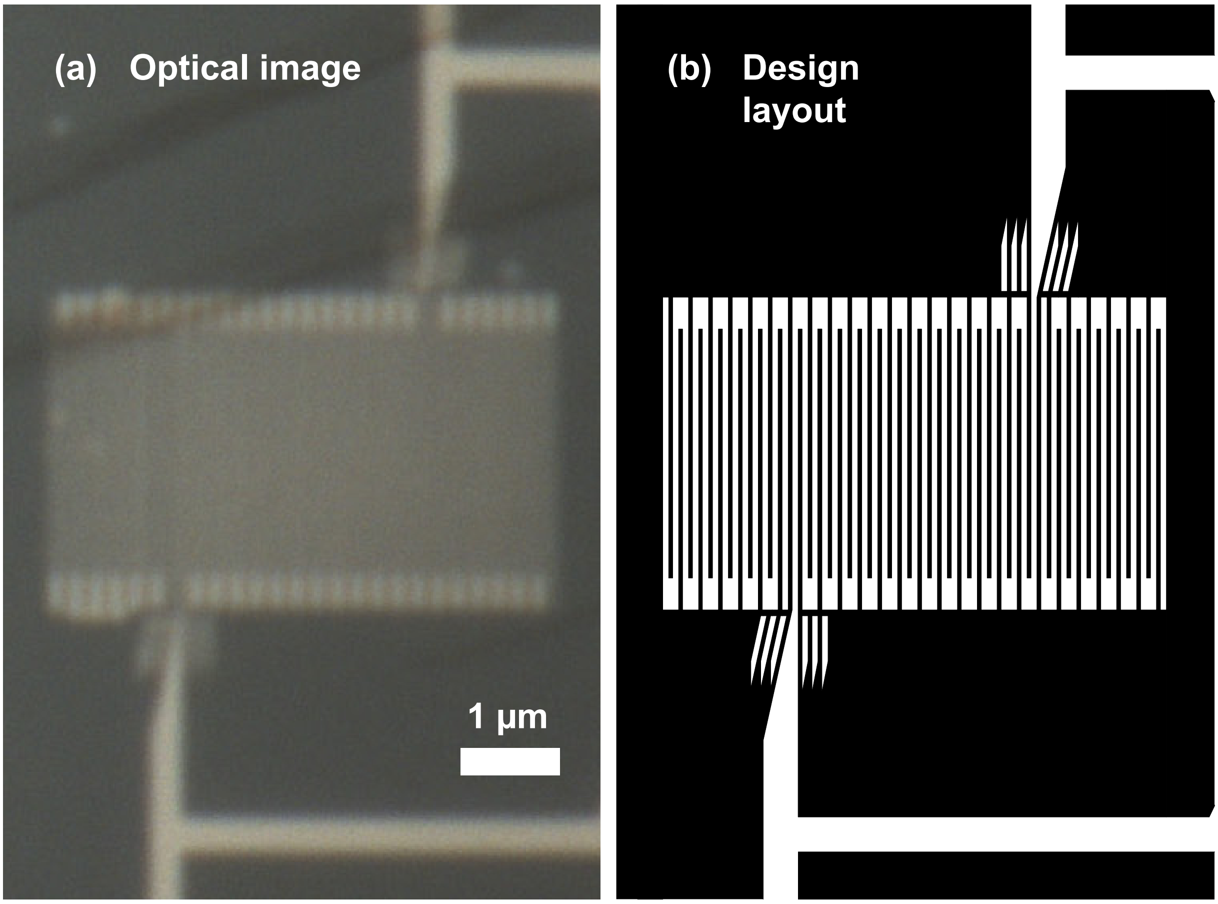

Figure 6.1: SNSPD from a 6 nm thin NbN film on sapphire: **(a)** Optical image of the detector. The nanowire width/gaps of ≈ 80 nm/120 nm are below the resolution limit of a standard optical microscope, and therefore only the large structures of the detector are discernible. The dark stripes in the upper area are residuals of the EBL resist, but they do not cover the active detector area. The original design layout is shown in subfigure **(b)**.

6.2 Kinetic inductance

In order to estimate the kinetic inductance L_{kin} of the SNSPD, the effective magnetic penetration depth λ_{eff} has to be determined. In the dirty limit, the bulk penetration depth at $T = 0$ K can be calculated from the critical temperature T_c and the normal-state resistivity ρ_n using Eq. 1.2.13 and the experimentally determined relation between T_c and the energy gap $\Delta(0)$ for NbN (Eq. 1.2.2), resulting in $\lambda_{bulk}(0) \approx 340$ nm. As $d_{sup} \ll \lambda_{bulk}$, the effective penetration depth (Eq. 1.2.15) is $\lambda_{eff} \approx 45$ μm and thus the bias current through the nanowires is homogeneously distributed in the nanowire cross-section. The resulting kinetic inductance of the SNSPD (Eq. 1.2.18) is $L_{kin} \approx 90$ nH.

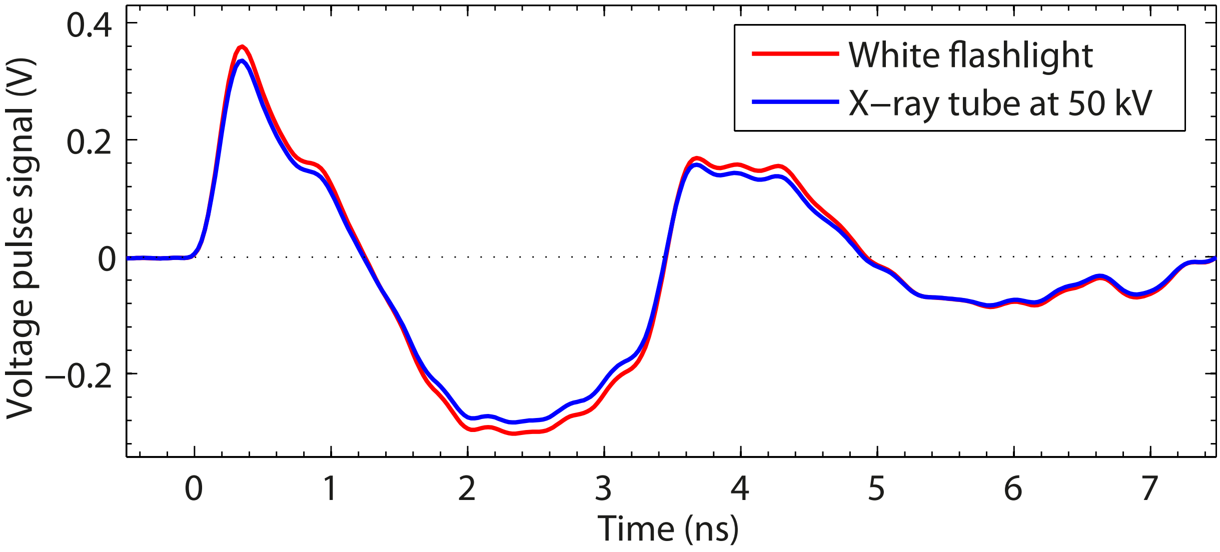

Figure 6.2: Averaged voltage pulse shapes at detection of photons from a flashlight and from the X-ray tube at $I_b/I_{c,exp} = 95\%$ and $V_A = 49.9$ kV at $T = 2.5$ K.

6.3 Experimental setup and voltage signal

The X-ray detection experiments were performed in the experimental setup described in section 5.2, using the 3.7 mm thick PMMA cryostat window (as at the time of the experiments the thin Kapton window was not yet available). The thermal shield at 4 K was not yet installed during the measurements presented in this chapter. The experimental critical current $I_{c,exp}$ of the detector was determined according to subsection 5.2.2.

The SNSPD was examined for its photon detection capability in the visible and the X-ray energy range. Fig. 6.2 shows the average voltage pulse signal upon detection of photons from both a flashlight ($E \approx 1$ eV) and from the X-ray tube at an acceleration voltage $V_A = 49.9$ kV at $I_b/I_{c,exp} = 95\%$ and $T = 2.5$ K. The averaged pulse shapes are almost identical for the two photon energy regimes.

As discussed in subsection 5.2.3, the damped oscillations following the pulse are a consequence of the fact that the detector is effectively part of an LC circuit. The voltage pulse shape is therefore very similar to the one observed in the same setup for detected optical photons with a thin-film TaN SNSPD, as compared in our work in Ref. [41] (appended to chapter 2). A lower theoretical limit for the pulse rise time of ≈ 190 ps was estimated for the electronics in subsection 5.2.3. For the pulses shown, the rise time is ≈ 210 ps $\pm$ 11 ps for both photon energy regimes and is therefore closely above the smallest resolvable value, which means that the intrinsic pulse rise time is even faster. The pulse length is also found to be ultrafast and identical for the two energy regimes, with 3.6 ns $\pm$ 0.3 ns.

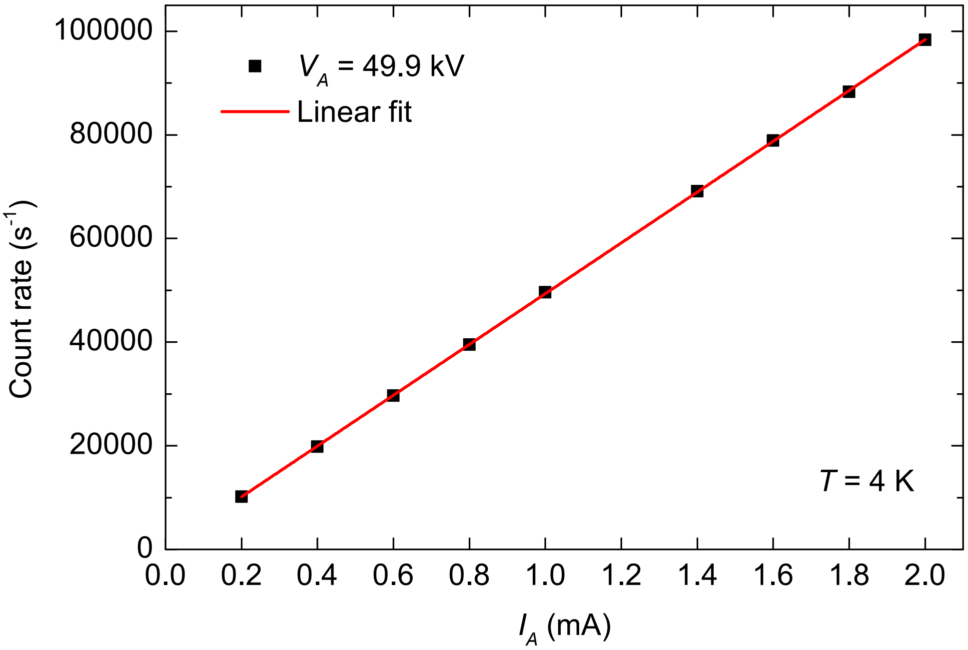

Figure 6.3: Linear behavior of the photon count rate (determined by the pulsecounter) on the X-ray tube photon flux given by the anode current I_A at $V_A = 49.9$ kV at $T = 4$ K and $I_b/I_{c,exp} = 94\%$, showing single-photon detection.

6.4 Single-photon detection mode and device detection efficiency

In Fig. 6.3, the photon count rate is plotted as a function of the X-ray tube anode current I_A at $V_A = 49.9$ kV at $T = 4$ K and $I_b/I_{c,exp} = 94\%$. As the anode current I_A is proportional to the photon flux emitted by the X-ray tube (which follows Poissonian photon statistics, see subsection 5.2.5) and the plotted dependence shows a perfect linear behavior, we can conclude that the SNSPD detects X-ray photons in a single-photon detection mode [1], similarly to the visible and near-IR single-photon and single-keV-electron detection with SNSPDs described in subsections 2.1.8 and 2.2.5, respectively.

If the SNSPD is irradiated with the X-ray tube set to $V_A = 10.0$ kV and $I_A = 2.00$ mA, a count rate of $\Gamma_{\text{Tot,SNSPD}} = 600$ counts/s is observed at $I_b/I_{c,exp} \approx 94\%$ and $T = 2.6$ K. Subtracting the measured dark count rate of $\Gamma_{\text{DC}} = 373$ counts/s results in a photon count rate of $\Gamma_{\text{Phot,SNSPD}} = \Gamma_{\text{Tot,SNSPD}} - \Gamma_{\text{DC}} = 227$ photons/s. Calibration measurements with a practically identical experimental setup (at approximately standard ambient temperature and pressure) and a commercial semiconducting Si-PIN X-ray photon counter (XPIN-BT by Moxtek) yield a photon flux of $\Gamma_{\text{Phot,Calibr}} = 21$ photons/s through the active SNSPD area at these X-ray tube settings (neglecting the finite X-ray absorptance of air), which is $\approx 10\times$ less than the observed SNSPD X-ray photon count rate. However, the photon absorption probability in a 6 nm thin NbN film is $\approx 1 \times 10^{-3}$ at 5.9 keV, $\approx 1 \times 10^{-4}$

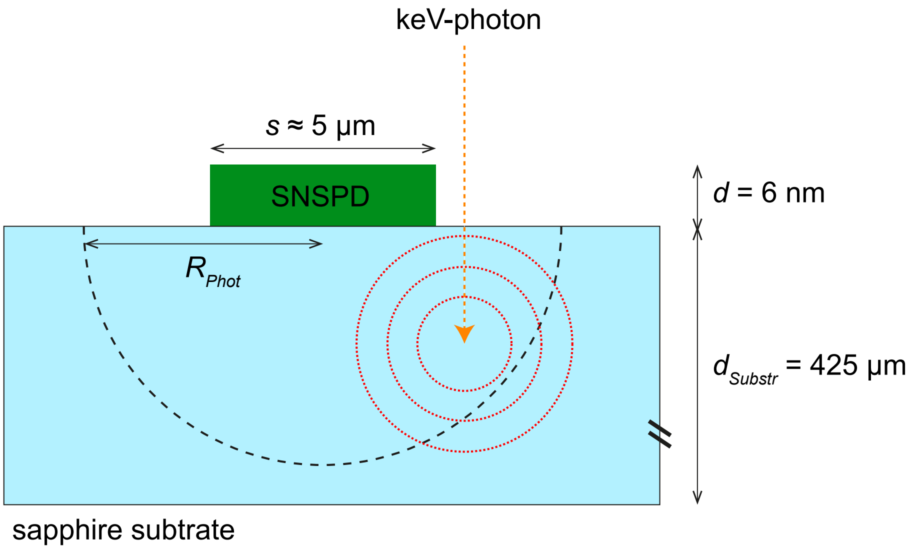

Figure 6.4: Schematics of the model described in the text for the substrate-mediated keV-photon detection in a thin-film SNSPD on top of a sapphire substrate: The photon is absorbed in the substrate. If the distance between photon absorption point and SNSPD is smaller than a certain maximum distance R_{Phot}, enough energy can diffuse into the SNSPD to lead to the detection of the photon. The schematics is not drawn to scale.

at 14 keV and $\approx 3 \times 10^{-5}$ at 50 keV (see subsection 2.3.2), and hence only a small fraction of the incident photons are absorbed in the superconducting structure. This is in qualitative agreement with the experiments by Perez de Lara *et al.* [75] (discussed in subsection 2.3.4), showing that more photons are detected in the SNSPD than are absorbed in the superconducting meander structure. It was argued that photons absorbed in the substrate underneath the detector area are responsible for almost all detection events.

As the SNSPD was shown to detect X-ray photons in single-photon mode, it is reasonable to attribute the surplus of photon counts to photons absorbed in the $d_{Substr} = 425\ \mu$m thick sapphire substrate. The details of the energy diffusion processes involved in this substrate-mediated detection process are unknown. However, a simple model, schematically illustrated in Fig. 6.4, can be used to estimate a lower limit R_{Phot} for the maximum distance between photon absorption point and SNSPD in order for the photon to deposit an energy of the order of ≈ 1 eV in the SNSPD and therefore to be detectable by the SNSPD: We assume that all photons absorbed in the substrate within a semi-sphere of radius R_{Phot} (with its center at the center of the SNSPD) are detected. Eq. 2.3.6 gives the absorption probability for photons with energy E in a film of thickness d using the penetration depth $\lambda(E)$, and thus integrating over the circular area of radius R_{Phot} yields the photon count rate of the SNSPD

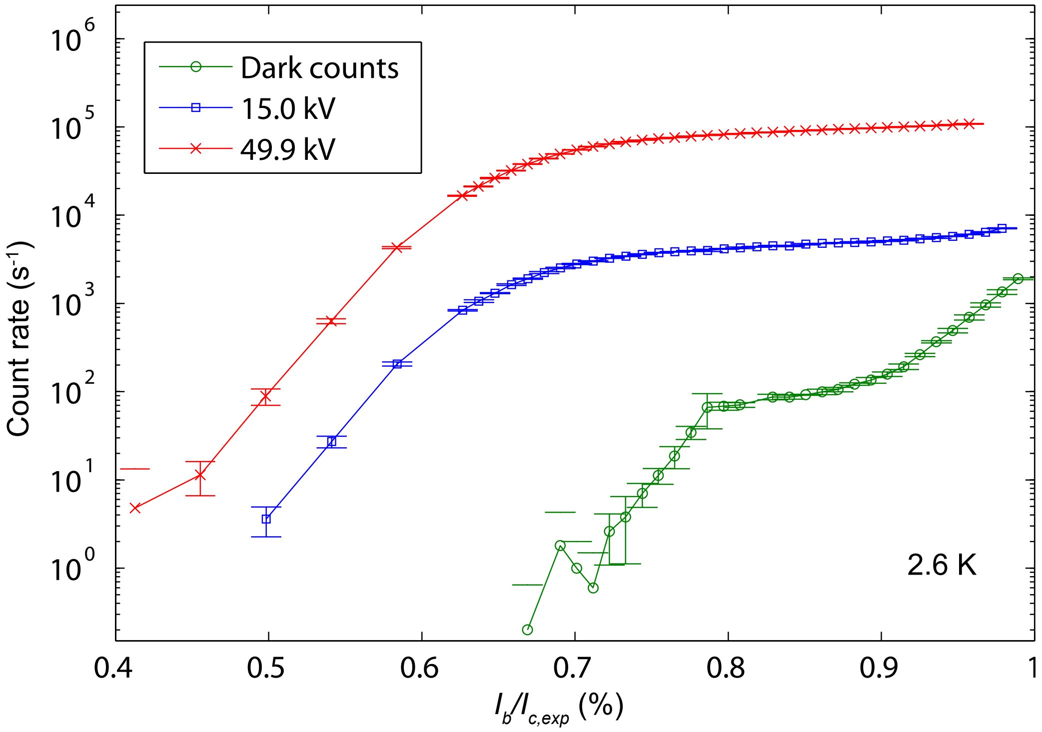

Figure 6.5: SNSPD count rates as functions of the reduced bias current for incident X-ray photons emitted by the X-ray tube at $V_A = 15.0$ kV (blue rectangles) and 49.9 kV (red crosses), both at $I_A = 2.00$ mA, together with the dark count rate (green circles), all at $T = 2.6$ K. These count rates were measured with the threshold pulsecounter.

$$\Gamma_{\text{Phot,SNSPD}} = \frac{\Gamma_{\text{Phot,Calibr}}}{s^2} \int_0^{2\pi} \int_0^{R_{Phot}} \left(1 - e^{-\frac{\sqrt{R_{Phot}^2 - r^2}}{\lambda(E)}} \right) r \, \mathrm{d}r \, \mathrm{d}\varphi. \tag{6.4.1}$$

From this equation, a radius of $R_{Phot} \gtrsim 17\ \mu$m can be determined for an assumed average photon energy $E = 5.9$ keV with $\lambda(5.9 \text{ keV}) = 33.6\ \mu$m for sapphire [85] and the values for $\Gamma_{\text{Phot,Calibr}}$ and $\Gamma_{\text{Phot,SNSPD}}$ found above. Hence, the resulting R_{Phot} is significantly larger than the SNSPD extension $s = 5\ \mu$m.

6.5 Bias current dependence

The SNSPD can be operated in continuous detection mode even at reduced bias currents up to $I_b/I_{c,exp} = 96\%$. The count rate was measured (using the pulsecounter, as described in subsection 5.2.4) as a function of the reduced bias current $I_b/I_{c,exp}$ under irradiation with X-ray photons at $V_A = 15.0$ kV and 49.9 kV (at $I_A = 2.00$ mA) at $T = 2.6$ K, and is presented in Fig. 6.5. Additionally, the bias current dependence of the dark count rate is also shown, which was measured with a powered off X-ray tube, but built-in cryostat window.

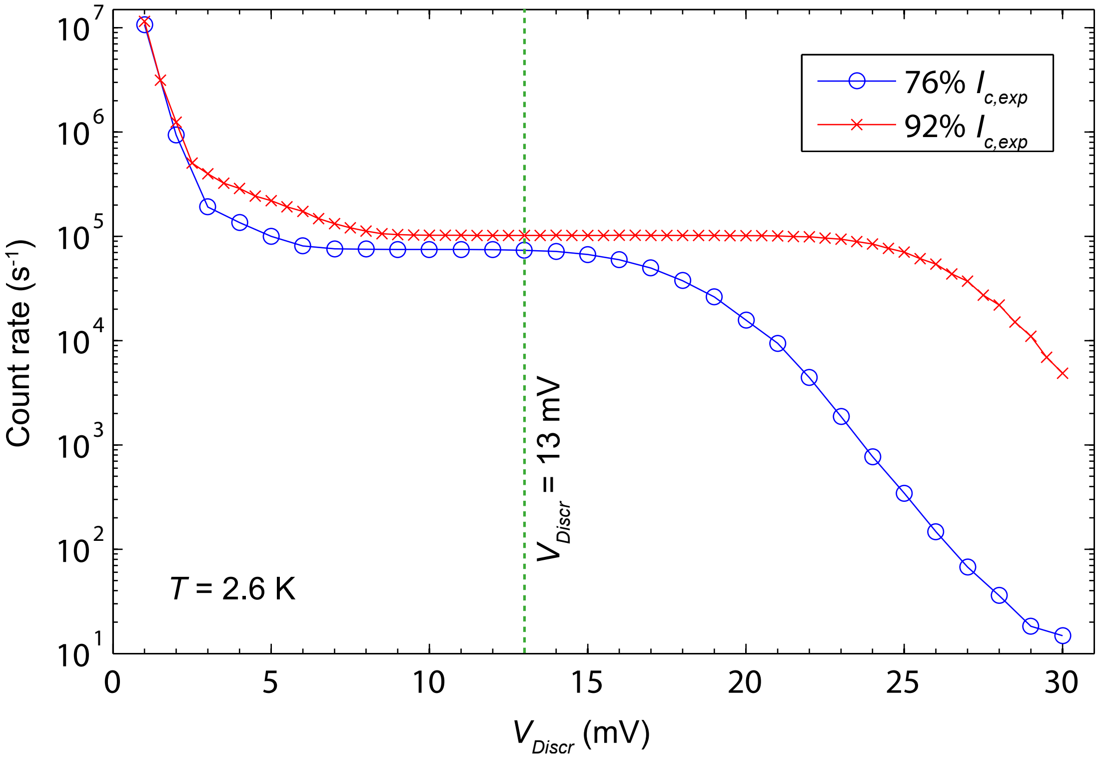

Figure 6.6: Dependence of the photon count rate on the pulsecounter discriminator voltage V_{discr} at $V_A = 49.9$ kV (at $I_A = 2.00$ mA) and 2.6 K for the two reduced bias currents $I_b/I_{c,exp}$ indicated in the legend. The vertical dashed green line at $V_{Discr} = 13$ mV indicates the setting used for the measurements presented in Fig. 6.5.

A plateau in the X-ray photon count rates forms for $I_b/I_{c,exp} \gtrsim 70\%$, and the count rates significantly decrease for lower bias currents. This SNSPD was also studied regarding optical photon detection in our work in Ref. [41] (appended to chapter 2), where also a plateau in the bias current-dependent count rate at $\lambda = 300$ nm above a threshold bias current of $I_{th} \approx 70\%$ is found.

Fig. 6.6 shows the count rate at $V_A = 49.9$ kV (at $I_A = 2.00$ mA) and 2.6 K (as above) in dependence of the pulsecounter threshold voltage V_{Discr} at the two reduced bias currents $I_b/I_{c,exp} = 76\%$ (blue circles) and 92% (red crosses). The increase in the count rate for low values of V_{Discr} originates from electronic noise, which increases in its amplitude with increasing bias current I_b. For larger values of V_{Discr} this pulsecounter threshold voltage becomes larger than most of the pulse amplitudes and therefore the count rate decreases. As the average pulse amplitude increases with the bias current I_b, this upper limit for V_{Discr} also increases with I_b. For every bias current I_b there is thus an interval with ideal values for V_{Discr}, with both its boundaries increasing with I_b. It is hence never possible to choose V_{Discr} ideal for all possible bias currents $I_b < I_{c,exp}$. The pulsecounter threshold voltage $V_{Discr} = 13$ mV used for the bias current-dependent count rate measurements discussed

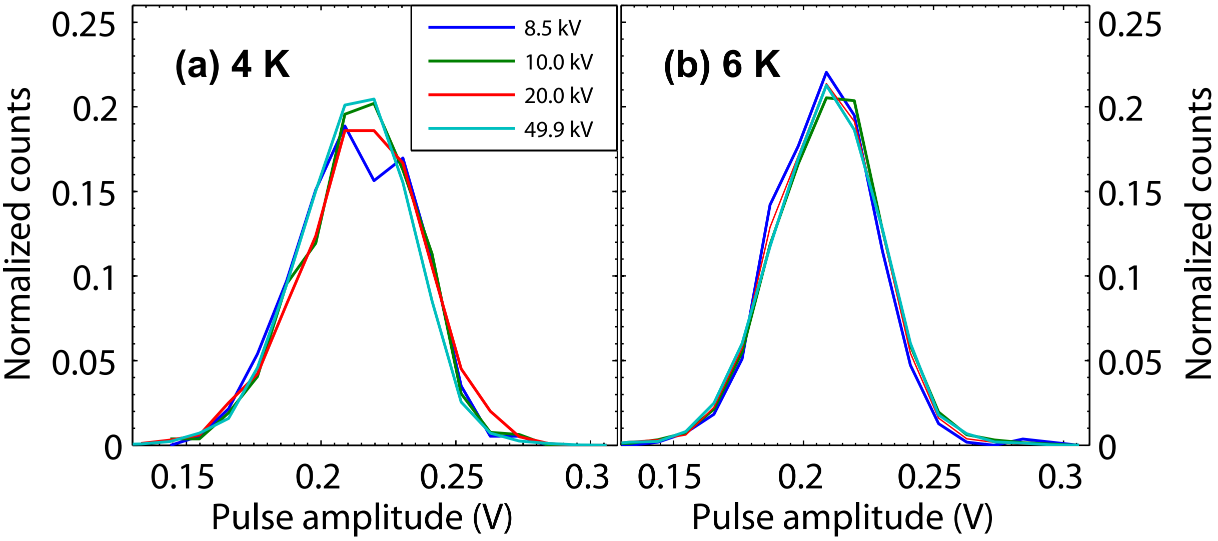

Figure 6.7: Pulse amplitude distribution at **(a)** $T = 4$ K and **(b)** 6 K for different photon energy spectra (the legends and axes are identical for both subfigures) at $I_b = 20.4$ μA, normalized to the area underneath the curves. The bins have a width of 10.8 mV.

above (from Fig. 6.5) is indicated with a vertical dashed green line. Keeping V_{Discr} fixed, it is clear that for $I_b/I_{c,exp} < 70\%$ the count rate decreases below the value observed at $I_b/I_{c,exp} = 76\%$, as the average pulse amplitude becomes smaller than V_{Discr}. Thus, in the case of our X-ray photon detection measurements with this SNSPD, the decrease in the count rate for $I_b/I_{c,exp} < 70\%$ in Fig. 6.5 can be attributed to the decreasing pulse amplitude at a constant pulsecounter signal threshold V_{Discr}, and not due to a threshold bias current I_{th} (as introduced in subsection 2.1.3) in this range.

The dark counts in Fig. 6.5 are a combination of counts originating from the thermal radiation promoted by the not yet installed thermal shield at the 4 K stage and intrinsic fluctuations (discussed in subsection 2.1.5). One might speculate, that the plateau visible for $80\% \lesssim I_b/I_{c,exp} \lesssim 90\%$ originates from thermal radiation, since, as expected, the observed bias current threshold $I_{th} \approx 80\%$ is larger than for the photons with $\lambda = 300$ nm discussed above. For $I_b/I_{c,exp} \gtrsim 90\%$, the steep increase in the count rate would then correspond to intrinsic fluctuations. The finite dark count rate also explains the increase in the count rate measurements at $V_A = 15.0$ kV for $I_b/I_{c,exp} > 92\%$ shown in Fig. 6.5.

6.6 Pulse amplitudes

Fig. 6.7 shows the pulse amplitude distribution for different X-ray tube settings V_A for a fixed bias current $I_b = 20.4$ μA at 4 K (corresponding to $I_b/I_{c,exp} = 66\%$) and 6 K (corresponding to $I_b/I_{c,exp} = 85\%$). No dependence on V_A and therefore the relative photon energy spectrum is found at both temperatures within the measurement accuracy.

This finding is expected, as the domain resistances in SNSPDs are usually significantly larger than the $Z_0 = 50\ \Omega$-impedance of the signal read-out line (as described in subsection 2.1.1), and thus the pulse amplitude is fixed by the constant value of Z_0.

Chapter 7

X-SNSPDs from a Thick Niobium and Tantalum Nitride Film

7.1 Device fabrication and geometry

X-SNSPDs have been fabricated according to the recipes described in detail in chapter 4, namely one detector from a Nb film and two detectors (called “TaN-A” and “TaN-B”) from a TaN film, both films with a thickness of $\approx$ 100 nm deposited on a sapphire substrate. The as-grown TaN film showed a normal state resistivity that is two orders of magnitude larger than that of the Nb film (see also subsection 4.1). Table 7.1 at the end of this chapter shows a compilation of the most important detector properties used for the discussion of the conventional NbN thin-film SNSPD presented in chapter 6 and the three X-SNSPDs in this chapter. Our publications related to these X-SNSPDs are also appended at the end of this chapter.

For the Nb X-SNSPD, an optical and an SEM image of meander details are shown in Fig. 7.1(a) and 7.2, respectively. Optical images of the X-SNSPDs TaN-A and TaN-B are presented in Fig. 7.3, and corresponding SEM images are shown in Fig. 7.4 and 7.5. The superconducting leads to the meander structures all have a length negligible compared to the total meander length l, and are much wider than the nanowires of the meander structure with width w. The film thicknesses d of the X-SNSPDs were measured by an atomic force microscope, and the nanowire widths w determined from the SEM images. Detector TaN-B has $\approx 5-7$ times wider nanowires than TaN-A, which results in a larger achievable filling factor. TaN-A has a slightly smaller nanowire width w than the Nb X-SNSPD.

For SEM imaging, all meanders were grounded in order to reduce the negative effect of electric charging of the non-conductive sapphire substrate on the image quality and resolution. However, electric charging cannot be prevented completely by this measure,

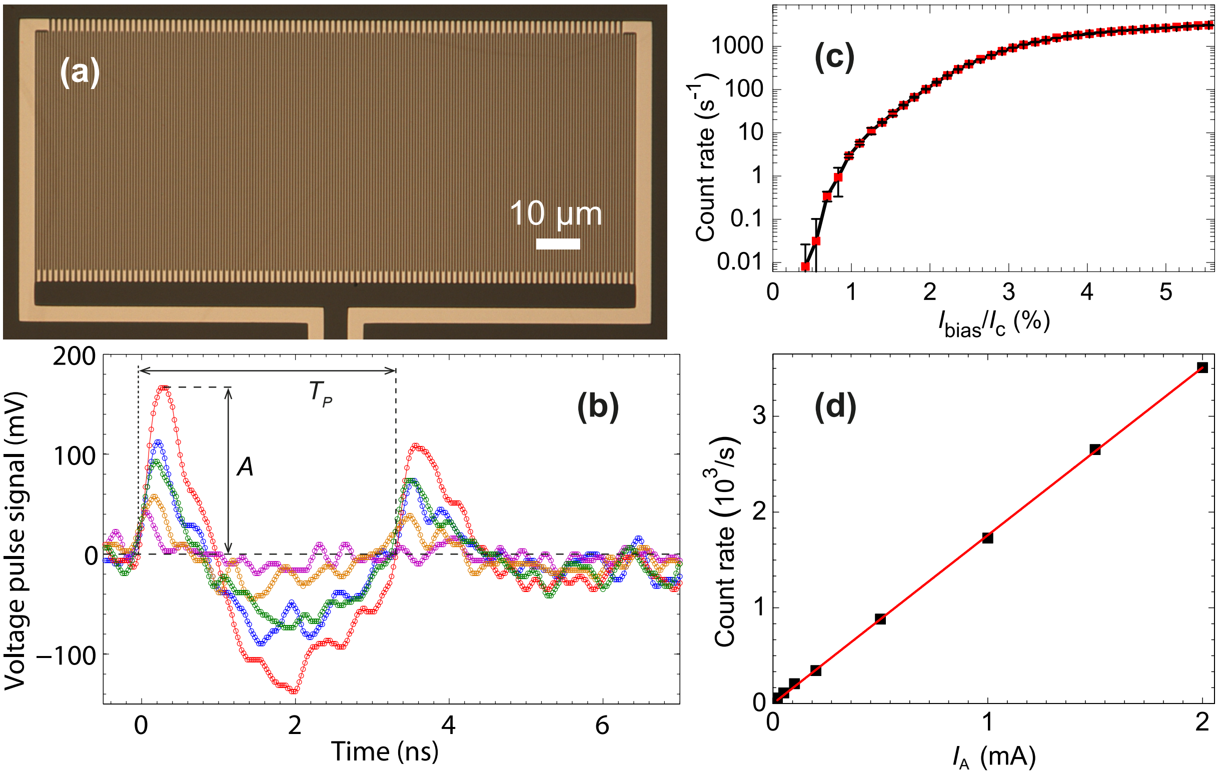

Figure 7.1: **(a)** Optical image of the examined X-SNSPD from 100 nm thick Nb. For **(b)**-**(d)** the X-SNSPD was irradiated by the X-ray tube at $V_A = 49.9$ kV and $I_A = 2.00$ mA. **(b)** Typical voltage pulses after photon absorption, with the definition of the pulse length T_P and the pulse amplitude A shown schematically. The different colors of the pulses are only a guide to the eye. **(c)** Photon count rate as a function of $I_b/I_{c,exp}$. **(d)** Photon count rate as a function of I_A, to be discussed in detail and shown again in section 7.4. Subfigure **(d)** is only shown here because it is part of the originally published figure in our work by Inderbitzin *et al.* [86]. The photon count rates in **(c)** and **(d)** were measured by the oscilloscope.

what limits the accuracy in determining the nanowire width w and leads to artifacts, as, for example, the white regions at the top and the right of the SEM image of detector TaN-A in Fig. 7.4. Probably electric charging is promoted for this TaN detector due to the orders of magnitude higher material resistivity and the smaller nanowire width w compared to the Nb X-SNSPD. For the TaN-B detector, electric charging did not occur to the same extent (see Fig. 7.5), probably due to the larger nanowire width w, leading to a smaller meander resistance. On the left and the right hand side of the light gray active meander structure, inactive nanowires were fabricated as described in subsection 4.4. The fact, that they are subject to electric charging effects in the SEM proves that they are not connected via the active meander to ground and are therefore not contributing to the active detector area.

Fig. 7.10 shows temperature-dependent resistance measurements for the four detectors

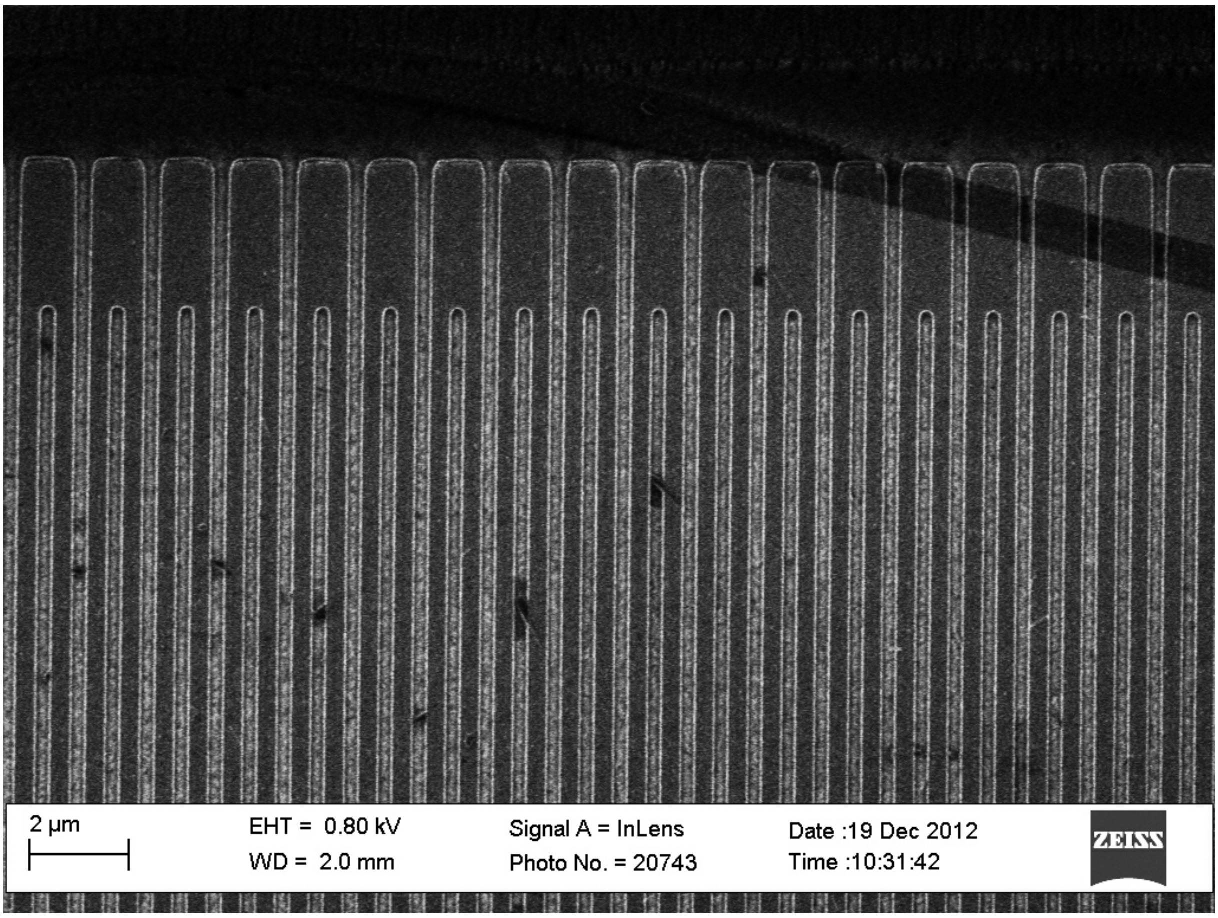

Figure 7.2: SEM image showing details of the Nb X-SNSPD meander structure. The contrast and brightness was further improved after SEM imaging by a graphics editing software. A nanowire width and gap of $w \approx 360 - 410$ nm and $g \approx 240 - 290$ nm can be deduced, respectively, giving a filling factor of about 55-65%. The dark stripe on the top right corner is non-conductive residual resist.

examined in this thesis, allowing the determination of the critical temperature T_c and the normal-state resistivity ρ_n according to subsection 5.1.1. In Fig 7.11 measurements of the upper critical magnetic flux density B_{c_2} as a function of the temperature T are plotted for the four detectors, as well as the corresponding linear fits. These fits allow for an estimate of $B_{c_2}(0)$ and therefore the GL coherence length $\xi(0)$ of the NbN SNSPD and the TaN X-SNSPD according to Eq. 5.1.2. The results for $\xi(0)$ are of the same order of magnitude as reported for thin-film NbN [38] and TaN SNSPDs [41]. For the Nb X-SNSPD, Eq. 5.1.2 obviously underestimates $B_{c_2}(0)$, as it is smaller than the measured value $B_{c_2}(T = 2\text{ K})$. Thus, the correct value for $B_{c_2}(0)$ is between $B_{c_2}(2\text{ K})$ and the linearly extrapolated value at $T = 0$ K, i.e. $1.7\text{ T} < B_{c_2}(0) \leq 2.3\text{ T}$. Therefore, a GL coherence length of $11.9\text{ nm} < \xi(0) < 13.9\text{ nm}$ is found for the Nb X-SNSPD, which is of the same order of magnitude as literature values [38].

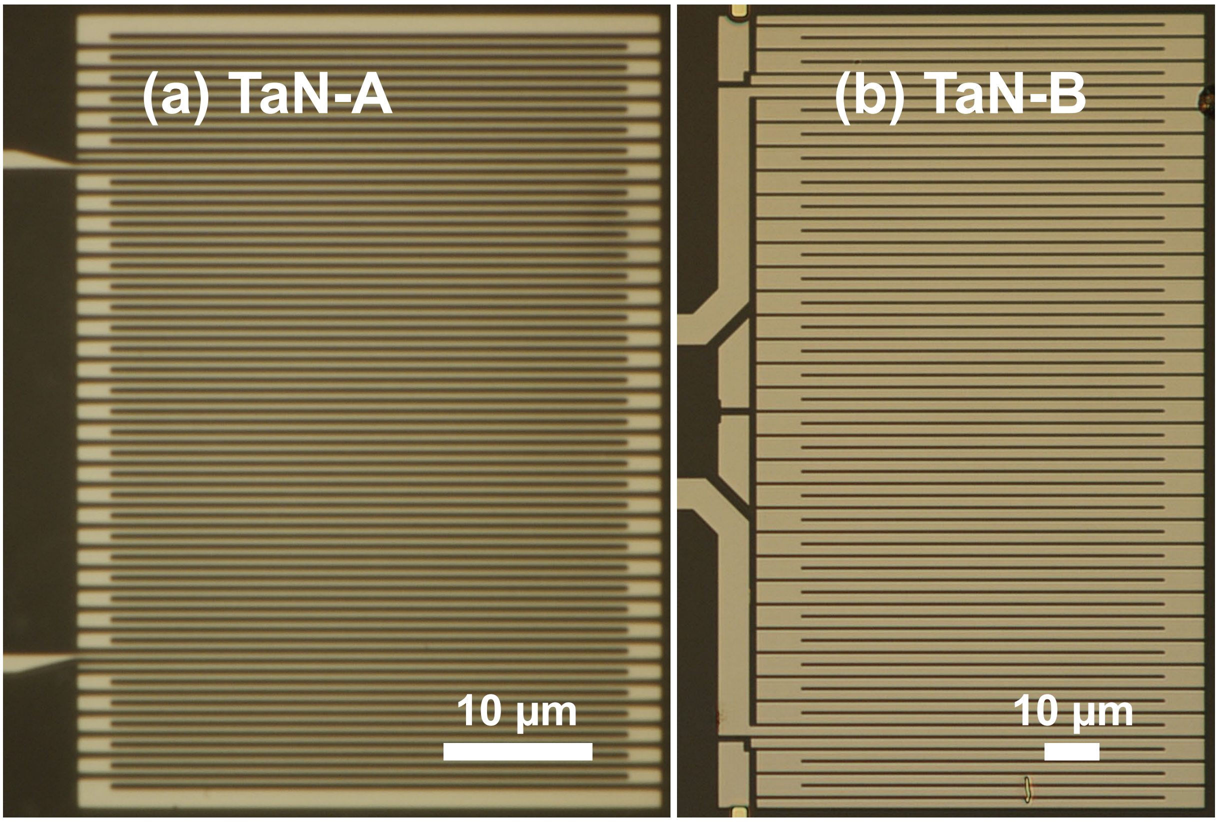

Figure 7.3: Optical images of the examined X-SNSPDs from 100 nm thick TaN: detector **(a)** TaN-A and **(b)** TaN-B. See Table 7.1 for the relevant geometric properties. The large effective penetration depth λ_{eff} ensures a homogeneous current distribution in these nanowires. This figure is taken from our work by Inderbitzin *et al.* [87].

7.2 Kinetic inductance

The used detector geometries ensure that the detectors have kinetic inductances that are small enough to allow for ultrafast recovery times [114], and are large enough to reduce problems with latching as previously reported [4, 80, 82, 88], therefore allowing their operation in continuous mode as discussed in subsections 2.1.9 and 2.3.5.

In order to estimate the kinetic inductance L_{kin} of the X-SNSPDs, the effective magnetic penetration depth λ_{eff} has to be determined for the different superconducting materials. For the Nb film, a literature value [125] of ≈ 100 nm at $T = 0$ K was used, and we assumed $\lambda(1.75\text{ K}) \approx \lambda(0)$ as the reduced temperature $t = T/T_c \approx 0.2$ of the experiment is sufficiently small. λ_{eff} is smaller than the nanowire width w, and the bias current is therefore not expected to be homogeneously distributed over the nanowire cross-section. In this case of a niobium film with a thickness $d = 100$ nm $\approx \lambda$, the kinetic inductance can be approximated by Eq. 1.2.19, resulting in $L_{kin} = \mu_0 \lambda l / w \approx 6$ nH. This kinetic inductance is smaller than the values reported [35] for functional detectors from thinner,

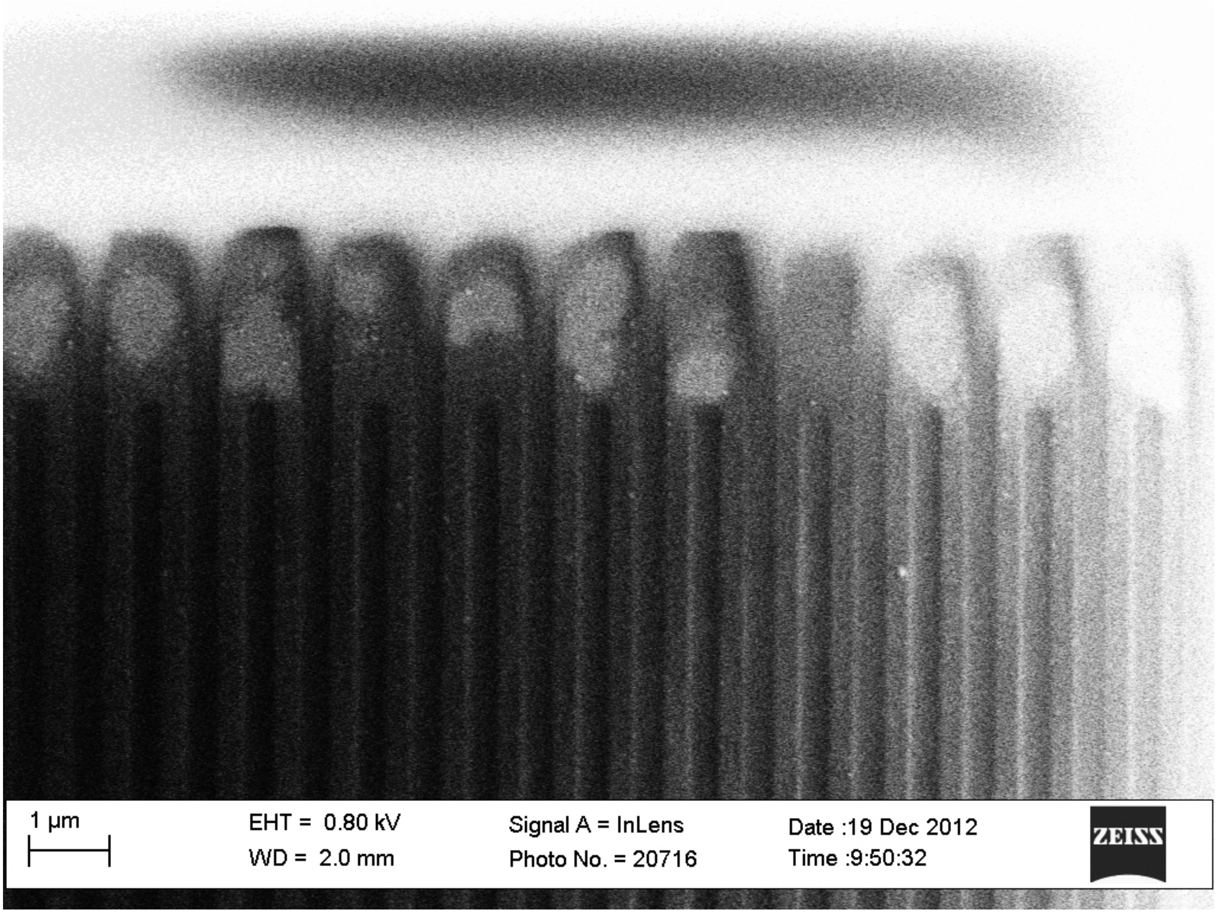

Figure 7.4: SEM image of details of the meander structure of detector TaN-A. A nanowire width and gap of $w \approx 275 - 340$ nm and $g \approx 360 - 425$ nm can be determined, respectively, giving a filling factor of about 40-50%. The white regions at the top and the right of the image are artifacts due to electric charging of the sapphire substrate (see text).

40 nm thick Nb films. Therefore, the tendency for latching of our X-SNSPD is expected to be stronger. It will be shown, however, that the X-SNSPD can still be operated in continuous mode.

For TaN, the bulk penetration depth can be calculated in the dirty limit, and therefore from the critical temperature T_c and the normal-state resistivity ρ_n by using Eq. 1.2.13 and 1.2.1. At $T = 1.85$ K a value of $\lambda_{bulk} \approx 1.0 - 1.2$ μm is found, and $\lambda_{bulk} \approx 1.2 - 1.5$ μm at $T = 5$ K if its temperature dependence is considered (see Eq. 1.2.14). As $d \ll \lambda_{bulk}$, the effective penetration depth can be determined to $\lambda_{eff} \approx 19 - 26$ μm (see Eq. 1.2.15) at $T = 1.85$ K, which ensures a homogeneous current distribution in TaN-A and TaN-B which is essential for maximizing DDE. The kinetic inductances can be calculated from Eq. 1.2.18 to $L_{kin} \approx 180$ nH and 50 nH for detector TaN-A and TaN-B, respectively.

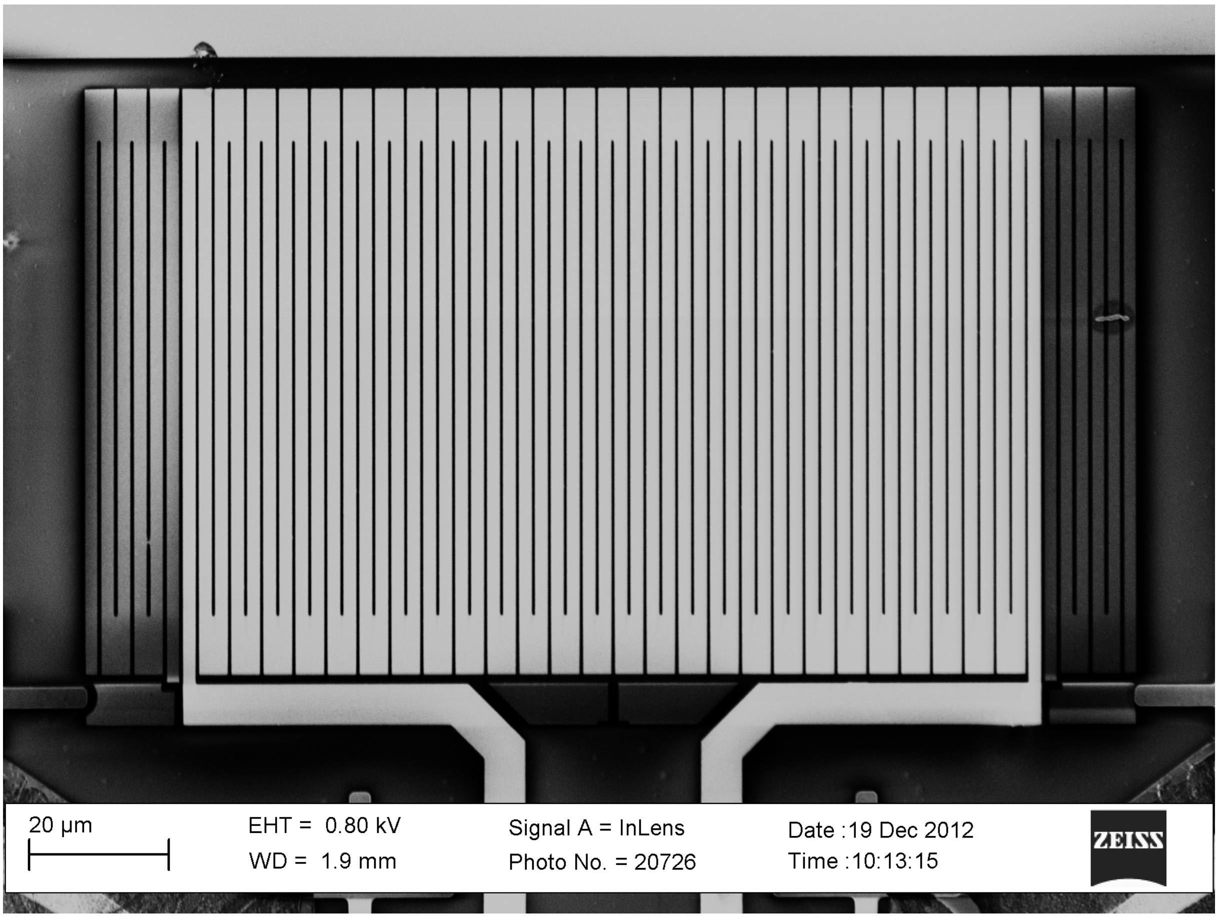

Figure 7.5: SEM image of the X-SNSPD TaN-B. A nanowire width and gap of $w \approx 1.8 - 1.9$ μm and $g \approx 0.3 - 0.4$ μm can be determined, respectively, giving a filling factor of about 80-85%.

7.3 Experimental setup and voltage signal

The characterization experiments were performed in the same experimental setup as used for the X-ray photon detection experiments with the thin-film NbN SNSPD presented in chapter 6 and as described in section 5.2, with the 100 μm thin cryostat window from Kapton installed, however. Only one detector was characterized at a time. For the measurements on the Nb X-SNSPD, the temperature was stabilized to 1.75 K ± 0.05 K. For the TaN X-SNSPDs, the measurement temperatures (varying from T = 0.37 K to 5.00 K) were stabilized within ±0.02 K. The experimental critical currents $I_{c,exp}$ of the detectors were determined according to subsection 5.2.2.

Examples of voltage pulses after X-ray photon absorption recorded by the oscilloscope are shown for the Nb X-SNSPD in Fig. 7.1(b) (at $I_b \approx 5.5\% \, I_{c,exp}$) and for the TaN X-SNSPDs in Fig. 5.3 (at $I_b/I_{c,exp} \approx 51\%$ and 28% for TaN-A and TaN-B, resprectively) at $T = 1.85$ K. As already found for the X-ray detection experiments with the thin-film

NbN SNSPD (see section 6.3), the characteristic voltage pulse shape is a consequence of the (X-)SNSPDs effectively being part of an LC circuit. Ultrafast pulse lengths T_P were observed for all X-SNSPDs under irradiation of the X-SNSPD with the X-ray tube at $V_A = 49.9$ kV. For the Nb X-SNSPD, a rise time T_R comparable to the value for our X-ray single-photon detection measurements with the thin-film NbN SNSPD was found, thus also being limited by the electronics (as describes in subsection 5.2.3). These rise times are shorter than the shortest reported value [77] for TOF-MS with superconducting nanowire detectors (T_R = 380 ps ± 50 ps). We can estimate the total inductance L_{tot} of their TOF-MS detector by calculating $L_{kin} \approx 16$ nH and adding a magnetic inductance of the same order of magnitude [35], which is not negligible for the parallel nanowire geometry of their detector. Therefore, L_{tot} is larger than the kinetic inductance $L_{kin} \approx 6$ nH of our Nb X-SNSPD examined, which explains the shorter pulse rise times, following subsection 2.1.9.

For the TaN X-SNSPDs, significantly longer rise times T_R were observed compared to the Nb X-SNSPD, which we explain with the larger kinetic inductances L_{kin} of the TaN detectors.

7.4 Single-photon detection

The count rate dependence on the X-ray photon flux, which was varied by the X-ray tube anode current I_A at $V_A = 49.9$ kV by keeping the relative photon energy distribution constant (see subsection 5.2.5), is plotted in Fig. 7.6(a) and (b) for the X-SNSPDs TaN-A (at $I_b/I_{c,exp} \approx 51\%$ at 1.85 K) and TaN-B (at $I_b/I_{c,exp} \approx 28\%$ at 1.85 K), and in subfigure (c) for the Nb X-SNSPD (at $I_b/I_{c,exp} \approx 5.5\%$ at 1.75 K). For detector TaN-B, measurements at $T = 4.0$ K at $V_A = 30.0$ kV (at $I_b/I_{c,exp} \approx 42\%$) are also shown. These dependences show a linear behavior as already found for the thin-film NbN SNSPD (see subsection 6.4), and we therefore conclude that our X-SNSPDs also detect in single-photon mode.

7.5 Latching

Above a reduced bias current $I_b/I_{c,exp} \approx 5.5\%$, the Nb X-SNSPD cannot be continuously used for X-ray photon detection due to latching, as discussed in subsections 2.1.9 and 2.3.5. This latching effect is promoted by the lower kinetic inductance L_{kin} of the X-SNSPD and the orders of magnitude smaller resistance of the normal conducting domains as compared to the situation in thin-film SNSPDs from NbN as in chapter 6, originating from the smaller normal state resistance ρ_n and the larger cross-section $A = wd$ of the niobium nanowires. For the same reasons, latching was observed at optical photon detection only

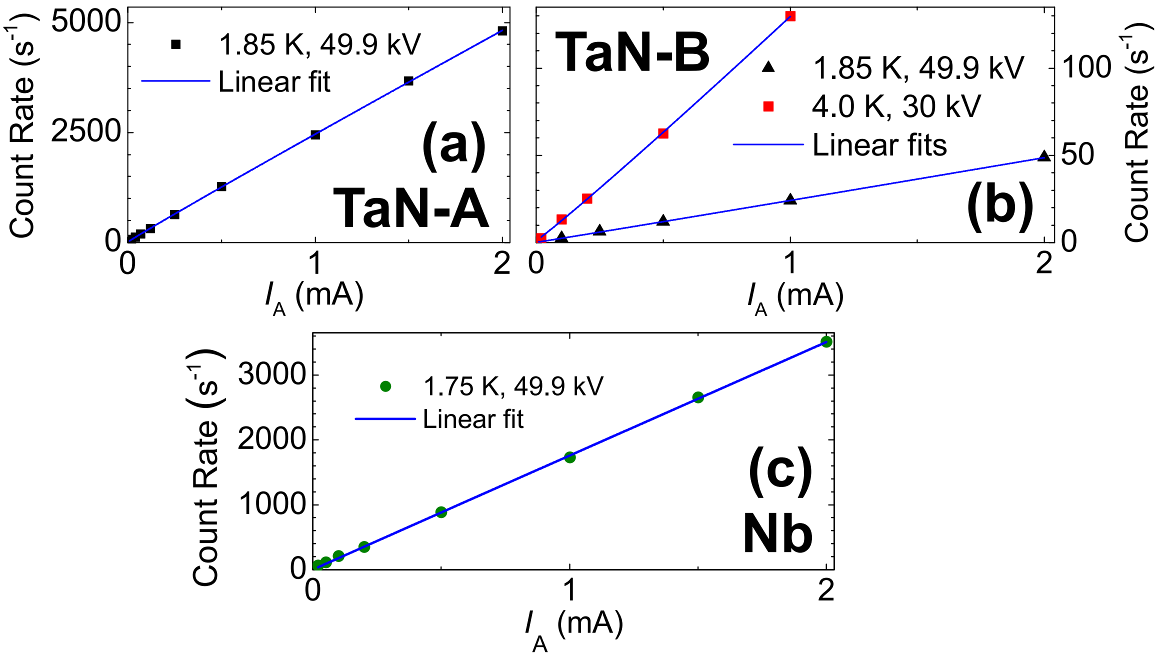

Figure 7.6: Photon count rates (determined by oscilloscope) as functions of I_A for the detectors **(a)** TaN-A, **(b)** TaN-B and **(c)** the Nb X-SNSPD, showing a linear dependence and therefore demonstrating single-photon detection. This figure is taken from our work by Inderbitzin *et al.* [87].

for bias current as large as $I_b/I_{c,exp} \gtrsim 60\%$ in a thin-film ($d \approx 7.5$ nm) Nb SNSPD [62] with narrow nanowires ($w = 100$ nm) and a large kinetic inductance ($L_{kin} = 235$ nH).

TaN-A and TaN-B latch for reduced bias currents $I_b/I_{c,exp} > 52\%$ and $> 32\%$, respectively. Latching occurs for much larger reduced bias currents in these detectors than found for the Nb X-SNSPD, due to the reasons discussed above. For the same reasons, detector TaN-B latches for lower reduced bias currents than detector TaN-A, as its wider nanowires lead to smaller domain resistances and its kinetic inductance is also lower.

7.6 Thermodynamical estimate for the hot-spot radius

The radius of the hot-spot emerging after photon absorption in the Nb and TaN X-SNSPDs can be estimated by the hot-spot model used by Gabutti *et al.* [4] for the detection of X-ray photons in superconducting strips from thick niobium films and is described in detail in subsection 2.3.1. The following results are slightly different from the ones published in the papers appended to this chapter, since slightly different formulas were used for the estimates. However, the qualitative implications remain practically identical. For the absorption of a 6 keV photon, a 8.4 keV photon (stemming from the strong characteristic emission peak, see Fig. 5.4) and a 50 keV photon in Nb, the hot-spot radius can be estimated to be $r_0 \approx 140$ nm, 160 nm and 290 nm at $T = 1.75$ K, respectively. In TaN, the hot-spot radius at $T = 1.85$ K for a 6 keV, a 8.4 keV and a 50 keV photon can be estimated to 260-270 nm, 300 nm and 540-550 nm, respectively. In this model, the hot-spot radius increases only slightly when the temperature is increased to $T = 5$ K, namely to 300-320 nm, 340-360 nm and 610-650 nm for 6 keV, 8.4 keV and 50 keV photons, respectively. For the discussion of bias current-dependent count rates in the next section, the reduction of the critical current at elevated temperatures is much more significant, however.

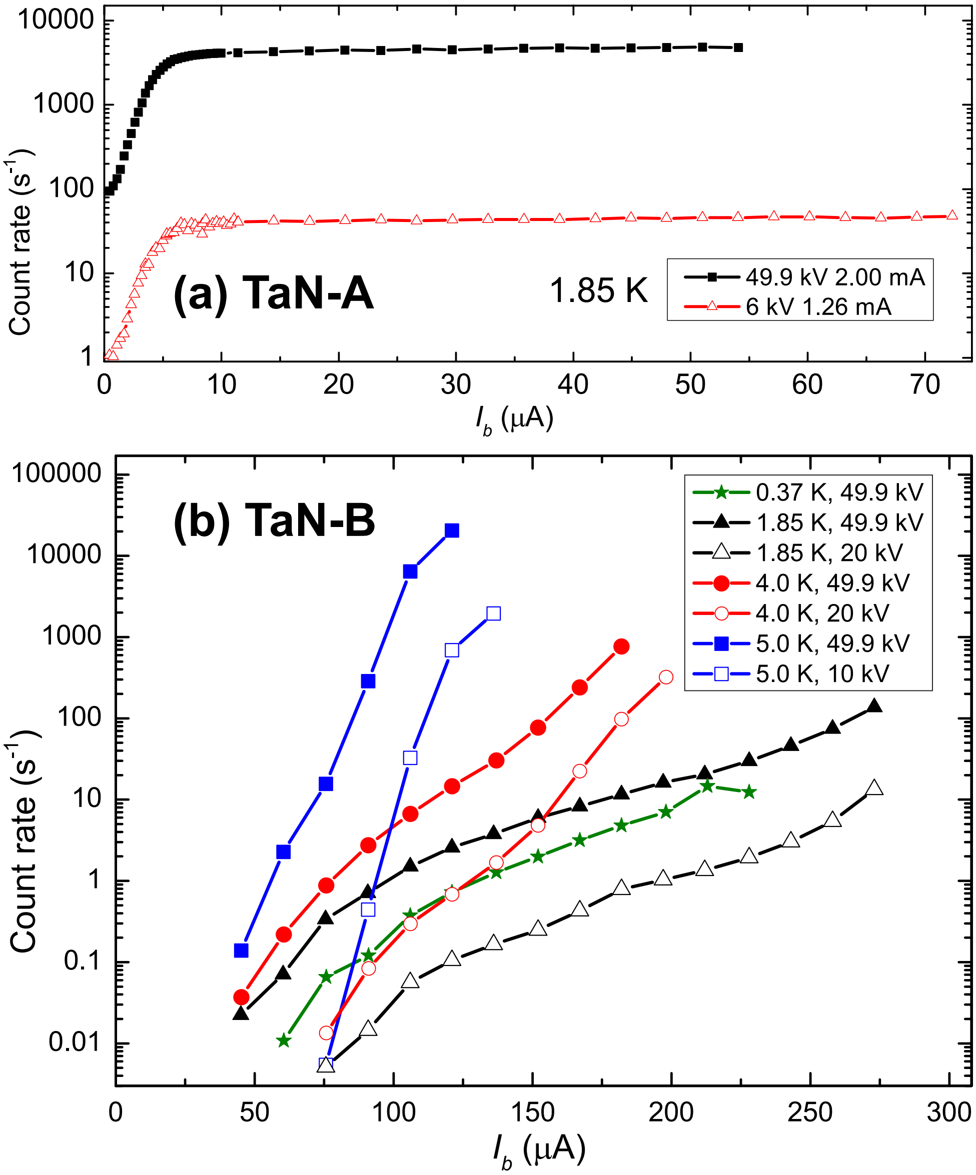

Figure 7.7: Bias current dependence of the photon count rate (determined by oscilloscope) for different X-ray tube acceleration voltages V_A for the detectors **(a)** TaN-A and **(b)** TaN-B. For detector TaN-B, we show measurements at different temperatures. This figure is adapted from our work by Inderbitzin *et al.* [87].

7.7 Bias current dependencies in the hot-spot model

The bias current dependence of the count rates for the Nb and the TaN X-SNSPDs are presented in Fig. 7.1(c) and 7.7, respectively. For the Nb and TaN-A X-SNSPD, a plateau was observed for bias currents down to $\approx 4\% \, I_{c,exp}$ (at 1.75 K) and $\approx 7\% \, I_{c,exp}$ (at 1.85 K) at $V_A = 49.9$ kV, respectively. This stands in sharp contrast to the behavior of SNSPDs for optical photon detection, even in the case of SNSPDs with especially low cut-off energy [6, 41], where the threshold bias current I_{th} is usually $\geq 40\% \, I_{c,exp}$ [6]. This finding can be explained with the fact that the hot-spot diameters for a 8.4 keV photon calculated above ($2r_0 = 320$ nm and 610 nm for the Nb and TaN-A X-SNSPD, respectively) are comparable or larger than the nanowire width for both detectors ($w_{\mathrm{Nb}} \approx 360 - 410$ nm and $w_{\mathrm{TaN-A}} \approx 275 - 340$ nm), and therefore such a hot-spot is expected to cover almost the whole cross-section on average. Eq. 2.3.5 then results in an almost vanishing reduced bias current threshold. The decrease of the count rate for low bias currents I_b for the Nb and TaN-A X-SNSPD could in principle also be partially attributed to a decreasing pulse amplitude with a decreasing bias current I_b at a constant oscilloscope trigger level.

For detector TaN-B there is no plateau in the count rate dependence on I_b (shown in Fig. 7.7(b) for different temperatures and acceleration voltages V_A). This is in agreement with the expectations from the hot-spot model: as the hot-spot diameter is smaller than the nanowire width ($w \approx 1.8 - 1.9$ μm) even for 50 keV photons ($2r_0 \approx 1.1$ μm), a bias current above a non-zero threshold [4] must be applied in order to detect photons efficiently. It has been demonstrated that this bias threshold can depend on the energy of detected β-particles [5] and keV-ions [74] and also on the operation temperature [5]. At $T = 1.85$ K, however, we expect from Eq. 2.3.5 that the energy-dependent bias thresholds are larger than 360 μA for photons with an energy of less than 50 keV (assuming a rectangular hot-spot cross-section [4]), which is already in the latching regime $I \geq I_{latch}(T = 1.85 \text{ K}) \approx 270$ μA. This explains why the count rates at $T = 1.85$ K remain low ($< 2 \times 10^2$ counts/s) even for high X-ray intensities (detector TaN-A shows $> 4 \times 10^3$ counts/s at the same X-ray tube settings).

The X-ray tube emits photons with a continuous background in the spectrum. Because the bias threshold depends on the photon energy, the count rate increases continuously with the bias current. As the high-energy part of the spectrum is reduced for low V_A, the count rate builds up more slowly with I_b for low V_A, and can therefore not simply be scaled with a constant factor (shown with filled and empty symbols in Fig. 7.7(b)).

The measurements at higher temperatures (4-5 K) show that the count rate increases more steeply with I_b, and count rates up to $\approx 2 \times 10^4$ counts/s are observed at $T = 5$ K. The increase of the count rate with temperature can be attributed to the temperature dependence of the bias threshold, which is smaller at higher temperatures. Using the hot-spot model, a threshold current $I_{th} = 170\ \mu$A can be calculated from Eq. 2.3.5 for 50 keV photons at $T = 4$ K. This estimate for $I_{th}(T = 4\text{ K})$ is right below the latching limit ($I_{latch}(4\text{ K}) \approx 180\ \mu$A) and might explain the elevated count rates at this temperature. At $T = 5$ K, the corresponding thresholds are $I_{th}(5\text{ K}) = 100\ \mu$A and $50\ \mu$A for 6 keV and 50 keV photons, respectively, which is within the measurable bias region ($I_b \leq I_{latch}(5\text{ K}) \approx 120\ \mu$A) and which therefore accounts for the steep increase of the count rate with increasing I_b.

Note that detector TaN-B covers a significantly larger area than detector TaN-A. Using the maximum count rate of TaN-A achieved at $V_A = 49.9$ kV and $I_A = 2.00$ mA, a maximum count rate of $\approx 6 \times 10^4$ counts/s can be estimated for a theoretical non-latching X-SNSPD of the size of detector TaN-B with the otherwise same properties as TaN-A, which is of the same order of magnitude as the count rate achieved by TaN-B at $T = 5$ K.

The thermodynamic hot-spot model used here to explain the temperature dependence of the count rates of detector TaN-B is equivalent to the hot-spot approach applied in subsection 2.1.4 to show that a temperature-dependent energy gap $\Delta(T)$ alone cannot reproduce the trend in the thin-film TaN SNSPD data for the temperature-dependent cut-off wavelength $\lambda_{co}(T)$ in the visible wavelength regime. It is interesting, that the here observed trend in the temperature dependence of the cut-off energy $E_{co}(T)$ of the TaN X-SNSPD is the opposite of the mentioned trend for optical photon detection, where the cut-off energy decreases for lower temperature due to a decreasing quasiparticle diffusion coefficient $D(T)$ (see subsection 2.1.4 for details). The temperature trend for the TaN X-SNSPD even extents down to at least $T = 0.37$ K, as shown in Fig. 7.7(b). This different temperature dependence can be explained by the orders of magnitude higher energy of the X-ray photons ($\approx 4 - 50$ keV) compared to the optical photons (≈ 1 eV), leading to the formation of a normal-conducting hot-spot immediately after photon absorption in the case of keV-photons, making the quasiparticle diffusion and thus its temperature dependence $D(T)$ less important for the formation of a detectable normal domain.

7.8 Dark count rate measurements

Investigations on possible dark counts can be performed with the X-SNSPDs biased at currents I_b close to the experimental critical currents $I_{c,exp}$, as long as no photon detection or dark count event and therefore latching occurs. Measurements were performed during 5 hours with the Nb X-SNSPD at $I_b/I_{c,exp} = 99\%$ (at $T = 1.75$ K) and during 30 min with the detectors TaN-A and TaN-B at $I_b/I_{c,exp} \approx 92\%$ and $\approx 98\%$ (at $T = 1.85$ K), respectively, without recording any dark counts. The dark count rate is therefore limited to $\leq 5.4 \times 10^{-5}$ counts/s and $< 5 \times 10^{-4}$ counts/s for the Nb and TaN X-SNSPDs, respectively.

The fact that the dark count rate is much lower in our X-SNSPD as compared to typical thin-film SNSPDs [126] is not surprising considering the geometric differences. It can be assumed, that thermally activated fluctuations are responsible for dark counts in SNSPDs [126]. The energy associated with thermal phase-slips due to fluctuations in the superconducting order parameter scales at least with the cross-section of the superconductor $A = wd$ [20], and the thermal nucleation of vortex-antivortex pairs is topologically suppressed for a film thickness $d \gg \xi$ [20]. Also, the typical energy required for a single vortex to thermally overcome the edge barrier, after Bulaevskii *et al.* [20] the only significantly contributing dark count mechanism in SNSPDs (see subsection 2.1.5), is proportional to the film thickness [20]. Thus the probability for any of these three considered dark count mechanisms is reduced to exceedingly small values in X-SNSPDs.

7.9 Pulse amplitudes

The sample photon detection pulses of the Nb X-SNSPD in Fig. 7.1(b) show that the amplitudes of different pulses vary significantly, much more than in the case of thin-film SNSPDs [60]. In Fig. 7.8 we plotted histograms of the pulse amplitudes at $I_b \approx 0.61$ mA for photons from the X-ray tube at different V_A and from the radioactive Fe-55 source, shown only for amplitudes right above the noise level (amplitudes below the noise level could not be recorded). We attribute the origin of this amplitude variation to the small resistance of the normal conducting domains in the Nb X-SNSPD, which we estimate to be of the order of 1 Ω, using the estimated values for the hot-spot radius from above as half the domain length. Since this value is smaller than the 50 Ω impedance of the coaxial signal line, the voltage drop over the detector varies with the resistance and thus the size of the normal conducting domains. In thin-film SNSPDs, however, the domain resistances are of the order of a few hundred Ohms (see subsection 2.1.1), and hence the voltage drop cannot vary to the same extent as in the present Nb detector.

The thicknesses d and widths w of the examined X-SNSPDs are of the same order of magnitude as the primary range R_e of a 6 keV photoelectron, calculated to ≈ 170 nm for Nb and to ≈ 100 nm for TaN in subsection 2.3.3. Assuming that a photon is absorbed in the meander, different fractions of its energy will therefore be absorbed in the meander for different absorption events due to the random primary path (even for identical absorption points). This leads to different resistances of the emerging normal conducting domain, which explains why the Fe-55 emitted photons lead to significantly varying pulse amplitudes of the Nb X-SNSPD (see Fig. 7.8) despite their well-defined photon energy of

≈ 6 keV (see subsection 5.2.5). At this point, indirect detection events originating from photons absorbed in the substrate close enough to the interface of the meander cannot be excluded and may also contribute to the histograms.

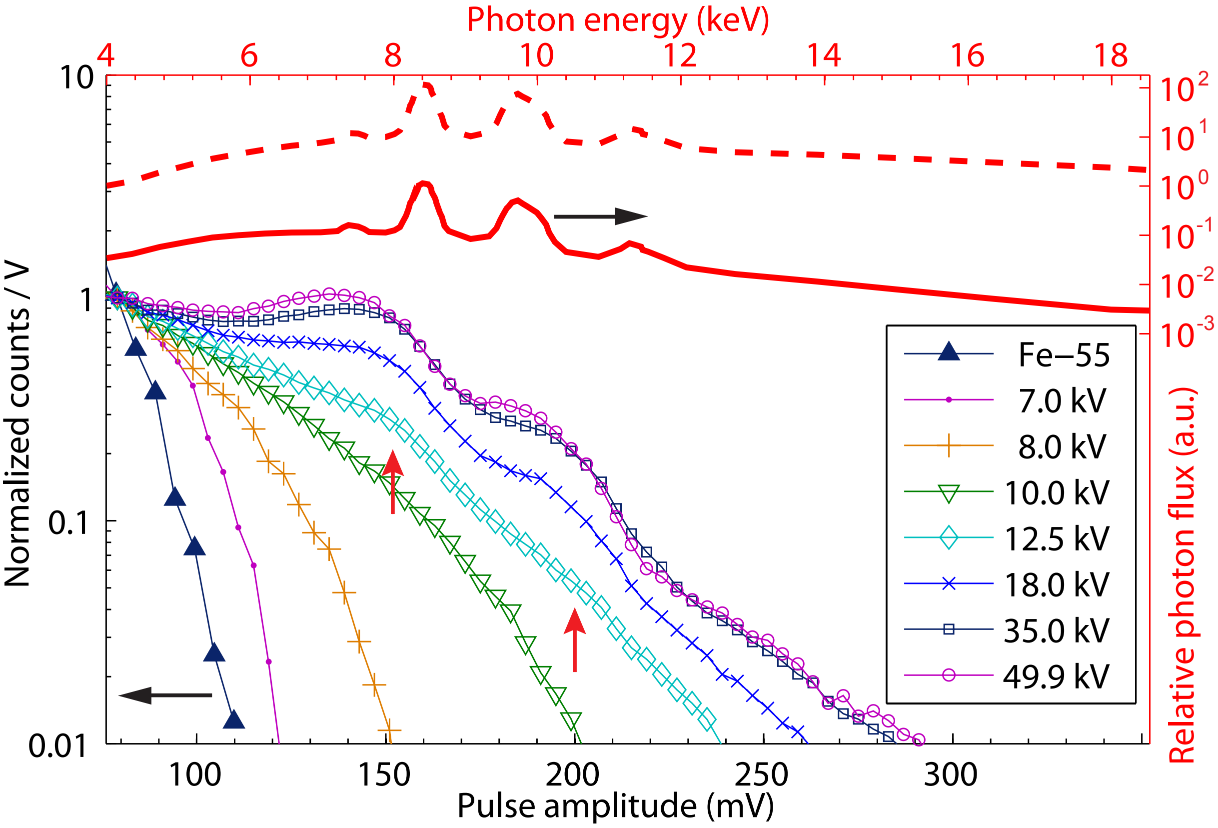

Figure 7.8: The top and right axes refer to the X-ray tube spectrum at $V_A \approx 30$ kV (dashed red line), also shown in Fig. 5.4. Taking into account the transmission through the 0.1 mm thick Kapton cryostat window, the thermal shield of 1 μm thin aluminum and the absorption in 100 nm thick niobium, the solid red line shows the relative probability for the absorption of a photon. The left and bottom axes refer to histograms of voltage pulse amplitudes from photons emitted by the X-ray tube at different V_A (markers are indicated in the legend) and by the radioactive Fe-55 source. The histograms use a bin size of 4 mV (5.2 mV for the Fe-55 data) and are normalized at 79 mV, which lies above the noise level. The two vertical red arrows indicate preferred pulse amplitudes which may tentatively be ascribed to the main characteristic emission lines at 8.3-8.4 kV and 9.7-10.0 kV. This figure is adapted from our work by Inderbitzin *et al.* [86].

In Fig. 7.9(a) and (b) we plotted pulse-amplitude histograms for detector TaN-A (at $I_b = 54$ μA) and TaN-B (at $I_b = 243$ μA) at $T = 1.85$ K, respectively, normalized with respect to the total number of counts. The amplitudes are much larger than for the Nb X-SNSPD at $I_b = 0.61$ mA shown in Fig. 7.9(d) despite the smaller bias currents used, which is expected from the larger domain resistances. This magnitude of the amplitudes therefore allows for the recording of all detection pulses at $T = 1.85$ K, and no pulses had

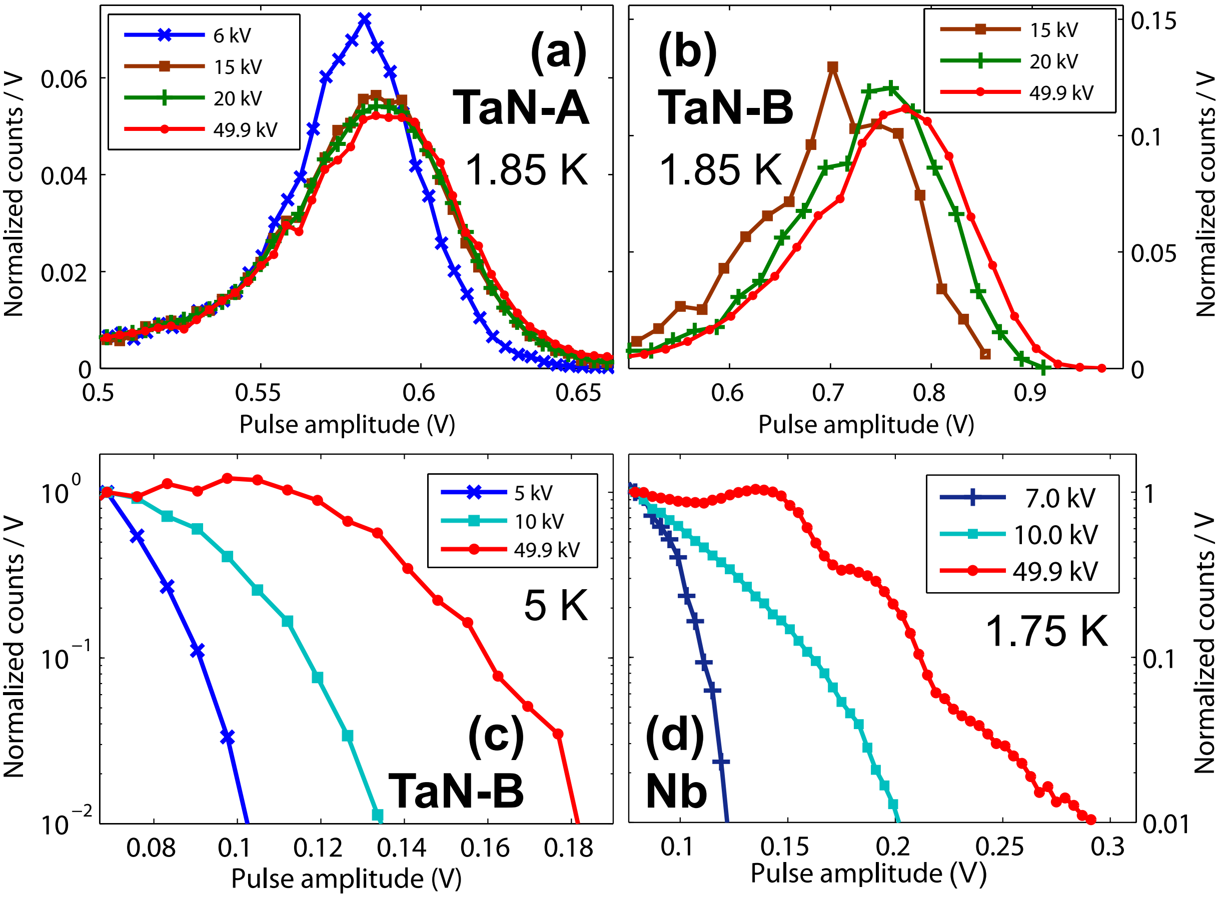

Figure 7.9: Pulse-amplitude histograms for different V_A for the detectors **(a)** TaN-A (at $T = 1.85$ K and $I_b = 54$ μA) and **(b)** TaN-B (at $T = 1.85$ K and $I_b = 243$ μA), normalized to the total number of counts. We also show a comparison for **(c)** TaN-B (at $T = 5$ K and $I_b = 121$ μA) and **(d)** the Nb X-SNSPD (at $T = 1.75$ K and $I_b = 0.61$ mA), here normalized relative to the counts at an amplitude of 69 mV and 79 mV, respectively. This figure is taken from our work by Inderbitzin *et al.* [87].

to be cut off to eliminate noise signals.

7.10 Energy dependence of the pulse amplitudes

Regarding the detection of non-monochromatic radiation, we expect that two absorbed photons with different energies E deposit on average different amounts of energy in the superconducting meander structure itself, thereby leading to different average sizes of normal conducting domains. Strikingly, Fig. 7.8 shows an amplitude distribution for the Nb X-SNSPD which indeed depends significantly on V_A. Since the detector operates in a single-photon detection mode, this dependence can be attributed to the variation of the photon energy spectrum by V_A itself.

In order to demonstrate the correlation between these recorded pulse amplitudes and the emission spectrum of the X-ray tube, we have overlaid the spectrum (dashed red line, top and right axes) for $V_A \approx 30$ kV [116], linearly scaled to the amplitude distribution with a common origin. We also plotted the relative absorption probability of a photon with a certain energy, taking into account the transmission through the two cryostat windows and the energy-dependent absorption in 100 nm thick Nb (solid red line). For $V_A \geq 12.5$ kV, our X-SNSPD shows distinct preferred pulse amplitudes (see vertical red arrows in Fig. 7.8), which we may tentatively ascribe to the two main characteristic emission lines of the tungsten target at 8.3-8.4 keV and 9.7-10.0 keV (described in detail in subsection 5.2.5). These preferred pulse amplitudes do not appear for $V_A \leq 10$ kV, since $V_A \geq 10.2$ kV and $V_A \geq 11.5$ kV are the conditions for the excitation of the different emission lines. Moreover, the maximum amplitudes scale approximately linearly with V_A up to about 12.5 kV. For larger voltages, the amplitude distribution appears to be truncated, probably due to the mean propagation distance of the primary becoming much longer than the film thickness.

Experiments with a 200 μm thick aluminum X-ray filter at X-ray tube settings of $V_A = 18.0$ kV and $I_A = 2.00$ mA show a reduction of the bin count rate for the preferred pulse amplitudes at $\approx 110 - 170$ mV and $\approx 170 - 220$ mV (indicated by the red arrows in Fig. 7.8) to $\approx 11 - 22\%$ and $\approx 22 - 39\%$, respectively. Assuming that every pulse amplitude value A is the average amplitude for detected photons with a certain energy E and this relation is unique, these bin count rate reductions can be attributed to finite transmission probabilities of the aluminum filter, and therefore the corresponding photon energies E can be identified. This argument results in photon energies of $8.4 - 9.6$ keV and $9.6 - 11.3$ keV [85], which further supports the hypothesis that the two preferred pulse amplitudes could be attributed to the main characteristic emission lines of the tungsten target. As the two preferred pulse amplitudes are distinguishable, the energy resolution of this Nb X-SNSPD could therefore be determined to be better than ≈ 1.5 keV in the photon energy range $E \approx 8 - 10$ keV.

The expected large domain resistances for detector TaN-A must also lead to a reduction of the amplitude dependence on the photon energy as compared to the Nb X-SNSPD, because the pulse amplitude can only be significantly varied for domain resistances of the order of 50 Ω or smaller. Indeed, only a weak amplitude dependence is visible and only between $V_A = 6$ kV and 15 kV for this detector. This is in qualitative agreement with the reported 1-9 keV argon-ion detection by a $d = 10$ nm thick and $w = 800$ nm wide NbN detector with comparable typical domain resistances [127], where no energy dependence in the amplitude distribution was found.

Detector TaN-B shows larger amplitudes than TaN-A despite its smaller domain resistances, which is a consequence of the larger applied bias current. Furthermore, the amplitude distribution shows a stronger dependence on the photon energy than for detector TaN-A, as the domain resistances must be smaller. Below $V_A = 15$ kV and at $T = 1.85$ K, the count rate is very small. However, as already shown in Fig. 7.7(b), it increases significantly at higher temperatures, and at $T = 5$ K measurable count rates are achieved even for $V_A = 5$ kV as shown in Fig. 7.9(c), as low-energy photons become detectable. However, the bias current needs to be reduced here due to a lower critical current, and therefore certain pulses may escape detection as the discriminator level is set above the noise level. We faced the same problem for the Nb X-SNSPD (see Fig. 7.9(d)), and we therefore normalized Fig. 7.9(c) and (d) each with respect to the counts of a bin right above the noise level. At $T = 5$ K, TaN-B shows a pronounced energy dependence of the amplitude distribution which is qualitatively very similar to that of the Nb X-SNSPD, where the amplitude distribution broadens along with a broader photon energy spectrum.

We note that a certain pulse amplitude variation has also been observed for superconducting stripline detectors made from 40 nm thick niobium films detecting molecules with keV energies [35], where it was ascribed to supercurrent variations among parallel striplines or multiple impact events. Semenov *et al.* [60] reported a certain energy resolution for 5 nm thin SNSPDs for infrared and visible photons, which only appears in the wavelength range where the detection mechanism crosses over from direct photon detection to fluctuation-assisted photon detection, as explained in detail in section 2.1.7. However, this latter detection mechanism is suppressed in our X-SNSPD due to the large film thickness, as explained above in section 7.8. In addition, this mechanism has been reported to result in smaller amplitudes for photons with larger energies, which is contrary to the findings for our X-SNSPD. Therefore an energy resolving capability from this very physical origin can be safely excluded.

7.11 Device detection efficiency

Considering the absorptance (see subsection 2.3.2 for details), geometry and filling factor of the Nb and TaN-A X-SNSPD, a maximum *DDE* of 1.6% and 2.3% could be achieved at 5.9 keV in principle, respectively, provided that exactly the photons absorbed in the superconducting meander are counted.

For the Nb X-SNSPD, we estimated a lower limit for *DDE* at 5.9 keV of 0.03%, using the Fe-55 X-ray source. Since different fractions of the photon energy are deposited inside the nanowires for different photon absorption events (see section 7.9) and because we could only consider pulses with amplitudes clearly above the noise level, our value is only a lower limit for *DDE*, as most detectable amplitudes from 6 keV-photons were not much larger than the noise amplitude and an unknown number of detection events with smaller amplitudes could therefore not be distinguished from the noise. However, the inhomogeneous bias current distribution over the Nb nanowire cross-section (see section 7.2) is not expected to diminish DDE significantly, as the hot-spot created by a 6 keV photon is expected to cover a significant part of the nanowire cross-section on average (see section 7.6).

For the TaN-A X-SNSPD, we determined a DDE for 5.9 keV photons to 1.4%, also using the Fe-55 X-ray source. This value is $\approx 60\%$ of the theoretical maximum value for DDE mentioned above. It is not realistic to achieve a DDE of 100% of this maximum value, however, due to the statistical nature of the energy-diffusion mechanisms involved, allowing photons to escape detection despite their absorption inside the superconducting meander structure.

7.12 Publications related to this chapter

These two publications are appended at the end of this chapter:

- **An ultra-fast superconducting Nb nanowire single-photon detector for soft X-rays**
  K. Inderbitzin, A. Engel, A. Schilling, K. Il'in, M. Siegel
  APPLIED PHYSICS LETTERS **101**, 162601 (2012)

  DOI: 10.1063/1.4759046
  Open access repositories: `http://arxiv.org/abs/1208.1656`

- **Soft X-ray single-photon detection with superconducting tantalum nitride and niobium nanowires**
  K. Inderbitzin, A. Engel, A. Schilling
  IEEE TRANSACTIONS ON APPLIED SUPERCONDUCTIVITY **23**, 2200505 (2013), SELECTED FOR THE OCT/NOV 2012 ISSUE OF THE EUROPEAN SUPERCONDUCTIVITY NEWS FORUM

  DOI: 10.1109/TASC.2012.2234496
  Open access repositories: `http://arxiv.org/abs/1210.3675`

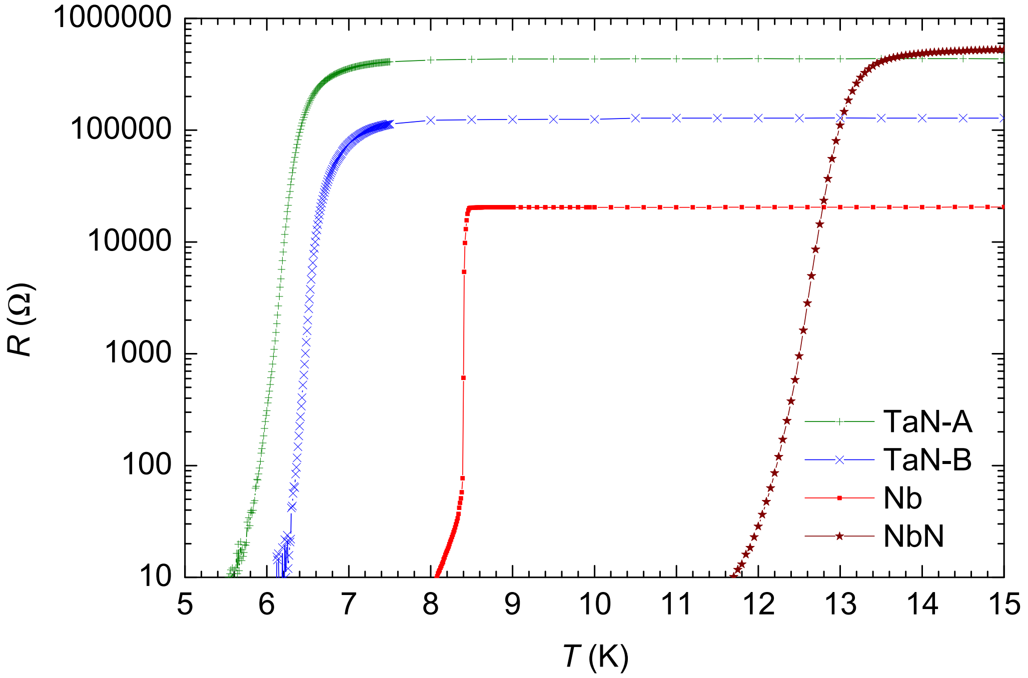

Figure 7.10: Temperature-dependent resistance data for the X-SNSPDs TaN-A (green horizontal crosses) and TaN-B (blue diagonal crosses), the 100 nm thick Nb X-SNSPD (red rectangles) and the 6 nm thin NbN SNSPD (brown stars).

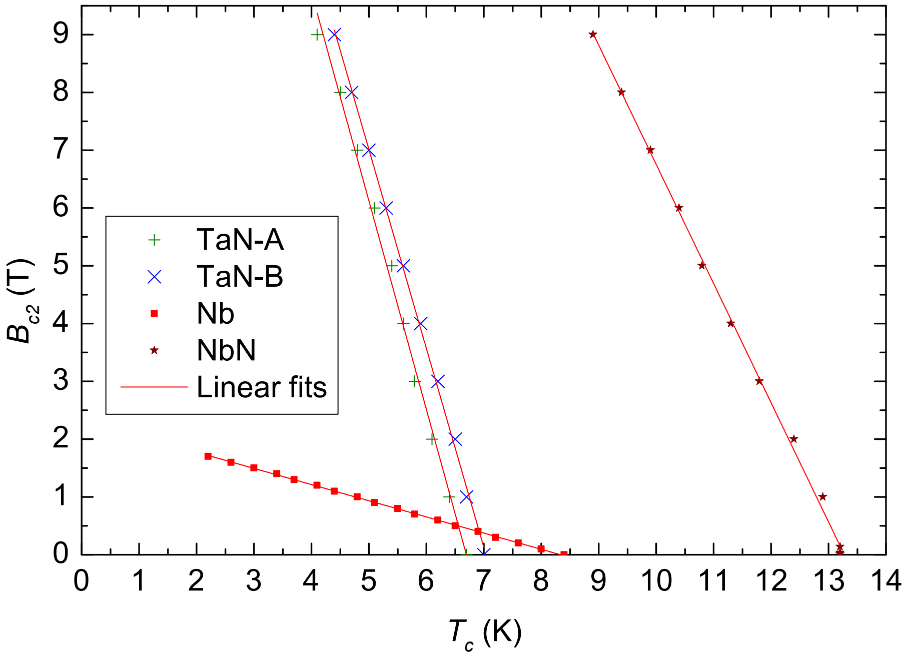

Figure 7.11: Measurements of the upper critical magnetic flux density B_{c_2} as a function of the temperature T for the X-SNSPDs TaN-A (green horizontal crosses) and TaN-B (blue diagonal crosses), the 100 nm thick Nb X-SNSPD (red rectangles) and the 6 nm thin NbN SNSPD (brown stars). The linear fits (red lines) allow for indirect estimates of the corresponding values for $B_{c_2}(0)$ and therefore $\xi(0)$ (see text).

Detector property	**NbN SNSPD**	**Nb X-SNSPD**	**TaN-A X-SNSPD**	**TaN-B X-SNSPD**
Geometrical film thickness d	6 nm ($d_{sup} \approx 5\ nm$)	102.9 nm $\pm$ 1.3 nm	100.8 nm $\pm$ 1.4 nm	like TaN-A
Film normal state resistivity ρ_n	190 $\mu\Omega$cm (at 14.5 K)	4 $\mu\Omega$cm (at 10 K)	500 $\mu\Omega$cm (at 10.3 K)	like TaN-A
Critical temperature T_c (before fabrication)	unknown	8.9 K	8.0 K	like TaN-A
Critical temperature T_c (after fabrication)	13.2 K	8.4 K	6.7 K	7.0 K
Estimated upper critical magnetic flux density $B_{c_2}(T = 0\text{ K})$	18.9 T	1.7-2.3 T	16.7 T	16.7 T
Calculated GL coherence length $\xi(T = 0\text{ K})$	4.2 nm	11.9-13.9 nm	4.4 nm	4.4 nm
Nanowire width w	≈ 80 nm	$\approx 360 - 410$ nm	$\approx 275 - 340$ nm	$\approx 1.8 - 1.9\ \mu m$
Total meander length l	126 μm	11 mm	1.67 mm	3.57 mm
Active detector area	$4.92 \times 5.00\ \mu m^2$	$131 \times 55\ \mu m^2$	$35 \times 33\ \mu m^2$	$66 \times 119\ \mu m^2$
Filling factor	$\approx 40\%$	$\approx 55 - 65\%$	$\approx 40 - 50\%$	$\approx 80 - 85\%$
Critical current $I_{c,exp}$	31.9 μA (at 2.6 K) 30.9 μA (at 4 K) 24.0 μA (at 6 K)	≈ 11 mA (at 1.75 K)	105 μA (at 1.85 K)	860 μA (at 1.85 K) 430 μA (at 4 K) 155 μA (at 5 K)
Effective magnetic penetration depth λ_{eff}	45 μm	≈ 100 nm	26 μm	19 μm
Calculated kinetic inductance L_{kin}	90 nH	6 nH	180 nH	50 nH
Latching bias current (at $V_A = 49.9$ kV and $I_A = 2.00$ mA)	no latching	$> 5.5\%\ I_{c,exp}$ (at 1.75 K)	$> 52\%\ I_{c,exp}$ (at 1.85 K)	$> 32\%\ I_{c,exp}$ (at 1.85 K)
Pulse rise time T_R (and std. deviation)	210 ps $\pm$ 11 ps	250 ps $\pm$ 70 ps	750 ps $\pm$ 60 ps	910 ps $\pm$ 120 ps
Pulse length T_P (and std. deviation)	3.6 ns $\pm$ 0.3 ns	3.4 ns $\pm$ 0.2 ns	on the order of 10 ns	like TaN-A

Table 7.1: Properties of detectors examined in this thesis: the conventional NbN thin-film SNSPD presented in chapter 6 and the thick-film X-SNSPDs from Nb and TaN examined in this chapter.

APPLIED PHYSICS LETTERS **101**, 162601 (2012)

An ultra-fast superconducting Nb nanowire single-photon detector for soft x-rays

K. Inderbitzin,[1] A. Engel,[1] A. Schilling,[1] K. Il'in,[2] and M. Siegel[2]
[1]*Physics Institute, University of Zurich, Winterthurerstr. 190, 8057 Zurich, Switzerland*
[2]*Institute of Micro- and Nano-Electronic Systems, Karlsruhe Institute of Technology, Hertzstr. 16, 76187 Karlsruhe, Germany*

(Received 7 August 2012; accepted 1 October 2012; published online 15 October 2012)

Although superconducting nanowire single-photon detectors (SNSPDs) are well studied regarding the detection of infrared/optical photons and keV-molecules, no studies on continuous x-ray photon counting by thick-film detectors have been reported so far. We fabricated a 100 nm thick niobium x-ray SNSPD (an X-SNSPD) and studied its detection capability of photons with keV-energies in continuous mode. The detector is capable to detect photons even at reduced bias currents of 0.4%, which is in sharp contrast to optical thin-film SNSPDs. No dark counts were recorded in extended measurement periods. Strikingly, the signal amplitude distribution depends significantly on the photon energy spectrum. © *2012 American Institute of Physics*. [http://dx.doi.org/10.1063/1.4759046]

Already more than a decade before the development of superconducting nanowire single-photon detectors (SNSPD) for the optical and near-infrared wavelength range, serious efforts had been undertaken to adapt this detection principle for x-ray photons with keV-energies.[1–4] However, these preliminary x-ray detectors struggled with latching, making it difficult to operate them as self-recovering detectors in which superconductivity recovers after photon detection events (called continuous operation mode in this Letter). The need to externally reduce the bias current to a value low enough for superconductivity to recover after a detection event results in long dead times and limits the count rates.

Very fast and sensitive x-ray single-photon detectors from superconducting nanowires would be very interesting for applications where very high count rates, precise timing, a good signal-to-noise ratio, and response in a wide spectral range for photon counting are required. Potential applications comprise experiments with synchrotron x-ray sources, free-electron lasers, and hot plasmas (as in nuclear fusion experiments), all emitting bright and pulsed x-ray radiation. In many medical imaging systems, ultrafast x-ray single-photon detectors with energy resolution are desirable in order to reduce patient radiation dose. In the recently developing photon-counting x-ray computer tomography, for example, long detection pulse durations can compromise the image quality by a possible overlap of succeeding photon pulses, as high photon fluxes have to be used in order to prevent motion blur.[5]

Recently, SNSPDs[6] and superconducting stripline detectors (SSLDs)[7–10] with superconducting film thicknesses of up to 50 nm were reported to be used in continuous mode for time-of-flight mass spectrometry (TOF-MS) of molecules with keV-energies, and ultrafast pulse recovery times and pulse rise times down to 380 ps ± 50 ps were reported.[11] There is only one report on continuous x-ray photon counting with SNSPDs: Perez de Lara *et al.*[12] reported on the detection of 6 keV photons by a SNSPD from 5 nm thin NbN. However, there are no published studies on continuous x-ray photon detection in thick-film SNSPDs (called X-SNSPDs in this work), although they are promising candidates for ultrafast detectors in continuous mode.

The absorptance of x-ray photons in thin-film superconductors is extremely low, in contrast to the underlying, commonly much thicker substrate. It was shown[12] that the 6 keV photon detection in thin-film SNSPDs mostly occurs through photon absorption in the substrate and the successive energy diffusion to the superconducting meander structure. In the reported case, this even leads to a device detection efficiency (DDE), which is higher than the photon absorption probability of the superconductor. The DDE is defined as the number of photon signal events, normalized to the number of photons crossing the active detector area. It is very likely, however, that this indirect detection principle for x-ray photons results in an increased timing jitter compared to optical photon detection, due to the random nature of the energy diffusion processes to the superconducting meander structure after photon absorption and the depth distribution of the absorption event. In order to enhance the absorptance of the superconducting detector and therefore promoting a more direct detection principle, we fabricated X-SNSPDs from a 100 nm thick niobium film. The absorptance of a 100 nm thick layer of niobium is 2.7% for 6 keV photons and 0.23% for 30 keV photons.[13]

A niobium film of 100 nm thickness was grown at room temperature by DC magnetron sputtering in an Ar atmosphere on R-plane cut sapphire substrates. The critical temperature T_c of the as-grown film was 8.9 K. From this film, X-SNSPDs were fabricated using electron-beam lithography of a multi-layer ZEP520A resist and reactive ion etching, mostly adapting previously published fabrication recipes.[14] After fabrication, the detector showed a critical temperature $T_c = 8.4\,\mathrm{K}$. Fig. 1(a) shows an optical image of the X-SNSPD with which the measurements in this report were performed. The meander covers an area of $131 \times 55\,\mu\mathrm{m}^2$ (meandering area) with a filling factor of about 50% by a conduction path of a uniform width $w \approx 250\,\mathrm{nm}$ and a length $l \approx 11\,\mathrm{mm}$. The accuracy in determining the width of the conduction path was limited by the optical resolution of the

0003-6951/2012/101(16)/162601/5/$30.00

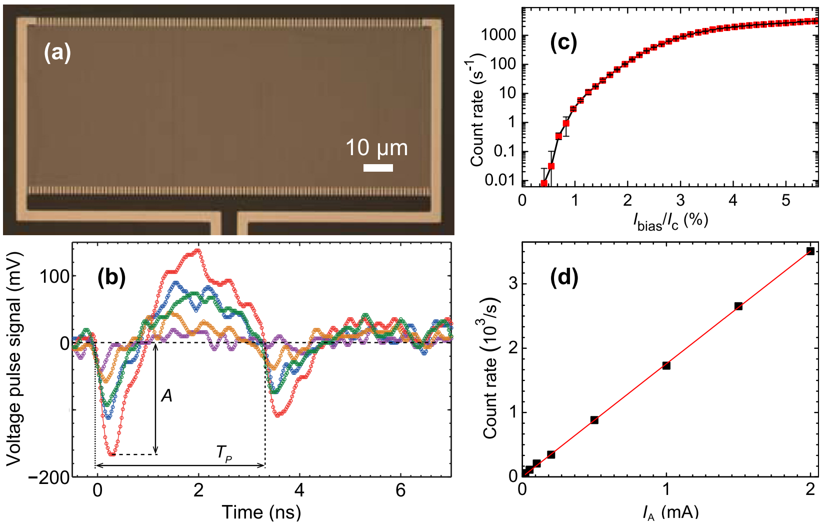

FIG. 1. (a) Optical image of examined X-SNSPD from 100 nm thick niobium. For (b)-(d), the X-SNSPD was irradiated by the x-ray tube at $V_A = 49.9\,\text{kV}$, which emits at maximum intensity at $I_A = 2.00\,\text{mA}$. (b) Typical voltage pulses after photon absorption, with the definition of the pulse length T_P and the pulse amplitude A shown schematically. The different colors of the pulses are only a guide to the eye. (c) Photon count rate as a function of $I_{\text{bias}}/I_{\text{c}}$. (d) Photon count rate as a function of I_A, which is proportional to the photon flux, showing a linear dependence and thus single-photon detection.

microscope. The superconducting leads to this meander structure have a length negligible for the total length l and are much wider ($w_{Leads} \approx 4\,\mu\text{m}$) than the conduction path of the meander structure.

This detector geometry ensures that the detector has a kinetic inductance small enough to allow for ultrafast recovery times[15] and is large enough to reduce problems with latching as previously reported,[1,3,4,16] therefore allowing its operation in continuous mode. In order to estimate the kinetic inductance L_K of the X-SNSPD, a literature value[17] for the penetration depth of $\lambda(0) \approx 100\,\text{nm}$ is used for the 100 nm thick niobium film, and we assume $\lambda(1.75\,\text{K}) \approx \lambda(0)$, as the reduced temperature $t = T/T_{\text{c}} \approx 0.2$ is sufficiently small at the measurement temperature. In this case of a niobium film with a thickness $d = 100\,\text{nm} \approx \lambda$, the kinetic inductance can be approximated by $L_K = \mu_0 \lambda l / w$,[18] resulting in $L_K \approx 6\,\text{nH}$. This kinetic inductance is smaller than the values reported[9] for functional SSLDs from thinner films with 40 nm thick niobium, therefore, the tendency for latching of our X-SNSPD is expected to be larger. However, it will be shown that the X-SNSPD can be operated in continuous mode.

The x-ray detection characterization measurements have been performed in a He-3 bath cryostat with a temperature stabilized at 1.75 K ± 0.05 K during the measurements. The detector signal was transmitted to a cryogenic amplifier at the 4 K-stage, and then further to a second amplifier at room temperature before fed into a 3.5 GHz digital oscilloscope. The amplifier chain had an effective bandwidth of about 40 MHz to 1.9 GHz. The bias current was applied in constant-voltage mode and was passed through a series of low-pass filters. The oscilloscope allowed for the recording of thousands of triggered voltage signals, hence a subsequent detailed signal analysis in order to distinguish between detector pulses (including possible dark counts) and unexpected noise signals with much higher voltage amplitude was performed for all measurements, which is not possible with the otherwise widely used threshold counters.

The X-SNSPD was irradiated by x-ray photons through a 100 μm thin window of polyimide (Kapton) at the cryostat, in order to minimize x-ray attenuation. A second window of 1 μm thin aluminum was installed at the 4 K-heat shield to minimize thermal radiation. Two qualitatively different x-ray sources were used: A tungsten-target x-ray tube with a maximum acceleration voltage $V_A = 49.9\,\text{kV}$ and a radioactive Fe-55 isotope source with an activity of 3.7 GBq, which emits photons with well defined energies around 6 keV. The emission characteristics of the x-ray sources and the geometry of the experimental setup allowed a homogeneous irradiation of the X-SNSPD by both sources.

Fig. 1(b) shows several examples of voltage pulses after x-ray photon absorption recorded by the oscilloscope, with the detector biased at $I_{\text{bias}} \approx 0.61\,\text{mA}$, which corresponds to about 5.5% of the experimentally measured critical current $I_{\text{c}} \approx 11\,\text{mA}$. The damped oscillations following the pulse are a consequence of the fact that the detector is effectively part of an LC circuit.[21] Defining the pulse length time T_P as the period of the first pulse oscillation, i.e., the time span between the first and the third zero crossing, ultrafast recovery times of 3.4 ns± 0.2 ns were measured under irradiation of the X-SNSPD with the x-ray tube at $V_A = 49.9\,\text{kV}$. The pulse amplitude A is defined as the absolute value of the first pulse minimum (shown in Fig. 1(b)) and hence the rise time as the time span between the absolute values $10\% \cdot A$ and $90\% \cdot A$. We obtained a rise time of 250 ps ± 70 ps, which is lower than any reported value for TOF-MS with SSLDs.[11] Furthermore, we can expect the intrinsic signal rise time to be even faster, since the effective bandwidth $BW = 1.9$ GHz of our electronics setup results in a theoretical minimum rise time $T_R \approx 0.35/BW \approx 190\,\text{ps}$.[19]

X-ray photon detection in this X-SNSPD was possible at bias currents as low as 0.4% I_{c} [Fig. 1(c)]. This stands in sharp contrast to the behavior of SNSPDs for optical photons, even in the case of SNSPDs with especially low cut-off energy.[20,21] This can be explained by the fact that the detected photons have about $r_E \approx 10^3$ times higher energy than visible photons, and that at the same time, the cross-section of the conduction path of this detector is only $r_A \approx 30$ times larger compared to a 7.5 nm thin niobium SNSPD in a reported work[22] on optical photon detection. A threshold value of $I_{\text{bias}}/I_{\text{c}} \approx 40\%$ can be extracted from their data, which we define as the reduced bias current for which the DDE is two orders of magnitude smaller than the maximum. For our X-SNSPD, the threshold value for $I_{\text{bias}}/I_{\text{c}}$ can, therefore, be estimated to be $r_E/r_A \approx 30$ times smaller, which gives $I_{\text{bias}}/I_{\text{c}} \approx 1\%$. At $V_A = 30\,\text{kV}$, a threshold value of $I_{\text{bias}}/I_{\text{c}} \approx 2\%$ is extracted from our measurements. This simple estimate cannot be applied for the detection of x-ray photons in thin-film SNSPDs, where photon detection was only reported down to relatively high bias-currents of the order of 70% I_{c},[12] as only a part of the photon energy is expected to diffuse into the superconducting meander after photon absorption in the substrate.

A second estimate for the threshold of $I_{\text{bias}}/I_{\text{c}}$ can be made with a hot-spot model following Gabutti *et al.*[1] for the detection of x-ray photons in superconducting strips from thick niobium films. They assume that the primary excitations of low keV-photons are created in a small volume centered at the absorption point of the photon, thereby creating a hot-spot resembling a sphere, in which superconductivity is destroyed. The bias current is, therefore, forced to flow in a smaller cross-section, where it can exceed I_{c} for high enough bias currents, which leads to a normal conducting domain. For the absorption of a 8.4 keV photon (of the strong characteristic emission peak for $V_A = 30\,\text{kV}$, see below and Fig. 2), the hot-spot radius can be estimated as $r_0 \approx 210\,\text{nm}$ using Eq. (3) in Ref. 1, Eq. (2) in Ref. 4, the BCS expression for the heat capacity of low-temperature superconductors (Eq. (22) in Ref. 23), and the electronic specific heat constant for niobium.[24] Using Eq. (1) in Ref. 1 results in a vanishing reduced bias current threshold, as the hot-spot is expected to cover the whole cross-section. A more detailed look at the absorption process (see below) shows that this is a very crude approximation. On the other hand, the observed reduced bias current threshold results in a hot-spot radius of $r_0 \approx 120\,\text{nm}$. However, the actual reduced bias current threshold could be even lower as observed, as the count rate will also decrease for lower bias currents due to a decreasing signal amplitude while keeping the trigger level constant. Therefore, this calculated hot-spot radius r_0 is only a lower limit, and the actual hot-spot could as well cover the whole cross-section.

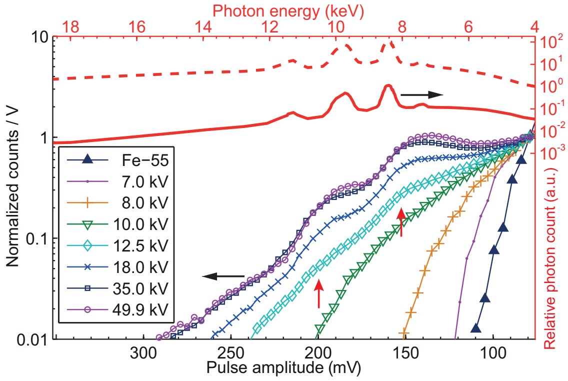

FIG. 2. The top and right axes refer to the x-ray tube spectrum at $V_A \approx 30\,\text{kV}$ (dashed red line). Taking into account the transmission through the cryostat windows and the absorption in 100 nm niobium, the solid red line shows the relative probability for the absorption of a photon. The left and bottom axes refer to histograms of voltage pulse amplitudes from photons emitted by the x-ray tube at different V_A (indicated in the legend, V_A determines the maximum energy of the tube emitted photons) and by the radioactive Fe-55 source, which mainly emits at 6 keV. The histograms use a bin size of 4 mV (5.2 mV for the Fe-55 data) and are normalized at 79 mV, which lies above the noise level. The two vertical red arrows indicate preferred signal amplitudes, which may tentatively be ascribed to the main characteristic emission at 8.3–8.4 kV and 9.7–10.0 kV.

Above a reduced bias current $I_{\text{bias}}/I_{\text{c}} \approx 5.5\%$, the device cannot be continuously used for x-ray photon detection, as the photon-induced normal conducting domain does not recover its superconducting state due to self-heating. This latching effect[16,25,26] is promoted by the low kinetic inductance L_K of the X-SNSPD and the orders-of-magnitude smaller resistance of the normal conducting domains as compared to the situation in thin-film SNSPDs from NbN, originating from the larger conductance, cross-section, and diffusivity of the niobium meander.

However, investigations on possible dark counts could be performed up to $I_{\text{bias}}/I_{\text{c}} = 99\%$, but no dark counts during more than 5 h of measurement time were recorded, thereby limiting the dark-count rate to $\leq 5.4 \times 10^{-5}\,\text{s}^{-1}$. The fact that the dark-count rate is much lower in our X-SNSPD compared to typical thin-film SNSPDs[27] is not surprising considering the geometric differences. Assuming thermally activated fluctuations to be responsible for dark counts, then the energy associated with phase-slips due to fluctuations in the superconducting order parameter scales at least with the cross-section of the superconductor wd, and the vortex-antivortex scenario is topologically suppressed for a film thickness $d \gg \xi$. Also, the typical energy required for a single vortex to overcome the edge barrier is proportional to the film thickness,[28] thus reducing the probability to exceedingly small values for all three fluctuation events considered to contribute to the dark-count rate in thin-film SNSPD.

Fig. 1(d) shows the count rate dependence on the x-ray photon flux, which was varied by the x-ray tube anode current I_A at $V_A = 49.9\,\text{kV}$, keeping the relative photon energy distribution constant.[29] This dependence shows a linear behavior, and we, therefore, conclude that the X-SNSPD detects in single-photon mode.[30]

The sample pulses in Fig. 1(b) show that the amplitudes A of different pulses vary significantly, much more than in the case of SNSPDs.[31] In Fig. 2 we plotted histograms of the pulse amplitudes at $I_{\text{bias}} \approx 0.61\,\text{mA}$ for photons from the x-ray tube at different V_A and from the radioactive Fe-55 source, shown only for amplitudes right above the noise level (amplitudes below the noise level could not be recorded). We attribute this amplitude variation to the small resistance of the normal conducting domains, which we estimate to be of the order of 1 Ω, using the estimated values for the hotspot radius from above as the half domain length. Since this value is smaller than the 50 Ω impedance of the coaxial signal line, the voltage drop over the detector varies with the resistance and thus the size of the normal conducting domains. In thin-film SNSPDs however, the domain resistances are of the order of a few hundred Ohms,[32] hence the voltage drop cannot vary to the same degree as in the examined detector.

Van Vechten and Wood[33] examined in detail the processes, which happen after absorption of a keV-photon in niobium: Initially, the x-ray photon energy is transferred to a primary photoelectron, which then scatters inelastically to produce secondary electrons causing the path of the primary to be irregularly kinked. The distance the primary electron will have travelled before becoming indistinguishable from the other electrons in the system (called primary range) depends on its initial energy and is estimated to be about 170 nm for 6 keV and 2.8 μm for 30 keV in niobium. This process takes place within 1 ps or less, and another bound of $\approx 10^{-14}$ s can be calculated by assuming a uniform deceleration from the initial kinetic energy to zero velocity. These electrons create excited quasiparticles, which eventually relax to energies of a few meV and finally recombine into Cooper pairs within 1 ps to 1 ns if no bias current is applied, similarly to the quasiparticle diffusion in SNSPDs. This timescale is orders of magnitude longer than the time necessary for the primary to lose its energy. Hence, the emerging hot-spot (in which superconductivity is destroyed) will not have a spherical shape in most cases, as assumed by the hot-spot model by Gabutti *et al.*[1] discussed above, but rather the shape of a growing quasiparticle cloud along the random paths of the primary and secondary electrons.

Our examined meander is 100 nm thick and $\approx$250 nm wide, which is of the same order of magnitude as the primary range of a 6 keV photoelectron given above. Assuming a photon is absorbed in the meander, different fractions of its energy will, therefore, be absorbed in the meander for different absorption events due to the random primary path (even for identical absorption points). This leads to different resistances of the emerging normal conducting domain and explains why the Fe-55 emitted photons lead to significantly varying pulse amplitudes [Fig. 2], despite their well-defined photon energy. At this point, indirect detection events originating from photons absorbed in the substrate close enough to the interface of the meander cannot be excluded. However, estimates of the absorption probability in 100 nm Nb and of the detection efficiency let us conclude that direct detection events dominate.

Nevertheless, we expect that two absorbed photons with different energies on average deposit different amounts of energy in the meander, therefore leading to different average sizes of normal conducting domains. Strikingly, Fig. 2 shows an amplitude distribution which depends significantly on V_A. Since the detector operates in a single-photon detection mode, this dependence can be attributed to the variation of the photon energy spectrum by V_A.

In order to demonstrate the correlation between the recorded pulse heights and the emission spectrum of the x-ray tube, we have overlaid the spectrum (dashed red line, top and right axes) for $V_A \approx 30$ kV,[34] linearly scaled to the amplitude distribution with a common origin. Additionally, we plotted the relative absorption probability of a photon with a certain energy taking into account the transmission through the two cryostat windows and the energy dependent absorption in 100 nm thick Nb (solid red line). For $V_A \geq 12.5$ kV, our X-SNSPD shows distinct preferred signal amplitudes (see vertical red arrows in Fig. 2), which we may tentatively ascribe to the two main characteristic emission lines of the tungsten target at 8.3–8.4 keV and 9.7–10.0 keV.[35] These preferred signal amplitudes do not appear for $V_A \leq 10$ kV, since $V_A \geq 10.2$ kV and ≥ 11.5 kV are conditions for the excitation of the different emission lines. Additionally, the maximum amplitudes scale approximately linearly with V_A up to about 12.5 kV. For higher voltages, the amplitude distribution appears to be truncated, probably due to the mean propagation distance of the primary becoming much longer than the film thickness.

We note that a certain pulse amplitude variation has also been observed for superconducting stripline detectors from 40 nm thick niobium films detecting molecules with keV-energies,[9] where it was ascribed to supercurrent variations among parallel striplines and multiple impact events.

In conclusion, our results show that the ultrafast dark-count-free X-SNSPDs from 100 nm thick niobium can be fabricated, which can operate in a large spectral range. Using a hot-spot model, the x-ray photon detection capability at very low reduced bias currents is explained. The small resistance of the normal conducting domains leads to significant variations in the pulse amplitude, which are susceptible to the photon energy spectrum. This raises the question of a potential energy resolution of X-SNSPDs. The kinetic inductance of the device has to be carefully chosen by proper design, in order to reduce the tendency of the detector to latch due to the small domain resistances. An increase of the DDE of X-SNSPDs by additional fabrication steps (e.g., by stacking of several active superconducting layers as previously suggested for SNSPDs[36]) or by using other superconducting materials could be possible.

This research received support from the Swiss National Science Foundation Grant No. 200021_135504/1 and is supported in part by DFG Center for Functional Nanostructures under sub-project A4.3.

[1] A. Gabutti, R. G. Wagner, K. E. Gray, R. T. Kampwirth, and R. H. Ono, Nucl. Instrum. Methods A **278**, 425 (1989).

[2] A. Gabutti, K. E. Gray, R. G. Wagner, and R. H. Ono, Nucl. Instrum. Methods A **289**, 274 (1990).

[3] A. Gabutti, K. E. Gray, G. M. Pugh, and R. Tiberio, Nucl. Instrum. Methods A **312**, 475 (1992).

[4] L. Parlato, G. Peluso, G. Pepe, R. Vaglio, C. Attanasio, A. Ruosi, S. Barbanera, M. Cirillo, and R. Leoni, Nucl. Instrum. Methods A **348**, 127 (1994).

[5] L. Yu, X. Liu, S. Leng, J. M. Kofler, J. C. Ramirez-Giraldo, M. Qu, J. Christner, J. G. Fletcher, and C. H. McCollough, Imaging Med. **1**, 65 (2009).

[6] K. Suzuki, S. Miki, Z. Wang, Y. Kobayashi, S. Shiki, and M. Ohkubo, J. Low Temp. Phys. **151**, 766 (2008).

[7] K. Suzuki, S. Miki, S. Shiki, Z. Wang, and M. Ohkubo, Appl. Phys. Express **1**, 031702 (2008).

[8] A. Casaburi, N. Zen, K. Suzuki, M. Ejrnaes, S. Pagano, R. Cristiano, and M. Ohkubo, Appl. Phys. Lett. **94**, 212502 (2009).

[9] N. Zen, A. Casaburi, S. Shiki, K. Suzuki, M. Ejrnaes, R. Cristiano, and M. Ohkubo, Appl. Phys. Lett. **95**, 172508 (2009).

[10] K. Suzuki, S. Shiki, M. Ukibe, M. Koike, S. Miki, Z. Wang, and M. Ohkubo, Appl. Phys. Express **4**, 083101 (2011).

[11] A. Casaburi, M. Ejrnaes, N. Zen, M. Ohkubo, S. Pagano, and R. Cristiano, Appl. Phys. Lett. **98**, 023702 (2011).

[12] D. Perez de Lara, M. Ejrnaes, A. Casaburi, M. Lisitskiy, R. Cristiano, S. Pagano, A. Gaggero, R. Leoni, G. Golt'sman, and B. Voronov, J. Low Temp. Phys. **151**, 771 (2008).

[13] B. L. Henke, E. M. Gullikson, and J. C. Davis, At. Data Nucl. Data Tables **54**(2), 181–342 (1993).

[14] H. Bartolf, K. Inderbitzin, L. B. Gómez, A. Engel, and A. Schilling, J. Micromech. Microeng. **20**, 125015 (2010).

[15] A. J. Kerman, E. A. Dauler, W. E. Keichler, J. K. W. Yang, K. K. Berggren, G. Gol'tsman, and B. Voronov, Appl. Phys. Lett. **88**, 111116 (2006).

[16] B. V. Estey, J. A. Beall, G. C. Hilton, K. D. Irwin, D. R. Schmidt, J. N. Ullom, and R. E. Schwall, IEEE Trans. Appl. Supercond. **19**, 382 (2009).

[17] A. I. Gubin, K. S. Il'in, S. A. Vitusevich, M. Siegel, and N. Klein, Phys. Rev. B **72**, 064503 (2005).

[18] P. Müller and A. V. Ustinov, *The Physics of Superconductors* (Springer, Berlin, 1997), p. 39.

[19] N. S. Nise, *Control Systems Engineering* (Wiley, Hoboken, NJ, 2004), pp. 179–180.

[20] B. Baek, A. E. Lita, V. Verma, and S. W. Nam, Appl. Phys. Lett. **98**, 251105 (2011).

[21] A. Engel, A. Aeschbacher, K. Inderbitzin, A. Schilling, K. Il'in, M. Hofherr, M. Siegel, A. Semenov, and H.-W. Hübers, Appl. Phys. Lett. **100**, 062601 (2012).

[22] A. J. Annunziata, D. F. Santavicca, J. D. Chudow, L. Frunzio, M. J. Rooks, A. Frydman, and D. E. Prober, IEEE Trans. Appl. Supercond. **19**, 327 (2009).

[23] M. A. Biondi, A. T. Forester, M. P. Garfunkel, and C. B. Satterthwaite, Rev. Mod. Phys. **30**, 1109 (1958).

[24] *CRC Handbook of Chemistry and Physics*, edited by D. R. Lide (CRC, Boca Raton, FL, 2005), p. 2142.

[25] A. J. Kerman, J. K. W. Yang, R. J. Molnar, E. A. Dauler, and K. K. Berggren, Phys. Rev. B **79**, 100509(R) (2009).

[26] A. J. Annunziata, O. Quaranta, D. F. Santavicca, A. Casaburi, L. Frunzio, M. Ejrnaes, M. J. Rooks, R. Cristiano, S. Pagano, A. Frydman, and D. E. Prober, J. Appl. Phys. **108**, 084507 (2010).

[27] H. Bartolf, A. Engel, A. Schilling, K. Il'in, M. Siegel, H.-W. Hübers, and A. Semenov, Phys. Rev. B **81**, 024502 (2010).

[28] L. N. Bulaevskii, M. J. Graf, C. D. Batista, and V. G. Kogan, Phys. Rev. B **83**, 144526 (2011).

[29] Oxford Instruments data sheet for the x-ray tube used in the experiments described in this letter, XTF5011 Flux Data (received 4/2010).

[30] G. N. Gol'tsman, O. Okunev, G. Chulkova, A. Lipatov, A. Semenov, K. Smirnov, B. Voronov, A. Dzardanov, C. Williams, and R. Sobolewski, Appl. Phys. Lett. **79**, 705 (2001).

[31] A. Semenov, P. Haas, K. Il'in, H.-W. Hübers, M. Siegel, A. Engel, and A. Smirnov, Physica C **460**, 1491 (2007).

[32] A. D. Semenov, P. Haas, B. Günther, H.-W. Hübers, K. Il'in, M. Siegel, A. Kirste, J. Beyer, D. Drung, T. Schurig, and A. Smirnov, Supercond. Sci. Technol. **20**, 919 (2007).

[33] D. Van Vechten and K. S. Wood, Phys. Rev. B **43**, 12852 (1991).

[34] Oxford Instruments Application Note: *Typical Spectrum For Tungsten-Target X-ray Tube* (AN012 Rev. A, revised 3/2007).

[35] A. Thompson, D. Attwood, E. Gullikson, M. Howells, K.-J. Kim, J. Kirz, J. Kortright, I. Lindau, Y. Liu, P. Pianetta, A. Robinson, J. Scofield, J. Underwood, G. Williams, and H. Winick, *X-Ray Data Booklet* (Lawrence Berkeley National Laboratory, Berkeley, 2009), p. 1–21.

[36] A. Matthew Smith, Proc. SPIE **8400**, 84000L (2012).

IEEE TRANSACTIONS ON APPLIED SUPERCONDUCTIVITY, VOL. 23, NO. 3, JUNE 2013 2200505

Soft X-Ray Single-Photon Detection With Superconducting Tantalum Nitride and Niobium Nanowires

Kevin Inderbitzin, Andreas Engel, and Andreas Schilling

***Abstract*—We have fabricated ultrafast dark count-free soft X-ray single-photon detectors (X-SNSPDs) from TaN with various conduction path widths, and we compare their properties with corresponding data from a Nb X-SNSPD. The TaN X-SNSPDs offer an improved detector performance regarding device detection efficiency, latching, and pulse amplitudes. Wide conduction paths allow for a certain energy-resolving capability in contrast to narrow TaN conduction paths. However, wide paths also limit the detection efficiency at low temperatures, which can be explained within a hot-spot model.**

***Index Terms*—Nanofabrication, soft X-ray detectors, superconducting nanowire single-photon detectors, superconductors, tantalum nitride.**

I. INTRODUCTION

X-RAY superconducting nanowire single-photon detectors (X-SNSPDs) are good candidates [1] for applications where very high count rates, precise timing, negligible dark counts and response in the soft X-ray energy range are required. Potential applications cover experiments with free-electron lasers, synchrotron X-ray sources and hot plasmas as in nuclear fusion experiments.

While superconducting nanowire single-photon detectors (SNSPDs) have been shown to be able to detect infrared and optical photons [2] as well as molecules with keV-energies [3] for time-of-flight mass spectrometry, we have very recently also demonstrated the successful operation of an X-SNSPD [1]. As Perez de Lara *et al.* [4] had shown, X-ray photon detection in conventional thin-film SNSPDs (with a typical thickness ≈5 nm) mainly occurs by photon absorption in the substrate and subsequent energy diffusion to the superconducting meander structure. Since this could hamper the timing jitter of a single-photon detector, we had fabricated and studied an SNSPD from a 100 nm thick niobium film (a so called X-SNSPD), in order to promote the direct X-ray photon absorption in the superconducting structure. We achieved dark count-free single-photon detection of keV-photons in continuous mode for reduced bias currents down to 0.4% of I_c with this detector, but with latching appearing above 5.5% of I_c. Very interestingly, the signal amplitude distribution depended significantly on the photon energy spectrum, which may allow for a certain energy resolution.

We have now also developed X-SNSPDs from a 100 nm thick tantalum nitride film in order to improve several detector properties as compared to the Nb X-SNSPD [1]. Firstly, TaN offers a slightly better soft X-ray absorptance than niobium. Secondly, TaN has an about two orders of magnitude larger resistivity than Nb, which can lead to larger resistances of the normal-conducting domains that emerge after photon detection. This should result in larger signal amplitudes and a better signal-to-noise ratio. In addition, larger domain resistances are expected to reduce problems with latching [5], thus allowing for continuous photon-counting at larger reduced bias currents. Thirdly, a 100 nm thick TaN film has an effective superconducting penetration depth large enough to guarantee for a homogeneous current distribution even in several μm-wide conduction paths, which is essential for a good device detection efficiency (DDE). However, the energy-dependence of the signal amplitude distribution as we observed it in the Nb X-SNSPD [1] is expected to be reduced by the larger domain resistances. In order to partially regain this energy-dependence with smaller domain resistances, we also fabricated and examined a TaN X-SNSPD with very wide conduction paths.

In this paper we report on experiments with TaN X-SNSPDs with an improved detector performance as compared to Nb X-SNSPDs regarding DDE, latching and pulse amplitudes. The energy-dependence of the signal amplitude in the keV-range is weak for ≈250 nm wide TaN conduction paths, but it is pronounced for $\approx 1.6\ \mu$m wide paths.

II. DEVICE FABRICATION

A tantalum nitride film of thickness $d \approx 100$ nm was grown at $T = 700\ ^\circ$C by DC reactive magnetron sputtering in an Ar/N$_2$ atmosphere on an R-plane cut sapphire substrate. The as-grown film showed a critical temperature $T_c = 8.0$ K and a resistivity of $\rho_{\mathrm{TaN}}(10.3\ \mathrm{K}) \approx 500\ \mu\Omega$cm, which is two orders of magnitude larger than for a 100 nm thick Nb film [1] with $\rho_{\mathrm{Nb}}(10\ \mathrm{K}) \approx 4\ \mu\Omega$cm right above T_c. Two different X-SNSPDs were fabricated using electron-beam lithography using ZEP520A resist and reactive ion etching [6]. Fig. 1 shows an optical image of both detectors with the most relevant properties summarized in Table I. Detector TaN-A has a uniform conduction path width w of ≈250 nm and a filling factor of 35%.

Manuscript received October 5, 2012; accepted December 12, 2012. Date of publication December 20, 2012; date of current version January 23, 2013. This work was supported by the Swiss National Science Foundation Grant 200021_135504/1.

The authors are with the Physics Institute, University of Zurich, 8057 Zurich, Switzerland (e-mail: kevin.inderbitzin@physik.uzh.ch).

Color versions of one or more of the figures in this paper are available online at http://ieeexplore.ieee.org.

Digital Object Identifier 10.1109/TASC.2012.2234496

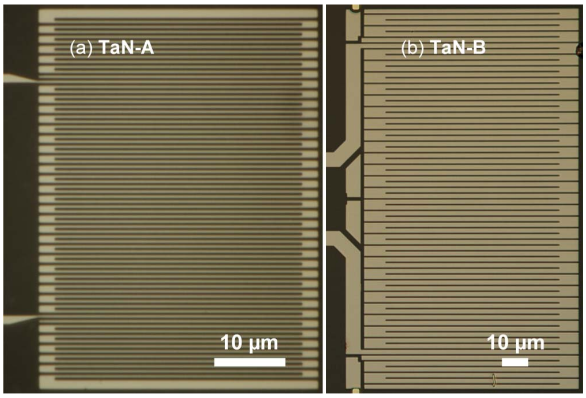

Fig. 1. Optical images of the examined X-SNSPDs from 100-nm-thick TaN: (a) Detector TaN-A with a conduction path width of ≈250 nm and a filling factor ≈35%. (b) Detector TaN-B has a much wider conduction path width ≈ 1.6 μm and a filling factor ≈75%. The large effective penetration depth λ_{eff} ensures a homogeneous current distribution in these conduction paths.

TABLE I
RELEVANT DETECTOR PROPERTIES

Detector property	Detector TaN-A	Detector TaN-B
Conduction path width w	≈ 250 nm	≈ 1.6 µm
Conduction path length l	1.67 mm	3.59 mm
Active detector area	35 x 33 μm^2	75 x 119 μm^2
Filling factor	≈ 35%	≈ 75%
Critical temperature T_c	6.7 K	7.0 K
Critical current I_c	105 µA (1.85 K)	860 µA (1.85 K) 430 µA (4 K) 155 µA (5 K)
Calculated kinetic inductance L_{kin}	180 nH	50 nH
Latching bias current (1.85 K, V_A = 49.9 kV)	> 52% I_c	> 32% I_c
Pulse rise time T_R	750 ps ± 60 ps	910 ps ± 120 ps

After fabrication, it showed a critical temperature $T_c = 6.7$ K. Detector TaN-B has a much wider conduction-path width of ≈ 1.6 μm, resulting in a higher filling factor of 75%. Its critical temperature is slightly higher than for detector TaN-A, with $T_c = 7.0$ K.

These detector geometries ensure that the kinetic inductances are small enough for ultrafast recovery times [1], [7], and are at the same time large enough to reduce problems with latching as observed in [1], [8]. In the dirty limit, the bulk penetration depth can be calculated [9] from T_c and the normal-state resistivity ρ_N to $\lambda_{\text{bulk}} \approx 0.9 - 1.0$ μm for $T = 1.85$ K, and $\lambda_{\text{bulk}} \approx 1.2 - 1.4$ μm for $T = 5$ K if its temperature dependence is considered [9]. As $d \ll \lambda_{\text{bulk}}$, the effective penetration depth can be determined [10] from $\lambda_{\text{eff}} = 2\lambda^2_{\text{bulk}}/d \approx 17{-}22$ μm at $T =$ 1.85 K, which ensures a homogeneous current distribution in both detectors. The kinetic inductances can be determined [11] to $L_{\text{kin}} = \mu_0 \lambda_{\text{eff}} l/w \approx 180$ nH and 50 nH for detector TaN-A and TaN-B, respectively.

III. EXPERIMENTAL SETUP

The experimental setup is identical to the one used for the characterization of the Nb X-SNSPD in [1]. Only one detector was characterized at a time. The detector signal was transmitted through a 50 Ω impedance signal line to a cryogenic amplifier at the 4 K-stage, and then further to a second amplifier at room temperature before fed into a 3.5 GHz digital oscilloscope. The amplifier chain had an effective bandwidth of about 40 MHz to 1.9 GHz. A quasi-constant-current bias [12] was applied and was passed through a series of low-pass filters.

The detectors were irradiated with X-ray photons through a 100 μm thin window of polyimide (Kapton) at the cryostat. A second window of 1 μm thin aluminum was installed at the 4 K-heat shield to minimize thermal radiation. Two qualitatively different X-ray sources were used: a tungsten-target X-ray tube with a maximum acceleration voltage $V_A =$ 49.9 kV, and a radioactive Fe-55 isotope source with an activity of 3.7 GBq, which emits photons with well defined energies around 6 keV. The homogeneous irradiation of the X-SNSPD by both sources was ensured.

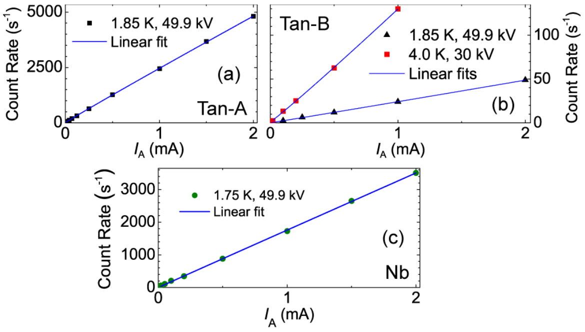

Fig. 2. Photon count rates as functions of I_A of the detectors (a) TaN-A and (b) TaN-B, and (c) the Nb X-SNSPD from [1], showing a linear dependence and therefore demonstrating single-photon detection.

IV. EXPERIMENTAL RESULTS AND DISCUSSION

A. Voltage Signal

Upon X-ray irradiation we recorded voltage signal pulses with a shape qualitatively very similar to the pulse shapes recorded for the Nb X-SNSPD in [1] and the TaN thin-film SNSPD in [13]. The rise time T_R, defined as the time span between 10% and 90% of the signal maximum, was determined to be 750 ps ± 60 ps and 910 ps ± 120 ps for detector TaN-A and TaN-B, respectively. This is significantly longer than reported for the Nb X-SNSPD (i.e. 250 ps ± 70 ps), which we explain with the larger kinetic inductances of the TaN detectors. The pulse fall time is on the order of 10 ns for both detectors.

B. Single-Photon Detection

Fig. 2 shows the count-rate dependences on the X-ray photon flux (which was varied by the X-ray tube anode current I_A) at $V_A = 49.9$ kV for the detectors TaN-A, TaN-B and the Nb X-SNSPD [1]. For detector TaN-B, measurements at $T = 4.0$ K are also shown. These dependences show a linear behavior, and we therefore conclude that these X-SNSPDs detect in single-photon mode [2].

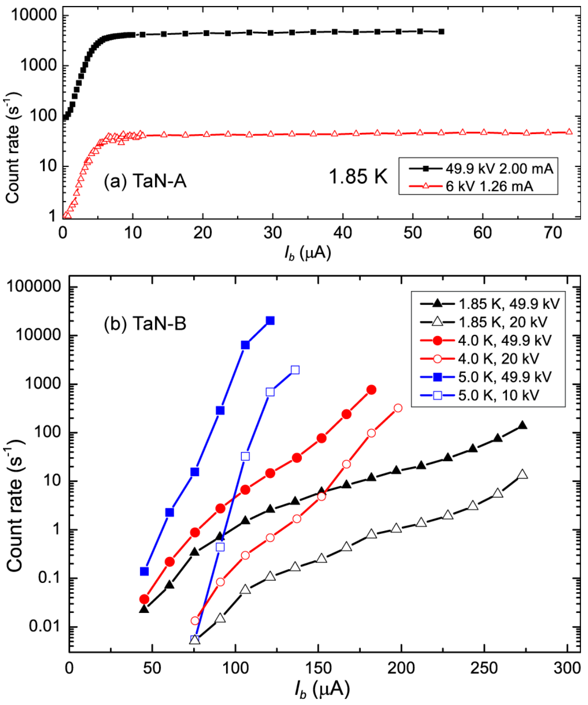

Fig. 3. Bias-current dependence of the photon count rate for different acceleration voltages, for the detectors (a) TaN-A and (b) TaN-B. For detector TaN-B, we show measurements at different temperatures.

C. Latching

The critical currents at 1.85 K were determined to $I_c =$ 105 μA and 860 μA for detector TaN-A and TaN-B, respectively (Table I also gives the values for 4.0 K and 5.0 K for detector TaN-B). Fig. 3 shows the bias current-dependence of the count rate at $V_A = 49.9$ kV at $T = 1.85$ K for detector TaN-A and TaN-B. They latch for reduced bias currents $I_\mathrm{b}/I_\mathrm{c} > 52\%$ and $> 32\%$, respectively, which means that the devices cannot be continuously used for X-ray photon detection above these currents [5]. In these X-SNSPDs, latching occurs for much higher reduced bias currents than previously reported for the Nb X-SNSPD [1], where latching was observed for $I_\mathrm{b}/I_\mathrm{c} > 5.5\%$. This improvement can be attributed to the larger domain resistances in the TaN X-SNSPDs and possibly the higher kinetic inductances. For the same reasons, detector TaN-B latches for lower reduced bias currents than detector TaN-A, as its wider conduction paths lead to lower domain resistances, and its kinetic inductance is also lower.

D. Hot-Spot Model

A hot-spot model used by [1], [14], [15] can be used to estimate the hot-spot radius after X-ray photon absorption. It is assumed that the primary excitations of low keV-photons are created in a small volume centered at the absorption point of the photon, thereby creating a hot-spot resembling a sphere in which superconductivity is destroyed. The bias current is therefore forced to flow in a smaller cross-section where it can exceed I_c for large enough bias currents, which leads to the formation of a normal-conducting domain. By using the density-of-states at the Fermi-energy in TaN from [13] to determine the electronic specific heat, the hot-spot radius at $T = 1.85$ K for a 6 keV and a 50 keV photon can be estimated to 180–190 nm and 370–380 nm (according to [1]), respectively. In this model, the hot-spot radius increases only slightly when increasing the temperature to $T = 5$ K, namely to 210 nm and 420 nm for 6 keV and 50 keV photons, respectively, assuming $T_c \approx 7$ K.

E. Bias-Current Dependence

Fig. 3(a) shows a plateau in the bias-dependent count rate for detector TaN-A down to $I_b < 7$ μA $\approx 7\%$ I_c, which can be explained with the fact that the calculated hot-spot diameter for a 6 keV photon is larger than the conduction path width, and therefore a hot-spot is expected to cover the whole cross-section, independent of the bias current. Hence the decrease of the count rate for $I_b < 7\%$ I_c is not necessarily due to a small hot-spot radius for low-keV photons, but it might be attributed to a decreasing signal amplitude with a smaller bias current, while the trigger level is kept constant.

For detector TaN-B there is no plateau in the count rate dependence on I_b (shown in Fig. 3(b) for different temperatures and acceleration voltages). This is in agreement with the expectations from the hot-spot model: as the hot-spot diameter is smaller than the conduction path width even for 50 keV photons, a bias current above a non-zero threshold [14] must be applied in order to detect photons efficiently. It has been demonstrated that this bias threshold can depend on the energy of detected β-particles [16] and keV ions [15] and also on the operation temperature [16]. At $T = 1.85$ K, however, we expect that the energy-dependent bias thresholds are larger than 460 μA (assuming a cylindrical hot-spot [14]), which is already in the latching regime. This explains why the count rates at $T = 1.85$ K remain low even for high X-ray intensities (detector TaN-A shows $> 4 \cdot 10^3$ cps at the same tube settings).

The X-ray tube emits photons with a continuous background in the spectrum. Because the bias threshold depends on the photon energy, the count rate increases continuously with the bias current. The exact form of this increase depends on the details of the tube spectrum. As the high-energy part of the spectrum is reduced for low V_A, the count rate builds up slower with I_b for lower V_A and cannot just be scaled with a constant factor [shown with filled and empty symbols in Fig. 3(b)].

Measurements at higher temperatures (4–5 K) show that the count rate increases more steeply with I_b, and count rates up to $\approx 2 \cdot 10^4$ s^{-1} are observed at $T = 5$ K. The increase of the count rate with temperature can be attributed to the temperature-dependence of the bias threshold, which is reduced at higher temperatures. Using the hot-spot model, a threshold of more than 220 μA (for 50 keV) can be calculated [14] for $T = 4$ K, which is right above the latching limit and might explain the elevated count rates at this temperature. At $T = 5$ K, the corresponding thresholds are calculated to 110 μA and 70 μA for 6 keV and 50 keV photons, respectively, which is within the measurable bias region and which therefore explains the steep increase of the count rate with increasing I_b.

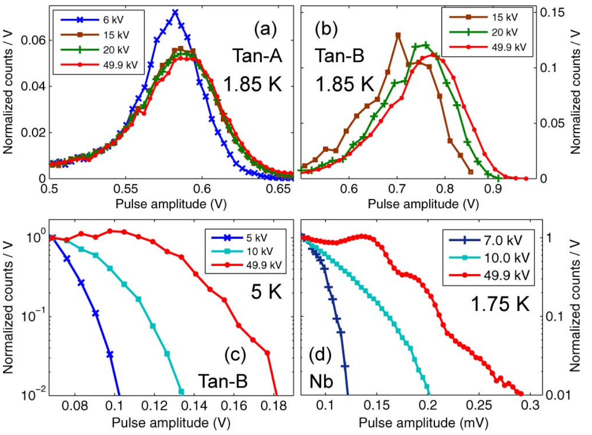

Fig. 4. Pulse-amplitude histograms for different V_A for the detectors (a) TaN-A (at $T = 1.85$ K and $I_b = 54$ μA) and (b) TaN-B (at $T = 1.85$ K and $I_b = 243$ μA), normalized to the total number of counts. We also show a comparison for (c) TaN-B (at $T = 5$ K and $I_b = 121$ μA) and (d) the Nb X-SNSPD from [1] (at $T = 1.75$ K and $I_b = 0.61$ mA), here normalized relative to the counts at an amplitude of 69 mV and 79 mV, respectively.

Note that detector TaN-B covers a significantly larger area than detector TaN-A, and a theoretical maximum count rate of $\approx 6 \cdot 10^4$ s^{-1} can be estimated for a non-latching X-SNSPD of the size of detector TaN-B with the same film properties.

F. Dark-Count Rate Measurements

Despite latching at photon detection for high bias currents, we performed measurements on possible dark counts for $I_\mathrm{b}/I_\mathrm{c} \approx 92\%$ and $\approx 98\%$ at $T = 1.85$ K for the detectors TaN-A and TaN-B, respectively. No dark counts were recorded during more than 30 min measurement time, thereby limiting the dark-count rate to $< 5 \times 10^{-4}$ s^{-1}. As explained in [1], negligible dark-count rates can be theoretically expected in principle for X-SNSPDs.

G. Pulse Amplitudes

In Fig. 4(a) and (b) we plotted pulse-amplitude histograms for detector TaN-A (at $I_b = 54$ μA) and TaN-B (at $I_b = 243$ μA) for $T = 1.85$ K, respectively, normalized with respect to the total number of counts. The amplitudes are much larger than for the Nb X-SNSPD [1] at $I_b = 0.61$ mA shown in Fig. 4(d) despite the smaller bias currents used, which is expected from the larger domain resistances. This magnitude of the amplitudes therefore allows for the recording of all detection pulses at $T = 1.85$ K, and no pulses had to be cut off to eliminate noise signals.

However, for detector TaN-A, the expected large domain resistances must also lead to a reduction of the amplitude dependence on the photon energy spectrum as compared to the Nb X-SNSPD, because the pulse amplitude can only be significantly varied for domain resistances of the order of 50 Ω or smaller [1]. A weak amplitude dependence is visible only between $V_A = 6$ kV and 15 kV for this detector. This is in qualitative agreement with the reported 1–9 keV argon ion detection by a 10 nm thick and 800 nm wide NbN detector with comparable typical domain resistances [17], where no energy-dependence in the amplitude distribution was found.

Detector TaN-B shows larger amplitudes than TaN-A despite its smaller domain resistances, which is a consequence of the larger applied bias current. Furthermore, the amplitude distribution shows a stronger dependence on the photon energy spectrum than for detector TaN-A, as the domain resistances must be smaller. Below $V_A = 15$ kV and at $T = 1.85$ K, the count rate is very small. However, as already shown in Fig. 3(b), it increases significantly at higher temperatures, and at $T = 5$ K measurable count rates are achieved even for $V_A = 5$ kV as shown in Fig. 4(c), as low-energy photons become detectable. However, the bias current needs to be reduced due to a lower critical current, and therefore certain pulses escape detection, as the discriminator level is set above the noise level. We faced the same problem for the Nb X-SNSPD [1] [see Fig. 4(d)], and we therefore normalized Fig. 4(c) and (d) with respect to the counts of a bin right above the noise level. At $T = 5$ K, TaN-B shows a pronounced energy dependence of the amplitude distribution which is qualitatively very similar to that of the Nb X-SNSPD, where the amplitude distribution broadens along with a broader photon energy spectrum.

H. Device Detection Efficiency

Using the Fe-55 X-ray source, we determined the DDE of detector TaN-A for 5.9 keV photons to 1.4%. Considering the absorptance [18], geometry and filling factor of the superconducting meander, a maximum DDE of 1.9% could in principle be achieved if all photons absorbed in the superconducting meander were counted. To achieve this value in the present detectors is not realistic, however, due to the nature of the energy-diffusion mechanisms involved [1].

V. CONCLUSION

In conclusion, our results show that 100 nm thick TaN X-SNSPDs offer an improved detector performance as compared to 100 nm Nb X-SNSPDs concerning DDE, latching and pulse amplitudes. Ultrafast dark count-free soft X-ray single-photon detection is observed. Wide conduction paths allow for a certain energy-resolving capability in contrast to narrow conduction paths. We expect that X-SNSPDs from thicker TaN films should provide an even larger DDE. The latching tendency might be further reduced by a recently proposed biasing scheme [19].

REFERENCES

[1] K. Inderbitzin, A. Engel, A. Schilling, K. Il'in, and M. Siegel, "An ultrafast superconducting Nb nanowire single-photon detector for soft X-rays," *Appl. Phys. Lett.*, vol. 101, p. 162601, Oct. 2012.

[2] G. N. Gol'tsman, O. Okunev, G. Chulkova, A. Lipatov, A. Semenov, K. Smirnov, B. Voronov, A. Dzardanov, C. Williams, and R. Sobolewski, "Picosecond superconducting single-photon optical detector," *Appl. Phys. Lett.*, vol. 79, pp. 705–707, Aug. 2001.

[3] K. Suzuki, S. Miki, Z. Wang, Y. Kobayashi, S. Shiki, and M. Ohkubo, "Superconducting NbN thin-film nanowire detectors for time-of-flight mass spectrometry," *J. Low Temp. Phys.*, vol. 151, pp. 766–770, Jan. 2008.

[4] D. Perez de Lara, M. Ejrnaes, A. Casaburi, M. Lisitskiy, R. Cristiano, S. Pagano, A. Gaggero, R. Leoni, G. Golt'sman, and B. Voronov, "Feasibility investigation of NbN nanowires as detector in time-of-flight mass

spectrometers for macromolecules of interest in biology (Proteins)," *J. Low Temp. Phys.*, vol. 151, pp. 771–776, Jan. 2008.

[5] A. J. Kerman, J. K. W. Yang, R. J. Molnar, E. A. Dauler, and K. K. Berggren, "Electrothermal feedback in superconducting nanowire single-photon detectors," *Phys. Rev. B*, vol. 79, p. 100509(R), Mar. 2009.

[6] H. Bartolf, K. Inderbitzin, L. B. Gómez, A. Engel, and A. Schilling, "Nanoscale fabrication by intrinsic suppression of proximity-electron exposures and general considerations for easy and effective top-down fabrication," *J. Micromech. Microeng.*, vol. 20, p. 125015, Aug. 2010.

[7] A. J. Kerman, E. A. Dauler, W. E. Keichler, J. K. W. Yang, K. K. Berggren, G. Gol'tsman, and B. Voronov, "Kinetic-inductance-limited reset time of superconducting nanowire photon counters," *Appl. Phys. Lett.*, vol. 88, p. 111116, Mar. 2006.

[8] B. V. Estey, J. A. Beall, G. C. Hilton, K. D. Irwin, D. R. Schmidt, J. N. Ullom, and R. E. Schwall, "Time-of-flight mass spectrometry with latching Nb meander detectors," *IEEE Trans. Appl. Supercond.*, vol. 19, pp. 382–385, Jun. 2009.

[9] M. Tinkham, *Introduction to Superconductivity,* 2nd ed. New York: McGraw-Hill, 1996.

[10] J. Pearl, "Current distribution in superconducting films carrying quantized fluxoids," *Appl. Phys. Lett.*, vol. 5, p. 65, Aug. 1964.

[11] R. H. Hadfield, A. J. Miller, S. W. Nam, R. L. Kautz, and R. E. Schwall, "Low-frequency phase locking in high-inductance superconducting nanowires," *Appl. Phys. Lett.*, vol. 87, p. 203505, Nov. 2005.

[12] D.-K. Liu, S.-J. Chen, L.-X. You, Y.-L. Wang, S. Miki, Z. Wang, X.-M. Xie, and M.-H. Jiang, "Nonlatching superconducting nanowire single-photon detection with quasi-constant-voltage bias," *Appl. Phys. Exp.*, vol. 5, p. 125202, Nov. 2012.

[13] A. Engel, A. Aeschbacher, K. Inderbitzin, A. Schilling, K. Il'in, M. Hofherr, M. Siegel, A. Semenov, and H.-W. Hübers, "Tantalum nitride superconducting single-photon detectors with low cut-off energy," *Appl. Phys. Lett.*, vol. 100, p. 062601, Feb. 2012.

[14] A. Gabutti, R. G. Wagner, K. E. Gray, R. T. Kampwirth, and R. H. Ono, "Superconducting detector for minimum ionizing particles," *Nucl. Instrum. Methods Phys. Res. A, Accel. Spectrom. Detect. Assoc. Equip.*, vol. A278, pp. 425–430, Dec. 1989.

[15] K. Suzuki, S. Shiki, M. Ukibe, M. Koike, S. Miki, Z. Wang, and M. Ohkubo, "Hot-spot detection model in superconducting nano-stripline detector for keV ions," *Appl. Phys. Exp.*, vol. 4, p. 083101, Jul. 2011.

[16] A. Gabutti, K. E. Gray, R. G. Wagner, and R. H. Ono, "Granular-aluminum superconducting detector for 6 keV X-rays and 2.2 MeV beta sources," *Nucl. Instrum. Methods Phys. Res. A, Accel. Spectrom. Detect. Assoc. Equip.*, vol. A289, pp. 274–282, 1990.

[17] K. Suzuki, M. Ukibe, S. Shiki, S. Miki, Z. Wang, Y. Takahashi, N. Yoshikawa, and M. Ohkubo, "Pulse-height distribution analysis for superconducting nano-stripline ion detector with a fast pulse-integration analog-to-digital converter," *Phys. Proc.*, vol. 36, pp. 172–176, 2012.

[18] B. L. Henke, E. M. Gullikson, and J. C. Davis, "X-ray interactions: Photoabsorption, scattering, transmission, and reflection at $E =$ 50–30 000 eV, $Z = 1-92$," *At. Data Nucl. Data Tables*, vol. 54, no. 2, pp. 181–342, Jul. 1993.

[19] A. J. Annunziata, O. Quaranta, D. F. Santavicca, A. Casaburi, L. Frunzio, M. Ejrnaes, M. J. Rooks, R. Cristiano, S. Pagano, A. Frydman, and D. E. Prober, "Reset dynamics and latching in niobium superconducting nanowire single-photon detectors," *J. Appl. Phys.*, vol. 108, p. 084507, Oct. 2010.

Conclusions and Outlook

During this thesis, (X-)SNSPDs were fabricated from three different types of superconducting films, namely from

- 6 nm thin NbN,
- 100 nm thick Nb,
- and 100 nm thick TaN,

which we then studied regarding their X-ray photon detection capability.

The experiments with the SNSPD from 6 nm thin NbN support the previously reported finding by Perez de Lara *et al.* [75] that soft X-ray photon detection in these thin-film detectors mostly occurs through photon absorption in the sapphire substrate and the successive energy diffusion to the superconducting meander structure. The X-ray device detection efficiency with such a thin-film detector is larger than with the 100 nm thick superconducting films, as the thickness of the substrate allows for a better photon absorption in the substrate than in the meander structures.

Our results show that ultrafast dark count-free X-SNSPDs from 100 nm thick niobium can be fabricated which can operate in a large spectral range. Using a hot-spot model, the X-ray photon detection capability at very low reduced bias currents can be explained. The small resistance of the normal conducting domains in these thick Nb film detectors leads to significant variations in the pulse amplitude, which is susceptible to the photon energy spectrum. We estimate that an energy resolution better than 1.5 keV is realized in the energy range $\approx 8 - 10$ keV. However, further experiments with optimized X-SNSPDs will be necessary to verify these results. The kinetic inductance of Nb X-SNSPDs has to be carefully chosen by proper design, in order to reduce the tendency of the detector to latch due to the small domain resistances.

It was further demonstrated that 100 nm thick TaN X-SNSPDs offer an improved detector performance as compared to equally thick Nb X-SNSPDs concerning device detection efficiency, latching and pulse amplitudes, and we also observed ultrafast dark count-free X-ray single-photon detection in these detectors. Wide TaN nanowires also allow for a certain energy-resolving capability in contrast to narrow TaN nanowires.

However, wide nanowires in TaN X-SNSPDs also limit the device detection efficiency at low temperatures, which can be explained within a hot-spot model. Interestingly, this trend in the temperature dependence of the cut-off energy is the opposite to the trend observed for optical photon detection in a thin-film TaN SNSPD, where the cut-off energy decreases for lower temperature. This discrepancy is explained by the immediate formation of a normal-conducting hot-spot after photon absorption in the case of keV-photons, in contrast to the absorption of optical photons in the eV-range, where the quasiparticle diffusion coefficient is influencing the detectability of photons. Thus, the temperature dependence of the diffusion coefficient is relevant in the case of near-IR and optical photon detection, but not in the case of keV-photon detection.

In general, the latching tendency of the X-SNSPDs might be further reduced by a recently presented biasing scheme by Liu *et al.* [128]. An increase of the device detection efficiency for X-SNSPDs might be achieved by additional fabrication steps (e.g. by stacking of several active superconducting layers as previously suggested for SNSPDs [129]), or, in the case of TaN X-SNSPD, by using thicker TaN films.

Our experiments have shown that X-SNSPDs with X-ray photon count rates in the $10^8 - 10^9$ counts/s range, sub-100 ps jitter and a certain energy-resolvability might be feasible. Such high count rates would make these detectors faster than single-photon avalanche photodiodes (and transition edge sensors). Experiments at a synchrotron X-ray facility could shed light on these open questions, as it would offer access to monochromatic X-ray radiation at high intensities. Such experiments would show if the above mentioned very high photon count rates can be achieved without heating of the X-SNSPDs above their superconducting critical temperature T_c by X-ray photon absorption. An improved device detection efficiency would also help reducing the effect of this speculative issue. Synchrotron radiation is pulsed with pulse lengths down to tens of Picoseconds, which would allow the determination of the X-SNSPD jitter with an accuracy in this range. The monochromatic radiation would allow to directly study the dependence of the signal amplitude on the photon energy, and thus determine the energy resolution and its dependence on the X-SNSPD material and geometry. The excellent energy resolution of transition edge sensors will most probably be out of reach, however.

The exact role of the substrate in the detection processes of X-ray photons in thin- and thick-film (X-)SNSPDs still needs further clarification and experiments are planned with X-SNSPDs on top of stress-free SiN-membranes on Si substrates. An X-SNSPD could be fabricated on top of a substrate section, where the SiN-membrane is freely suspended from the Si substrate. By varying the SiN and superconductor thickness, the influence of the substrate on the detection capabilities of the X-SNSPD could then be examined.

In terms of X-SNSPD performance optimization, a quantity to examine for optimization potential is the detector thickness, which was kept to 100 nm in the examined X-SNSPDs in this thesis. A thicker superconducting structure could not only increase the device detection efficiency, but could also increase the energy fraction of an absorbed photon deposited inside the structure, which could improve the energy resolution of the X-SNSPDs. Therefore, as a possible next step, the author suggests to fabricate X-SNSPDs from e.g. 200 nm thick TaN films with a nanowire width of the order of magnitude of the hot-spot diameter for 6 keV photons estimated in this thesis, i.e. ≈ 600 nm. Characterization should also take place at various temperatures below T_c, which was shown to influence the device detection efficiency for certain X-SNSPD geometries. For 200 nm thick X-SNSPDs, latching is expected to play a more important role. In this thesis, however, X-SNSPDs were shown to detect X-ray photons for low reduced bias currents as well, in contrast to thin-film SNSPDs, which helps to avoid problems with latching.

Bibliography

[1] G. N. Gol'tsman, O. Okunev, G. Chulkova, A. Lipatov, A. Semenov, K. Smirnov, B. Voronov, A. Dzardanov, C. Williams, and R. Sobolewski, "Picosecond superconducting single-photon optical detector," *Appl. Phys. Lett.*, vol. 79, p. 705, 2001.

[2] N. K. Sherman, "Superconducting nuclear particle detector," *Phys. Rev. Lett.*, vol. 8, p. 438, 1962.

[3] D. E. Spiel, R. W. Boom, and J. E. C. Crittenden, "Thermal spikes in superconducting thin films of Sn and In," *Appl. Phys. Lett.*, vol. 7, p. 292, 1965.

[4] A. Gabutti, R. G. Wagner, K. E. Gray, R. T. Kampwirth, and R. H. Ono, "Superconducting detector for minimum ionizing particles," *Nucl. Instrum. Methods A*, vol. 278, p. 425, 1989.

[5] A. Gabutti, K. E. Gray, R. G. Wagner, and R. H. Ono, "Granular-aluminium superconducting detector for 6 keV X-rays and 2.2 MeV beta sources," *Nucl. Instrum. Methods A*, vol. 289, p. 274, 1990.

[6] B. Baek, A. E. Lita, V. Verma, and S. W. Nam, "Superconducting a-$W_x Si_{1-x}$ nanowire single-photon detector with saturated internal quantum efficiency from visible to 1850 nm," *Appl. Phys. Lett.*, vol. 98, p. 251105, 2011.

[7] A. Aeschbacher, "Superconducting nanowire single-photon detectors based on TaN thin films," Master's thesis, University of Zürich, October 2011.

[8] C. M. Natarajan, M. G. Tanner, and R. H. Hadfield, "Superconducting nanowire single-photon detectors: physics and applications," *Supercond. Sci. Technol.*, vol. 25, p. 063001, 2012.

[9] J. Stefan, "Über die Beziehung zwischen der Wärmestrahlung und der Temperatur," *Sitzungsberichte der mathematisch-naturwissenschaftlichen Classe der kaiserlichen Akademie der Wissenschaften*, vol. 79, p. 391, 1879.

[10] L. Boltzmann, “Ableitung des Stefan’schen Gesetzes, betreffend die Abhängigkeit der Wärmestrahlung von der Temperatur aus der electromagnetischen Lichttheorie,” *Annalen der Physik und Chemie*, vol. 22, p. 291, 1884.

[11] U. S. Pracht, E. Heintze, C. Clauss, D. Hafner, R. Bek, S. Gelhorn, D. Werner, M. Scheffler, M. Dressel, D. Sherman, B. Gorshunov, K. S. Il’in, D. Henrich, and M. Siegel, “Electrodynamics of the superconducting state in ultra-thin films at THz frequencies,” *submitted to IEEE Transactions on THz Science and Technology*, 2013.

[12] R. C. Weast and M. J. Astle, eds., *CRC Handbook of chemistry and physics.* CRC Press, Boca Raton FL, 61st ed., 1980.

[13] M. Tinkham, *Introduction to superconductivity.* McGraw-Hill, New York NY, 2nd ed., 1996.

[14] V. Novotny and P. P. M. Meincke, “Single superconducting energy gap in pure niobium,” *J. Low Temp. Phys.*, vol. 18, p. 147, 1975.

[15] H. F. Braun, D. W. Capone II, R. Flükiger, A. L. Giorgi, D. Gubser, F. Hulliger, J. L. Jorda, H. Khan, G. Kieselmann, R. N. Shelton, J. Sosnowski, T. Wolf, J.-Q. Xu, and D. Yu, *Landolt-Börnstein: Numerical Data and Functional Relationships in Science and Technology - Group III: Crystal and Solid State Physics - Volume 21: Superconductors (Editors: R. Flükiger and W. Klose).* Springer, Berlin, 1990.

[16] R. Romestain, B. Delaet, P. Renaud-Goud, I. Wang, C. Jorel, J.-C. Villegier, and J.-P.. Poizat, “Fabrication of a superconducting niobium nitride hot electron bolometer for single-photon counting,” *New J. Phys.*, vol. 6, p. 129, 2004.

[17] A. Carrington and F. Manzano, “Magnetic penetration depth of MgB_2,” *Physica C*, vol. 385, p. 205, 2003.

[18] H. Padamsee, J. E. Neighbor, and C. A. Shiffman, “Quasiparticle phenomenology for thermodynamics of strong-coupling superconductors,” *J. Low Temp. Phys.*, vol. 12, p. 387, 1973.

[19] C. P. Bean and J. D. Livingston, “Surface barrier in type-II superconductors,” *Phys. Rev. Lett.*, vol. 12, p. 14, 1964.

[20] L. N. Bulaevskii, M. J. Graf, C. D. Batista, and V. G. Kogan, “Vortex-induced dissipation in narrow current-biased thin-film superconducting strips,” *Phys. Rev. B*, vol. 83, p. 144526, 2011.

[21] L. N. Bulaevskii, M. J. Graf, and V. G. Kogan, "Vortex-assisted photon counts and their magnetic field dependence in single-photon superconducting detectors," *Phys. Rev. B*, vol. 85, p. 014505, 2012.

[22] J. R. Clem and K. K. Berggren, "Geometry-dependent critical currents in superconducting nanocircuits," *Phys. Rev. B*, vol. 84, p. 174510, 2011.

[23] D. Henrich, P. Reichensperger, M. Hofherr, J. M. Meckbach, K. Il'in, M. Siegel, A. Semenov, A. Zotova, and D. Y. Vodolazov, "Geometry-induced reduction of the critical current in superconducting nanowires," *Phys. Rev. B*, vol. 86, p. 144504, 2012.

[24] H. L. Hortensius, E. F. C. Driessen, T. M. Klapwijk, K. K. Berggren, and J. R. Clem, "Critical-current reduction in thin superconducting wires due to current crowding," *Appl. Phys. Lett.*, vol. 100, p. 182602, 2012.

[25] A. J. Kerman, E. A. Dauler, J. K. W. Yang, K. M. Rosfjord, V. Anant, K. K. Berggren, G. N. Gol'tsman, and B. M. Voronov, "Constriction-limited detection efficiency of superconducting nanowire single-photon detectors," *Appl. Phys. Lett.*, vol. 90, p. 101110, 2007.

[26] J. Bardeen, L. N. Cooper, and J. R. Schrieffer, "Theory of superconductivity," *Phys. Rev.*, vol. 108, p. 1175, 1957.

[27] W. Buckel and R. Kleiner, *Supraleitung - Grundlagen und Anwendungen.* Wiley-VCH, Weinheim, 6th ed., 2004.

[28] A. Einstein, "On the theory of the Brownian movement," *Ann. d. Phys.*, vol. 19, p. 371, 1906.

[29] M. Smoluchowski, "Zur kinetischen Theorie der Brownschen Molekularbewegung und der Suspensionen," *Ann. d. Phys.*, vol. 21, p. 756, 1906.

[30] F. London and H. London, "The electromagnetic equations of the supraconductor," *Proc. Roy. Soc. (London)*, vol. A149, p. 71, 1935.

[31] T. P. Orlando, J. E. J. McNiff, S. Foner, and M. R. Beasley, "Critical fields, Pauli paramagnetic limiting, and material parameters of Nb_3Sn and V_3Si," *Phys. Rev. B*, vol. 19, p. 4545, 1979.

[32] H. Bartolf, *Fabrication and characterization of superconducting nanowire highspeed single-photon detectors.* PhD thesis, University of Zürich, 2009.

[33] J. Pearl, "Current distribution in superconducting films carrying quantized fluxoids," *Appl. Phys. Lett.*, vol. 5, p. 65, 1964.

[34] A. Casaburi, N. Zen, K. Suzuki, M. Ejrnaes, S. Pagano, R. Cristiano, and M. Ohkubo, "Subnanosecond time response of large-area superconducting stripline detectors for keV molecular ions," *Appl. Phys. Lett.*, vol. 94, p. 212502, 2009.

[35] N. Zen, A. Casaburi, S. Shiki, K. Suzuki, M. Ejrnaes, R. Cristiano, and M. Ohkubo, "1 mm ultrafast superconducting stripline molecule detector," *Appl. Phys. Lett.*, vol. 95, p. 172508, 2009.

[36] R. H. Hadfield, A. J. Miller, S. W. Nam, R. L. Kautz, and R. E. Schwall, "Low-frequency phase locking in high-inductance superconducting nanowires," *Appl. Phys. Lett.*, vol. 87, p. 203505, 2005.

[37] P. Müller and A. V. Ustinov, *The physics of superconductors.* Springer, Berlin, 1st ed., 1997.

[38] A. Engel, A. Semenov, H.-W. Hübers, K. Il'in, and M. Siegel, *New frontiers in superconductivity research (Editor: Barry P. Martins).* Nova Science Publishers, Hauppauge NY, 1st ed., 2006.

[39] F. Marsili, F. Najafi, E. Dauler, F. Bellei, X. Hu, M. Csete, R. J. Molnar, and K. K. Berggren, "Single-photon detectors based on ultranarrow superconducting nanowires," *Nano Letters*, vol. 11, p. 2048, 2011.

[40] S. N. Dorenbos, P. Forn-Díaz, T. Fuse, A. H. Verbruggen, T. Zijlstra, T. M. Klapwijk, and V. Zwiller, "Low gap superconducting single photon detectors for infrared sensitivity," *Appl. Phys. Lett.*, vol. 98, p. 251102, 2011.

[41] A. Engel, A. Aeschbacher, K. Inderbitzin, A. Schilling, K. Il'in, M. Hofherr, M. Siegel, A. Semenov, and H.-W. Hübers, "Tantalum nitride superconducting single-photon detectors with low cut-off energy," *Appl. Phys. Lett.*, vol. 100, p. 062601, 2012.

[42] K. Il'in, M. Hofherr, D. Rall, M. Siegel, A. Semenov, A. Engel, K. Inderbitzin, A. Aeschbacher, and A. Schilling, "Ultra-thin TaN films for superconducting nanowire single-photon detectors," *J. Low Temp. Phys.*, vol. 167, p. 809, 2012.

[43] A. Engel, A. Semenov, H.-W. Hübers, K. Il'in, and M. Siegel, "Superconducting single-photon detector for the visible and infrared spectral range," *J. Mod. Optic*, vol. 51, p. 1459, 2004.

[44] A. D. Semenov, G. N. Gol'tsman, and A. A. Korneev, "Quantum detection by current carrying superconducting film," *Physica C*, vol. 351, p. 349, 2001.

[45] A. Semenov, A. Engel, H.-W. Hübers, K. Il'in, and M. Siegel, "Spectral cut-off in the efficiency of the resistive state formation caused by absorption of a single-photon in current-carrying superconducting nano-strips," *Eur. Phys. J. B*, vol. 47, p. 495, 2005.

[46] J. K. W. Yang, A. J. Kerman, E. A. Dauler, V. Anant, K. M. Rosfjord, and K. K. Berggren, "Modeling the electrical and thermal response of superconducting nanowire single-photon detectors," *IEEE Trans. Appl. Supercond.*, vol. 17, p. 581, 2007.

[47] A. D. Semenov, P. Haas, B. Günther, H.-W. Hübers, K. Il'in, M. Siegel, A. Kirste, J. Beyer, D. Drung, T. Schurig, and A. Smirnov, "An energy-resolving superconducting nanowire photon counter," *Supercond. Sci. Technol.*, vol. 20, p. 919, 2007.

[48] J. A. O'Connor, M. G. Tanner, C. M. Natarajan, G. S. Buller, R. J. Warburton, S. Miki, Z. Wang, S. W. Nam, and R. H. Hadfield, "Spatial dependence of output pulse delay in a niobium nitride nanowire superconducting single-photon detector," *Appl. Phys. Lett.*, vol. 98, p. 201116, 2011.

[49] L. Maingault, M. Tarkhov, I. Florya, A. Semenov, R. E. de Lamaëstre, P. Cavalier, G. Gol'tsman, J.-P. Poizat, and J.-C. Villégier, "Spectral dependency of superconducting single photon detectors," *J. Appl. Phys.*, vol. 107, p. 116103, 2010.

[50] A. Engel, K. Inderbitzin, A. Schilling, R. Lusche, A. Semenov, H.-W. Hübers, D. Henrich, M. Hofherr, K. Il'in, and M. Siegel, "Temperature-dependence of detection efficiency in NbN and TaN SNSPD," *IEEE Trans. Appl. Supercond.*, vol. 23, p. 2300505, 2013.

[51] A. Semenov, B. Günther, U. Böttger, H.-W. Hübers, H. Bartolf, A. Engel, A. Schilling, K. Il'in, M. Siegel, R. Schneider, D. Gerthsen, and N. A. Gippius, "Optical and transport properties of ultrathin NbN films and nanostructures," *Phys. Rev. B*, vol. 80, p. 054510, 2009.

[52] V. Anant, A. J. Kerman, E. A. Dauler, J. K. W. Yang, K. M. Rosfjord, and K. K. Berggren, "Optical properties of superconducting nanowire single-photon detectors," *Optics Express*, vol. 16, p. 10750, 2008.

[53] S. N. Dorenbos, E. M. Reiger, N. Akopian, U. Perinetti, V. Zwiller, T. Zijlstra, and T. M. Klapwijk, "Superconducting single photon detectors with minimized polarization dependence," *Appl. Phys. Lett.*, vol. 93, p. 161102, 2008.

[54] J. K. W. Yang, A. J. Kerman, E. A. Dauler, B. Cord, V. Anant, R. J. Molnar, and K. K. Berggren, "Suppressed critical current in superconducting nanowire single-photon detectors with high fill-factors," *IEEE Trans. Appl. Supercond.*, vol. 19, p. 318, 2009.

[55] R. H. Hadfield, P. A. Dalgarno, J. A. O'Connor, E. Ramsay, R. J. Warburton, E. J. Gansen, B. Baek, M. J. Stevens, R. P. Mirin, and S. W. Nam, "Submicrometer photoresponse mapping of nanowire superconducting single-photon detectors," *Appl. Phys. Lett.*, vol. 91, p. 241108, 2007.

[56] K. M. Rosfjord, J. K. W. Yang, E. A. Dauler, A. J. Kerman, V. Anant, B. M. Voronov, G. N. Gol'tsman, and K. K. Berggren, "Nanowire single-photon detector with an integrated optical cavity and anti-reflection coating," *Optics Express*, vol. 14, p. 527, 2006.

[57] X. Hu, E. A. Dauler, R. J. Molnar, and K. K. Berggren, "Superconducting nanowire single-photon detectors integrated with optical nano-antennae," *Optics Express*, vol. 19, p. 17, 2011.

[58] M. G. Tanner, C. M. Natarajan, V. K. Pottapenjara, J. A. O'Connor, R. J. Warburton, R. H. Hadfield, B. Baek, S. Nam, S. N. Dorenbos, E. B. Ureña, T. Zijlstra, T. M. Klapwijk, and V. Zwiller, "Enhanced telecom wavelength single-photon detection with NbTiN superconducting nanowires on oxidized silicon," *Appl. Phys. Lett.*, vol. 96, p. 221109, 2010.

[59] J. P. Sprengers, A. Gaggero, D. Sahin, S. Jahanmirinejad, G. Frucci, F. Mattioli, R. Leoni, J. Beetz, M. Lermer, M. Kamp, S. Höfling, R. Sanjines, and A. Fiore, "Waveguide superconducting single-photon detectors for integrated quantum photonic circuits," *Appl. Phys. Lett.*, vol. 99, p. 181110, 2011.

[60] A. Semenov, P. Haas, K. Il'in, H.-W. Hübers, M. Siegel, A. Engel, and A. Smirnov, "Energy resolution and sensitivity of a superconducting quantum detector," *Physica C*, vol. 460, p. 1491, 2007.

[61] P. Haas, A. Semenov, H.-W. Hübers, J. Beyer, A. Kirste, T. Schurig, K. Il'in, M. Siegel, A. Engel, and A. Smirnov, "Spectral sensitivity and spectral resolution

of superconducting single-photon detectors," *IEEE Trans. Appl. Supercond.*, vol. 17, p. 298, 2007.

[62] A. J. Annunziata, O. Quaranta, D. F. Santavicca, A. Casaburi, L. Frunzio, M. Ejrnaes, M. J. Rooks, R. Cristiano, S. Pagano, A. Frydman, and D. E. Prober, "Reset dynamics and latching in niobium superconducting nanowire single-photon detectors," *J. Appl. Phys.*, vol. 108, p. 084507, 2010.

[63] S.-Z. Lin, O. Ayala-Valenzuela, R. D. McDonald, L. N. Bulaevskii, T. Holesinger, F. Ronning, N. R. Weisse-Bernstein, T. L. Williamson, A. H. Mueller, M. A. Hoffbauer, M. R. Rabin, and M. J. Graf, "Characterization of thin-film NbN superconductor for single-photon detection by transport measurements," *ArXiv e-prints: 1212.2258*, Dec. 2012.

[64] K. Il'in, M. Lindgren, M. Currie, A. D. Semenov, G. N. Gol'tsman, R. Sobolewski, S. I. Cherednichenko, and E. M. Gershenzon, "Picosecond hot-electron energy relaxation in NbN superconducting photodetectors," *Appl. Phys. Lett.*, vol. 76, p. 2752, 2000.

[65] M. K. Akhlaghi and A. H. Majedi, "Gated mode superconducting nanowire single photon detectors," *Optics Express*, vol. 20, p. 1608, 2012.

[66] A. Korneev, P. Kouminov, V. Matvienko, G. Chulkova, K. Smirnov, B. Voronov, G. N. Gol'tsman, M. Currie, W. Lo, K. Wilsher, J. Zhang, W. Słysz, A. Pearlman, A. Verevkin, and R. Sobolewski, "Sensitivity and gigahertz counting performance of NbN superconducting single-photon detectors," *Appl. Phys. Lett.*, vol. 84, p. 5338, 2004.

[67] A. Pearlman, A. Cross, W. Słysz, J. Zhang, A. Verevkin, M. Currie, A. Korneev, P. Kouminov, K. Smirnov, B. Voronov, G. Gol'tsman, and R. Sobolewski, "Gigahertz counting rates of NbN single-photon detectors for quantum communications," *IEEE Trans. Appl. Supercond.*, vol. 15, p. 579, 2005.

[68] R. H. Hadfield, "Single-photon detectors for optical quantum information applications," *Nature Photonics*, vol. 3, p. 696, 2009.

[69] E. A. Dauler, A. J. Kerman, B. S. Robinson, J. K. Yang, B. Voronov, G. Gol'tsman, S. A. Hamilton, and K. K. Berggren, "Photon-number-resolution with sub-30-ps timing using multi-element superconducting nanowire single photon detectors," *J. Mod. Optic*, vol. 56, p. 364, 2009.

[70] M. J. Stevens, R. H. Hadfield, R. E. Schwall, S. W. Nam, R. P. Mirin, and J. A. Gupta, “Fast lifetime measurements of infrared emitters using a low-jitter superconducting single-photon detector,” *Appl. Phys. Lett.*, vol. 89, p. 031109, 2006.

[71] X. Yang, T. Yamashita, S. Miki, M. Fujiwara, M. Sasaki, L. You, and Z. Wang, “Performances of superconducting nanowire single-photon detectors with different designs,” in *Superconducting Centennial Conf. EUCAS (The Hague)*, 2011.

[72] S. Miki, H. Terai, T. Yamashita, K. Makise, M. Fujiwara, M. Sasaki, and Z. Wang, “Superconducting single photon detectors integrated with single flux quantum readout circuits in a cryocooler,” *Appl. Phys. Lett.*, vol. 99, p. 111108, 2011.

[73] K. Suzuki, S. Miki, Z. Wang, Y. Kobayashi, S. Shiki, and M. Ohkubo, “Superconducting NbN thin-film nanowire detectors for time-of-flight mass spectrometry,” *J. Low Temp. Phys.*, vol. 151, p. 766, 2008.

[74] K. Suzuki, S. Shiki, M. Ukibe, M. Koike, S. Miki, Z. Wang, and M. Ohkubo, “Hotspot detection model in superconducting nano-stripline detector for keV ions,” *Appl. Phys. Expr.*, vol. 4, p. 083101, 2011.

[75] D. Perez de Lara, M. Ejrnaes, A. Casaburi, M. Lisitskiy, R. Cristiano, S. Pagano, R. L. A. Gaggero, G. Gol’tsman, and B. Voronov, “Feasibility investigation of NbN nanowires as detector in time-of-flight mass spectrometers for macromolecules of interest in biology (proteins),” *J. Low Temp. Phys.*, vol. 151, p. 771, 2008.

[76] K. Suzuki, M. Ohkubo, M. Ukibe, K. Chiba-Kamoshida, S. Shiki, S. Miki, and Z. Wang, “Charge-state-derivation ion detection using a superconducting nanostructure device for mass spectrometry,” *Rapid Commun. Mass Spectrom.*, vol. 24, p. 3290, 2010.

[77] A. Casaburi, M. Ejrnaes, N. Zen, M. Ohkubo, S. Pagano, and R. Cristiano, “Thicker, more efficient superconducting strip-line detectors for high throughput macromolecules analysis,” *Appl. Phys. Lett.*, vol. 98, p. 023702, 2011.

[78] M. Rosticher, F. R. Ladan, J. P. Maneval, S. N. Dorenbos, T. Zijlstra, T. M. Klapwijk, V. Zwiller, A. Lupaşcu, and G. Nogues, “A high efficiency superconducting nanowire single electron detector,” *Appl. Phys. Lett.*, vol. 97, p. 183106, 2010.

[79] M. Berger, J. Coursey, M. Zucker, and J. Chang, *NIST Standard Reference Database: Stopping-power and range tables for electrons, protons, and helium ions.* No. 124, NIST, Physical Measurement Laboratory, August 2005.

[80] B. V. Estey, J. A. Beall, G. C. Hilton, K. D. Irwin, D. R. Schmidt, J. N. Ullom, and R. E. Schwall, "Time-of-flight mass spectrometry with latching Nb meander detectors," *IEEE Trans. Appl. Supercond.*, vol. 19, p. 382, 2009.

[81] D. V. Vechten and K. S. Wood, "Probability of quasiparticle self-trapping due to localized energy deposition in nonequilibrium tunnel-junction detectors," *Phys. Rev. B*, vol. 43, p. 12852, 1991.

[82] L. Parlato, G. Peluso, G. Pepe, R. Vaglio, C. Attanasio, A. Ruosi, S. Barbanera, M. Cirillo, and R. Leoni, "X-rays operation of a thin film NbVN superconducting-strip particle detector," *Nucl. Instrum. Methods A*, vol. 348, p. 127, 1994.

[83] M. A. Biondi, A. T. Forester, M. P. Garfunkel, and C. B. Satterthwaite, "Experimental evidence for an energy gap in superconductors," *Rev. Mod. Phys.*, vol. 30, p. 1109, 1958.

[84] C. Chantler, K. Olsen, R. Dragoset, J. Chang, A. Kishore, S. Kotochigova, and D. Zucker, *NIST Standard Reference Database: Detailed tabulation of atomic form factors, photoelectric absorption and scattering cross section, and mass attenuation coefficients for* $Z = 1 - 92$ *from* $E = 1 - 10\ eV$ *to* $E = 0.4 - 1.0\ MeV$. No. 66, NIST, Physical Measurement Laboratory, August 2005.

[85] B. Henke, E. Gullikson, and J. Davis, "X-ray interactions: photoabsorption, scattering, transmission, and reflection at $E = 50 - 30000$ eV," *Atomic Data and Nuclear Data Tables*, vol. 54 (no.2), pp. 181–342, 1993.

[86] K. Inderbitzin, A. Engel, A. Schilling, K. Il'in, and M. Siegel, "An ultra-fast superconducting Nb nanowire single-photon detector for soft X-rays," *Appl. Phys. Lett.*, vol. 101, p. 162601, 2012.

[87] K. Inderbitzin, A. Engel, and A. Schilling, "Soft X-Ray single-photon detection with superconducting tantalum nitride and niobium nanowires," *IEEE Trans. Appl. Supercond.*, vol. 23, p. 2200505, 2013.

[88] A. Gabutti, K. E. Gray, G. M. Pugh, and R. Tiberio, "A fast, self-recovering superconducting strip particle detector made with granular tungsten," *Nucl. Instrum. Methods A*, vol. 312, p. 475, 1992.

[89] R. H. Haitz, "Mechanisms contributing to the noise pulse rate of avalanche diodes," *J. Appl. Phys.*, vol. 36, p. 3123, 1965.

[90] S. Cova, A. Longoni, and A. Andreoni, "Towards picoseconds resolution with single-photon avalanche diodes," *Rev. Sci. Inst.*, vol. 52, p. 408, 1981.

[91] R. G. W. Brown, R. Jones, J. G. Rarity, and K. D. Ridley, "Characterization of silicon avalanche photodiodes for photon correlation measurements 2: active quenching," *Appl. Opt.*, vol. 26, p. 2383, 1987.

[92] A. R. Dixon, Z. L. Yuan, J. F. Dynes, A. W. Sharpe, and A. J. Shields, "Gigahertz decoy quantum key distribution with 1 Mbit/s secure key rate," *Opt. Express*, vol. 16, p. 18790, 2008.

[93] C. Gobby, Z. L. Yuan, and A. J. Shields, "Quantum key distribution over 122 km of standard telecom fiber," *Appl. Phys. Lett.*, vol. 84, p. 3762, 2004.

[94] A. Thompson, D. Attwood, E. Gullikson, M. Howells, K.-J. Kim, J. Kirz, J. Kortright, I. Lindau, Y. Liu, P. Pianetta, A. Robinson, J. Scofield, J. Underwood, G. Williams, and H. Winick, *X-Ray data booklet.* Lawrence Berkeley National Laboratory, Berkeley, 3rd ed., 2009.

[95] B. Cabrera, R. M. Clarke, P. Colling, A. J. Miller, S. Nam, and R. W. Romani, "Detection of single infrared, optical and ultraviolet photons using superconducting transition edge sensors," *Appl. Phys. Lett.*, vol. 73, p. 735, 1998.

[96] A. J. Miller, S. W. Nam, J. M. Martinis, and A. V. Sergienko, "Demonstration of a low-noise near-infrared photon counter with multiphoton discrimination," *Appl. Phys. Lett.*, vol. 83, p. 791, 2003.

[97] A. Verevkin, A. Pearlman, W. Słysz, J. Zhang, M. Currie, A. Korneev, G. Chulkova, O. Okunev, P. Kouminov, K. Smirnov, B. Voronov, G. N. Gol'tsman, and R. Sobolewski, "Ultrafast superconducting single-photon detectors for near-infrared-wavelength quantum communications," *J. Mod. Optic*, vol. 51, p. 1447, 2004.

[98] B. Cabrera, "Introduction to TES physics," *J. Low Temp. Phys.*, vol. 151, p. 82, 2008.

[99] A. E. Lita, A. J. Miller, and S. W. Nam, "Counting near-infrared single-photons with 95% efficiency," *Opt. Express*, vol. 16, p. 3032, 2008.

[100] D. Rosenberg, A. E. Lita, A. J. Miller, and S. W. Nam, "Noise-free high-efficiency photon-number-resolving detectors," *Phys. Rev. A*, vol. 71, p. 061803(R), 2005.

[101] S. Bandler, R. Brekosky, A.-D. Brown, J. Chervenak, E. Figueroa-Feliciano, F. Finkbeiner, N. Iyomoto, R. Kelley, C. Kilbourne, F. Porter, J. Sadleir, and S. Smith, "Performance of TES X-ray microcalorimeters with a novel absorber design," *J. Low Temp. Phys.*, vol. 151, p. 400, 2008.

[102] Joel Ullom, NIST Boulder, URL: http://www.slac.stanford.edu/econf/C0604032/talks/snic_ullom.pdf (08.01.2013), "Transition-edge sensors for precision measurements from γ-ray to sub-mm wavelengths," April 2008.

[103] P. Lerch and A. Zehnder, *Cryogenic particle detection (Editor: Ch. Enss)*, vol. 99 of *Topics in applied physics*. Springer, Berlin, 1st ed., 2005.

[104] S. Friedrich, "Superconducting tunnel junction photon detectors: theory and applications," *J. Low Temp. Phys.*, vol. 151, p. 277, 2008.

[105] J. H. J. de Bruijne, A. P. Reynolds, M. A. C. Perryman, F. Favata, and A. Peacock, "Analysis of astronomical data from optical superconducting tunnel junctions," *Opt. Eng.*, vol. 41, p. 1158, 2002.

[106] G. Angloher, P. Hettl, M. Huber, J. Jochum, F. v. Feilitzsch, and R. L. Mößbauer, "Energy resolution of 12 eV at 5.9 keV from Al-superconducting tunnel junction detectors," *J. Appl. Phys.*, vol. 89, p. 1425, 2001.

[107] Hamamatsu Photonics K.K., Systems Division, Japan, URL: http://sales.hamamatsu.com/assets/pdf/catsandguides/e_streakh.pdf (08.01.2013), "A guide to streak cameras," April 2008.

[108] J. Feng, K. Engelhorn, B. I. Cho, H. J. Lee, M. Greaves, C. P. Weber, R. W. Falcone, H. A. Padmore, and P. A. Heimann, "A grazing incidence X-ray streak camera for ultrafast, single-shot measurements," *Appl. Phys. Lett.*, vol. 96, p. 134102, 2010.

[109] L. Yu, X. Liu, S. Leng, J. M. Kofler, J. C. Ramirez-Giraldo, M. Qu, J. Christner, J. G. Fletcher, and C. H. McCollough, "Radiation dose reduction in computed tomography: techniques and future perspective," *Imaging Med.*, vol. 1, p. 65, 2009.

[110] H. Bartolf, K. Inderbitzin, L. B. Gómez, A. Engel, and A. Schilling, "Nanoscale fabrication by intrinsic suppression of proximity-electron exposures and general considerations for easy and effective topdown fabrication," *J. Micromech. Microeng.*, vol. 20, p. 125015, 2010.

[111] K. Il'in, M. Siegel, A. Engel, H. Bartolf, A. Schilling, A. Semenov, and H.-W. Hübers, "Current-induced critical state in NbN thin-film structures," *J. Low Temp. Phys.*, vol. 151, p. 585, 2008.

[112] J. K. W. Yang, E. Dauler, A. Ferri, A. Pearlman, A. Verevkin, G. Gol'tsman, B. Voronov, R. Sobolewski, W. E. Keicher, and K. K. Berggren, "Fabrication development for nanowire GHz-counting-rate single-photon detectors," *IEEE Trans. Appl. Supercond.*, vol. 15, p. 626, 2005.

[113] E. Helfand and N. R. Werthamer, "Temperature and purity dependence of the superconducting critical field, H_{c2}. II," *Phys. Rev.*, vol. 147, p. 288, 1966.

[114] A. J. Kerman, E. A. Dauler, W. E. Keichler, J. K. W. Yang, K. K. Berggren, G. Gol'tsman, and B. Voronov, "Kinetic-inductance-limited reset time of superconducting nanowire photon counters," *Appl. Phys. Lett.*, vol. 88, p. 111116, 2006.

[115] N. S. Nise, *Control Systems Engineering.* Wiley, Hoboken NJ, 4th ed., 2004.

[116] "Oxford instruments application note: Typical spectrum for tungsten-target X-ray tube (AN012 rev. A)," tech. rep., Oxford Instruments, 2007.

[117] "XTF5011 flux data," tech. rep., Oxford Instruments, 2010.

[118] T. M. Buzug, *Computed tomography - from photon statistics to modern cone-beam CT.* Springer, Berlin, 1st ed., 2008.

[119] "Certificate No. 148273 - NK 765 for a sealed radioactive source," tech. rep., Eckert & Ziegler, Nuclitec GmbH, January 2012.

[120] G. Audia, O. Bersillon, J. Blachot, and A. Wapstra, "The NUBASE evaluation of nuclear and decay properties," *Nucl. Phys. A*, vol. 729, p. 3, 2003.

[121] E. M. A. Hussein, *Handbook on radiation probing, gauging, imaging and analysis - Volume 1: basics and techniques.* Kluwer Academic Publishers, Dordrecht (Netherlands), 1st ed., 2003.

[122] "Beryllium X-ray window coatings," tech. rep., Brush Wellman Inc., 44036 South Grimmer Blvd., Fremont, CA 94538, Octobre 2003.

[123] E. T. Arakawa, T. A. Callcou, and Y.-C. Chang, "The optical properties of Berryllium," Tech. Rep. ORNL/OMIS-89/9, Oak Ridge National Laboratory, Health and Safety Research Division, Oak Ridge TN, February 1990.

[124] K. Il'in, R. Schneider, D. Gerthsen, A. Engel, H. Bartolf, A. Schilling, A. Semenov, H.-W. Hübers, B. Freitag, and M. Siegel, "Ultra-thin NbN films on Si: crystalline and superconducting properties," *Journal of Physics: Conference Series*, vol. 97, p. 012045, 2008.

[125] A. I. Gubin, K. S. Il'in, S. A. Vitusevich, M. Siegel, and N. Klein, "Dependence of magnetic penetration depth on the thickness of superconducting Nb thin films," *Phys. Rev. B*, vol. 72, p. 064503, 2005.

[126] H. Bartolf, A. Engel, A. Schilling, K. Il'in, M. Siegel, H.-W. Hübers, and A. Semenov, "Current-assisted thermally activated flux liberation in ultrathin nanopatterned NbN superconducting meander structures," *Phys. Rev. B*, vol. 81, p. 024502, 2010.

[127] K. Suzuki, M. Ukibe, S. Shiki, S. Miki, Z. Wang, Y. Takahashi, N. Yoshikawa, and M. Ohkubo, "Pulse-height distribution analysis for superconducting nano-stripline ion detector with a fast pulse-integration analog-to-digital converter," *Physics Procedia*, vol. 36, p. 172, 2012.

[128] D.-K. Liu, S.-J. Chen, L.-X. You, Y.-L. Wang, S. Miki, Z. Wang, X.-M. Xie, and M.-H. Jiang, "Nonlatching superconducting nanowire single-photon detection with quasi-constant-voltage bias," *Appl. Phys. Expr.*, vol. 5, p. 125202, 2012.

[129] A. M. Smith, "A multi-layer three dimensional superconducting nanowire photon detector," *Proceedings of SPIE Volume 8400*, p. 84000L, 2012.

Publikationsliste

Während Promotionsstudium publiziert:

- **Temperature-dependence of detection efficiency in NbN and TaN SNSPD**
  A. Engel, K. Inderbitzin, A. Schilling, R. Lusche, A. Semenov, H.-W. Hübers, D. Henrich, M. Hofherr, K. Il'in, M. Siegel
  IEEE Transactions on Applied Superconductivity **23**, 2300505 (2013)

- **Soft X-ray single-photon detection with superconducting tantalum nitride and niobium nanowires**
  K. Inderbitzin, A. Engel, A. Schilling
  IEEE Transactions on Applied Superconductivity **23**, 2200505 (2013), Selected for the Oct/Nov 2012 issue of the European Superconductivity News Forum

- **An ultra-fast superconducting Nb nanowire single-photon detector for soft X-rays**
  K. Inderbitzin, A. Engel, A. Schilling, K. Il'in, M. Siegel
  Applied Physics Letters **101**, 162601 (2012)

- **Tantalum nitride superconducting single-photon detectors with low cut-off energy**
  A. Engel, A. Aeschbacher, K. Inderbitzin, A. Schilling, K. Il'in, M. Hofherr, M. Siegel, A. Semenov, H.-W. Hübers
  Applied Physics Letters **100**, 062601 (2012)

- **Ultra-thin TaN films for superconducting nanowire single-photon detectors**
  K. Il'in, M. Hofherr, D. Rall, M. Siegel, A. Semenov, A. Engel, K. Inderbitzin, A. Aeschbacher, A. Schilling
  Journal of Low Temperature Physics **167**, 809-814 (2012)

- **Nanoscale fabrication by intrinsic suppression of proximity-electron exposures and general considerations for easy and effective top-down fabrication**
  H. Bartolf, K. Inderbitzin, L. B. Gómez, A. Engel, A. Schilling
  JOURNAL OF MICROMECHANICS AND MICROENGINEERING **20**,125015 (2010)

Sonstige:

- **Franck-Condon blockade in suspended carbon nanotube quantum dots**
  R. Leturcq, Ch. Stampfer, K. Inderbitzin, L. Durrer, Ch. Hierold, E. Mariani, M. G. Schultz, F. von Oppen, K. Ensslin
  NATURE PHYSICS **5**, 327-331 (2009)

Lebenslauf

INDERBITZIN,
Kevin Michel
Geburtsdatum: 15. Mai 1984
aus Baar ZG und Schwyz SZ

Ausbildung:

1997 - 06.2003:	**Kantonsschule Zug**
	Matura
	Schwerpunktsfach Physik und Anwendungen der Mathematik
10.2003 - 02.2008:	**ETH Zürich**
	Diplomstudium Experimentalphysik
	Spezialisierung: Nichtlineare Optik und Halbleiter-Nanostrukturen
	Diplomarbeit: “Transport in Carbon Nanotubes”
10.2006 - 04.2012:	**ETH Zürich**
	Lehrdiplom für Maturitätsschulen in Physik
02.2009 - 05.2013:	**Universität Zürich**
	Promotion in Experimentalphysik

Berufserfahrung:

08.2008 - 01.2009:	**Kantonsschule Zug**
	Physik-Fachlehrer an Gymnasium und Wirtschaftsmittelschule
02.2009 - 06.2013	**Universität Zürich**
(auch 06. - 07.2008):	Doktorand, Übungsleiter und -assistent in Experimentalphysik

Einige Danksagungen

Allen voran möchte ich Beatrice, Jörg und Dennis, meiner Familie, danken für die unglaubliche Unterstützung, die sie mir in all den vielen Jahren gegeben haben und immer noch geben, insbesondere meiner Mutter Beatrice. Sie haben mir durch alle Hoch und Tiefs hindurch geholfen, und dafür bin ich ihnen von tiefstem Herzen dankbar.

Prof. Andreas Schilling, Andreas Engel und Holger Bartolf bin ich zu grossem Dank verpflichtet, dass ich die letzten vier Jahre mit ihnen zusammen in einer menschlich sehr angenehmen Atmosphäre an diesem sehr spannenden und fruchtbaren Forschungsprojekt arbeiten durfte. Diese Jahre waren für mich nicht nur fachlich, sondern auch persönlich eine sehr grosse Bereicherung, und nicht zuletzt hat die Arbeit an diesem Projekt auch grossen Spass gemacht. Die Tatsache, dass das Projekt erfolgreich war, zeigt deutlich, dass die Zusammenarbeit sehr gut funktioniert hat. Prof. Schilling möchte ich besonders dafür danken, dass er stets für alle Ideen, Bedenken und Sorgen ein offenes Ohr hatte, wie auch stets bereit war, konkreten Input zu Messungen und Papern zu geben, was ich als aussergewöhnlich empfunden habe. Andreas Engel will ich dafür danken, dass er sich stets persönlich verpflichtet gefühlt hat, Probleme bei Messungen zu lösen, mir bei meinen Interpretationen der Daten sowie beim Korrekturlesen der Paper zu helfen, sowie mir manche theoretische Finesse zu erklären. Er hat mich nicht nur in die Welt dieser Detektoren eingeführt, sondern mich auch auf meinem Weg an die Forschungs-Front dieses Gebietes begleitet und unterstützt. Holger Bartolf bin ich zu äusserst grossem Dank verpflichtet, da er mich einerseits gründlich in die Welt der Nanostrukturierung im Reinraum eingeführt hat, und mit mir mit Geduld alle Prozessschritte eingeübt hat. Andererseits waren auch die Diskussionen mit ihm über mögliche Detektor-Realisierungen und physikalische Modelle sehr konstruktiv.

Olaf Bossen, Henrik Grundmann, Stefan Siegrist, Fabian von Rohr und meinen anderen Freunden vom Institut möchte ich herzlich danken für die menschlich tolle Atmosphäre und die vielen guten Unterhaltungen, die wir bei manchem Mittagessen, Kaffee und sonstigen Unternehmungen gehabt haben. Und nicht zuletzt natürlich für ihre stete Hilfsbereitschaft und Geduld. Speziellen Dank möchte ich auch an unsere ausgesprochen mo-

tivierten Master- und Bachelor-Studenten Simon Gross, Adrian Aeschbacher und Daniel Destraz richten, die äussert geduldig an unserem Projekt gearbeitet haben, selbst wenn die Dinge nicht auf Anhieb funktioniert haben. Adrian möchte ich besonders danken für seinen unermüdlichen Einsatz über ein ganzes Jahr hinweg.

Konstantin Il'in, Prof. Michael Siegel, Dagmar Henrich und Matthias Hofherr vom Karlsruhe Institute of Technology möchte ich herzlich danken für die tolle Kollaboration über die vielen Jahre hinweg. Die vielen produktiven, aber auch menschlichen Gespräche und Lektorate waren für mich und dieses Projekt von grosser Bedeutung. Speziell möchte ich auch Konstantin Il'in danken für die hochqualitativen Filme, die er uns jeweils in kürzester Zeit hergestellt hat.

Unseren Metall- und Elektronik-Werkstätten bin ich sehr dankbar, da sie innert kurzer Zeit jeweils wichtige Bestandteile für unsere Experimente geliefert haben, bei technischen Problemen immer kurzfristig ausgeholfen haben und auch bei Fehlern unsererseits stets eine Lösung gefunden haben.

Peter Robmann möchte ich für seine spontane Hilfsbereitschaft danken im Umgang mit der Isotopenquelle.

Einen grossen Dank möchte ich den Mitarbeitenden und Kollegen vom FIRST aussprechen. Ihre stete und spontane Hilfsbereitschaft hat mich immer wieder überrascht, und ich bin dankbar, dass ich meine Proben in einem so tollen Umfeld herstellen konnte.

Dieses Projekt wurde grosszügig unterstützt vom Schweizerischen Nationalfonds zur Förderung der wissenschaftlichen Forschung.